Universiteit
Antwerpen

Faculteit Wetenschappen
Departement Fysica

Strongly correlated electronic systems: influence of electric field and doping

Sterk Gecorreleerde elektronische systemen: Invloed van het elektrisch veld en dotering

Proefschrift voorgelegd tot het behalen van de graad van doctor in de wetenschappen aan de Universiteit Antwerpen te verdedigen door

Davoud Nasr Esfahani

Promotor: Prof. Dr. François Peeters,
Co-promotor: Dr. L. Covaci.

Antwerpen 2014

Members of the Jury:

Chairman
Prof. Dr. Jacques Tempere, Universiteit Antwerpen, Belgium.

Supervisor
Prof. Dr. François Peeters, Universiteit Antwerpen, Belgium,
Dr. Lucian Covaci, Universiteit Antwerpen, Belgium.

Members
Prof. Dr. Dirk Lamoen, Universiteit Antwerpen, Belgium,
Prof. Dr. Jean-Pierre Locquet, Universiteit KU Leuven, Belgium,
Dr. Jörg Bünemann, Philipps Universität Marburg, Germany,
Prof. Dr. Panagiotis Vasilopoulos, Concordia University, Montreal, Canada.

Contact Information

Davoud Nasr Esfahani
G.U. 206
Groenenborgerlaan 171
2020 Antwerpen
Belgium
dd.nasr@gmail.com

Acknowledgement

This research work could not have been done without the support and encouragement from numerous individuals.

First of all, I am indebted to my supervisor, Prof. François Peeters for his guidance, patience, motivation, and enthusiasm during my PhD study. He has given me the opportunity and complete freedom to work on interesting research topics. It is my privilege to be his student. I would like to express my gratitude to my copromoter Dr. Lucian Covaci who has been a significant support throughout my PhD work. I am grateful to my collaborators Prof. Dr. Bart Partoens, Dr. Ortween Leenaerts, Dr. Koen Martens, Dr. Hasan Sahin and Petar Bakalov. I would like to thank to my thesis committee: Prof. Dr. Jacques Tempére, Prof. Dr. Dirk Lamoen, Prof. Dr. Jean-Pierre Locquet, Dr. Jörg Bünemann, and Prof. Dr. Panagiotis Vasilopoulos for reviewing my thesis and giving their insightful comments. I would like thank all the CMT group members and our secretary Ms. Evans Hilde, an incredibly nice person for all her administrative support. I would also like to thank especially the Iranian student community for being such nice friends. Last but not least, I want to give my deepest appreciation to my whole family and friends in Iran for their support and love. I would like in particularly thank the ones who brings joy and happiness every day of my life: my wife Mitra and my son Behrad. Finally, I thank the Flemish Science Foundation (FWO-Vl) for financial support.

Davoud Nasr Esfahani

Contents

List of Abbreviations

1D	One dimensional
2D	Two dimensional
3D	Three dimensional
MIT	Metal Insulator Transition
BO	Bloch oscillations
DFT	Density functional theory
DOS	Density of states
GA	Gutzwiller approximation
NRG	Numerical renormalization group
QP	Quasi-particle
LZ	Landau-Zener
ED	Exact diagonalization
DMRG	Density matrix renormalization group
SDW	Spin density wave
CDW	Charge density wave
SBMFT	Slave boson mean field theory
LDA	Local density approximation
DMFT	Dynamical mean field theory
CTQMC	Continuous time quantum Monte Carlo

Chapter 1

Introduction

Any change of an external parameter like electric field, magnetic field or pressure leads to changes in the properties of a system. Sometimes the change of these external parameters, either small or large, leads to a significant change in the behavior of the system i.e., a phase transition may happen. Among the different kind of phase transitions, the transition form a metallic (insulating) state to an insulating (metallic) state has been one of the most important one both from a fundamental and a technological point of view. Significant efforts have been devoted to phase transitions induced by the application of an electric field, which could lead to either a magnetic phase transition in multifferoic materials [1] or a metal insulator transition (MIT). The MIT when induced by an external electric field is of special importance and it may been exploited in the microelectronic industry as a base for the production of switching devices. A three terminal device, like the one shown in Fig. 1.1 is normally used for switching proposes. Upon gating, the active material is either a metal or an insulator, resulting in a tunable manipulation of the current. The mechanism which leads to MIT could be different for different kinds of active materials. From the beginning, since the invention of transistors by Shockley, Brattain and Bardeen in 1948, silicon has been the most prominent material which is used as an active material. From the early development of microelectronics, a large effort has been devoted to mak the devices smaller and more efficient in the sense of e.g. energy consumption. The down-scaling of the devices has been one of the most important aspects of the industry. This was pointed out by Intel's co-founder Gordon E. Moore, in his paper [2], which resulted in Moore's law. Moore's law relies on his observation that since the invention of computing hardware, the number of transistors in each device doubles in approximately each 2 years as is presented in Fig. 1.2. Surprisingly, Moore's law has remained valid and works accurately since that time. The prediction of Moore's law is extensively used by the microelectronic industry to set targets for long-term planning for future research and development. Although this

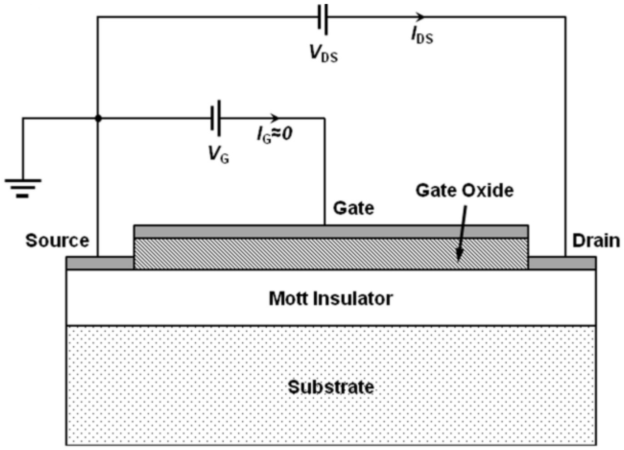

Figure 1.1: Schematics of a three terminal device setup, proposed for Mott-MIT devices, adopted from [4].

historical trend has continued for more than half a century, Moore's law is only an observation and not a natural law. In order to keep Moore's law valid the main trend has long been the scaling of the devices dimensions according to scaling laws. However semiconducting devices based on silicon are approaching their fundamental limitations [3]. For example, by scaling the planar bulk metal-oxide-semiconductor field-effect-transistor (MOSFET), in order to gain enough control of short-channel effects and to set the threshold voltage accordingly, one needs to increase the level of doping to very large levels, and as a result of such high channel doping, carriers (hole or electrons) mobility decrease considerably. At the same time the junction leakage due to band-to-band tunneling will increase. To subdue these difficulties several attempts have been made and crucial developments have been achieved. In particular one of the most recent advancements achieved by Intel found that a the 22nm TriGate transistor performance is better than that of a 32nm planar transistor, and therefore it keeps Moore's law still going [5]. Sources in 2005 expected it to remain valid until at least 2015 or 2020. However, the 2010 update of the International Technology Road map for Semiconductors predicted that growth will slow at the end of 2013, when transistor counts and densities are to double only every three years. Therefore because of the expected limitations of silicon based devices several attempts have been proposed to replace them by alternations.

1.1 Alternative candidates for silicon devices

Among these are the replacement of silicon by high mobility semiconductors such as Ge and GaAs, or materials for which the MIT is not doping based, i.e. piezoelectric transis-

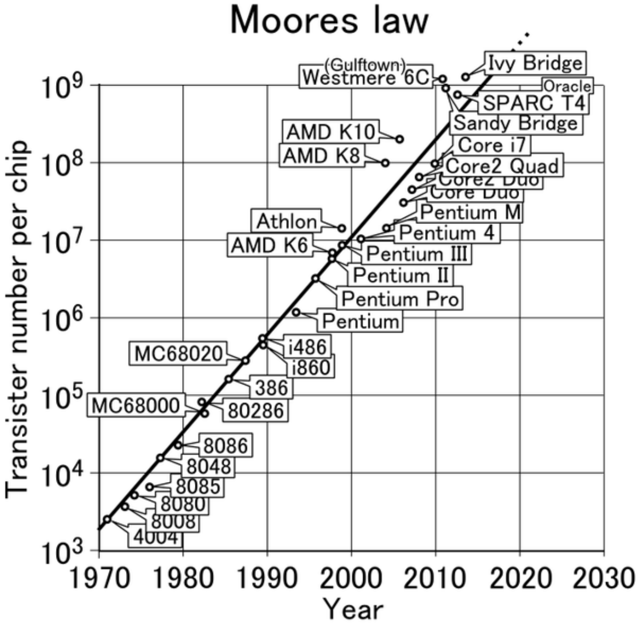

Figure 1.2: Illustration of Moore's law: Doubling of number of components on a chip roughly every two years.

tors, where a piezoelectric material is used as channel and the MIT happens by a gate-induced pressure upon changing the gate voltage [6]. Switching phenomena is not limited to MIT materials that undergo a metal to insulator transition upon gating, but other kinds of off/on control of the current have recently also been realized experimentally based on a superconductor to insulator transition at the interface of $LaAlO_3$/$SrTiO_2$ structures [7]. Another class of materials that has been proposed as channel material are those which exhibit a Mott-metal insulator transition, for which the electronic phase diagram depends on doping levels and Coulomb interaction strength. The rich phase diagram of these systems make them a potential candidate for which the amount of the concentration of free carriers induced by gate voltage could possibly lead to large modulations of free carriers, more effectively in comparison to conventional field-effect transistors (FET).

Among these correlated materials is V_2O_3, which is considered as a prototype Mott insulator which suffers from a first order MIT from a paramagnetic insulator to a paramagnetic metal without any modification of the point group of the crystal structure [8]. Another commonly used material is VO_2 which has been shown to have a more band like insulating character while correlation effects could not be ruled out [9], and furthermore it suffers from a MIT due to a structural transition from a monoclinic M1 to a Rutile phase as function of temperature at room temperature [10]. From the technological point of view, thanks to recent advances in fabrication facilities, such as Pulsed Laser Deposition (PLD) or oxygen-assisted molecular beam epitaxy(MBE), the fabrication of heterostructures with very high quality has becomes possible. For the specific device in Fig. 1.3(a), a cross-section of a three terminal device is shown and it consist of a VO_2 channel which is grown on the single crystalline (001) TiO_2 substrate by PLD. The main feature which is common in all three former cases is the presence of transitional metals in their chemical composition, which have an open shell with d orbitals. The main character of the d-orbitals is the fact that they are less spread in space in comparison to s or p type orbitals which results in a weak overlap of orbitals from nearest neighbor atoms. This in turn leads to small kinetic energy and a narrower band-width . The lower kinetic energy results in a longer time each electron spends around the specific atom in which it is localized and thus feels more the presence of other electrons in other orbitals in comparison to wider band-width materials and therefore stronger local interactions between electrons occurs locally.

Following reference [11], this could be qualitatively explained as follows, considering that the correlated electrons have a well defined single particle dispersion as ϵ_k then the velocity of this quasi-particles (QP) is defined as $v_k = \frac{1}{\hbar}\nabla_k \epsilon_k$. This velocity could be estimated as $v_k \sim a/\tau$, where a is the lattice constant and τ is the amount of the time each electron spends in each atomic site. On the other hand the velocity could be approximated as $\frac{1}{\hbar}\nabla_k \epsilon_k \sim \frac{1}{\hbar} aW$, where W is the band width which is proportional to hopping amplitude between nearest neighbor sites (the energy overlap between orbitals in nearest neighbor sites). Finally after combining the two velocities, one achieves an approximate measure for the amount of time each electron spends at each atomic center as: $\tau = \hbar/W$. Therefore smaller band width leads to a larger time each electron spends around the atomic centers. This implies that when the band-width is narrower, the local interaction between electrons in the different orbitals is locally enhanced.

While the presence of correlations leads to many exotic phenomena inclusive of high temperature superconductivity [12], heavy fermions [13], multifferoics [1] and metal insulator transitions [14, 15], the presence of strong local interactions also leads to collective correlated dynamics, i.e. simple single electron approaches do not work properly for this kind of systems because the electrons are not independent anymore. Correlation effects in turn lead to significant quantitative and qualitative changes of the physical properties of the system when compared to materials with weak interactions.

In particular, theoretical predictions imply the presence of different energy scales in the spectral function, i.e. in the metallic regime the low energy scales near the Fermi surface, which results in a renormalized QP peak near the Fermi surface. These QP excitations are well defined at low enough temperatures, and correlation effects lead to an enhanced effective mass for QP excitations near the Fermi surface with very large life time based on the Fermi liquid theory. The other energy scale is the one defined by the lower and higher Hubbard bands and does not obey Fermi liquid theory. In this case single particle excitations are significantly scattered and have a small life time. These features are illustrated in Fig. 1.4 , which shows that the lower and higher Hubbard bands are reproduced as the interaction increases. The appearance of the Hubbard bands is simultaneous with the narrowing of the spectral peak at the center. Finally the QP peak disappears when the system turns into an insulating state and the effective mass diverges, i.e. a Mott-MIT occurs. Another feature of the spectral function is its non-rigid behavior, showing that, there are spectral changes due to the changing of the chemical potential. This happens either if the chemical potential is within the gap of the insulating state at half filling, or for a doped insulator, or in weakly correlated metallic regimes [16].

The essence of surface effects manifests itself in photo-emission experiments. For $(V_{1-x}Cr_x)_2O_3$ as a prototype material which shows the Mott transition [8], early photoemission experiments failed to uncover the coexistence of a sharp peak near the Fermi surface together with the lower and higher Hubbard bands in the spectral function [17–20], instead the electronic spectral function was dominated by the lower Hubbard band with small spectral weight at the Fermi surface towards weak metallization. The same phenomenon was reported much earlier in f-electron materials [21] and later assigned to large surface effects due to strong correlation effects [22]. In the end, the inconsistency between theory and experiments was resolved by using photoelectrons with larger kinetic energy such that they could penetrate deep inside the bulk material and eventually a QP peak coexisting with the lower and higher Hubbard bands was revealed [23–28].

From a theoretical point of view it is known that the modified parameters of the Hamiltonian, i.e. the lower coordination number at the surface, leads to the lack of kinetic energy for the electrons at the surface which pushes the surface closer to the Mott transition in comparison with the bulk. Furthermore, noninteracting or weakly interacting correlated metals do not have any intrinsic length-scale other than the Fermi length scale, therefore any disorder like surface or interface can only penetrate into the bulk as a power law decaying disturbance, which is related to Friedel oscillations. However this is not the case for the strongly correlated regime, where imperfections could penetrate into the bulk at very large distances with a length scale that is affected by the proximity to the transition point. These imperfections, manifest themselves in variations of the coherent part of the spectral function as function of distance from the surface [29–35]. In other words, when the parameters of the system are chosen such that it is closer to the Mott-MIT, the correlation length is larger. This length scale is only a function of bulk properties and does not depend on the strength and type of the perturbation [29, 33]. This feature was recently realized experimentally, and it was shown that the surface region is extended much more than in the case of a normal metallic system. This becomes important in particular in the

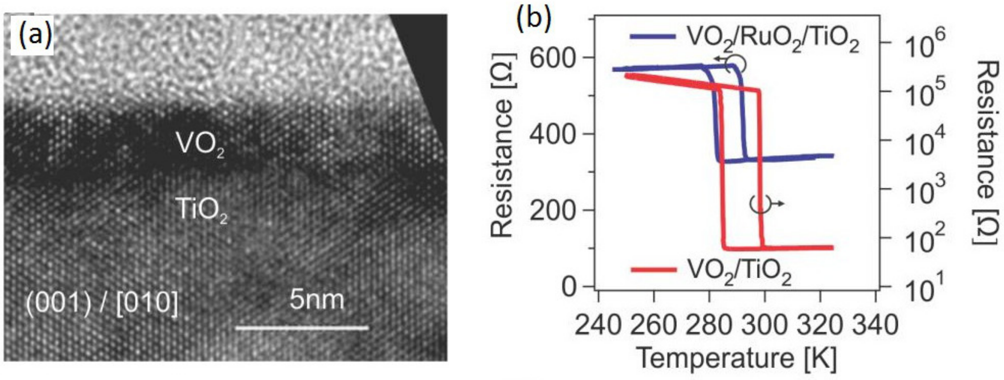

Figure 1.3: (a) TEM cross section of VO$_2$ film, (b) First order MIT as function of temperature, adopted from [37].

vicinity of the Mott MIT with a length scale that is only a characteristic feature of the bulk properties [36]. This in turn leads to an extended dead zone layer with very low QP weight, the signature of an insulating character. The presence of this well defined length scale which characterizes how a perturbation could penetrate into the bulk by affecting the QP weight implies the surfaces and interfaces and the thickness of the devices which are produced with these kind of materials will be important. This behavior is important not only for the charge neutral systems but also when the system is doped or is subjected to an external electric field [34].

In order to understand the behavior of this class of systems under the influence of doping or an external electric field, in addition to bulk calculations, theoretical investigations and numerical simulations based on inhomogeneous systems are vital. Realistic theoretical calculations based on combined dynamical mean field theory (DMFT) [38] and electronic structure methods are quite expensive computationally and the complexity of the calculations is much larger for translational broken systems such that it becomes almost impossible to perform full realistic LDA+DMFT calculations for heterostructures (the complexity of the calculations scales linearly at least with the number of sites that one should consider for DMFT self consistency).

On the other hand it appears that simplified model Hamiltonians based on single band or two band Hubbard models could capture qualitatively at least the main features of correlated electron systems in translational broken configurations [33]. Furthermore, full DMFT calculations for systems described by single or two band Hubbard models are also expensive for heterostructures and simplifications could help to reveal the main features of correlated system while the computational expenses are still manageable. One of the goals of this dissertation is to investigate and understand the effects of doping, together with the effect of an external electric field in the presence of surfaces (interfaces) in strongly correlated materials. The models which we will investigate are slab geometries, motivated by the presence of a capacitor setup in the normal three terminal field effect transistors, as is shown in Fig. 1.1.

Another promising class of systems which has recently grasped lots of attention are 2D transition metal dichalcogenide materials [39]. Among this class of materials belong monolayers of $\mathrm{MoS_2}$, which have recently been interested as an active material for FET applications. The presence of a direct bandgap ($\sim 1.8eV$) in monolayer $\mathrm{MoS_2}$ make it possible to use it as a FET with an on/off ratio of about $\sim 10^8$ [40]. The presence of high-κ dielectrics in these devices leads to an enhancement of their mobility $\sim 100cm^2/Vs$ [40], which is much lower in comparison with graphene but it is high in comparison with layered semiconductors [39]. Due to the presence of a transition metal element in $\mathrm{MoS_2}$ it is predicted that it acquires a larger ratio r_s , i.e. the average electron-electron interaction energy to the Fermi energy, and therefore larger correlation effects are expected in comparison to normal 2D systems like graphene. This enhanced correlation effects therefore could lead to more exhaustive phenomena/phase transitions such as superconductivity or superfluidity, unpon gating or equivalently doping. Another promising feature of this material is the presence of structural degrees of freedom, i.e. a conventional insulating H structure (see chapter.7) and a metallic T structure, and therefore a tunable stabilization of the T structure by using an external perturbation may lead to an enhancement of the mobility for these kind of devices.

At the end of this section we emphasize again that due to the rich phase diagram of strongly correlated systems, specially as a function of doping, practical applications of these systems are not restricted to MIT applications. New many-body phase transitions could lead to new functionalities for these class of devices, which are not expected from the conventional FET devices. For instance carrier-mediated ferromagnetic or antiferromagnetic transitions, could be interesting for magnetic logic devices.

1.2 Non adiabatic transitions in many body systems

So far our attention has been directed to adiabatic phenomena, in the sense that we only consider the electric field response of the correlated system subjected to external electric field such that there in no leakage in the capacitor setup. This approximation is still valid because these effects are already avoided by either using very strong insulators between the channel and gate contacts [37] or by using ionic liquids as gate material [42, 43]. This in turn allows the application of high electric fields in a capacitor setup without large gate

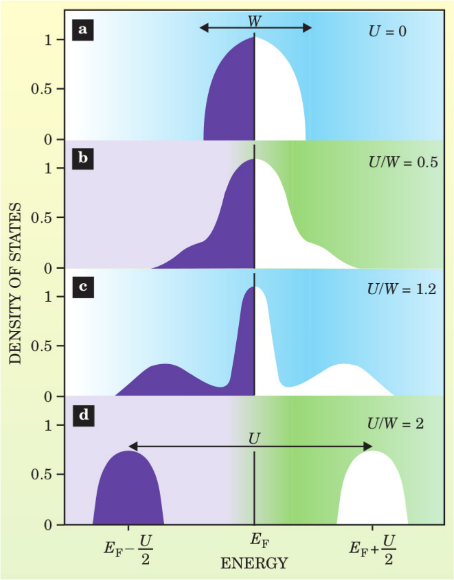

Figure 1.4: Density of states for a Hubbard model on a Bethe lattice, as a prototype system which shows a Mott-MIT at finite interaction strength, taken from [41].

leakage and therefore it avoids Joule heating. Another aspect that grasped the attention in the field of strongly correlated systems are non-adiabatic and non-equilibrium phenomena. Both from the theoretical and experimental point of view it is well known that there is a first order MIT as function of temperature in strongly correlated materials as is shown in Fig. 1.3(b). This first order transition could be accompanied by a structural phase transition like the one that occurs in VO_2 and Ca_2RuO_4 [44] or it could be a purely electronic one as seen in V_2O_3 [8]. The electric breakdown of these kinds of insulators has been the matter of long lasting debates, and the question is whether the nature of the transition is purely electronic or that Joule heating is the actual reason for the transition [45–47]. From experimental investigations it appears that explanations based on combined electro-chemical phenomena are the most relevant ones [48–52]. Shortly, this mechanism generally relies on a combined electro-chemical phenomena such that upon the application of a strong electric field in two terminal devices Joule heating, due to the passage of the current, then leads to the formation of metallic domains inside the insulating background. The formation and growth of these metallic domains finally leads to an electric breakdown of the bridge material. We show this schematically in Fig. 1.5. The nucleation of these metallic regions inside the insulating domain could be generated by imperfections inside the sample [48].

While based on the above mentioned discussions the electric breakdown in the strongly

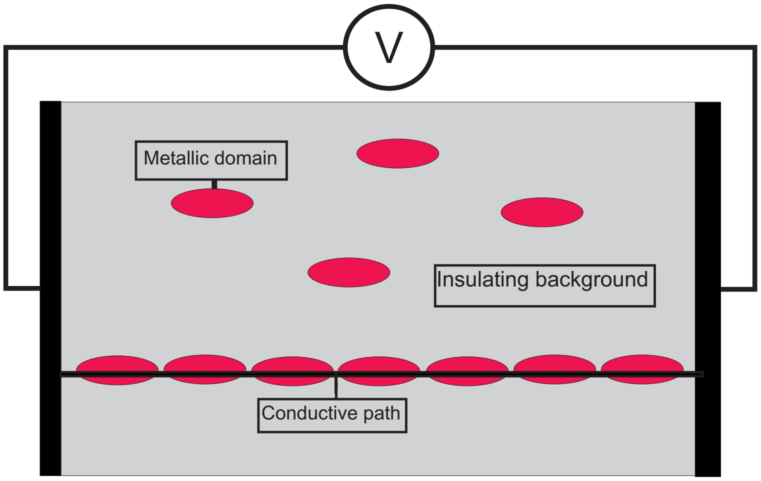

Figure 1.5: Schematics of the formation of the metallic domains in insulating back-ground.

correlated systems appears to be mostly governed by Joule heating at finite temperatures and at macroscopic length scales, the breakdown or nonlinear response to an external electric field should be also connected to a microscopic picture [53]. In particular this is important when a system is subjected to the sudden turn on of an electric field, where microscopic-electronic properties dominate the electric field response. From the fundamental point of view the problem of electric breakdown or in general electric field response to an external electric field for a closed system of interacting fermions could provide insight about the electric field response in the thermodynamic limit. This is specially important for understanding short time response of a correlated system to sudden changes of the electric field. These kind of investigations could be experimentally realized in more idealized correlated setups i.e.fermionic cold atomic traps [54–56]. The concept of an optical lattice has became experimentally feasible after the invention of laser cooling [57,58] and it was originally proposed in the context of laser spectroscopy [59, 60]. The idea behind it is to manipulate ultra cold quantum gases in an optical lattice created by laser standing waves. Therefore the atoms feel a periodic potential because of the interaction between the induced electric dipole moment of the atoms with laser standing waves [61]. Furthermore it is possible to tune the dimensionality of the trap by tuning the intensity of the laser beams, for instance it is possible to have a 1D trap by choosing the laser beam with large intensity in two directions and a small intensity in the third direction. Therefore, the quantum atomic species could move only in the direction for which the laser standing wave has smaller extrema at the anti-nodes. In most experiments the Fermi gas is produced as a mixture of two spin states, which correspond to magnetic states of the atomic ground states. Realistic experiments have been performed with fermionic isotopes of potassium

(^{40}K) and Lithium (^{6}Li) [55]. Subsequently, by using Feshbach resonances [62, 63], it is possible to tune the collisional interaction between the atoms and therefore the repulsive or attractive interaction between two atoms with different spins. This in turn gives the possibility to simulate fermionic or bososnic Hubbard models. For example, the fermionic Hubbard regime has been achieved for optical lattices constructed with $^{(40)}$K atoms [55].

1.3 Organization and contribution of the thesis

Motivated by the above mentioned discussions we performed several studies on the electric field effects on strongly correlated systems based on model Hamiltonians, including as well realistic effects of dopants and charge transfer on the correlated 2D materials. The dissertation is organized as follows:

In Chapter. 2, we present and explain the theoretical tools we have used. In particular we present a brief introduction to the different methods in the field of interacting systems, in particular we present preliminary information about the Gutzwiller variational method and the Gutzwiller approximations (GA) as well as DMFT. Furthermore we present a brief introduction to exact numerical approaches and some implementation hints, and finally we give some introductory notions about non-adiabatic phenomena and real time propagation techniques.

In Chapter. 3, the ground state properties of a paramagnetic Mott insulator are investigated in the presence of an external electrical field using the inhomogeneous GA for a single band Hubbard model in a slab geometry. The metal insulator transition is shifted towards higher Hubbard repulsions by applying an electric field perpendicular to the slab. The spatial distribution of site dependent QP weight shows that the QP weight is maximum in few layers beneath the surface. Moreover only at higher Hubbard repulsion, larger than the bulk critical interaction, the electric field will be totally screened only for centeral cites. Our results show that by presence of an electric field perpendicular to a thin film made of a strongly correlated material, states near the surface will remain metallic while the bulk becomes insulating after some critical interaction. In contrast, in the absence of the electric field the surface becomes insulating before the bulk.

In Chapter. 4, surface effects of a doped thin film made of a strongly correlated material are investigated both in the absence and presence of a perpendicular electric field. We use an inhomogeneous GA for a single band Hubbard model in order to describe correlation effects. For low doping, the bulk value of the QP weight is recovered exponentially deep into the slab, but with increasing doping, additional Friedel oscillations appear near the surface. We show that the inverse correlation length has a power-law dependence on the doping level. In the presence of an electrical field, considerable changes in the QP weight can be realized throughout the system. We observe a large difference (as large as five orders of magnitude) in the QP weight near the opposite sides of the slab. This effect can be significant in switching devices that use the surface states for transport.

In Chapter. 5, using an extension of the GA for an inhomogeneous system, we study the two band Hubbard model with unequal band widths for a slab geometry. The aim is to investigate the mutual effect of individual bands on the spatial distribution of QP weight and charge density, especially near the surface of the slab. The main effect of the difference in band width is the presence of two different length scales corresponding to the QP profile of each band. This is enhanced in the vicinity of the critical interaction of the narrow band where an orbitally selective Mott transition happens and a surface dead layer forms for the narrow band. For the doped case, two different regimes of charge transfer between the surface and the bulk of the slab are revealed. The charge transfer from surface/center to center/surface depends on both the doping level and the average relative charge accumulated in each band. Such effects could be of importance also when describing the accumulation of charges at the interface between structures made of multi-band strongly correlated materials.

In Chapter. 6, the electric-field response of a one-dimensional ring of interacting fermions, where the interactions are described by the extended Hubbard model, is investigated. By using an accurate real-time propagation scheme based on the Chebyshev expansion of the evolution operator, we uncover various non-linear regimes for a range of interaction parameters that allows modeling of metallic and insulating (either charge density wave or spin density wave insulators) rings. The metallic regime appears at the phase boundary between the two insulating phases and provides the opportunity to describe either weakly or strongly correlated metals. We find that the *fidelity susceptibility* of the ground state as a function of magnetic flux piercing the ring provides a very good measure of the short-time response. Even completely different interacting regimes behave in a similar manner at short time-scales as long as the fidelity susceptibility is the same. Depending on the strength of the electric field we find various types of responses: persistent currents in the insulating regime, dissipative regime or damped Bloch-like oscillations with varying frequencies or even irregular in nature. Furthermore, we also consider the dimerization of the ring and describe the response of a correlated band insulator. In this case the distribution of the energy levels is more clustered and the Bloch-like oscillations become even more irregular.

In Chapter. 7, based on first-principles calculations, we study the relative structural stability of the metallic T and insulating H phase of monolayer MoS_2 upon Li doping, the primary task was to investigate the problem of relative stability of two system by electrostatic doping as a result of the application of an electric field. However technical difficulties in plan-wave implementations of ab-initio calculations for inducing pure charges, for the layered structures, forced us to use Lithium atoms as a source for the charge transfer to the monolayer MoS_2. Our calculations show that the H structure of MoS_2 is stable for single-side adsorption for arbitrary concentrations of lithium atoms. However, it is possible to energetically stabilize the T phase of MoS_2 against H phase if Li atoms are adsorbed on both sides of the MoS_2 layer. However, the resulting T structure is dynamically unstable against distortions towards in-plane clustering of the molybdenum atoms. Two processes are examined that allow for two-sided adsorption of Li atoms on MoS_2 supported by a substrate. First, the penetration of Li atoms through the MoS_2 layer is investigated. Our calculations show that the amount of energy needed to pass through a pure MoS_2 layer is of the order of ~ 2 eV, which is too large to make penetration possible. However, when the MoS_2 layer is covered with Li atoms the amount of energy that Li atoms should gain to pass the layer is drastically reduced by at least two order of magnitude and penetration becomes feasible. Another way to achieve two-side adsorption which we investigate is the migration of Li atoms from the edge of the sample.

Finally I conclude by highlighting the remarkable results of the thesis in chapter 8. Every chapter is relatively independent of the others, and can be read separately.

Chapter 2

Models and Methods

In condensed matter physics one often (in principle always) encounters the overwhelming task of explaining the behavior of a system which consists of a large number of interacting particles. For the energy scales which are relevant in condensed matter physics the particles are sets of either electrons or atomic nuclei. Due to the quantum mechanical nature of the problem, the fundamental equation that particles have to satisfy is the time independent Schrödinger equation,

$$\hat{H}\Psi(\vec{x}_1, ..., \vec{x}_n; \vec{R}_1, ..., \vec{R}_n) = E\Psi(\vec{x}_1, ..., \vec{x}_n; \vec{R}_1, ..., \vec{R}_n), \tag{2.1}$$

where $\Psi(\vec{x}_1, ..., \vec{x}_n; \vec{R}_1, ..., \vec{R}_n)$ is the many body wave function and $\hat{H}$ is the Hamiltonian given by,

$$\hat{H} \;=\; -\sum_i \frac{\hbar^2\nabla_i^2}{2m_e} - \sum_I \frac{\hbar^2\nabla_I^2}{2M_I} + \frac{1}{2}\sum_{i\neq j}\frac{e^2}{|\vec{x}_i - \vec{x}_j|} + \frac{1}{2}\sum_{I\neq J}\frac{Z_I Z_J e^2}{|\vec{R}_I - \vec{R}_J|} - \sum_{i,I}\frac{Z_I e^2}{|\vec{x}_i - \vec{R}_I|}, \tag{2.2}$$

where ϵ_0 is vacuum perminivity, $\hbar$ is Planck quantum divide by 2π, $\vec{x}_i$ is the position of the electrons with index i, $\vec{R}_I$ is the position of the atomic nuclei, M_I is the atomic mass, Z_I is the atomic charge, m_e is the electron mass and e is the electron charge. Here the relativistic contributions are considered at lowest order, which manifest itself as particles with spin. Hereby, we define the different terms in Eq. (2.2) as follows, the first two terms correspond to the kinetic energy of the electrons (T_e) and nuclei (T_N) respectively, the third and forth terms indicate the Coulomb interaction between electrons (internal potential V_{ee}) and between atomic nucleus (V_{II}) respectively, and the last term corresponds to the electron-nuclei Coulomb interaction (external potential V_{ext}). Therefore, by knowing the particles and interactions between them, together with the equation of motion (here the Schrödinger equation) the problem is completely defined. However, the solution of the innocent looking eigenvalue problem in Eq. (2.1) is intricate and too complicated to be solvable. Therefore the central problem in condensed matter physics is to search for accurate and practical approximations for solving Eq. (2.1) with $\hat{H}$ defined in Eq. (2.2). This was already remarked in the early stages of quantum mechanics by Dirac [64]. The first approximation which is usually considered arises from the fact that the mass of the atomic nuclei is much larger than that of the electron ($\frac{m_e}{M_I} \simeq 10^{-4}$), therefore one may neglect the kinetic energy of the atomic nuclei. This approximation then requires the electrons move in an external potential which is produced by the atomic nuclei that are fixed in their positions (naturally equilibrium). This is the essence of the Born-Oppenheimer approximation that in turn leads to the following Hamiltonian,

$$H = T_e + V_{ee} + V_{II} + V_{ext}. \tag{2.3}$$

Even after the decoupling of the electronic degrees of freedom from the lattice degrees of freedom the problem is still difficult to solve. Therefore further approximations are yet to be constructed. The heart of almost all approximations is to map the real problem to an auxiliary problem that could capture the essential features of the system, while its solution is manageable. Rather than working with the Schrödinger equation one may favor to work directly with the total energy as,

$$E = \frac{\int d^3x_1 ... \int d^3x_N \Psi^*(\vec{x}_1, ..., \vec{x}_N) \hat{H} \Psi(\vec{x}_1, ..., \vec{x}_N)}{\int d^3x_1 ... \int d^3x_N \Psi^*(\vec{x}_1, ..., \vec{x}_N) \Psi(\vec{x}_1, ..., \vec{x}_N)}. \tag{2.4}$$

Then by using the variational principle $\frac{\delta E}{\delta \Psi *} = 0$, one arrives at the original Schrödinger equation. In order to evaluate the total energy E, based on the Hamiltonian $\hat{H}$ in Eq .(2.2), we need to perform 2^N integrations in 3N spatial dimensions. However, because there are only either single particle or two particle interactions in Eq. 2.2 then only two relevant quantities remains. The first one is the single particle density matrix as,

$$\rho^{(1)}(\vec{x}, \vec{x}') = N \int d^3x_1 ... d^3x_N \Psi^*(\vec{x}, \vec{x}_1, ..., \vec{x}_N) \Psi(\vec{x}', \vec{x}_1, ..., \vec{x}_N), \tag{2.5}$$

and the two particle density matrix as,

$$\rho^{(2)}(\vec{x}, \vec{x}') = N(N-1) \int d^3x_1 ... d^3x_N \Psi^*(\vec{x}, \vec{x}', \vec{x}_1, ..., \vec{x}_N) \Psi(\vec{x}, \vec{x}', \vec{x}_1, ..., \vec{x}_N), \tag{2.6}$$

Where $\Psi(\vec{x}_1, ..., \vec{x}_N)$ is the many body wave function which consist of N particles and the labels $\vec{x}_1, ..., \vec{x}_N$ are position of particles in real space. Notice that $\vec{x}$ and $\vec{x}'$ in Eq. (2.5) correspond to the same particle, however $\vec{x}$ and $\vec{x}'$ in Eq. (2.6) correspond to two different particles. In other words, the two particle density matrix is the joint probability of finding two particles at $\vec{x}$ and $\vec{x}'$, while $n^{(1)}(\vec{x}) = \rho^{(1)}(\vec{x}, \vec{x})$ is the probability to find the particle at the position $\vec{x}$. By considering the above definitions, one may write the total energy as the following equation,

$$E = \int d^3x d^3x' \delta(\vec{x} - \vec{x}')(-\frac{\hbar^2\nabla^2}{2m_e} + V_{ext})\rho(\vec{x}, \vec{x}') + \frac{1}{2}\int d^3x d^3x' \frac{e^2\rho^{(2)}(\vec{x}, \vec{x}')}{4\pi\epsilon_0|\vec{x} - \vec{x}'|}. \quad (2.7)$$

The heart of next approximation is how to find a good approximation for the two particle density matrix. The simplest approximation to the two-particle density matrix is to consider that the electrons move independently and they do not satisfy the Pauli exclusion principle, then one may write the many body wave function $\Psi(\vec{x}_1, ..., \vec{x}_N) = \phi_1(\vec{x}_1)...\phi_N(\vec{x}_N)$, where the $\phi_1(\vec{x}_1), ...\phi_N(\vec{x}_N)$ are single particle wavefunctions. One can easily check that by considering this approximation we have $\rho^{(2)}(\vec{x}, \vec{x}') = n^{(1)}(\vec{x})n^{(1)}(\vec{x}')$. Afterwards by using the variational principle for Eq. (2.7), one achieves the following Schrödinger-like equation for single particle wave functions $\phi_1(\vec{x}_1), ...\phi_N(\vec{x}_N)$,

$$\left[-\frac{\nabla_i^2}{2m_e} + V_{ext}(\vec{x}_i) + \sum_j \int d^3x_j \phi_j^*(\vec{x}_j) \frac{e^2}{4\pi\epsilon_0|\vec{x}_i - \vec{x}_j|}\phi_j(\vec{x}_j)\right]\phi_i(\vec{x}_i) = \epsilon_i\phi_i(\vec{x}_i). \quad (2.8)$$

Due to the fact that the quantum mechanical particles are indistinguishable, the Hamiltonian Eq. (2.1) commutes with the permutation operator and thus the many body wave function is also an eigenstate of the permutation operator. By considering this observation a more advanced approximation arises if we consider an anti-symmetrized (because of the fermionic nature of the electrons) wave function which is constructed with single particle terms. This wave function is nothing but a Slater determinant, which is produced by a linear combination of all possible mutual permutations P between the different particles as,

$$\Psi(\vec{x}_1, ..., \vec{x}_N) = \frac{1}{\sqrt{N!}}\sum_P (-1)^P \phi_{P_1}(\vec{x}_1)...\phi_{P_N}(\vec{x}_N), \quad (2.9)$$

where the summation over P accounts for the summation over all mutual possible permutations. It is clear that the anti-symmetrized wave function, Eq. (2.9), is an eigenstate of the permutation operator. Inserting back the above ansatz into the total energy expression in Eq. (2.7) together with the variational principle, one obtains the following equation for the single particle wave functions,

$$\begin{aligned}&\left[-\frac{\nabla_i^2}{2m_e} + V_{ext}(\vec{x}_i) + \sum_j \int d^3x_j \phi_j^*(x_j)\frac{1}{|\vec{x}_i - \vec{x}_j|}\phi_j(\vec{x}_j)\right]\phi_i(\vec{x}_i) \\ &-\sum_j \left[\int d^3x_j \phi_j^*(\vec{x}_j)\frac{e^2}{4\pi\epsilon_0|\vec{x}_i - \vec{x}_j|}\phi_i(\vec{x}_j)\right]\phi_j(\vec{x}_i) = \epsilon_i\phi_i(\vec{x}_i)\end{aligned} \tag{2.10}$$

This is called the Hartree-Fock approximation. Following the Hartree decomposition of the two particle density matrix one may reorganize Eq. (2.7) as follows. If one particle is located at the position $\vec{x}_0$, then the amount of charge that an observer charge located at $\vec{x}$ feels is the conditional density $\frac{\rho^{(2)}(\vec{x}, \vec{x}_0)}{n^{(1)}(\vec{x}_0)}$ with $n^{(1)}(\vec{x}_0)$ defined as $n^{(1)}(\vec{x}) = \rho^{(1)}(\vec{x}, \vec{x})$. This conditional charge accounts for the charge which the remaining N-1 particles produce. Therefore the observer charge does not feel the charge of itself. The Hartree decomposition of the two particle density matrix makes it more convenient to write the two particle density matrix as $\rho^{(2)}(\vec{x}, \vec{x}') = n^{(1)}(\vec{x})[n^{(1)}(\vec{x}') + h(\vec{x}, \vec{x}')]$. Where $h(\vec{x}, \vec{x}')$ is called the hole function. By substitution of the former expression for the hole function into the total energy functional Eq. (2.7) one may reorganize the energy functional as,

$$\begin{aligned}E &= \int d^3x d^3x' \delta(\vec{x} - \vec{x}')(-\frac{\hbar^2\nabla^2}{2m_e} + V_{ext})\rho(\vec{x}, \vec{x}') + \frac{1}{2}\int d^3x d^3x' \frac{e^2 n^{(1)}(\vec{x}) n^{(1)}(\vec{x}')}{4\pi\epsilon_0|\vec{x} - \vec{x}'|} \\ &+ \frac{1}{2}\int d^3x n^{(1)}(\vec{x}) \int d^3x' \frac{e^2 h(\vec{x}, \vec{x}')}{4\pi\epsilon_0|\vec{x} - \vec{x}'|}.\end{aligned} \tag{2.11}$$

Here we define the second and third terms as E_H and U_{XC}. Where the first term is only the Hartree term and the second is the exchange correlation interaction energy.
Often, considering the many body wave function just as a Slater determinant of single body wave functions is not a satisfactory approximation and one may need more elaborate approximations to deal with the many body problem. One of the most successful and prominent approaches is density function theory (DFT). This theory also maps the full many body problem on a simplified single particle one, but it uses more sophisticated ways to approximate the two body density matrix or equally the hole function in the energy functional in Eq. (2.11), while it does not introduce many computational difficulties.

2.1 Density Functional Theory

The density functional theory relies on two fundamental theorems that were proposed and proved exactly by Hohenberg-Kohn (HK), which are mentioned in the following:

- **Theorem I** : *For any system of interacting particles in an external potential $V_{ext}(\vec{x})$ the potential $V_{ext}(\vec{x})$ is determined uniquely, except for a constant, by the ground state density $n_0(\vec{x})$.*
  The essential point of this theorem is the fact that ground state electron density uniquely determines an external potential and the Hamiltonian and therefore all the properties of the system. The prove of this theorem is as follows. Assume that there are two different external potentials $V_{ext}(\vec{x})$ and $V^{'}_{ext}(\vec{x})$, which both give the same ground state density $n_0(\vec{x})$. Therefore, there are two different Hamiltonians H and $H^{'}$, two different normalized groundstate wave functions Ψ and $\Psi^{'}$ corresponding to H and $H^{'}$ respectively and two ground-state energies E_0 and $E^{'}_0$. The the variational principle, Eq. (2.4), for H with $\Psi^{'}$ as a trial wave function leads:

$$E_0 < \langle\Psi^{'}|H|\Psi^{'}\rangle = \langle\Psi^{'}|H^{'}|\Psi^{'}\rangle + \langle\Psi^{'}|H - H^{'}|\Psi^{'}\rangle \tag{2.12}$$

$$E_0 < E^{'}_0 + \int n_0(\vec{x})[V_{ext}(\vec{x}) - V^{'}_{ext}(\vec{x})]d\vec{x} \tag{2.13}$$

  Likewise, by considering Ψ as a trial wave function for H',

$$E^{'}_0 < \langle\Psi|H^{'}|\Psi\rangle = \langle\Psi|H|\Psi\rangle + \langle\Psi|H^{'} - H|\Psi\rangle \tag{2.14}$$

$$E^{'}_0 < E_0 + \int n_0(\vec{x})[V^{'}_{ext}(\vec{x}) - V_{ext}(\vec{x})]d\vec{x} \tag{2.15}$$

  Summing Eqs. (2.13) and (2.15) yields,

$$E_0 + E^{'}_0 < E^{'}_0 + E_0 \tag{2.16}$$

  which is a contradiction. Therefore there cannot be two different potentials (and therefore Hamiltonians) which give the same density for their ground state.

- **Theorem II** : *A universal energy functional $F_U[n]$, in terms of the density $n(\vec{x})$ can be defined, independent of external potential $V_{ext}(\vec{x})$, which the ground state energy of the system is the global minimum of total energy functional $E[n^{(1)}(\vec{x})] = F_{\hat{U}}[n^{(1)}(\vec{x})] + \int d^3v_{ext}(\vec{x})n^{(1)}(\vec{x})$, which the density that minimizes the total functional is the exact ground state density $n_0(\vec{x})$.*

The proof of the second theorem is presented by Levy in his seminal paper [65,66]. This in fact could be proven for the ground state of a many-particle system. Suppose that one is able to construct all normalized fermionic many-particle wavefunctions and calculate for each wave function the density $n^{(1)}(\vec{x})$. Now construct for each density $n^{(1)}(\vec{x})$ a subspace of wave functions that produce the same density profile $n^{(1)}(\vec{x})$, we call this subspace $\Re[n^{(1)(\vec{x})}]$. To proceed with the proof we need to consider only the kinetic energy, $\hat{T}$ and the interaction energy, $\hat{U}$, this is because of the fact that the contribution of the V_{ext} is the same for all the wave functions with the same $n^{(1)}(\vec{x})$. One may construct a universal energy functional for each $n^{(1)}(\vec{x})$ by searching for a wavefunction in $\Re[n^{(1)}(\vec{x})]$ as,

$$F_U[n^{(1)}(\vec{x})] = min_{|\Psi\rangle \in \Re[n^{(1)}(\vec{x})]} \langle \Psi | \hat{T} + \hat{U} | \Psi \rangle \tag{2.17}$$

The same argument also holds for the system with $\hat{U} = 0$. Next one can rewrite the total energy as,

$$E[n^{(1)}(\vec{x})] = F_{\hat{U}}[n^{(1)}(\vec{x})] + \int d^3 v_{ext}(\vec{x}) n^{(1)}(\vec{x}). \tag{2.18}$$

While the above theorems are exact, however it is still necessary to access the full many-particle wave function to evaluate the energy functional and perform the minimization. To tackle this difficulty the first approximation which was proposed by W. Kohn and L. J. Sham(KS) states that rather than doing the minimization with respect to the full many-particle wavefunction, the minimization could be performed with respect to an auxiliary non-interacting wave function with kinetic energy part $T_{NI}(n^{(1)}(\vec{x}))$. The minimization has to be performed with this new non-interacting system such that the density of the auxiliary system equals to the density of the original interacting one. Then the explicit form of the Lagrange function that should be optimized will have the following form,

$$\begin{aligned} E &= \{ \sum_s \int d^3x \phi_s^*(\vec{x}) \frac{-\hbar^2}{2m_e} \nabla^2 \phi_s(\vec{x}) + \int d^3x v_{eff}(\vec{x}) (\sum_s \phi_s^*(\vec{x}) \phi_s(\vec{x}) - n^{(1)}(\vec{x})) \\ &+ \int d^3x v_{ext}(\vec{x}) n^{(1)}(\vec{x}) + \frac{1}{2} \int d^3x d^3x' \frac{n^{(1)}(\vec{x}) n^{(1)}(\vec{x}')}{4\pi\epsilon_0 |\vec{x} - \vec{x}'|} \\ &+ E_{XC}[n^{(1)}(\vec{x})] - \sum_{sk} \Lambda_{sk}(\langle \phi_k | \phi_s \rangle - \delta_{s,k}) \}. \end{aligned} \tag{2.19}$$

Where E_{XC} is defined as $E_{XC}[n^{(1)}(\vec{x})] = U_{XC} + T_I - T_{NI}$, $\phi_s(\vec{x})$ are single particle wave functions of the new non-interacting system and summation over s runs over number of occupied states of non-interacting system. Finally the optimization is performed by searching for the stationary points of the above Lagrange function by $\frac{\delta E}{\delta \phi^*} = 0$, $\frac{\delta E}{\delta n^{(1)}(\vec{x})} = 0$ and $\frac{\delta E}{\delta v_{eff}} = 0$ one arrives at the following set of equations that have to be solved self consistently,

$$\frac{\delta E}{\delta \phi^*} = 0 \quad : \quad [\frac{-h^2}{2m_e}\nabla^2 + v_{eff}(\vec{x}) - \epsilon_s]\phi_s(\vec{x}) = 0, \tag{2.20}$$

$$\frac{\delta E}{\delta n^{(1)}(r)} = 0 \quad : \quad v_{eff}(\vec{x}) = v_{ext}(\vec{x}) + \int d^3x \frac{n^{(1)}(\vec{x}')}{4\pi\epsilon_0|\vec{x}-\vec{x}'|} + v_{XC}[n^{(1)}(\vec{x})], \tag{2.21}$$

$$\frac{\delta E}{\delta v_{eff}} = 0 \quad : \quad n^{(1)}(\vec{x}) = \sum_{s=1}^{occupied} \phi_s^*(\vec{x})\phi_s(\vec{x}). \tag{2.22}$$

With $\epsilon_s = \Lambda_{ss}$ and $v_{XC}[n^{(1)}(\vec{x})] = \delta E_{XC}[n^{(1)}(\vec{x})]/\delta n^{(1)}(\vec{x})$. The above set of equations has to be solved self-consistency until desired convergence is achieved. While the KS method provides a great simplification of calculations, further approximations are necessary because an exact form of exchange-correlation energy (E_{XC}) is not known. The first approximation for the exchange-correlation energy is the Local Density Approximation (LDA). The idea behind it is to assumed that the local XC energy per particle depends on the local density, and it is equal to the XC energy per particle of a homogeneous electron gas with the same density, in a neutralizing positive background. Therefore the exchange-correlation energy E_{XC} is obtained as the following form,

$$E_{XC}^{LDA}(n) = \int n(\vec{x})\epsilon_{XC}(n(\vec{x}))d\vec{x}, \tag{2.23}$$

where $\epsilon_{XC}(n(\vec{x}))$ is the exchange-correlation energy per particle of a uniform electron gas of density $n(\vec{x})$. Thus E_{XC} only depends on the value of the local electronic density at each point. The quantity $\epsilon_{XC}(n(\vec{x}))$ could be linearly decomposed into exchange and correlation contributions as,

$$\epsilon_{XC}(n(\vec{x})) = \epsilon_X(n(\vec{x})) + \epsilon_C(n(\vec{x})). \tag{2.24}$$

where the exchange part ϵ_X, represents the exchange energy of an electron in a uniform electron gas of a particular density and is given by [67],

$$\epsilon_X = -\frac{3}{4}\left(\frac{3n(\vec{x})}{\pi}\right)^{1/3}. \tag{2.25}$$

Since there is no explicit expression for the correlation part ϵ_C, several approaches have been proposed. Ceperly and Alder used numerical quantum Monte-Carlo simulations for the homogeneous electron gas in order to find a numerical solution for ϵ_C [68]. Moreover,

another accurate approximation for ϵ_C was presented by Perdew and Wang in 1992 [69]. The LDA relays on the local nature of the exchange-correlation potential, this is accurate as long as the density distribution does not vary too rapidly spatially [70].
The big surprise is that the accuracy of this simple approximation is good and usually leads to a correct results for the binding energies, structural parameters, bond lengths, vibrational energies, phonon spectra. However, there are some drawbacks for this method, it usually underestimates the band gap, overestimates the binding energy and also underestimates the bond lengths [71].

In order to resolve some drawbacks of the LDA, the generalized gradient approximation (GGAs) is proposed for the exchange-correlation energy. It improves the description of atoms, molecules, and solids in comparison with LDA. This approximation does not only consider the local density $(n(\vec{x}))$, but also it considers the density in the neighboring positions by including the dependence on the gradient $(\nabla n(\vec{x}))$. Using this approximation, the non-homogeneity of the electron density is taken into account. Therefore, the XC energy is written as follows,

$$E_{XC}^{GGA}(n) = \int n(\vec{x})\epsilon_{XC}\left(n(\vec{x}), \nabla n(\vec{x})\right) d\vec{x}. \tag{2.26}$$

In general, the GGA method gives better results for bond lengths, binding energies in comparison with LDA. However, in practice it has some shortcomings. Several investigations have been made to find out the advantages and disadvantages of LDA versus GGA [72–74]. For instance, the results of LDA calculation for the lattice constants are in general 2% smaller than the experimental results, on the other hand GGA gives the lattice constants in most cases in agreement with experiments or it slightly overestimates the experimental values. The overestimation of lattice constants by GGA, in turn could lead to an underestimation of the bond strengths, in contrast to experiments and LDA. There are several forms for GGA functionals. Among them is the Perdew-Burke-Ernzerhof (PBE-GGA) form, which is free of empirical parameters and starting from physical principles [72]. The Becke exchange [75] and Lee-Yang-Parr (LYP) correlation [76] (BLYP) uses parameters that are fitted to experimental data.

2.2 Models for quantum lattice particles

Representing the interaction term as a single particle term as is normally done in DFT often fails to describe systems with strong interactions such as transition metal oxides. In order to subdue this kind of difficulties another kind of simplification of the problem is suggested. It relies on the fact that one may be able to simplify the problem by representing the full problem with few number of important coupling constants while keeping the full interacting structure of the problem unaffected. Examples of these kinds of simplifications are the Hubbard models [77] or the Anderson impurity model. To do this it is more convenient to represent Eq. (2.2) in second quantization form as,

$$\begin{aligned} \hat{H} = & \int d^3x d^3x' \delta(\vec{x}-\vec{x}')\hat{\psi}^\dagger(\vec{x}')(-\frac{\hbar^2\nabla^2}{2m_e}+v_{ext}(\vec{x}))\hat{\psi}(\vec{x}) \\ + & e^2\int d^3x d^3x' \hat{\psi}^\dagger(\vec{x})\hat{\psi}(\vec{x})\frac{1}{4\pi\epsilon_0|\vec{x}-\vec{x}'|}\hat{\psi}^\dagger(\vec{x}')\hat{\psi}(\vec{x}'), \end{aligned} \tag{2.27}$$

where $\hat{\psi}^\dagger(\vec{x})$ and $\hat{\psi}(\vec{x})$ create and annihilate one particle at position $\vec{x}$ respectively.

These operators obey (anti-)commutation relations for (fermionic) bosonic particles as $[\hat{\psi}^\dagger(\vec{x}),\hat{\psi}(\vec{x}')]_\pm = \delta(\vec{x}-\vec{x}')$, ± sign corresponds to fermionic and bosonic fields, respectively. In solid state physics v_{ext} is usually a periodic potential that is produced by a lattice of atomic nuclei. Therefore in order to make Eq. (2.27) more convenient, one uses a transformation for $\hat{\psi}^\dagger(\vec{x})$ and $\hat{\psi}(\vec{x})$ to a basis in which electrons are normally localized around the center of each atomic nuclei. It is more convenient to expand $\hat{\psi}(\vec{x})$ based on maximally localized Wannier wave functions, which are defined as,

$$\phi_\gamma(\vec{x}-\vec{X}_i) = \frac{1}{\sqrt{N}}\int d^3k e^{-i\vec{k}.\vec{X}_i}\psi_{\vec{k}\gamma}(\vec{x}). \tag{2.28}$$

where the $\psi_{\vec{k}\gamma}(\vec{x})$ are Bloch functions of the noninteracting Hamiltonian and the X_i are the positions of the atomic nuclei around which the electrons are localized , γ is combined orbital and spin index. It is easy to check that these kind of localized basis sets are orthogonal. By expanding $\hat{\psi}(\vec{x}) = \sum_{i\gamma}\phi_{i\gamma}(\vec{x})\hat{c}_{i\gamma}$, which $\hat{c}_{i\gamma}$ creates a particle in orbital γ at site i, and substituting it into Eq. (2.27) one may arrive at the following form for the Hamiltonian operator,

$$\hat{H} = \sum_{ij\alpha\beta} t_{ij}^{\alpha\beta}\hat{c}_{i\alpha}^\dagger\hat{c}_{j\beta} + \frac{1}{2}\sum_{ijkl;\alpha\beta\gamma\theta} u_{ijkl}^{\alpha\beta\gamma\theta}\hat{c}_{i\alpha}^\dagger\hat{c}_{j\beta}^\dagger\hat{c}_{k\gamma}\hat{c}_{j\theta}, \tag{2.29}$$

where the matrix elements are given by,

$$t_{ij}^{\alpha\beta} = \int d^3x\phi_\alpha^*(\vec{x}-\vec{X}_i)[-\frac{\hbar^2\nabla^2}{2m_e}+V_{ext}(\vec{x})]\phi_\beta(\vec{x}-\vec{X}_j), \tag{2.30}$$

$$u_{ijkl}^{\alpha\beta\gamma\theta} = \int d^3x\int d^3x' e^2\frac{\phi_\alpha^*(\vec{x}-\vec{X}_i)\phi_\beta^*(\vec{x}-\vec{X}_j)\phi_\gamma(\vec{x}-\vec{X}_k)\phi_\theta(\vec{x}-\vec{X}_l)}{4\pi\epsilon_0|\vec{x}-\vec{x}'|}, \tag{2.31}$$

where the Greek letters correspond to combined index of spin and local orbitals and Latin letters correspond to lattice sites. Hereafter, in all of the following chapters we cosider $e = a = 1$, where e is charge of the carrier (here electrons) and a is the lattice constant. From the Eq. (2.29) one may derive even more simplified models, the most prominent one is the single band extended Hubbard model,

$$\hat{H} = -\sum_{i \neq j\sigma} t_{ij} c^{\dagger}_{i\sigma} c_{j\sigma} + \sum_{i \neq j} \frac{1}{2} v_{ij} \hat{n}_i \hat{n}_j + \sum_i U \hat{n}_{i\sigma} \hat{n}_{i\bar{\sigma}}, \tag{2.32}$$

where σ is the spin index, t_{ij} is the hopping parameters, v_{ij} is long-range Coulomb interaction and U accounts for the local interaction between different spins. Variants of multi-band Hubbard models can be written as,

$$\hat{H} \;=\; -\sum_{i \neq j;\gamma\gamma'} t^{\gamma\gamma'}_{ij} c^{\dagger}_{i\gamma} c_{j\gamma'} + \sum_{i\gamma} v_{i\gamma} \hat{n}_{i\gamma} + \sum_i \hat{H}^{int}_i, \tag{2.33}$$

where γ are combined orbital and spin index, $t^{\gamma\gamma'}_{ij}$ are the hopping amplitudes between site i and j, the local potentials $v_{i\gamma}$ are introduced in order to mimic the crystal field splitting or the effect of external electric field for the translationally broken systems [78]. And the interaction part of the Hamiltonian is defined as follows:

$$\hat{H}^{int}_i = \sum_{\gamma_1,\gamma_2,\gamma_3,\gamma_4} U^{\gamma_1,\gamma_2,\gamma_3,\gamma_4}_i c^{\dagger}_{i\gamma_1} c^{\dagger}_{i\gamma_2} c_{i\gamma_3} c_{i\gamma_4}, \tag{2.34}$$

where γ are combined orbital and spin indices. Even with these simplifications the solution of the Schrödinger equation based on the above mentioned Hamiltonians is not a trivial task, when one deals with large systems that we have normally in solid state physics.

2.3 Exact diagonalization

Looking at the variants of the Hubbard or Anderson impurity models often one may need to form the Hilbert-space of clusters containing sites. The number of sites and particle that could be considered numerically depends on the size of the memory that is accessible given that the memory requirements grow exponentially as function of the number of sites and particles. On a normal desktop computer, this restricts one to construct the Hamiltonian with up to 12 or 14 sites at half-filling. Although these numbers are small, however this has indirect applications to Gutzwiller approximations for the construction and manipulation of local part of the Hamiltonian, it could be used as a solver for Anderson impurity model in a combined exact diagonalization (ED) with DMFT approach, for more detailed description see [38], furthermore it is applied for the calculation of the trace of the local part of Hamiltonian in the continuous time quantum Monte Carlo (CTQMC) Anderson impurity solver [79, 80]. Moreover, although the number of sites and particles is small, the number of states is large enough such that these systems could be used for fundamental investigations of quantum systems such as non-adiabatic behavior of many-body quantum systems (specially one dimensional systems) and investigation of quantum statistical mechanics.

2.3.1 Construction of the Hilbert space

For normal systems without any spontaneous symmetry breaking one may exploit the symmetries of the system as much as possible. For instance for a normal system without any superconducting order it is possible to restrict the Hilbert-space only to a fixed number of particles. For fermions with spin, furthermore, it is also possible to fix the magnetization of the system by fixing $N_\uparrow - N_\downarrow = M$ when there is not any process which changes the spin of the particles in the Hamiltonian, or equivalently there are no inelastic scattering terms in the Hamiltonian. By incorporating the above mentioned considerations one may write the many body wave function for fermions with spin degrees of freedom as follows,

$$|\psi_{(N\uparrow,N\downarrow)}\rangle = \sum_{1\le x_i\le L} \gamma_{x_1,...,x_{N_\uparrow};x_{N_\uparrow+1},...,x_{N_{tot}}} |x_1,...,x_{N_\uparrow}\rangle_\uparrow \bigotimes |x_{N_\uparrow+1},...,x_{N_{tot}}\rangle_\downarrow, \tag{2.35}$$

with $N_{tot} = N_\uparrow + N_\downarrow$, $|x_1,...,X_i,...\rangle_\sigma$ are configuration state elements for each spin and $x_1,...,X_i,...$ are positions of sites or indices of orbitals. Notice here γ coefficients are not symmetric or anti symmetric against permutation of $x_1,...,X_{N_{tot}}$. The configuration state elements of each spin therefore are defined as,

$$\begin{aligned} |...,x_i,...,x_j,...\rangle_\sigma &= \prod ...\hat{c}^\dagger_{x_i\sigma}...\hat{c}^\dagger_{x_j\sigma}...|0\rangle = -\prod ...\hat{c}^\dagger_{x_j\sigma}...\hat{c}^\dagger_{x_i\sigma}...|0\rangle \\ &= -|...,x_j,...,x_i,...\rangle_\sigma. \end{aligned} \tag{2.36}$$

It is best to order all creation and annihilation operators in some way. For instance for a chain we could consider $1 \le x_1 < ... < X_{N_\uparrow} \le L$, where $x_1 < ... < X_{N_\uparrow}$ are site indices. Therefore one may expand the Hilbert space as function of reduced (ordered) configurations as $|I\rangle = |x_1,...,x_{N_\uparrow}\rangle_\uparrow \bigotimes |x_{N_\uparrow+1},...,x_{N_{tot}}\rangle_\downarrow$. The dimension of the reduced Hilbert space restricted to a specific block with fixed $N_\uparrow, N_\downarrow$ is the product of the total number of configurations in which it is possible to distribute the particles with specific spins between

Table I. The memory requirement for the storage of the full sparse Hamiltonian matrix.

Number of sites(L)	$N_\downarrow = N_\uparrow = L/2$	Number of states	Memory requirement
10	5	63,504	10MB
12	6	853,776	500MB
14	7	11,778,624	6GB
16	8	165,636,900	—-

the L sites. Furthermore, because quantum particles are indistinguishable, the total number of configurations reads,

$$Dim(H)(N_\uparrow, N_\downarrow) = \binom{L}{N_\uparrow} \times \binom{L}{N_\downarrow}. \tag{2.37}$$

In table. I based on Eq. (2.37) we present the dimension of the Hilbert space as function of the number of sites at $N_\uparrow = N_\downarrow = L/2$. The exponential growth of the Hilbertspace therefore imposes sever restrictions on number of the sites and particles which one could consider. And this is why reliable approximations are necessary in order to deal with problems for which correlations are important.

In order to implement the above mentioned ideas it is possible to efficiently exploit the bitwise patterns in computers. This could be easily done by assigning to each configuration state one integer number with bit pattern of length L (now L=10): $|x_1, ..., x_{N_\uparrow}\rangle_\sigma \longrightarrow 1100110010$. The zeros are representative of empty sites, while ones shows occupied sites. For instance an element of a full configuration for a system with $L = 10$ and $N_\uparrow = N_\downarrow = 5$ could be represented as $|x_1, ..., x_{N_\uparrow}\rangle_\uparrow \otimes |x_{N_\uparrow+1}, ..., x_N\rangle_\downarrow \longrightarrow 1100110010 \times 1001100110$. The the bitwise patterns are extracted from the assigned integer for each up and down configuration. In practice we search for integers with a fixed number of non-zero elements in their bitwise pattern. This should be done according to the number of particles for each spin, then store all of these integers in two vectors, each vector corresponds to one spin. These vectors consist of integers as representative of states of each spin and an index. Therefore the actual index of each state, i, in the full Hilbert space is expressed as $i = i_\uparrow + dim(H_\uparrow) \times i_\downarrow$.

The next step is to apply operators that appear in the Hamiltonian on these configuration states in order to find the matrix elements of the Hamiltonian. As an example we consider an extended Hubbard model with periodic boundary conditions and nearest neighbor hopping elements,

$$\hat{H}_U = -\sum_{\langle ij\rangle\sigma} t_{ij} c^{\dagger}_{i\sigma} c_{j\sigma} + \sum_{\langle ij\rangle\sigma} \frac{1}{2} v_{ij} \hat{n}_i \hat{n}_j + \sum_i U \hat{n}_{i\sigma} \hat{n}_{i\bar{\sigma}}. \tag{2.38}$$

In order to construct the matrix element of the above Hamiltonian, we first construct the matrix element of the hopping terms, i.e. the first term in the Eq. (2.38). For the construction of these terms one should define the creation and annihilation operators which act for each spin on different places(sites), moreover the fermionic sign should be considered. Therefore, the hopping processes acquire an extra sign when it couples between sites i and j as $-(-1)^{N_{ij}} t_{ij}$, where the N_{ij} counts number of particles between site i and j only the number of electrons for the spin for which the hopping operation is applied , therefore non-diagonal parts of the above Hamiltonian acquires $\mp t_{ij}$ terms. For our example, the fermionic signs, which hopping processes acquire, are positive for nearest neighbor hopping processes, however for the hopping between atoms in the boundary, for which the periodic boundary condition is defined, depends on the number of electrons between two sites.

The second and third terms in the Hamiltonian mentioned in Eq. (2.38) do not acquire any sign, and are constructed very easily. In particular for the last term it is necessary to perform a bitwise "AND" operation between bit pattern of states of spin up and spin down configurations. This gives the number of overlaps between spin up and spin down configurations which easily could be just multiplied with the interaction U in order to produce the diagonal terms. The terms related to nearest neighbor density-density interactions also contribute as only diagonal matrix elements and could be simply considered by checking the nearest neighbor occupations.

Here we notice that the presence of non local interactions which contribute to exchange and pair hopping or the cases with hopping elements beyond nearest neighbors, the fermionic sign contribution should be considered with more care. In our implementation we also consider a generic case for which we perform exact creation and annihilation operators on the configurations in order to calculate the matrix elements.

There are ways in which one could perform rigorous checks against the above implementation. First of all it is possible to check the ground state of the noninteracting system with the one which could be extracted from the direct diagonalization of the single particle hopping matrix (the first term in Eq. (2.38)) such that the eigenvalues of the hopping matrix should be summed up to the number of electrons for each spin. Therefore, if both cases results in the same ground state energy then the implementation of the hopping matrix construction is correct. On the other side the ground state energy of the system with only density-density interactions but without hoppings could be calculated without diagonalization of the full Hamiltonian matrix in Eq. (2.38), this in turn could be compared with the ground state energy which is attained by finding the ground state of the full Hamiltonian matrix, these two also have to be equal. We further checked our implementation for open boundary condition against the DMRG++ code which was written by Alvarez et. al. [81]. Finally we checked our implementation more rigorously by comparing single particle spectral function peaks of the full non-interacting Hamiltoian with those obtained from the diagonalization of the single particle hopping matrix. We show the results in the following section.

2.3.2 Lanczos Method

Now we know how to construct the Hamiltonian numerically, next we search first for the ground-state of the Hamiltonian because it is the relevant state for zero temperature and the exited states are necessary as long as one needs to deal with finite temperatures. Therefore it is necessary to use methods to be able to deal with selective eigenvalues, rather than the full diagonalization of the Hamiltonian. Full diagonalization of the Hamiltonian is very expensive even for $L = 10$ sites at half filling, furthermore it is not necessary in most cases. One of the most prominent methods which is devised to find the extreme eigenpairs of a matrix is the Lanczos [82] method which is based on the Krylov [83] space methods. The idea is to search for lowest energy in the the span $(|v_0\rangle, H|v_0\rangle, H^2|v_0\rangle, ..., H^n|v_0\rangle)$. This could be understood based on the variational principle. In order to find the ground state of any matrix H one should minimize the functional $E[\Psi] = \langle\Psi|H|\Psi\rangle/\langle\Psi|\Psi\rangle$ as,

$$\frac{\delta E[|\Psi\rangle]}{\delta\langle\Psi|} = \frac{H|\Psi\rangle - E[\Psi]|\Psi\rangle}{\langle\Psi|\Psi\rangle} = |\Psi'\rangle, \tag{2.39}$$

where $|\Psi'\rangle$ gives the direction of steepest-descent of the functional at $|\Psi\rangle$. Therefore, moving in the opposite direction reduces the energy, $E[\Psi - \alpha\Psi'] < E[\Psi]$. To find the optimal value of α we have to minimize the energy in a restricted space created by,

$$\begin{aligned} |v_0\rangle &= |\Psi\rangle/\sqrt{\langle\Psi|\Psi\rangle}, \\ |v_1\rangle &= \frac{1}{\sqrt{\langle\tilde{v}_1|\tilde{v}_1\rangle}}|\tilde{v}_1\rangle, \end{aligned} \tag{2.40}$$

with $|\tilde{v}_1\rangle = H|v_0\rangle - \langle v_0|H|v_0\rangle|v_0\rangle$, therefore the construction of the matrix H in this basis leads to a 2 matrix as,

$$H_{span(|v_0\rangle,|v_1\rangle)} = \begin{pmatrix} a_0 & b_1 \\ b_1 & a_1 \end{pmatrix}, \tag{2.41}$$

with $a_n = \langle v_n|H|v_n\rangle$, and $b_1 = \sqrt{\langle\tilde{v}_1|\tilde{v}_1\rangle}$. Finally one could diagonalize the above matrix to find the ground state in this restricted subspace and repeat the procedure by choosing the new ground state as starting point for the next step. Continuing this process further it finally leads to convergence to the actual ground state of H, because we are moving in the direction which reduces energy at each step. By performing the steepest-descent minimization N times by starting from a $|v_0\rangle$ then the resulting minimized vector lies in span($|v_0\rangle, H|v_0\rangle, ..., H^N|v_0\rangle$) which is called Krylov space [83]. Therefore, instead of repeating several steepest-descent searches as one may directly work with Krylov space and find the ground state in this larger restricted space. In order to do this we construct an orthonormal basis-set $|v_n\rangle$ within Krylov space. By starting from any arbitrary vector $|v_0\rangle$ then the first vector is only a vector in the steepest-descent direction: $b_1|v_1\rangle = H|v_0\rangle - \langle v_0|H|v_0\rangle|v_0\rangle$, the rest could be orthogonalized as follows,

$$\begin{aligned}
b_1|v_1\rangle &= H|v_0\rangle - \langle v_0|H|v_0\rangle|v_0\rangle, \\
b_2|v_2\rangle &= H|v_1\rangle - \langle v_1|H|v_1\rangle|v_1\rangle - \langle v_0|H|v_1\rangle|v_0\rangle, \\
&\vdots \\
b_n|v_n\rangle &= H|v_{n-1}\rangle - \langle v_{n-1}|H|v_{n-1}\rangle|v_{n-1}\rangle - \langle v_{n-2}|H|v_{n-1}\rangle|v_{n-2}\rangle,
\end{aligned}$$

with $b_i = \langle v_{i-1}|H|v_i\rangle$. By defining $a_n = \langle v_n|H|v_n\rangle$ and reorganizing terms, we find that H is tridiagonal when it is represented in this new basis set,

$$H|v_n\rangle = b_n|v_{n-1}\rangle + a_n|v_n\rangle + b_{n+1}|v_{n+1}\rangle, \tag{2.42}$$

and it can be written as,

$$\tilde{H} = \begin{pmatrix} a_0 & b_1 & 0 & \cdots & 0 \\ b_1 & a_1 & b_2 & 0 & \vdots \\ 0 & b_2 & a_2 & \ddots & 0 \\ \vdots & 0 & \ddots & \ddots & b_n \\ 0 & \cdots & 0 & b_n & a_n \end{pmatrix}, \tag{2.43}$$

This tridiagonalization of H is named the Lanczos method after its inventor by C. Lanczos [82]. In practice we diagonalize the above mentioned matrix at each step n of the Lanczos process and compare its ground state energy with the ground state energy $E^{(n-1)}$ of the previous step, then the convergence criteria is chosen such that $|E^{(n)} - E^{(n-1)}| < \epsilon$. In our systems we achieved ground state convergence with $\epsilon = 10^{-12}$ in less than 100 iterations. Furthermore, by looking at Eq. (2.42) it is possible to design the algorithm such that only 2 vectors should be stored during the Lanczos iterations. In this case in order to calculate the ground state wave function it is necessary to restart the Lanczos iteration but the starting vector should be the same as the one in the first Lanczos process. In order to calculate the ground state wave function we first need to calculate the ground state of $\tilde{H}$ which is a vector with a length equal to the number of Lanczos iterations. By calling this ground state $\tilde{\Psi}_0$, then one could find the ground state of the original matrix H as: $|\Psi_0\rangle = \sum_{i=0}^{i=L} \tilde{\Psi}_0^{(i)} |v_i\rangle$, where $\tilde{\Psi}_0^{(i)}$ are the elements of $\tilde{\Psi}_0$.

2.3.3 Spectral functions and the Lehmann representation

Matrix elements of the Green's function in the basis set of the combined site-spin or orbital-spin have the following form,

$$G_{i\sigma}(\omega) = \langle \Psi_0 | \hat{c}^{\dagger}_{i\sigma} \frac{1}{\omega + (H - E_0 - i\eta)} \hat{c}_{i\sigma} | \Psi_0 \rangle + \langle \Psi_0 | \hat{c}_{i\sigma} \frac{1}{\omega - (H - E_0 - i\eta)} \hat{c}^{\dagger}_{i\sigma} | \Psi_0 \rangle, \tag{2.44}$$

where $|\Psi_0\rangle$ is the groundstate wavefunction and E_0 is the groundstate energy. In order to evaluate the Green's function it is necessary to calculate the inverse of the matrices of the form $z \pm H$. To do this it is possible to exploit the Lanczos tridiagonalization. By starting from an initial state $|v_0\rangle$ and performing a Lanczos iteration, one may express the matrix $z - H$ in the following form,

$$z - \tilde{H} = \begin{pmatrix} z - a_0 & -b_1 & 0 & \cdots & 0 \\ -b_1 & z - a_1 & -b_2 & 0 & \vdots \\ 0 & -b_2 & z - a_2 & \ddots & 0 \\ \vdots & 0 & \ddots & \ddots & -b_n \\ 0 & \cdots & 0 & -b_n & z - a_n \end{pmatrix}. \tag{2.45}$$

The above mentioned matrix could be reorganized by partitioning it as,

$$z - \tilde{H} = \begin{pmatrix} z - a_0 & B^{(1)^T} \\ B^{(1)} & z - \tilde{H}^{(1)} \end{pmatrix}, \tag{2.46}$$

with $B^{(1)^T} = [-b_1 0 \cdots 0]$, therefore by inverting the block matrix in Eq. (2.46) we find that,

$$[(z - \tilde{H})^{-1}]_{00} = (z - a_0 - B^{(1)^T}(z - \tilde{H}^{(1)})^{-1} B^{(1)})^{-1} = (z - a_0 - b_1^2 [z - \tilde{H}^{(1)}]^{-1}_{00})^{-1}. \tag{2.47}$$

Continuing the above procedure for $[z - \tilde{H}^{(1)}]^{-1}_{00}$ and so on, finally one may express the Green's function in the form of the continued fractions as,

$$[(z-\tilde{H})^{-1}]_{00} = \frac{1}{z-a_0-\frac{b_1^2}{z-a_1-\ldots}}. \tag{2.48}$$

With this approximation we are now able to calculate the full spectral function as in Eq. (2.44). After finding the ground state, two more Lanczos iterations with starting vectors $|v_0\rangle = |\Psi_0^<\rangle = \hat{c}_{i\sigma}|\Psi_0\rangle/\sqrt{n_{i\sigma}}$ and $|v_0\rangle = |\Psi_0^>\rangle = \hat{c}_{i\sigma}^\dagger|\Psi_0\rangle/\sqrt{1-n_{i\sigma}}$, for the calculation of the first term and second term in Eq. (2.44), should be performed respectively, where $n_{i\sigma} = \langle\Psi_0|\hat{c}_{i\sigma}^\dagger\hat{c}_{i\sigma}|\Psi_0\rangle$. Finally one has the following expression for the Green's function as a continued-fractions,

$$G_{ii\sigma}(\omega) = \frac{n_{i\sigma}}{\omega-E_0-i\eta+a_0^<-\frac{b_1^{<2}}{\omega-E_0-i\eta+a_1^<-\ldots}} + \frac{1-n_{i\sigma}}{\omega+E_0+i\eta-a_0^>-\frac{b_1^{>2}}{\omega+E_0+i\eta-a_1^>+\ldots}}, \tag{2.49}$$

where a_i^x and b_i^x with $x =>, <$, are the coefficients which are related to Lanczos iteration that was performed with $|\Psi_0^>\rangle = \hat{c}_{i\sigma}^\dagger|\Psi_0\rangle/\sqrt{1-n_{i\sigma}}$ and $|\Psi_0^<\rangle = \hat{c}_{i\sigma}|\Psi_0\rangle/\sqrt{n_{i\sigma}}$ respectively. Notice here that the idea behind choosing the first diagonal element of the inverted matrix as Green's function arises from the fact that for the calculation of the terms in Eq. (2.44) we chose $|v_0\rangle = |\Psi_0^<\rangle$ or $|v_0\rangle = |\Psi_0^>\rangle$ which already belong to the basis set in which the Hamiltonian is tridiagonal. Finally one may express the spectral function $A(\omega)$ as,

$$A(\omega) = -\frac{1}{\pi} Im G_{i\sigma}(\omega). \tag{2.50}$$

As we state in section 2.3.1 one way to check the validity of the construction of the matrix elements is to find the eigenvalues of the non-interacting hopping matrix and then compare these with the peaks of the spectral function, the place of the peaks in the spectral function in energy axis has to be the same as the eigenvalues of the single particle part of the Hamiltonian. To show this we present in Fig. 2.1 the spectral function of a system with $L = 10$ and $N_\uparrow = N_\downarrow = 5$ with $v_{ij} = 0$, $U = 0$ and $t_{ij} = 1$ with periodic boundary condition. As can be seen in the figure, the position of the peaks in the spectral function and the eigenenergies of the noninteracting hopping matrix match.

2.4 Gutzwiller wave function and Gutzwiller approximation

As it is obvious from the former section finding the groundstate and therefore the properties of a system with the inclusion of correlations is almost impossible except for small

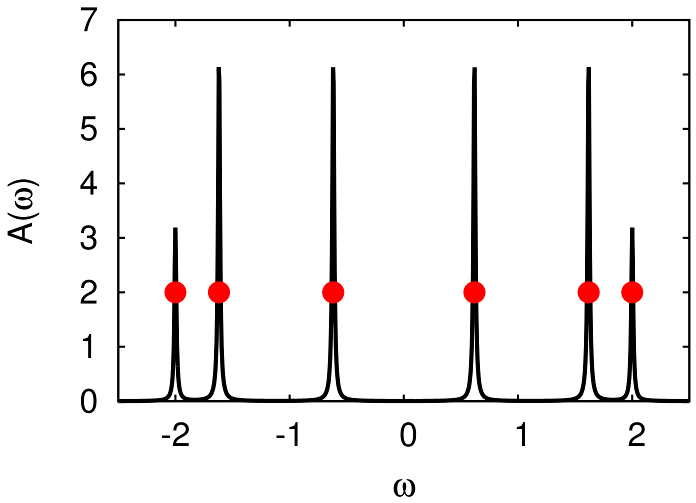

Figure 2.1: Spectral function for a system with $L = 10$ and $N_{\uparrow} = N_{\downarrow} = 5$, $t_{ij} = 1, U = v_{ij} = 0$ and with periodic boundary condition. Circles show the place of exact eigenvalues of the hopping matrix.

clusters. Therefore approximations are necessary. To exemplify, we consider the single band Hubbard model with only local interaction. As,

$$\hat{H}_U = -\sum_{\langle ij\rangle\sigma} t_{ij} c^{\dagger}_{i\sigma} c_{j\sigma} + \sum_{i} U \hat{n}_{i\sigma} \hat{n}_{i\bar{\sigma}}, \tag{2.51}$$

The most straight forward approximation is the Hartree-Fock approximation which relies on the fact that one may write the groundstate of the system as the product of single particle terms,

$$|\Psi_0\rangle = \prod_{i\sigma} \hat{h}^{\dagger}_{i\sigma} |0\rangle. \tag{2.52}$$

This in turn leads to a Hartree-Fock decomposition of the last term in Eq. (2.51). In principle there is no rigorous ground for this kind of decomposition (we will address this in the following sections). Moreover the local charge fluctuations can only be suppressed by spurious symmetry breaking towards magnetization, therefore it usually overestimates the phases with broken symmetry. However one may exploit the single particle form of Eq. (2.52) in order to construct a many body wave function which has more degrees of freedom and one may approach the true ground state with these new form of the wavefunction. The standard way is to include a projector, which includes variational parameters and could project out high energy configurations when acting on $|\Psi_0\rangle$,

$$|\Psi_J\rangle = \hat{P}_J|\Psi_0\rangle, \tag{2.53}$$

where $|\Psi_J\rangle$ is the so called Jastrow wavefunction [84]. The Gutzwiller wavefunction is related to the specific choice of the projector $\hat{P}_J$ which was introduced by Gutzwiller as [85],

$$|\Psi_G\rangle = \prod_i \hat{P}_i|\Psi_0\rangle, \tag{2.54}$$

here i is the lattice site index and $\hat{P}_i = g_i^{\hat{d}_i} = 1 - (1 - g_i)\hat{d}_i$, with $0 \leq g_i \leq 1$ and $\hat{d}_i = \hat{n}_{i\uparrow}\hat{n}_{i\downarrow}$. This choice of projector therefore makes it possible to suppress high energy contributions, i.e., local double occupancies, that are energetically unfavorable when $U > 0$. In order to perform total energy evaluations based on Eq. (2.51) as,

$$\langle\hat{H}\rangle_G = \frac{\langle\Psi_G|\hat{H}|\Psi_G\rangle}{\langle\Psi_G|\Psi_G\rangle}, \tag{2.55}$$

therefore one needs to evaluate the following quantities,

$$\begin{aligned}
\langle\Psi_G|\hat{c}_{i\sigma}^{\dagger}\hat{c}_{j\sigma}|\Psi_G\rangle &= \langle\Psi_0|\hat{P}_i\hat{c}_{i\sigma}^{\dagger}\hat{P}_i\hat{P}_j\hat{c}_{j\sigma}\hat{P}_j\prod_{k\neq i,j}\hat{P}_k^2|\Psi_0\rangle,\\
\langle\Psi_G|\hat{d}_i|\Psi_G\rangle &= \langle\Psi_0\hat{P}_i\hat{d}_i\hat{P}_i\prod_{k\neq i}\hat{P}_k^2|\Psi_0\rangle,\\
\langle\Psi_G|\Psi_G\rangle &= \langle\Psi_0|\prod\hat{P}_i^2|\Psi_0\rangle.
\end{aligned} \tag{2.56}$$

Up to now the only approximation we have considered is to use the Gutzwiller wave function (GWV) to mimic the true groundstate. After this approximation, in principle the variational energy functional could be calculated numerically exact. As is stated by Metzner and Volhardt [86–88], these evaluations could be performed by means of Wick's theorem because the wavefunction $|\Psi_0\rangle$ is only a single particle product. In this way any contribution could be represented by a diagram which consists of internal vertices, related to $\hat{P}_k^2$ and external vertices related to $\hat{P}_i$ and $\hat{P}_j$ in Eqs. (2.56). Moreover these vertices are connected by contractions which here are nothing but $P_{ij}^{\sigma\sigma} = \langle\hat{c}_{i\sigma}^{\dagger}\hat{c}_{j\sigma}\rangle_0$ the single particle density matrix elements of $|\Psi_0\rangle$. However, these evaluations are difficult to perform even for a single band Hubbard model and an exact analytical evaluation of the groundstate energy has been achieved only for the 1D Hubbard model [86]. To make the problem even easier and tractable more approximations are required. One of the most prominent ways to tackle this problem is to use the inverse of the dimensionality of the system as a perturbation parameter. This in turn leads to great simplification of diagrammatic evaluations when one deals with the infinite dimension limit.

2.4.1 Mean field treatment

As is already mentioned in the former section the external and internal vertices are connected with lines that are representative of the density matrix of the noninteracting state $|\Psi_0\rangle$, therefore for each site i the probability which each particle could hop from a nearest neighbor site j is proportional to $P_{ij}^{\sigma\sigma 2}$. Because each site has $2d$ nearest neighbors, therefore the condition that the summation of probability contributions to site i has to be finite leads to $P_{ij}^{\sigma\sigma} \sim 1/\sqrt{2d}$. One may write the Hamiltonian Eq. (2.51) in terms of $P_{ij}^{\sigma\sigma}$ as,

$$\hat{H}_U = -\sum_{\langle ij\rangle\sigma} t_{ij} P_{ij}^{\sigma\sigma} + \sum_i U \hat{n}_{i\sigma}\hat{n}_{i\bar{\sigma}}. \tag{2.57}$$

By considering the scaling of $P_{ij}^{\sigma\sigma}$ and the fact that each site has $2d$ nearest neighbors, one may infer that in order to have finite kinetic energy for each site it is necessary to scale $t_{ij} = \tilde{t}_{ij}/\sqrt{2d}$, with a fixed $\tilde{t}_{ij}$. A more rigorous justification of this scaling was presented by Metzner and Volhardt [87]. Moreover based on the above mentioned analysis it is possible to see that there is no meaningful mean field argument about the local part of the Hamiltonian, in the other words it is finite in all dimensions and could not be scaled in this way. This ideas further could be extended to general multiband system such that $t_{ij}^{\gamma\gamma'} \simeq 1/\sqrt{2d}$, where γ and γ' are combined orbital and spin index. By considering the above scaling for the hopping parameter finally one may infer the general scaling for the density matrix as $P_{ij}^{\gamma\gamma'} \simeq 1/\sqrt{2d}^{|i-j|}$, where $|i-j|$ is the Manhattan metric that counts the shortest number of lattice steps between sites i and j.

2.4.2 Expectation values in infinite dimensions

As is obvious from the scaling law of the $P_{ij}^{\sigma\sigma}$, the local density matrices do not obey the scaling law. This is true only for the nonlocal lines in the diagrammatic expansion. Furthermore these local density matrices contribute in the diagrammatic expansion of various expectation values. This in turn makes the diagrammatic evaluations very difficult even in the infinite dimension limit. However, as is shown in references [88–90] in detail these difficulties could be avoided by redefining the projector and the non-interacting wavefunction $|\Psi_0\rangle$. Therefore rather than the projector in Eq. (2.54), a new projector is defined as,

$$\hat{P}_i = \sum_{\Gamma} \lambda_{\Gamma_i} |\Gamma\rangle_{ii}\langle\Gamma|, \tag{2.58}$$

where $|\Gamma\rangle$ are the full local eigenstates of the local part of the Hamiltonian and $|\Gamma\rangle_{ii}\langle\Gamma|$ are projectors into specific states. For the specific case of the single band Hubbard model these local eigenstates are $|0\rangle$, $|\uparrow\rangle$, $|\downarrow\rangle$ and $|\uparrow\downarrow\rangle$. By choosing these kind of projectors, as is stated in more detail in [89, 90], and by imposing the following set of local constraints it is ensured that diagrams which contains local Hartree-Fock contributions are discarded,

$$\begin{aligned}&\langle P_i^2\rangle_0 = 1,\\ &\langle P_i^2 \hat{c}^\dagger_{i\sigma}\hat{c}_{i\sigma'}\rangle_0 = \delta_{\sigma\sigma'}\langle \hat{c}^\dagger_{i\sigma}\hat{c}_{i\sigma}\rangle_0.\end{aligned} \tag{2.59}$$

In other words the effect of local diagrams is absorbed into $|\Psi_0\rangle$ as $|\Psi_0\rangle$ is a variational parameter in this new formulation and it is not the simple Hartree-Fock solution of the non-interacting system. Notice that in general the second equation in the above set of equations is not diagonal with respect to σ and σ', this is true in particular for multiband cases which we will address it in the following. These extra constraints do not restrict the number of variational parameters because by introducing new definitions for the new projectors an extra number of variational parameters are already included in the local correlator in Eq. (2.58). Notice here that the elimination of diagrams with local contribution only happens for the diagrams which contain internal vertices, however for external vertices the local Hartree-Fock contribution should be considered.

In the following sections we use this point in order to calculate the renormalization factors. By considering the scaling of the $P_{ij}^{\sigma\sigma} \sim 1/\sqrt{2d}^{|i-j|}$ then it is possible to show that a diagram vanishes if it contains an internal vertex which is connected to other vertices by three or more lines. Furthermore, as is shown in [86, 89, 90] the disconnected terms are cancelled out by denominators in Eq. (2.55) and only connected diagrams remains.

In short, the evaluation of the expectation values are reduced to the following forms in the limit of infinite dimensions,

$$\langle\Psi_G|\hat{c}^\dagger_{i\sigma}\hat{c}_{j\sigma}|\Psi_G\rangle =^{D\to\infty} \langle\Psi_0|\hat{P}_i\hat{c}^\dagger_{i\sigma}\hat{P}_i\hat{P}_j\hat{c}_{j\sigma}\hat{P}_j|\Psi_0\rangle, \tag{2.60}$$

$$\langle\Psi_G|\hat{m}_{i\Gamma}|\Psi_G\rangle =^{D\to\infty} \langle\Psi_0|\hat{P}_i\hat{m}_{i\Gamma}\hat{P}_i|\Psi_0\rangle, \tag{2.61}$$

$$\langle\Psi_G|\Psi_G\rangle =^{D\to\infty} \langle\Psi_0|\Psi_0\rangle = 1. \tag{2.62}$$

Where $\hat{m}_{i\Gamma} = |\Gamma\rangle_{ii}\langle\Gamma|$, and $|\Gamma\rangle$ are the eigenbasis of the local part of the Hamiltonian. The above set of equations together with equations Eqs.(2.59), define the so called Gutzwiller approximation, which is exact in the limit of infinite dimensions. Notice that the above mentioned analysis about infinite dimension limit is also valid for multiband systems. In the following we present conventions and GA for generic multiband model.

Convention for the representation of the local term in generic multiband system(see Eqs. (2.33) and (2.34)):
In order to fix the convention of the representation of the Hilbert space of the local part of

the Hamiltonian, like Sec.2.3.1 we define a state corresponding to an ordered configuration as,

$$|I\rangle = \hat{c}^{\dagger}_{\gamma_1} \cdots \hat{c}^{\dagger}_{\gamma_{|I|}} |0\rangle, \tag{2.63}$$

where γ are the index of local atomic orbitals and spin (or combined site, orbitals and spin for the cluster version), the creation operators as stated before are ordered operators as $\gamma_1 < \cdots < \gamma_I$. for convenience we therefore define the operator $\hat{C}_I$ as a product of the single particle creation and annihilation operators as,

$$\hat{C}^{\dagger}_I = \hat{c}^{\dagger}_{\gamma_1} \cdots \hat{c}^{\dagger}_{\gamma_{|I|}} |0\rangle, \tag{2.64}$$

Notice here also that the orbitals are ordered with $\gamma_1 < \cdots < \gamma_I$. Likewise the conjugate operator could be written as,

$$\hat{C}_I = \hat{c}_{\gamma_{|I|}} \cdots \hat{c}_{\gamma_1} |0\rangle. \tag{2.65}$$

Following reference [89], we therefore introduce the sign function as,

$$f(\gamma, I) = \langle I \cup \gamma | \hat{c}^{\dagger}_{\gamma} | I \rangle, \tag{2.66}$$

which counts for the number of permutations that is required to create a particle in the correct ordered place in the configuration state. Another necessary definition are local projectors defined as,

$$\hat{m}_{I,I'} = \hat{C}^{\dagger}_I \hat{C}_{I'} \prod_{\gamma \notin I,I'} (1 - \hat{n}_{\gamma}). \tag{2.67}$$

For the special case of the diagonal projector,

$$\hat{m}_I = \hat{C}^{\dagger}_I \hat{C}_I \prod_{\gamma \notin I} (1 - \hat{n}_{\gamma}). \tag{2.68}$$

For the sake of simplicity we only consider that the density matrix of the local non interacting part of the Hamiltonian is diagonal. This does not impose any approximation because it is always possible to find an orbital basis set which can diagonalize the local noninteracting part of the Hamiltoninan. This in turn leads to a great simplification for the evaluation of expectation values, however it leads to a more complicated form of the local two body interactions. Therefore, we consider the following condition for the local density matrix,

$$\langle c^{\dagger}_{i\gamma} c_{i\gamma'} \rangle_0 = \delta_{\gamma\gamma'} \langle c^{\dagger}_{i\gamma} c_{i\gamma} \rangle_0 = n^{\gamma}_0. \tag{2.69}$$

After diagonalizing the local part of the Hamiltonian, which is now represented in some local orbital basis set with diagonal local density matrix, one may write the eigenbasis of the local part of the Hamiltonian as a function of local configurations $|I\rangle$ as,

$$|\Gamma\rangle = \sum_I T_I^\Gamma |I\rangle, \tag{2.70}$$

where each eigenstate $|\Gamma\rangle$ corresponds to an eigenvalue E_Γ, with $\hat{H}_{Local}|\Gamma\rangle = E_\Gamma|\Gamma\rangle$. Notice that, here each Γ belongs to a subspace of the total local Hilbert space with a fixed number of particles. For one band, two bands or for systems with only density-density interactions (with diagonal local orbital basis) the above mentioned diagonalization could be performed easily by hand. However for a system with larger number of bands, $N > 2$, one needs to follow the ideas of Sec.2.3 in order to perform the diagonalization exactly, and further use the machinery of the ED to perform the action of creation and annihilation operators.

Afterwards it is possible to design a correlator for a specific problem. In principle a correlator could be an operator, it consist of all mutual combination of eigenstates $|\Gamma\rangle$ as,

$$P = \sum_{\Gamma\Gamma'} \lambda_{\Gamma\Gamma'} |\Gamma\rangle\langle\Gamma'|. \tag{2.71}$$

By considering that the total number of states of the local Hilbert space is equal to 2^{4N}, where N is the number of orbitals, this in turn leads to 2^{8N} variational parameters for the correlator. Therefore it is necessary to eliminate some variational parameters based on symmetries or based on physical arguments. In the following we consider only a diagonal form for the correlator as,

$$P = \sum_{\Gamma} \lambda_{\Gamma} |\Gamma\rangle\langle\Gamma|. \tag{2.72}$$

Hereafter we define $\hat{m}_\Gamma = |\Gamma\rangle\langle\Gamma|$.

Evaluation of the local terms:

Then by choosing the correlator as is defined in Eq. (2.72) the evaluation of the local operators $\hat{m}_\Gamma$ is straight forward,

$$\begin{aligned} \langle\Psi_0|\hat{P}_i\hat{m}_{i\Gamma}\hat{P}_i|\Psi_0\rangle &= \langle\Psi_0|\hat{P}_i\hat{m}_{i\Gamma}\hat{P}_i|\Psi_0\rangle_0, \\ &= \lambda_\Gamma^2 m_\Gamma^0, \end{aligned} \tag{2.73}$$

where,

$$m_\Gamma^0 = \sum_I T_{\Gamma I}^2 m_I^0, \tag{2.74}$$

with $m_I^0 = \prod_{\gamma} n_\gamma^0 \prod_{\gamma' \notin I} (1 - n_{\gamma'}^0)$. Notice here that we use the condition that the local density matrix is diagonal.

Hopping expectation values:
In order to calculate $\langle \Psi_0 | \hat{P}_i \hat{c}_{i\gamma}^\dagger \hat{P}_i \hat{P}_j \hat{c}_{j\gamma'} \hat{P}_j | \Psi_0 \rangle$, one may first find an expression for $\hat{P}_i \hat{c}_{i\gamma}^\dagger \hat{P}_i$ as,

$$\hat{P}_i \hat{c}_{i\gamma}^\dagger \hat{P}_i \;=\; \sum_{\Gamma\Gamma'} \lambda_\Gamma \lambda_{\Gamma'} \langle \Gamma | c_\gamma^\dagger | \Gamma' \rangle | \Gamma \rangle \langle \Gamma' |. \tag{2.75}$$

By using Eq. (2.70) for the expression of the local eigenstates as function of local configurations, the following equations yields for $|\Gamma\rangle\langle\Gamma|$ and $|\Gamma'\rangle\langle\Gamma'|$,

$$|\Gamma\rangle\langle\Gamma| = T_{\Gamma I_1'}^* T_{\Gamma I_1} | I_1 \rangle \langle I_1' |, \tag{2.76}$$

$$|\Gamma'\rangle\langle\Gamma'| = T_{\Gamma I_2}^* T_{\Gamma I_2'} | I_2' \rangle \langle I_2 |. \tag{2.77}$$

By substitution of the above expressions into Eq. (2.75), we have,

$$\hat{P}_i \hat{c}_{i\gamma}^\dagger \hat{P}_i = \sum_{\Gamma\Gamma'} \lambda_\Gamma \lambda_{\Gamma'} \sum_{I_1 I_2 I_1' I_2'} \langle I_1' | c_\gamma^\dagger | I_2' \rangle T_{\Gamma I_1'}^* T_{\Gamma I_1} T_{\Gamma I_2}^* T_{\Gamma I_2'} \hat{m}_{I_1 I_2}. \tag{2.78}$$

After substitution of the above equation into the Eq. (2.60), one end up with the calculation of the following expectation value for the evaluation of the hopping expectation values,

$$E(I_1, I_2, J_1, J_2) = \langle \hat{m}_{i;I_1 I_2} \hat{m}_{j;J_1 J_2} \rangle_0. \tag{2.79}$$

This quantity could be calculated by means of Wick's theorem. This is possible because $|\Psi_0\rangle$ is a noninteracting single particle product. In general the diagrammatic evaluation of this quantity leads to diagrams with several lines which connect the sites i and j, however exploiting the infinite dimension approximation which results in the scaling of counteractions $P_{ij}^{\gamma\gamma'} \sim 1/\sqrt{2d}^{|i-j|}$, here $|i-j| = 1$, together with scaling of the hopping amplitudes $t_{ij} \sim 1/\sqrt{2d}$, then ensures that all diagrams with two or more lines will be discarded in the infinite dimension limit. Therefore the only remaining diagram is one which connects i and j with only one line. This in turn leads to the following form for $E(I_1, I_2, J_1, J_2)$ (by considering Eq. (2.69)),

$$E(I_1, I_2, J_1, J_2) = \sum_{\alpha} f(\alpha, I_2) \delta_{I_2 \cup \alpha, I_1} \frac{m_{I_2}^0}{1 - n_\alpha^0} \sum_{\alpha'} f(\alpha', J_1) \delta_{J_1 \cup \alpha', J_2} \frac{m_{J_1}^0}{1 - n_\alpha^0} \langle \hat{c}_{i,\alpha}^\dagger \hat{c}_{j,\alpha'} \rangle_0 \tag{2.80}$$

Finally one obtains the following form for the hopping expectation values,

$$\langle \hat{c}^\dagger_{i,\gamma}\hat{c}_{j,\gamma'}\rangle_G = \sum_{\alpha\alpha'} q^\alpha_\gamma q^{\alpha'}_{\gamma'}\langle \hat{c}^\dagger_{i,\alpha}\hat{c}_{j,\alpha'}\rangle_0 \tag{2.81}$$

with the following expression for the renormalization factors,

$$\begin{aligned} q^\alpha_\gamma &= \frac{1}{1-n^0_\alpha}\sum_{\Gamma\Gamma'}\lambda_\Gamma\lambda_{\Gamma'}\sum_{I_1,I_2} f(\gamma, I'_2) f(\alpha, I_2) T^*_{\Gamma I'_2\cup\gamma} T_{\Gamma I_2\cup\alpha} T^*_{\Gamma I_2} T_{\Gamma I'_2} m^0_{I_2}, \\ &= \frac{1}{n^0_\alpha}\sum_{\Gamma\Gamma'}\lambda_\Gamma\lambda_{\Gamma'}\langle\Gamma|\hat{c}^\dagger_\gamma|\Gamma'\rangle\langle(|\Gamma\rangle\langle\Gamma'|\hat{c}_\alpha)\rangle_0, \\ &= \frac{1}{n^0_\alpha}\langle\hat{P}\hat{c}^\dagger_\gamma\hat{P}\hat{c}_\alpha\rangle_0. \end{aligned} \tag{2.82}$$

by considering Eq. (2.69) the explicit form of the constraints will have the following form,

$$\begin{aligned} \langle P^2\rangle_0 &= \sum_\Gamma \lambda^2_\Gamma \sum_I |T_{\Gamma,I}|^2 m^0_I = 1, \\ \langle P^2 \hat{c}^\dagger_\gamma \hat{c}_\gamma\rangle_0 &= \langle \hat{c}^\dagger_\gamma P^2 \hat{c}_\gamma\rangle_0 = \sum_\Gamma \lambda^2_\Gamma \sum_{I(\gamma\in I)} |T_{\Gamma,I/\gamma}|^2 m^0_I, \\ &= \sum_\Gamma \lambda^2_\Gamma \sum_{I(\gamma\in I)} |T_{\Gamma,I}|^2 m^0_I = \langle \hat{c}^\dagger_\gamma \hat{c}_\gamma\rangle_0. \end{aligned} \tag{2.83}$$

where I/γ means configuration which is constructed by removing particle γ from configuration I. Notice here that the square of the projector P^2_i could be freely permuted with $\hat{c}^\dagger_\gamma$ and $\hat{c}_\gamma$, and this is why we have two different expressions for the second constraint in Eqs. (2.83), However, it is easy to prove that these two expressions are equivalent. Therefore, the final form of the energy functional is,

$$E = \sum_{\langle ij\rangle;\gamma\gamma';\alpha\alpha'} t^{\alpha\alpha'}_{ij} q^\gamma_\alpha q^{\gamma'}_{\alpha'}\langle c^\dagger_{i\gamma} c_{j\gamma'}\rangle_0 + \sum_{i\gamma} v_{i\gamma}\langle c^\dagger_{i\gamma} c_{i\gamma}\rangle_0 + \sum_i \langle H^{(i)}_I\rangle_G, \tag{2.84}$$

with $\langle H^{(i)}_I\rangle_G = \sum_\Gamma E_{i\Gamma}\lambda^2_{i\Gamma} m^0_{i\Gamma}$. In practice the above mentioned energy functional should be optimized together with the constraints in Eqs.(2.83). We will address the problem of the optimization in the following sections for the cases we have studied. Furthermore we used an inhomogeneous version of the Gutzwiller approximation in order to investigate slabs and surfaces which will be addressed in the rest of the thesis.

Single band Hubbard model as example:

We now calculate the normalization factors and energy expectation value of the single band Hubbard model as the simplest example of correlated system based above mentioned evaluation of the expectation values. The local Hilbert space of this system consist of $|0\rangle$, $|\uparrow\rangle, \downarrow\rangle, |\downarrow\uparrow\rangle$ we therefore define the local projectors as,

$$\begin{aligned}
\hat{m}_{\varnothing} &= |0\rangle\langle 0| = (1-\hat{n}_{\sigma})(1-\hat{n}_{\bar{\sigma}}), \\
\hat{m}_{\sigma} &= |\sigma\rangle\langle\sigma| = \hat{n}_{\sigma}(1-\hat{n}_{\bar{\sigma}}), \\
\hat{m}_{\bar{\sigma}} &= |\bar{\sigma}\rangle\langle\bar{\sigma}| = \hat{n}_{\bar{\sigma}}(1-\hat{n}_{\sigma}), \\
\hat{m}_{d} &= |\downarrow\uparrow\rangle\langle\uparrow\downarrow| = \hat{n}_{\sigma}\hat{n}_{\bar{\sigma}},
\end{aligned} \tag{2.85}$$

and one may define the correlator as,

$$P = \lambda_{\varnothing}\hat{m}_{\varnothing} + \lambda_{\sigma}\hat{m}_{\sigma} + \lambda_{\hat{\sigma}}\hat{m}_{\hat{\sigma}} + \lambda_{d}\hat{m}_{d}. \tag{2.86}$$

The local constraints have the following form,

$$\begin{aligned}
\langle\hat{P}^2\rangle_0 = \lambda_{\varnothing}^2 m_{\varnothing}^0 + \sum_{\sigma=\downarrow,\uparrow} \lambda_{\sigma}^2 m_{\sigma}^0 + \lambda_d^2 m_d^0 = 1, \\
\langle\hat{P}^2\hat{c}_{\sigma}^{\dagger}\hat{c}_{\sigma}\rangle_0 = \lambda_{\sigma}^2 m_{\sigma}^0 + \lambda_d^2 m_d^0 = \langle\hat{c}_{\sigma}^{\dagger}\hat{c}_{\sigma}\rangle_0.
\end{aligned} \tag{2.87}$$

and the renormalization factors could be calculated easily in this way as,

$$\begin{aligned}
q_{\sigma} = {q_{\sigma}}^{\sigma} &= \lambda_{\sigma}\lambda_{\varnothing}\langle\hat{n}_{\sigma}\rangle_0 + \lambda_{\bar{\sigma}}\lambda_d\langle\hat{n}_{\bar{\sigma}}\rangle_0 \\
&= \frac{1}{\sqrt{\langle\hat{n}_{i\sigma}\rangle_0(1-\langle\hat{n}_{i\sigma}\rangle_0)}}\left[\sqrt{d_i(\langle\hat{n}_{i\sigma}\rangle_0 - d_i)} + \sqrt{(\langle\hat{n}_{i\bar{\sigma}}\rangle_0 - d_i)(1-n_{i,0}+d_i)}\right],
\end{aligned} \tag{2.88}$$

with $d_i = \lambda_d^2 m_d^0$. The final form of the energy functional for a single band Hubbard model could be written as follows,

$$E(\{\lambda_{\Gamma}\}, |\Psi_0\rangle) = \sum_{\langle ij\rangle,\sigma} t_{ij} q_{i\sigma} q_{j\sigma} \langle\hat{c}_{i\sigma}^{\dagger}\hat{c}_{j\sigma}\rangle_0 + U\sum_i d_i(\{\lambda_{\Gamma}\}, \{\langle\hat{n}_{\sigma}\rangle_0\}). \tag{2.89}$$

Finally the above mentioned energy functional should be minimized as function of all variational parameters in the correlator and $|\psi_0\rangle$, but subjected to constraints in Eqs. (2.87).

Remark. 1: in the chapters 3 and 4, the $\sqrt{q_\sigma}$ is the representative of q_σ factors here. In those chapters q_σ is directly refered as QP weight, while here q_σ^2 plays the same rule.

Remark. 2: in the chapters 3-5, we consider paramagnetic solution of the system, while the true ground state of the system should be magnetic. The main reason for neglecting the magnetization is because our aim was to simulate the paramagnetic cases which happen in higher temperatures which is more realistic. This is why we neglect the magnetization which is true ground-state of the system. The magnetization is expected to occur in very low temperatures. Because GA works only at zero temperatures, therefore neglecting magnetization within GA is an extra approximation.

2.5 DMFT for full local correlations

Another promising theoretical tool used for solving the many body lattice problems, is the so called dynamical mean field theory (DMFT) [38]. This approximation also relies on the dimensionality of the lattice and is exact in $d = \infty$. Because this theory is formulated at finite temperature, the central objects in the formulation are imaginary time ordered Green's functions. In particular the single particle Green's function is defined as,

$$\begin{aligned} G_{\alpha\gamma}(\tau) &= -\langle T_\tau \hat{c}_\gamma(\tau)\hat{c}_\alpha^\dagger(0)\rangle, \\ &= -\theta(\tau)\langle \hat{c}_\gamma(\tau)\hat{c}_\alpha^\dagger(0)\rangle + \theta(-\tau)\langle \hat{c}_\alpha^\dagger(0)\hat{c}_\gamma(\tau)\rangle, \\ &= -G_{\alpha\gamma}(\tau+\beta), \end{aligned} \tag{2.90}$$

where α and γ represent combined lattice site, spin and orbital indices, β is the inverse of the temperature, the $\langle\rangle$ is the average over grand-canonical density matrix operator $e^{-\beta(\hat{H}-\mu\hat{N})}$ and the time dependent operators are defined through the imaginary time Heisenberg operators as $O(\tau) = e^{\hat{H}\tau}Oe^{-\hat{H}\tau}$. The anti-periodicity arises from cyclic properties of the trace. The Fourier transform of $G(\tau)$ to imaginary Matsubara frequencies could be performed as,

$$G_{\alpha\gamma}(\imath\omega_n) = \int_0^\beta d\tau G_{\alpha\gamma}(\tau)e^{\imath\omega_n\tau}, \tag{2.91}$$

$$G_{\alpha\gamma}(\imath\omega_n) = \frac{1}{\beta}\sum_{-\infty}^{\infty} G_{\alpha\gamma}(\imath\omega_n)e^{-\imath\omega_n\tau}, \tag{2.92}$$

where $\omega_n = \dfrac{2\pi}{\beta}(2n+1)$. For free particles with spin σ and a Hamiltonian diagonal in momentum space $\hat{H} - \mu\hat{N} = (\epsilon_k - \mu)\hat{c}^{\dagger}_{k\sigma}\hat{c}_{k\sigma}$, the non-interacting Green's function reads,

$$G^0_{k\sigma}(\imath\omega_n) = \frac{1}{\imath\omega_n + \mu - \epsilon_k}, \tag{2.93}$$

For interacting systems the self energy, $\Sigma_{k\sigma}(\imath\omega_n)$, is defined as the difference between the inverse of the non-interacting Green's function and full interacting one as,

$$\Sigma_{k\sigma}(\imath\omega_n) = G^{-1}_{0k\sigma}(\imath\omega_n) - G^{-1}_{k\sigma}(\imath\omega_n). \tag{2.94}$$

The effect of the interactions is fully encoded in the properties of the self-energy $\Sigma_{k\sigma}(\imath\omega_n)$. By reorganizing Eq. (2.94) one may express $G_{k\sigma}(\imath\omega_n)$ as function of $\Sigma_{k\sigma}(\imath\omega_n)$ as,

$$G_{k\sigma}(\imath\omega_n) = \frac{1}{\imath\omega_n + \mu - \epsilon_k - \Sigma_{k\sigma}(\imath\omega_n)}, \tag{2.95}$$

The equations (2.94) and (2.95) are the so called Dyson equations. In general there is no explicit form for the self-energy and approximations are necessary.

The aim of any mean-field approximation is to map the lattice problem to a single site effective problem, which has less degrees of freedom and could be solved with less difficulties in comparison to the original problem. The meaning of the mean field approximation is to freeze some wild fluctuations (here we are interested in freezing spatial fluctuations) and only consider an average of the quantity in order to evaluate expectation values. In particular, as is stated in the former section the dimensionality of the system could be used as a measure to indicate in which level the spatial fluctuations are important i.e. the larger dimensionality leads to less effective spatial contributions. This concept is already used in the context of Gutzwiller approximations to drive non-trivial mean-field like static approximation in the limit of infinite dimensions, in that case $d = \infty$ requires the evaluation of expectation values only locally.

Another way to drive the mean-field approximations for lattice fermions and in particular for Hubbard models, is to use again the hopping scaling $t/\sqrt{2d}$, like the scaling of the density matrices in the section 2.4.1, the Green's functions also obey the same scaling properties $G_{ij}(\imath\omega_n) \sim 1/\sqrt{d}^{|i-j|}$, where $|i-j|$ is the Manhattan metric which counts the shortest lattice steps between site i and site j. Therefore, rather than working with single particle density matrices for the diagrammatic expansion of the Gutzwiller wave function, one may exploit this scaling in diagrammatic expansions of the Green's functions and self-energies. Therefore the limit of $d = \infty$ (infinite coordination number) has two consequences:

First, it leads the self energy being spatially local in this limit [87].

Second, it allows for the mapping of the full lattice problem to an effective single site problem.

This mapping could be performed most easily by representing the partition function in the fermionic path integral formalism, in particular we consider the single band Hubbard model as,

$$\Xi = \int \prod_i D[c^*_{i\sigma}(\tau), c_{i\sigma}(\tau)] e^{-S[c^*_{i\sigma}, c_{i\sigma}]}, \tag{2.96}$$

where $c^*_{i\sigma}$ and $c_{i\sigma}$ are independent Grassman variables which like Green's functions obey the anti-periodic relation $c^*_{i\sigma}(\tau) = -c^*_{i\sigma}(\tau + \beta)$ [91] and the action is defined as $S = S_0 + S^{(0)} + \Delta S$. S_0 contains only the contribution of site 0 and is defined as,

$$S_0 = \int_0^\beta d\tau [\sum_\sigma c^*_{0\sigma}(\tau)(\partial_\tau + \mu) c_{0\sigma}(\tau)] + U c^*_{0\sigma}(\tau) c_{0\sigma}(\tau) c^*_{0\bar{\sigma}}(\tau) c_{0\bar{\sigma}}(\tau)]. \tag{2.97}$$

ΔS contains the terms which couples site 0 to the rest of the lattice,

$$\Delta S = -\int_0^\beta d\tau \sum_{i\sigma} [t_{0i\sigma} c^*_{0\sigma}(\tau) c_{i\sigma}(\tau) + t_{0i\sigma} c^*_{i\sigma}(\tau) c_{0\sigma}(\tau)]. \tag{2.98}$$

Finally $S^{(0)}$ contains the contribution of lattice sites other than site 0, which reads,

$$\begin{aligned} S^{(0)} &= \int_0^\beta d\tau [\sum_{i \neq 0 \sigma} c^*_{i\sigma}(\tau)(\partial_\tau + \mu) c_{i\sigma}(\tau) - \sum_{i,k \neq 0, \sigma} t_{ij} c^*_{i\sigma}(\tau) c_{k\sigma}(\tau) \\ &+ \sum_{i \neq 0} U c^*_{i\sigma}(\tau) c_{i\sigma}(\tau) c^*_{i\bar{\sigma}}(\tau) c_{i\bar{\sigma}}(\tau)]. \end{aligned} \tag{2.99}$$

By defining the average of an operator A over $S^{(0)}$ in the following way,

$$\langle A \rangle_0 = \frac{1}{\Xi^{(0)}} \int \prod_{i \neq 0} D[c^*_{i\sigma}(\tau), c_{i\sigma}(\tau)]_{i \neq 0} A e^{-S^{(0)}[c^*_{i\sigma}, c_{i\sigma}]}, \tag{2.100}$$

the partition function is reorganized as follows,

$$\Xi = \Xi^{(0)} \int D[c^*_{0\sigma}(\tau), c_{0\sigma}(\tau)] e^{-S_0[c^*_{0\sigma}, c_{0\sigma}]} \langle e^{-S_0[c^*_{0\sigma}, c_{0\sigma}, c^*_{i\sigma}, c_{i\sigma}]} \rangle_0, \tag{2.101}$$

where $\Xi^{(0)}$ is the partition function of a system from which site 0 is removed. In the next step one may expand the exponential term which contains the coupling between the site 0 and the rest of the lattice as,

$$\Xi = \Xi^{(0)} \int D[c^*_{0\sigma}(\tau), c_{0\sigma}(\tau)] e^{-S_0[c^*_{0\sigma}, c_{0\sigma}]} \sum_0^{\infty} \frac{1}{n!} \langle (\Delta S)^n \rangle_{(0)}. \tag{2.102}$$

Because we do not work with symmetry broken phases therefore $\langle c^*_{i\sigma}\rangle_{(0)} = \langle c_{i\sigma}\rangle_{(0)} = 0$, only perturbation series with even expansion exponent contribute and those with odd expansion exponents are discarded. Thus, the lowest order in the expansion is the second order term,

$$\begin{aligned} \frac{1}{2!}\int_0^{\beta} d\tau d\tau' \langle \Delta S(\tau)\Delta S(\tau')\rangle_{(0)} &= \frac{1}{2!}\int_0^{\beta} d\tau d\tau' \sum_{i,k\neq 0\sigma} [t_{j0}t_{k0}\langle c^*_{j\sigma}(\tau)c_{k\sigma}(\tau')\rangle_0 c_{0\sigma}(\tau)c^*_{0\sigma}(\tau') \\ &+ \ t_{j0}t_{k0}\langle c_{j\sigma}(\tau)c^*_{k\sigma}(\tau')\rangle_0 c^*_{0\sigma}(\tau)c_{0\sigma}(\tau')], \end{aligned} \tag{2.103}$$

where here the property that $\langle c^*_{i\sigma}c^*_{j\sigma}\rangle_{(0)} = \langle c_{i\sigma}c_{j\sigma}\rangle_{(0)} = 0$ is used, which ensures there are no symmetry broken phases. After reordering and collecting equivalent terms one may express the second order terms as,

$$\frac{1}{2!}\int_0^{\beta} d\tau d\tau' \langle \Delta S^2\rangle_{(0)} = \int_0^{\beta} d\tau d\tau' \sum_{i,k\neq 0\sigma} [t_{j0}t_{k0}G^{(0)}_{ij}(\tau-\tau')c^*_{0\sigma}(\tau)c_{0\sigma}(\tau')], \tag{2.104}$$

where $G^{(0)}_{ij}(\tau-\tau') = \langle c_{j\sigma}(\tau)c^*_{k\sigma}(\tau')\rangle_{(0)}$ is the two time correlation function. Similarly, one obtains expressions which contains higher order correlation functions by performing higher order expansions in Eq. (2.102). Finally, by using the linked-cluster theorem one may achieve the following effective action,

$$\begin{aligned} S_{eff} = S_0 + \sum_{n=1}^{\infty}\sum_{i_1\cdots i_n} & \int_0^{\beta} d\tau_1 d\tau'_1 \cdots \int_0^{\beta} d\tau_n d\tau'_n G^{(0)}_{i_1 j_1\cdots i_n j_n}(\tau_1\cdots\tau_n;\tau'_1\cdots\tau'_n) t_{0i_1}t_{0j_1}, \\ \times & \cdots t_{0i_n}t_{0j_n} c^*_{0\sigma}(\tau_1)c_{0\sigma}(\tau'_1)\cdots c^*_{0\sigma}(\tau_n)c_{0\sigma}(\tau'_n), \end{aligned} \tag{2.105}$$

where $G^{(0)}_{i_1 j_1\cdots i_n j_n}(\tau_1\cdots\tau_n;\tau'_1\cdots\tau'_n) = (-1)^n\langle c_{i_1\sigma}(\tau_1)c^*_{j_1\sigma}(\tau'_1)\cdots c_{i_n\sigma}(\tau_n)c^*_{j_n\sigma}(\tau'_n)\rangle_0$ is the $2n$ time correlation function. Notice again here that the $1/n!$ terms are canceled by reordering and collecting the similar terms in the perturbation series.

As is stated before the scaling of $t/\sqrt{2d}$ ensures the scaling of the two time correlation functions $G^{(0)}_{ij} \sim 1/\sqrt{2d}^{|i-j|}$. Because i and j are nearest neighbors of site 0 therefore $|i-j| \geq 2$, moreover $t_{i0}t_{j0} \sim 1/d$, this in turn implies $t_{i0}t_{j0}G^{(0)}_{ij} \sim 1/d^2$. By considering the fact that there are two summations over lattice sites the first order term survive in

Eq .2.105 in the limit of infinite dimensions. By using the same arguments it is inferred that higher order terms fall off at least as $1/d$ and are discarded in the limit of infinite dimensions [38]. Finally, one may rewrite S_{eff} in the limit of infinite dimensions as,

$$S_{eff} = -\sum_{\sigma} \int_0^{\beta} d\tau d\tau' c^*_{0\sigma}(\tau) g^{-1}_{0\sigma}(\tau - \tau') c_{0\sigma}(\tau'), \tag{2.106}$$

where $g^{-1}_{0\sigma}(\tau - \tau')$ is defined as,

$$\begin{aligned} g^{-1}_{0\sigma}(\tau - \tau') &= (\partial_\tau + \mu)\delta(\tau - \tau') - \sum_{i,j\neq 0} t_{0i} t_{0j} G^{(0)}_{ij\sigma}(\tau - \tau'), \\ g^{-1}_{0\sigma}(\imath\omega_n) &= (\imath\omega_n + \mu) - \sum_{i,j\neq 0} t_{0i} t_{0j} G^{(0)}_{ij\sigma}(\imath\omega_n). \end{aligned} \tag{2.107}$$

For a general lattice the following relation holds between $G^{(0)}_{ij}$ and full lattice Green's function G_{ij} [38],

$$G^{(0)}_{ij} = G_{ij} - G_{j0} G^{-1}_{00\sigma} G_{0i}, \tag{2.108}$$

where G_{00} is the local Green's function (the Green's function of site 0). Inserting back the above equation in to Eq. (2.107), after some algebra one obtains the following relation between the $g^{-1}_{0\sigma}$ (Weiss field) and local self-energy and Green's function as,

$$g^{-1}_{0\sigma}(\imath\omega_n) = \Sigma_{0\sigma}(\imath\omega_n) + G^{-1}_{00}(i\omega_n), \tag{2.109}$$

Notice that the spatial locality of the lattice self energy is assumed and was proven to be exact in the limit of infinite dimensions [87]. Therefore it is proven that in the limit of infinite dimensions it is possible to focus only on a single site problem which the effect of the other sites only contribute as a bilinear term term in the effective action in Eq. (2.106). This in turn implies the similarity between the effective action and the action of an Anderson impurity model [38]. By fixing the Weiss field $g^{-1}_{0\sigma}$ this auxiliary problem could be solved by means of non-perturbative numerical schemes the most prominent ones are variants of CTQMC methods [79, 92], Hirsch-Fye quantum Monte Carlo methods [93], methods based on ED [94] or semi-analytic methods based on perturbation expansions around atomic limit or around non-interacting limits [14]. In particular, the impurity Green's function could be calculated as,

$$G^{(imp)}_{\sigma}(\imath\omega_n) = \int D[c^*_{0\sigma}, c_{0\sigma}] c_{0\sigma}(\imath\omega_n) c^*_{0\sigma}(\imath\omega_n) e^{-S_{eff}[c^*_{0\sigma}, c_{0\sigma}]}. \tag{2.110}$$

This impurity Green's function has to be coincide with the local lattice Green's function at the solution. The local Green's function of the lattice has to be evaluated by means of the Fourier or Hilbert transform of the lattice Green's function as,

$$\begin{aligned} G_{Local,\sigma}(\imath\omega_n) &= \frac{1}{N_k}\sum_k \frac{1}{\imath\omega_n + \mu - \epsilon_k - \Sigma_{Local,\sigma}(\imath\omega_n)} \\ &= \int \frac{\rho(\epsilon)}{\imath\omega_n + \mu - \epsilon - \Sigma_{Local,\sigma}(\imath\omega_n)} d\epsilon, \end{aligned} \tag{2.111}$$

where $\rho(\epsilon)$ the density of states of the non-interaction system (related to dispersion ϵ_k). The above equation finally closes the sets of required equations. Neither the Weiss field nor the local self energy are known a priori. In practice, the sets of equations (2.109), (2.110) and (2.111), have to be solved self consistently, the procedure consist of the following steps,

I. Starting from a guess for the local lattice self-energy (often $\Sigma(\imath\omega_n) = 0$) the local lattice Green function is evaluated by using Eq. (2.111).

II. The Weiss field is evaluated by using local Green's function and Eq. (2.109).

III. The Weiss field which is evaluated in the step **II** has to be used for the evaluation of impurity Green's function by solving impurity problem through Eq. (2.110), then a new self energy has to be calculated by means of impurity Dyson equation $\Sigma_\sigma^{(imp)}(\imath\omega_n) = g_{0\sigma}^{-1}(\imath\omega_n) - G_\sigma^{-1(imp)}(i\omega_n)$. By inserting back the new self-energy into step **I** the whole procedure should be repeated until desired convergence is achieved.

Following reference [95], the real space version of the DMFT equations for systems which are not translational invariant follows the same as translational invariant one, however there are some small differences. First, in general, the non-interacting part of the Hamiltonian is a matrix with a dimension equal to number of inequivalent sites. Therefore the lattice Green's function has to be evaluated by using a matrix version of the Dyson equation from which the local Green's function is directly accessible by using the following matrix inversion procedure,

$$\hat{G}_{ii\sigma}(\imath_n) = [(\imath\omega_n + \mu)I - \hat{H}_0 - \hat{\Sigma}_\sigma(\imath\omega_n)]_{ii}^{-1}. \tag{2.112}$$

Here $\hat{H}_0$ is the non-interacting part of the Hamiltonian with a dimension equal to number of inequivalent lattice sites, I is the unit matrix, and $\hat{\Sigma}(\imath\omega_n)$ is a diagonal self energy matrix. The second difference is that the impurity problem has to be solved for all inequivalent lattice sites independently by using a site dependent Weiss field $g_{ii\sigma}(\imath\omega_n)^{-1} = G_{ii\sigma}(\imath\omega_n)^{-1} + \Sigma_{ii\sigma}(\imath\omega_n)$ and the corresponding self-energy has to be solved by means of impurity Dyson equation for the impurity embedded to each site. After forming the diagonal self-energy matrix $\hat{\Sigma}_\sigma(\imath\omega_n)$ it should be fed back into step **I** in the DMFT equations.

2.5.1 Mott insulator thin film subjected to an electric field

Here we show results of DMFT equations for an insulating thin film described by the single band Hubbard model. Our system consists of a simple cubic lattice system which has translational invariance in (100) and (010) directions, with $L = 24$ number of layers in the direction of (001). Therefore the Hamiltonian has the following form in a combined momentum and layers index representation,

$$\hat{h}_\sigma(k_\parallel) = \sum_i (\epsilon_{\sigma k_\parallel} + v_i)\hat{c}^\dagger_{i\sigma k_\parallel}\hat{c}_{i\sigma k_\parallel} - t_\perp \sum_{\langle ij\rangle} \hat{c}^\dagger_{i\sigma k_\parallel}\hat{c}_{j\sigma k_\parallel}, \tag{2.113}$$

where $k_\parallel = (k_x, k_y)$, $\epsilon_{\sigma k_\parallel} = -2t_\parallel(\cos k_x + \cos k_y)$, $t_\parallel$ and $t_\perp$ are inter-layer and intra-layer hopping elements and v_i are local potentials to mimic the effect of external electric field. The lattice Dyson equation for the above mentioned Hamiltonian reads,

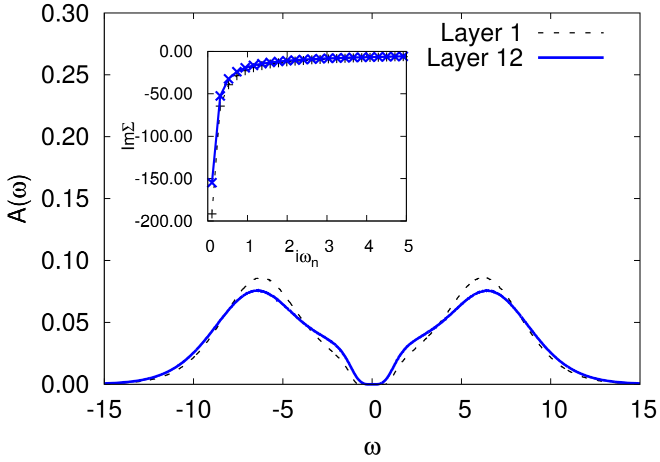

Figure 2.2: Spectral function for a system with $L = 24$ layers, $U = 12.5$, and $\beta = 30$. Inset: imaginary part of the self energy for different layers.

$$G_{ii\sigma}(\imath\omega_n) = \frac{1}{N_{k_\parallel}} \sum_{k_\parallel} [(\imath\omega_n + \mu)I - \hat{h}_\sigma(k_\parallel) - \hat{\Sigma}_\sigma(\imath\omega_n)]^{-1}_{ii}, \tag{2.114}$$

with $N_{k_\parallel} = N_{k_x}N_{k_y}$. In the following we consider $t_\parallel = t_\perp = 1$ and every other coupling constants are scaled by $t_\perp$, moreover we consider a system at half filling $\mu = U/2$ and we

---

This study is in progress, the results presented in this section were obtained in collaboration with group of Prof. Dr. Jean-Pierre Locquet at KULeuven.

focus on paramagnetic solution which means the spin symmetry $\hat{\Sigma}_\sigma = \hat{\Sigma}_{\bar{\sigma}}$ is considered in the following. We have implemented our real space DMFT based in Toolbox for Research on Interacting Quantum Systems (TRIQS) library, in particular we used CTQMC hybridization expansion [96] as impurity solver. For the spectral functions we employed the maximum entropy method for the analytic continuation of the local imaginary time Green's function to real energies [97]. Here we show the results for a system with $L = 24$ layers, $\beta = 30/t_\parallel$. In addition we apply a linear potential profile from $+v/2$ to $-v/2$, in the z-direction ((001) direction), with $v = 3.0$ and $v = 0.0$, moreover we used the interaction strength $U = 12.5$. We therefore stabilize an insulating solution for these set of parameters.

In Fig. 2.2, we present the spectral function at the surface layer and central layers, when the electric field is not applied to the system. As stated before this system is insulating and both spectral functions of the central layer and surface layers show a gap. It is possible to recognize the differences between the two spectral functions such that the spectral function of the surface layer has more pronounced Hubbard bands in comparison to the central layer spectral function this is a signature of the larger correlation effects at the surface. This is further supported by the inset which shows the imaginary part of the self energy as a function of Matsubara frequencies. It is again possible to recognize, that in both cases the imaginary part of the self energies shows insulating behavior (almost divergent, but not real divergence because we work with finite temperature). For the surface layer this behavior is more pronounced.

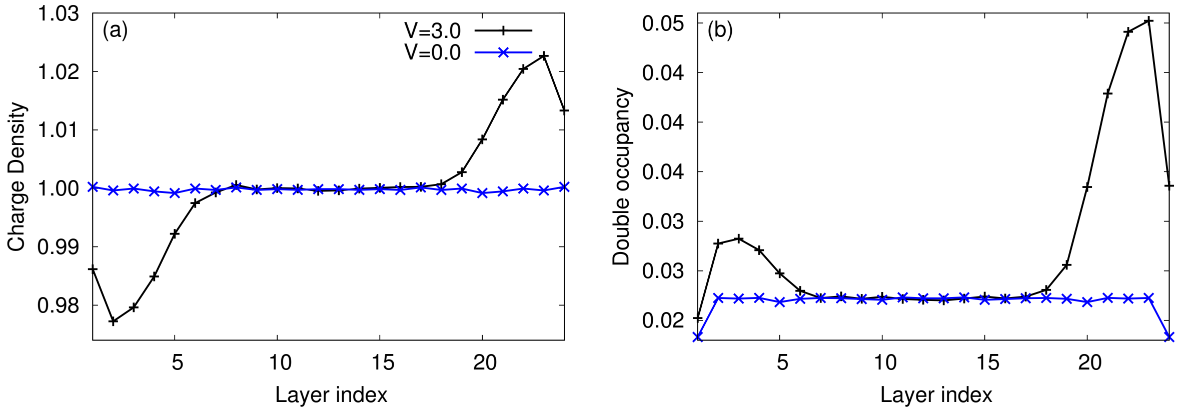

Figure 2.3: (a) The distribution charge density for systems with $L = 24$ layers, $U = 12.5$, $\beta = 30$ and different v, (b) Double occupancy distribution for systems with the same parameters.

In Fig. 2.3, we show the charge density and double occupancy distribution for a system with $v = 0$ and $v = 3.0$. It is possible to see that for the case with $v = 0$, in Fig. 2.3(a), all the layers are at the half filling due to particle hole symmetry.

Furthermore, in Fig. 2.3(b), the double occupancy is suppressed at the surface due to the lower coordination number for the surface layer. Upon application of the electric field with $v = 3.0$, as is shown in Fig. 2.3(a), the local charge distribution is away from half filling for the edge layers. The maximum deviation from the half filling is not exactly at the surface but at the layer subsequent to the surface. This is also due to the lower coordination number at the surface (we will address this in Chapter.3 with Gutzwiller approximation in more details). Furthermore, the electric field effects appears to be screened out upon approaching the central layers, where the local charge is at half filling and the electric field has no effects on these sites (from the charge redistribution point of view). Different from the charge distribution the double occupancy distribution is not symmetric around the center, as is obvious in Fig. 2.3(b). The reason for this is the fact that for the places with larger density the double occupancy is pronounced due to the presence larger number of particles together with reduced correlation effects due local over doping, however for the places with lower particle density the double occupancy is only pronounced due to suppression of correlation effects due to local under doping while the reduced occupations reduces the double occupancy in comparison with over doped regions. The double occupancy shows the same layer dependent feature as $v = 0.0$ case, it is suppressed at the surface due to the low coordination number.

In Fig. 2.4(a), we present the spectral function for different layers for the system subjected to electric field. As seen from the figure there is a QP peak at the Fermi level for the

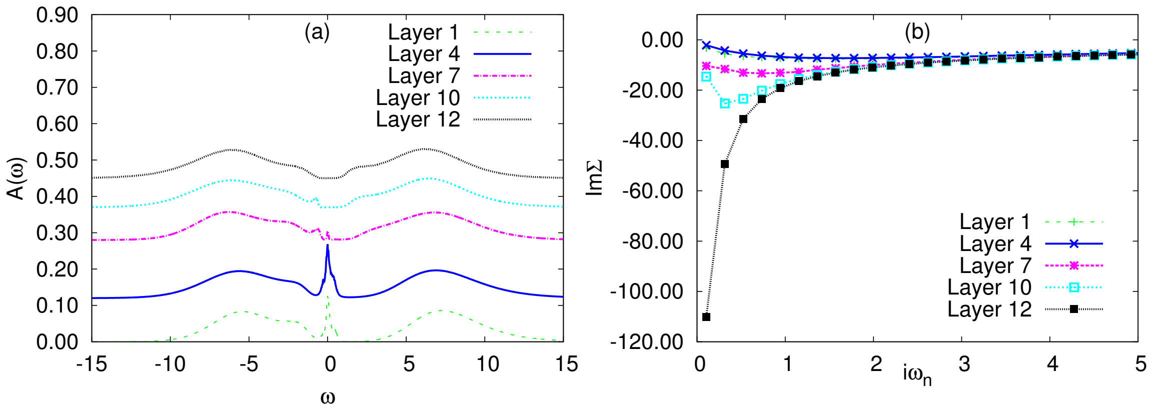

Figure 2.4: (a) Layer dependent spectral functions for different layers, starting from below 1,4,7,10 and 12, (b) Layer dependent imaginary part of the self-energy.

spectral functions of the surface layers up to the layer number 7. The QP peak disappears in the subsequent layers. By looking at the imaginary part of the self-energy in Fig. 2.4(b), it is seen that the $Im\Sigma(\imath\omega_0)$ has divergent behavior only for the layer number 12 where the electric field has the lowest effect. Moreover, a comparison between the $Im\Sigma(\imath\omega_0)$ shown in the inset of Fig. 2.2 for central layer ($v = 0.0$) and the $Im\Sigma(\imath\omega_0)$ at the central layer for the case with electric field shows that the effect of electric field is to suppress the insulating behavior although a MIT is not happened for this layer. Here, we emphasize that the above mentioned results appear to support the Gutzwiller approach we used in the analysis of slabs with larger sizes for describing the QP and charge distribution, which we will present in the following sections. Finally, I acknowledge that the DMFT results are obtained with collaboration with Petar Bakalov, a member of the group of Professor Jean Pierre Locquet at KULeuven.

2.6 Different gauges for electric field

It is possible to consider the electric field in two different gauges. One way is by considering time dependent vector potentials. This could be considered as Peierls substitution as,

$$\hat{H}_{\phi}(t) = -\sum_{\langle ij\rangle\sigma}[h_{ij}e^{\frac{ie}{\hbar c}\int_{x_i}^{x_j} A(x,t)dx}\hat{c}^{\dagger}_{i\sigma}\hat{c}_{j\sigma} + h.c.] + H_{int}, \tag{2.115}$$

where $\langle ..\rangle$ represents a summation over the nearest neighbor sites. $\hat{c}^{\dagger}_{i\sigma}$ and $\hat{c}_{j\sigma}$ are the creation and annihilation fermion operators. The fermion density is defined as usual, as $\hat{n}_i = \hat{n}_{i\uparrow} + \hat{n}_{i\downarrow}$ with $\hat{n}_{i\sigma} = \hat{c}^{\dagger}_{i\sigma}\hat{c}_{i\sigma}$. This gauge is appropriate for both translationally invariant system or translational broken system. However for a translational broken system one may write the effect of the electric field as,

$$\hat{H}_F = -\sum_{\langle ij\rangle\sigma}[h_{ij}\hat{c}^{\dagger}_{i\sigma}\hat{c}_{j\sigma} + h.c.] + \sum_i v_i\hat{n}_i + H_{int}, \tag{2.116}$$

For an uniform constant electric field the potential could be written as $v_s = x_sF$, where $x_s = sa$ and a is the lattice constant. For translational broken systems (one dimensional chains) it is possible to map between the two gauges for the uniform constant electric field. This could be performed by considering $\phi_{ij}(t) = \int_{x_i}^{x_j} A(x,t)dx = \phi(t) = -Ft$, therefore by expressing $\hat{H}_{\phi}(t)$ as,

$$\hat{H}_{\phi}(t) = \hat{B}^{\dagger}(t)\hat{H}_{\phi}(0)\hat{B}(t), \tag{2.117}$$

with $\hat{B}(t) = e^{-i\sum_{s=1}^{s=L} x_s \hat{n}_s \phi(t)}$, we can define,

$$|\Psi(t)\rangle = \hat{B}^{\dagger}(t)|\tilde{\Psi}(t)\rangle. \tag{2.118}$$

By substituting the above equation into the time dependent Schrödinger equation, $\hat{H}_{\phi}(t)|\Psi(t)\rangle = i\partial_t|\Psi(t)\rangle$, here we set $\hbar = 1$, one may find the following equation for $|\tilde{\Psi}(t)\rangle$,

$$\hat{H}_{\phi}(0)|\tilde{\Psi}(t)\rangle = i\hat{B}(t)\partial_t(\hat{B}^{\dagger}(t)|\tilde{\psi}(t)\rangle) = i\hat{B}\dot{\hat{B}}^{\dagger}(t)|\tilde{\psi}(t)\rangle + i\partial_t|\tilde{\psi}(t)\rangle. \tag{2.119}$$

By substitution of $\hat{B}(t) = e^{-i\sum_{s=1}^{s=L} x_s \hat{n}_s \phi(t)}$ into the former equation, finally one may arrive at the following effective Hamiltonian $\tilde{\hat{H}} = \hat{H}_{\phi}(0) + \sum_i x_i F \hat{n}_i$ for a system with uniform constant electric field. However this gauge is not consistent with a system with periodic boundary conditions because the unitary transformation $B(t)$ already breaks the translational symmetry. Therefore, as it appears from the form of the effective Hamiltonian, the effect of an uniform electric field for a finite chain system could be mapped to the evolution of a time independent system.

2.7 Landau-Zener tunneling

In the field of quantum non-adiabatic transitions one of the most prominent models which has been extensively studied and used in different fields is the simple two level Hamiltonian, with parabolic band dispersion as,

$$H = \begin{pmatrix} -\lambda(t) & \Delta \\ \Delta & \lambda(t) \end{pmatrix}, \tag{2.120}$$

where the diagonal terms are time dependent. Therefore the time dependent eigen energies are $E_{\pm}(t) = \pm\sqrt{\Delta^2 + \lambda^2(t)}$. This simplified system was studied by Landau and Zener for the first time [98,99]. For this simplified two level system the time dependent Schrödinger equation could be solved analytically under certain conditions. As initial boundary conditions we consider that the system is in its ground state at $t = -\infty$ when the time dependent perturbation is absent. By setting $\hbar = 1$ the time dependent Schrödinger equation has the following form,

$$\begin{pmatrix} -\lambda(t) & \Delta \\ \Delta & \lambda(t) \end{pmatrix} \begin{pmatrix} \psi_1(t) \\ \psi_2(t) \end{pmatrix} = i \begin{pmatrix} \dot{\psi}_1(t) \\ \dot{\psi}_2(t) \end{pmatrix}. \tag{2.121}$$

By using the following set of gauge transformations,

$$\psi_1(t) = e^{i\int_0^t \lambda(\tau)d\tau}\tilde{\psi}_1(t) \tag{2.122}$$

$$\psi_2(t) = e^{-i\int_0^t \lambda(\tau)d\tau}\tilde{\psi}_2(t), \tag{2.123}$$

the following set of equations is obtained for the $\tilde{\psi}_1(t)$ and $\tilde{\psi}_2(t)$,

$$\dot{\tilde{\psi}}_1(t) = -i\Delta e^{-2i\int_0^t \lambda(\tau)d\tau}\tilde{\psi}_2(t) \tag{2.124}$$

$$\dot{\tilde{\psi}}_2(t) = -i\Delta e^{2i\int_0^t \lambda(\tau)d\tau}\tilde{\psi}_1(t). \tag{2.125}$$

Notice here for the first component $\tilde{\psi}_1(t)$, because at $t = -\infty$, $|\lambda| >> \delta$ the system could be considered as unperturbed. Therefore at $t = -\infty$, $|\tilde{\psi}_1| = 1$ and $|\tilde{\psi}_2| = 0$. By removing the $\tilde{\psi}_2(t)$ in the latter set of equations one may achieve the following equation for $\tilde{\psi}_1(t)$ as,

$$i\ddot{\tilde{\psi}}_1(t) + 2i\lambda(t)\dot{\tilde{\psi}}_1(t) + \Delta^2\tilde{\psi}_1(t) = 0. \tag{2.126}$$

Again we use the gauge transformation $\tilde{\psi}_1(t) = e^{-i\int_0^t \lambda(\tau)d\tau}\psi_1(t)$ to find a differential equation for $\psi_1(t)$ as,

$$\ddot{\psi}_1(t) + (\lambda^2(t) + \Delta^2 - i\dot{\lambda}(t))\psi_1(t) = 0. \tag{2.127}$$

There is no analytical solution for Eq. (2.127) for a generic $\lambda(t)$. However if $\lambda(t) = (\alpha/2)t$ then the differential equation, Eq. (2.127), becomes,

$$\ddot{\psi}_1(t) + (\frac{\alpha^2}{4}t^2 + \Delta^2 - i\frac{\alpha}{2})\psi_1(t) = 0. \tag{2.128}$$

The aim is to find the asymptotic values of $\psi_1(\infty)$ and $\psi_2(\infty)$, such that the transition probability is defined as $P_{LZ} = |\psi_1(\infty)|^2 = 1 - |\psi_2(\infty)|^2$. Zener in his paper [98] used the asymptotic properties of Weber functions and concluded that the transition probability has the following asymptotic form,

$$P_{LZ} = e^{-2\pi\frac{\Delta^2}{|\alpha|}}. \tag{2.129}$$

Therefore, the transition probability is large as long as the Landau-Zener parameter $\Delta^2/|\alpha|$ is small, which could arise from a large rate with which two states approach each other or from the smaller gap at the anti-crossing. The dependence of the transition probability on the gap at the anti-crossing in turn implies that the largest probability transfer should happen at the time at which the two states are closest. However, the Landau-Zener

(LZ) formula does not provide any clues for this. This could be understood by using the instantaneous eigen-basis of the LZ Hamiltonian rather than the unperturbed eigenstates at $-\infty$. This in turn gives the opportunity to study the change of the eigen-basis as function of an external parameter. The generic form of the solution of the time dependent Schrödinger equation $H(\lambda(t))|\psi(t)\rangle = i|\dot{\psi}(t)\rangle$ could be written as a superposition of the instantaneous eigenstates of the time-dependent Hamiltonian as,

$$|\psi(t)\rangle = \sum_n c_n(t)|n_\lambda(t)\rangle, \tag{2.130}$$

where $|n_\lambda(t)\rangle$ are the instantaneous eigenstates of $H(\lambda(t))$ with,

$$H(\lambda(t))|n_\lambda(t)\rangle = E_n(t)|n_\lambda(t)\rangle. \tag{2.131}$$

By substituting $|\psi(t)\rangle$ as expressed by Eq. (2.130) into the Schrödinger equation and by using the change of variables $\tilde{c}_n(t) = c_n(t)e^{i\theta_n(t)}$, with,

$$\theta_n(t) = \int_0^t E_n(\tau)d\tau - i\int_0^t \langle n_\lambda(\tau)|\dot{n}_\lambda(\tau)\rangle d\tau, \tag{2.132}$$

one obtains the following set of coupled differential equations for the coefficients $c_n(t)$,

$$\dot{\tilde{c}}_n(t) = -\sum_{m\neq n} e^{i\theta_{nm}(t)}\tilde{c}_m(t)\langle n_\lambda(t)|\dot{m}_\lambda(t)\rangle, \tag{2.133}$$

where $\theta_{nm}(t) = \theta_n(t) - \theta_m(t)$, this change of variables is in fact a gauge transformation because $\theta_{nm}(t)$ is purely real [100]. The change of basis set as function of time manifests itself in the $\langle n_\lambda(t)|\dot{m}_\lambda(t)\rangle$ term in the right-hand side of Eq. (2.133). By starting from an eigenstate of the Hamiltonian at $t = 0$ with $|c_n(0)| = 1$, as long as the terms $\langle n_\lambda(t)|\dot{m}_\lambda(t)\rangle \simeq 0$ during the evolution, then one arrives at the adiabatic regime where $|\psi(t)\rangle$ only follows the eigenstate of the instantaneous Hamiltonian and the coefficients $|c_n(t)| = 1$ only consist of a phase that is a combination of a geometrical Berry and a dynamical phase. For the non adiabatic regime, Eq. (2.130) not only ensures the change in the magnitude of $c_n(t)$ but each coefficient further accumulates a complicated phase consisting of dynamical and Berry phases produced by the other states. If we consider the ground-state as the starting state for the time evolution, the quantity that measures the change of basis set as function of the external parameter λ is the *ground-state fidelity* [101] which is defined as

$$\varXi(\lambda) = |\langle\psi_0(\lambda)|\psi_0(\lambda+\delta\lambda)\rangle|. \tag{2.134}$$

By using perturbative arguments it is possible to see that there is a close relationship between the ground-state fidelity and the coefficients that appear in the right hand side of Eq. (2.133),

$$\langle n(t)|\dot{m}(t)\rangle = \dot{\lambda}\frac{\langle n_\lambda(t)|\partial_\lambda H(\lambda(t))|m_\lambda(t)\rangle}{(E_n - E_m)}. \tag{2.135}$$

Therefore the change in the ground-state wave-function under an infinitesimal change of flux can be written as:

$$|\psi_0(\lambda+\delta\lambda)\rangle = \Lambda\left[|\psi_0(\lambda)\rangle + \delta\lambda\sum_{n\neq 0}\frac{\langle n_\lambda|\partial_\lambda H(\lambda)|\psi_0(\lambda)\rangle}{E_0 - E_n}|n_\lambda\rangle\right], \tag{2.136}$$

where Λ is the normalization factor as,

$$\Lambda = 1 + \sum_{n\neq 0}\delta\lambda^2\frac{\langle n|\partial_\lambda H(\lambda)|m\rangle^2}{(E_0 - E_n)^2}. \tag{2.137}$$

After normalization and considering $\delta\lambda << 1$ one obtains that

$$|\langle\psi_0(\lambda)|\psi_0(\lambda+\delta\lambda)\rangle|^2 \simeq 1 - (\delta\lambda)^2\chi_\Xi(\lambda), \tag{2.138}$$

where $\chi_\Xi(\lambda)$ is the *fidelity susceptibility* which is defined as [102, 103],

$$\chi_\Xi(\lambda) = \frac{1 - \Xi^2(\lambda)}{(\delta\lambda)^2} = \sum_{n\neq 0}\frac{\langle\psi_0(\lambda)|\partial_\lambda H(\lambda)|n_\lambda\rangle\rangle^2}{(E_0 - E_n)^2}. \tag{2.139}$$

The leading term in the fidelity expansion is of the order of $\delta\lambda^2$. When comparing the terms in the right-hand side of Eq. (2.135) with the terms that appear in the right-hand side of Eq. (2.139) one may infer that a larger $\chi_\Xi(\lambda)$ leads to a more non-adiabatic character of the transition due to the driving of the system by an external electric field. For a simplified two level system the instantaneous eigenstates of the Hamiltonian in Eq. (2.120) with eigenvalues $E_\pm(\lambda) = \pm\sqrt{\lambda^2 + \Delta^2}$ could be written as,

$$|\psi_\pm\rangle = \frac{1}{\sqrt{(E_\pm - \lambda)^2 + \Delta^2}}\begin{pmatrix}\Delta \\ E_\pm - \lambda\end{pmatrix}. \tag{2.140}$$

Therefore one arrives at the following expression for the fidelity susceptibility,

$$\begin{aligned}\chi_{\Xi}(\lambda) &= \frac{\langle\psi_-|\partial_\lambda H(\lambda)|\psi_+\rangle^2}{(E_- - E_+)^2}, \\ &= \frac{\Delta^2 - (\lambda - E_-(\lambda))(\lambda - E_+(\lambda))}{(E_- - E_+)\sqrt{[(E_+(\lambda)-\lambda)^2+\Delta^2][(E_-(\lambda)-\lambda)^2+\Delta^2]}} \\ &= \frac{\Delta^2}{(\Delta^2+\lambda^2)^2}. \end{aligned} \tag{2.141}$$

Therefore at anti-crossing $\chi_{\Xi}(0) = 1/\Delta^2$. As is obvious if the gap vanishes the fidelity susceptibility diverges and the transition to the exited state of instantaneous Hamiltonian happens. Furthermore, the fidelity susceptibility is largest at the anti-crossing $\lambda = 0$.

Chapter 3

Electric shift of the Mott metal insulator transition in thin films

The ground state properties of a paramagnetic Mott insulator at half-filling are investigated in the presence of an external electric field using the inhomogeneous GA for a single band Hubbard model in a slab geometry. We find that the metal insulator transition is shifted towards higher Hubbard repulsions by applying an electric field perpendicular to the slab. The main reason, is the accumulation of charges near the surface. The spatial distribution of site dependent QP weight shows that it is maximal in few layers beneath the surface while the central sites where the field is screened have a very low QP weight. Our results show that above a critical field value, states near the surface will be metallic while the bulk QP weight is extremely suppressed but never vanishing, even for large Hubbard repulsions above the bulk zero field critical value. Below the critical field value, our results hint towards an insulating state in which the electric field is totally screened and the slab is again at half-filling.

3.1 Introduction

The rich physics of strongly correlated materials in combination with the need to overcome the scaling limits of current silicon based semi-conductor materials in microelectronic industry has resulted in an increased activity in this field. Special attention has been focused on vanadium dioxide (VO_2) which shows an abrupt MIT near room temperature due to a structural phase transition [104]. One has found that an electric field is able to trigger MIT

The results of this chapter were published as: Davoud Nasr Esfahani, L. Covaci and F. M. Peeters, Phys. Rev. B. **85**, 085110 (2012).

in VO_2, without any structural transition, which is mostly dominated by electron correlations rather than a Peierls distortion [105]. Also, a first order MIT is observed by applying an electric field in a two terminal model of VO_2 [7, 106] without electrical breakdown of the material. Note that an, electric field driven MIT and metal-superconductor transitions have been observed at the interface between $LaAlO_3$ and $SrTiO_3$ [7].

These kind of transitions may be related to a charge transfer mechanism. A nonlinear dependence of the conductivity on the electric field is reported for the highly correlated transition metal chalcogenide $Ni(S, Se)_2$ and a continuous MIT is observed in this case [107].

In this chapter we investigate the behavior of the ground state of a single band Hubbard model [77] in the presence of a perpendicular electric field by using the GA [85]. Originally GA is rooted in the Gutzwiller wave function used to reduce the contribution of high energy states due to Hubbard repulsion and it was shown to be exact in the limit of infinite dimensions. [86–88] While an analytical solution exists only for one dimension [108], in comparison to other approximate methods the GA is equivalent to a slave boson mean field theory (SBMFT) [109] for zero temperature but in contrast to DMFT [38], it is not able to give any information about higher and lower Hubbard bands. Instead it gives a reasonable understanding about the low energy excitations near the Fermi surface [110] by supplying the QP weight of electrons such that one is then able to describe the mobility of electrons. Also, GA cannot give any information about the insulating state, instead we are only able to investigate the properties of the system by approaching the transition point, U_c, from below [88].

This method was used by Brinkman-Rice [111] to investigate the MIT of the single band Hubbard model and it allowed them to predict the critical Hubbard repulsion which is finite in two and three dimensions ($U_c = 16t$ for 3D). While not as accurate as DMFT, GA is less computationally intensive and thus allows the description of inhomogeneous systems such as thin films subjected to a perpendicular electric field. Although our simplified approach is only qualitative, it gives important information about how one may be able to spatially tune the QP weight distribution near surfaces and interfaces. This could be relevant for future studies; for example for an inhomogeneous bad metal-superconductor transition by the charge transfer mechanism which may be responsible for the SC-Insulator transition observed at the interface of a band insulator and a strongly correlated material [7]. We will show that by applying a perpendicular electric field, charges will be trapped at the surface of the Mott insulator and shift the MIT for the surface states.

The outline of the chapter is as follows. In section 3.2 we review the concept of GA and how the inclusion of on site potentials change the situation. In section 3.3 we introduce our model for the slab geometry, present the numerical scheme used and analyze the corresponding results. Finally in section 3.4 we present our conclusions.

3.2 GA in the presence of an electric field

In order to address the narrow band effects in transition metals with d or f orbitals for which correlation effects play a major role in the behavior of the system the simplest model that is able to explain the most important terms of the Coulomb interaction between electrons is the well known Hubbard model,

$$\hat{H}_U = -\sum_{\langle ij\rangle\sigma} t_{ij}(c^\dagger_{i\sigma}c_{j\sigma} + c^\dagger_{j\sigma}c_{i\sigma}) + \sum_i U\hat{n}_{i\sigma}\hat{n}_{i\bar{\sigma}}, \tag{3.1}$$

Where $\langle\rangle$ means the summation over nearest neighbor sites. $c^\dagger_{i\sigma}$ and $c_{i\sigma}$ are creation and annihilation operators at site i for spin index σ. t_{ij} is nearest neighbor hopping amplitude and U is the local interaction between spin up and spin down, with $\hat{n}_{i\sigma} = c^\dagger_{i\sigma}c_{i\sigma}$ and $\sigma =\uparrow,\downarrow$.

We will describe the ground state properties of the Hubbard model by using the GA which suppresses the contribution of high energy configurations (here configurations with higher number of double occupancies). This is done by introducing a trial wave function which contains variational parameters to be used subsequently to minimize the total energy of the system. Our aim is to investigate the properties of a strongly correlated system in the presence of an external electric field which will appear in the Hamiltonian as a position dependent potential. The induction of such an inhomogeneity is not random and we still have translational invariance in the direction perpendicular to the applied field. To study the ground state properties in the absence of the electric field, the Gutzwiller wave function is defined as:

$$|\psi_G\rangle = \prod_i g_i^{\hat{D}_i}|\psi_0\rangle = \prod_i \left[1 - (1-g_i)\,\hat{D}_i\right]|\psi_0\rangle, \tag{3.2}$$

where the double occupancy operator is $\hat{D}_i = \hat{n}_{i\sigma}\hat{n}_{i\bar{\sigma}}$, the variational parameters g_i are introduced to reduce the contribution of high energy configuration's in the many body wave function $|\psi_G\rangle$, and $|\psi_0\rangle$ is the unprojected non-interacting (Fermi sea) single particle many body wave function. Although it is obvious that by the inclusion of on site potentials no new variational parameters are needed because they do not induce any new correlations since the term is a single body interaction, nevertheless we will prove it rigorously. To obtain the normalization factors in the limit of spatial infinite dimensions, for which the GA is exact [87,88], we have to remove spatial correlations which occur in infinite dimensions together with on-site Hartree contributions which remain in the $d = \infty$ limit. This can be done by introducing a new expansion parameter following the guidelines of [88]]. If we include on-site potentials for capturing the effects of external fields, the Hamiltonian becomes:

$$\hat{H} = \hat{H}_U + \sum_{i\sigma} v_i\hat{n}_{i\sigma}. \tag{3.3}$$

In order to find the ground state of the Hamiltonian in Eq. (3.3) we introduce new variational parameters, $\zeta_{i\sigma}$ and $\zeta_{i\bar{\sigma}}$, to decrease the weight of the occupancy of the sites with higher on-site energy. The Gutzwiller wave function now becomes:

$$\begin{aligned} |\psi_G\rangle &= [1-(1-\zeta_{i\sigma})\hat{n}_{i\sigma}]\,[1-(1-\zeta_{i\bar{\sigma}})\hat{n}_{i\bar{\sigma}}]\times \\ & \quad \left[1-(1-g_i)\hat{D}_i\right]|\psi_0\rangle. \end{aligned} \tag{3.4}$$

The standard way of removing on-site Hartree contributions is to introduce the fugacity factors $\mu_{i\sigma}$ and $\mu_{i\bar{\sigma}}$ [88], the expansion parameter x_i and the non interacting state $|\varphi_0\rangle$. Then the Gutzwiller wave-function can be written as:

$$|\psi_G\rangle = \prod_i {\zeta_{i\sigma}}^{\hat{n}_{i\sigma}} {\zeta_{i\bar{\sigma}}}^{\hat{n}_{i\bar{\sigma}}} {g_i}^{2(\gamma_i-\mu_{i\bar{\sigma}}\hat{n}_{i\bar{\sigma}}-\mu_{i\sigma}\hat{n}_{i\sigma}+\hat{D}_i)}|\varphi_0\rangle \tag{3.5}$$

$$= \prod_i (1+x_i(\hat{D}_i-{\hat{D}_i}^{HF}))|\varphi_0\rangle, \tag{3.6}$$

The Hartree double occupancy operator can be defined as ${\hat{D}_i}^{HF} = \hat{n}_{i\sigma}\langle\hat{n}_{i\bar{\sigma}}\rangle_0 + \langle\hat{n}_{i\sigma}\rangle_0\hat{n}_{i\bar{\sigma}} - \langle\hat{n}_{i\sigma}\rangle_0\langle\hat{n}_{i\bar{\sigma}}\rangle_0$ and it is the result of the usual mean field decomposition $\hat{n}_{i\sigma}\to\hat{n}_{i\sigma}-\langle\hat{n}_{i\sigma}\rangle_0$. By defining $\zeta_{i\sigma}={g_i}^{\beta_{i\sigma}}$, $\zeta_{i\bar{\sigma}}={g_i}^{\beta_{i\bar{\sigma}}}$, ${\mu_{i\sigma}}'=\beta_{i\sigma}+\mu_{i\sigma}$ and ${\mu_{i\bar{\sigma}}}'=\beta_{i\bar{\sigma}}+\mu_{i\bar{\sigma}}$ we have:

$$|\psi_G\rangle = \prod_i {g_i}^{2(\gamma_i-{\mu_{i\bar{\sigma}}}'\hat{n}_{i\bar{\sigma}}-{\mu_{i\sigma}}'\hat{n}_{i\sigma}+\hat{D}_i)}|\varphi_0\rangle. \tag{3.7}$$

Therefore by using the above change of variables it is possible to obtain the same renormalization factors for the infinite dimensions limit as stated in [88]. In the minimization procedure we need to minimize the energy with respect to $|\varphi_0\rangle$ together with local variational parameters g_i that one needed to describe the correlation effects. In short, the addition of on-site potentials does not add any new variational parameters and the procedure of finding the ground state is the same as in the conventional Gutzwiller method. Thus the expectation value of the Hamiltonian over Gutzwiller wave function:

$$\begin{aligned} \langle\hat{H}\rangle_G &= -\sum_{\langle ij\rangle\sigma}\sqrt{q_{i\sigma}}\sqrt{q_{j\sigma}}t_{ij}\langle\varphi_0|\hat{c}^{\dagger}_{j\sigma}\hat{c}_{i\sigma}+h.c.|\varphi_0\rangle \\ &+ \sum_i v_i\langle\varphi_0|\hat{n}_i|\varphi_0\rangle + \sum_i U d_i, \end{aligned} \tag{3.8}$$

has to be minimized only with respect to g_i and $|\varphi_0\rangle$, where $\langle\rangle_G$ means the expectation values over $|\psi\rangle_G$. Here the renormalization factors $q_{i\sigma}$ depend on the local density of the non-interacting state $|\varphi_0\rangle$ and g_i:

$$\begin{aligned} q_{i\sigma} = & \frac{1}{\langle \hat{n}_{i\sigma}\rangle_0 (1-\langle \hat{n}_{i\sigma}\rangle_0)} \times \\ & \left[\sqrt{d_i(\langle \hat{n}_{i\sigma}\rangle_0 - d_i)} + \sqrt{(\langle \hat{n}_{i\bar{\sigma}}\rangle_0 - d_i)(1-n_{i,0}+d_i)}\right]^2, \end{aligned} \tag{3.9}$$

where d_i is the double occupancy expectation value over Gutzwiller wave function in the limit of infinite dimensions and $n_{i,0} = \langle \hat{n}_{i\sigma}\rangle_0 + \langle \hat{n}_{i\bar{\sigma}}\rangle_0$, with $\langle\rangle_0$ is defined as expectation over $|\phi_0\rangle$, while g_i are described by the following equations which holds in infinite dimensions [88]:

$$g_i{}^2 = \frac{d_i(1-n_{i,0}+d_i)}{(\langle \hat{n}_{i\bar{\sigma}}\rangle_0 - d_i)(\langle \hat{n}_{i\sigma}\rangle_0 - d_i)}. \tag{3.10}$$

Moreover, $\langle \hat{n}_{i\sigma}\rangle_0 = \langle \hat{n}_{i\sigma}\rangle_G$ holds in the limit of infinite dimensions [88]. In practice minimizing the expectation value of the Hamiltonian is difficult because of the existence of a large number of variational parameters in $|\varphi_0\rangle$ together with the dependence of the renormalization factors on $|\varphi_0\rangle$. This will lead to a highly nonlinear set of equations. In order to alleviate some of the difficulties it is possible to allow local densities, $\langle \hat{n}_{i\sigma}\rangle_0$, and $|\varphi_0\rangle$ to vary independently in the minimization procedure. This could be performed by introducing some new $n_{i\sigma}$ which plays the rule of local densities in which appears in renormalization factors and double occupancies. Then by introducing $\lambda_{i\sigma}$ as Lagrange multipliers it is possible to ensure that these new variables are equal to the local charge densities of the non interacting state at the solution. Other multipliers, Λ and E_{NI}, are introduced in order to ensure total charge conservation and guarantee that $|\varphi_0\rangle$ is normalized. Therefore the final form of the Lagrange function that has to be optimized is as follows:

$$\begin{aligned} \langle \hat{H}\rangle_G \quad &= -\sum_{\langle ij\rangle\sigma} \bar{t}_{ij}\langle\varphi_0|\hat{c}^\dagger_{j\sigma}\hat{c}_{i\sigma} + h.c.|\varphi_0\rangle + \sum_{i,\sigma} v_i \langle\varphi_0|\hat{n}_{i\sigma}|\varphi_0\rangle + \sum_i U d_i \\ &+ \sum_{i,\sigma} \lambda_{i\sigma}(\langle \hat{n}_{i\sigma}\rangle_0 - n_{i\sigma}) + \Lambda(N - \sum_{i\sigma} n_{\sigma i}) + E_{NI}(1-\langle\varphi_0|\varphi_0\rangle), \end{aligned} \tag{3.11}$$

where $\bar{t}_{ij} = \sqrt{q_{i\sigma}}\sqrt{q_{j\sigma}}t_{ij}$ are the renormalized hopping amplitudes and N is the total number of particles (or total number of states that has to be filled). To find the optimum energy first of all we vary the $|\varphi_0\rangle$ for which we have the following Schrödinger like equation:

$$\sum_{\langle ij\rangle} -\bar{t}_{ij}(\hat{c}^\dagger_{j\sigma}\hat{c}_{i\sigma} + h.c.)|\varphi_0\rangle + \sum_i (v_i + \lambda_{i\sigma})\hat{n}_{i\sigma}|\varphi_0\rangle = E_\sigma|\varphi_0\rangle, \tag{3.12}$$

which has to be diagonalized for both spins. Then $|\varphi_0\rangle$ is substituted in Eq. (3.11) and the expectation value becomes:

$$\langle \hat{H} \rangle_G = E_{NI} + \sum_i U d_i + \Lambda(N - \sum_{i,\sigma} n_{i\sigma}) - \sum_{i,\sigma} \lambda_{i\sigma} n_{i\sigma}, \tag{3.13}$$

with $E_{NI} = \sum_{s\sigma}^{occupied} E_{s\sigma}$ and $|\varphi_0\rangle = \prod_{s\sigma}^{occupied} \hat{c}^\dagger_{s\sigma}|0\rangle$, where s is the quantum number for the eigenstates of Eq. (3.12). E_{NI} depends on the variational parameters g_i, $n_{i\sigma}$, $\lambda_{i\sigma}$ and $|\varphi_0\rangle$. $|\varphi_0\rangle$ is now a function of the variational parameters $\lambda_{i\sigma}$, $n_{i\sigma}$ and g_i, and the above energy functional has to be optimized in accordance to all these parameters. This leads to the following set of saddle point conditions:

$$\begin{aligned} \frac{\partial \langle \hat{H} \rangle_G}{\partial \Lambda} &= 0, \frac{\partial \langle \hat{H} \rangle_G}{\partial \lambda_{i\sigma}} = 0, \\ \frac{\partial \langle \hat{H} \rangle_G}{\partial n_{i\sigma}} &= 0, \frac{\partial \langle \hat{H} \rangle_G}{\partial g_i} = 0. \end{aligned} \tag{3.14}$$

Notice that we consider that during the optimization $|\phi_0\rangle$ is updated throught Eg. 3.12 during the optimization for each change of variational parameters. In general the on site potential profile is a functional of the spatial density distribution due to the effects of long range electron-electron and electron-ion interactions. This effect should be addressed by considering an additional Poisson equation in the set of equations. Although the effect of charge redistribution due to long range interactions has major effects in weak Hubbard coupling it has minor effects in intermediate and strong coupling regimes due to very large screening effects of Hubbard interaction in half filling.

3.3 Model and Numerical scheme

3.3.1 Model

Our model is a slab geometry in which we have translational invariance in x and y direction and finite size in z direction. In addition we apply a linear potential profile from $-v/2$ to $+v/2$, in the z-direction. With the above assumptions the expectation value of the

Hamiltonian can be written as:

$$\begin{aligned}\langle\hat{H}\rangle_G \quad &= \frac{1}{N_{k\|}}\langle\varphi_0|\sum_{i,k_\|,\sigma}[-2tq_{i\sigma}(cosk_x+cosk_y)+v_i+\lambda_{i\sigma})\hat{c}^\dagger_{ik_\|\sigma}\hat{c}_{ik_\|\sigma}\\ &-\frac{1}{N_{k\|}}\sum_{\langle ij\rangle k_\|\sigma}\sqrt{q_{i\sigma}}\sqrt{q_{j\sigma}}t(\hat{c}^\dagger_{ik_\|\sigma}\hat{c}_{jk_\|\sigma}+\hat{c}^\dagger_{jk_\|\sigma}\hat{c}_{ik_\|\sigma})]|\varphi_0\rangle\\ &-\sum_{i\sigma}\lambda_{i\sigma}n_{i\sigma}+\Lambda(\sum_{i\sigma}n_{i\sigma}-\frac{N}{N_{k_\|}})+E_{NI}(1-\langle\varphi_0|\varphi_0\rangle)\\ &+\sum_i Ud_i, \end{aligned}\tag{3.15}$$

where i and j correspond to atoms in the z direction and $N_{k_\|}=N_{k_x}N_{k_y}$ is the total number of k points. First we optimize the Lagrange function Eq. (3.15) with respect to $|\varphi_0\rangle$ which leads to the following eigenvalue problem:

$$\begin{aligned}&\sum_i(-2tq_{i\sigma}(cosk_x+cosk_y)+v_i+\lambda_{i\sigma})\hat{c}^\dagger_{ik_\|\sigma}\hat{c}_{ik_\|\sigma}|\varphi_0\rangle\\ &-\sum_{\langle ij\rangle}\sqrt{q_{i\sigma}}\sqrt{q_{j\sigma}}t(\hat{c}^\dagger_{ik_\|\sigma}\hat{c}_{jk_\|\sigma}+\hat{c}^\dagger_{jk_\|\sigma}\hat{c}_{ik_\|\sigma})|\varphi_0\rangle=E_{k_\|,\sigma}|\varphi_0\rangle.\end{aligned}\tag{3.16}$$

Eq. (3.16) has to be solved for each $k_\|$ point and and spin component σ, in order to find the non-interacting ground state the eigenvalues will be summed up to the desired filling level:

$$\begin{aligned}E_{NI}&=\frac{1}{N_{k_\|}}\sum_{k_\|,n\sigma}^{occupied}E_{k_\|,n\sigma},\\ |\varphi_0\rangle&=\prod_{k_\|,n\sigma}^{occupied}\hat{c}^\dagger_{k_\|,n\sigma}|0\rangle,\end{aligned}\tag{3.17}$$

where n is the quantum number for the energy levels of each k point. In the next step the above non-interacting state $|\varphi_0\rangle$, which is now an implicitly function of all variational parameters $\lambda_{i\sigma}$, $n_{i\sigma}$, g_i and Λ, should be inserted into Eq. (3.15):

$$\langle\hat{H}\rangle_G=E_{NI}[\lambda_{i\sigma},n_{i\sigma},g_i,\Lambda]-\sum_{i,\sigma}\lambda_{i\sigma}n_{i\sigma}+\Lambda(\sum_{i,\sigma}n_{i\sigma}-\frac{N}{N_{k_\|}})+U\sum_i d_i.\tag{3.18}$$

By using the Hellman-Feynman equation:

$$\frac{\partial}{\partial\lambda}\langle\psi[\lambda]|H[\lambda]|\psi[\lambda]\rangle=\langle\psi[\lambda]|\frac{\partial}{\partial\lambda}H[\lambda]|\psi[\lambda]\rangle,\tag{3.19}$$

which holds when the wave-function is an eigenfunction of the non-interacting Hamiltonian, we obtain the following set of saddle point equations for the paramagnetic case ($\langle \hat{n}_{i\sigma}\rangle_0 = \langle \hat{n}_{i\bar{\sigma}}\rangle_0$):

$$\begin{aligned}\frac{\partial\langle\hat{H}\rangle_G}{\partial g_i} &= \frac{2}{N_{k_\|}}\frac{\partial q_{i\sigma}}{\partial g_i}\langle\varphi_0|\sum_{k_\|}[-2t(cosk_x+cosk_y)\hat{c}^\dagger_{ik_\|\sigma}\hat{c}_{ik_\|\sigma}-\sum_j\delta_{i,j\pm1}\frac{1}{2}\sqrt{\frac{q_{j\sigma}}{q_{i\sigma}}}\\ &\times\ t(\hat{c}^\dagger_{ik_\|\sigma}\hat{c}_{jk_\|\sigma}+\hat{c}^\dagger_{jk_\|\sigma}\hat{c}_{ik_\|\sigma})]|\varphi_0\rangle+U\frac{\partial d_i}{\partial g_i}=0,\end{aligned}\tag{3.20}$$

$$\begin{aligned}\frac{\partial\langle\hat{H}\rangle_G}{\partial n_{i\sigma}} &= \frac{2}{N_{k_\|}}\frac{\partial q_{i\sigma}}{\partial n_{i\sigma}}\langle\varphi_0|\sum_{k_\|}[-2t(cosk_x+cosk_y)\hat{c}^\dagger_{ik_\|\sigma}\hat{c}_{ik_\|\sigma}-\sum_j\delta_{i,j\pm1}\frac{1}{2}\sqrt{\frac{q_{j\sigma}}{q_{i\sigma}}}\\ &\times\ t(\hat{c}^\dagger_{ik_\|\sigma}\hat{c}_{jk_\|\sigma}+\hat{c}^\dagger_{jk_\|\sigma}\hat{c}_{ik_\|\sigma})]|\varphi_0\rangle-2\lambda_{i\sigma}-2\Lambda+U\frac{\partial d_i}{\partial n_{i\sigma}}=0,\end{aligned}\tag{3.21}$$

$$\frac{\partial\langle\hat{H}\rangle_G}{\partial\lambda_{i\sigma}}=\frac{1}{N_{k_\|}}\langle\varphi_0|\sum_{k_\|}\hat{c}^\dagger_{ik_\|\sigma}\hat{c}_{ik_\|\sigma}|\varphi_0\rangle-n_{i\sigma}=0,\tag{3.22}$$

$$\frac{\partial\langle\hat{H}\rangle_G}{\partial\Lambda}=(2\sum_i n_{i\sigma}-\frac{N}{N_{k\|}})=0.\tag{3.23}$$

Notice, here we work at half filling in the following. This means half number of states are occupied in $|\phi_0\rangle$ i. e. number of occupied states is $N_{occupied}=N=N_{k\|}N_z$, which is half of the total number of states $2N_{k\|}N_z$, where factor 2 is related to number of spin components, and N_z is number of layers in z direction. Moreover in order to impose paramagnetic condition we consider $N_{occupied,\sigma}=N_{occupied,\bar{\sigma}}=N_{occupied}/2$, where $N_{occupied,\sigma}$ is the number of occupied states with spin σ in $|\phi_0\rangle$ (notice that there is not any hopping process in single particle part of the Hamiltonian which hop between states with different spin).

In addition to the above equations, the electrostatic stability of the system should be considered by the inclusion of the Poisson equation. The effects of long range electron-electron and electron-ion interactions on the electric potential could be evaluated by considering a simple version of the Poisson equation for slab geometry as follows:

$$v_i=v_i^{(0)}-\sum_{j,i\neq j}\alpha|z_i-z_j|(n_j-1),\tag{3.24}$$

where z_i is the position of plane i. Here $\alpha=\dfrac{e^2}{2a\epsilon_0\epsilon_r}$ where ϵ_0 is vacuum permittivity, ϵ_r is relative permittivity, a is lattice constant, e is electron charge and $n_j=n_{j\sigma}+n_{j\bar{\sigma}}$.

We considered three values of the Poisson coupling parameter, $\alpha = 0$, 0.02 and 0.2. For $\alpha < 0.02$ the effect of the Poisson term on the relevant quantities is negligible while for larger values, $\alpha > 0.2$, additional screening occurs but we observe the same qualitative behavior. Experimental data show that for transition metal oxides the relative permittivity is usually very large [112]. Therefore, because $\epsilon_r = \infty$ is a good approximation for strongly correlated materials, we choose $\alpha = 0$ and neglect the additional screening of charges induced by the Poisson term.

In order to numerically solve the above set of non-linear equations (3.20)-(3.23), we use MinPack.1 [113, 114] which uses a trust-region-dogleg method, while for the k-space summation we choose a 16×16 Monkhorst-Pack [115] k-grid for which the energy is well converged for this kind of grid. From the above equations it is obvious that the Jacobian matrix required by the nonlinear solver has to be calculated by a finite difference method because no analytical evaluation of the Jacobian matrix is possible. Notice that $|\phi_0\rangle$ is implicitly function of all variational parameters and is updated through Eq. (3.16) during each variation of variational parameters and Lagrange multipliers during optimization process. Also note that the Jacobian matrix is dense and all of its elements are nonzero. We also tried to implement another approach by solving Eqs. (3.16) and (3.20)-(3.23) iteratively by starting from an estimation of the variational parameters and a calculation of $|\varphi_0\rangle$ which are then supplied to the set of Eqs. (3.20)-(3.23) to find a new set of variational parameters and then repeat the whole procedure. The iterative approach did not converge for values of $U > 4t$ which could be because of the high non-linearity of the equations for large U. Other authors also reported similar problems with such an iterative scheme [116]. Although the second approach is less costly, because the Jacobin matrix in the first method is updated at each variation of the parameters through Eq. (3.16) it is more likely that the first method converges better particularly for large U when we have a large dependence of $|\varphi_0\rangle$ on the variational parameters. In the next sections we report results for q_i as the position dependent QP weight which is an indication of the mobility of the electrons in Fermi liquid theory. It is possible to show that the inverse of this factor is proportional to the mass renormalization which is divergent for $q_i = 0$ and which corresponds to an insulating phase [117]. The quantity $\tilde{v_i} = v_i + \lambda_{i\sigma} + \Lambda$ is considered as an effective potential which acts effectively only on $|\varphi_0\rangle$. The parameters U and v are scaled with the tight binding parameter t. Furthermore, we set $e = a = 1$ where e is charge of the particles and a is the lattice constant. Hereafter, the reported value of charge densities consist of the summation of charge density of both spin components.

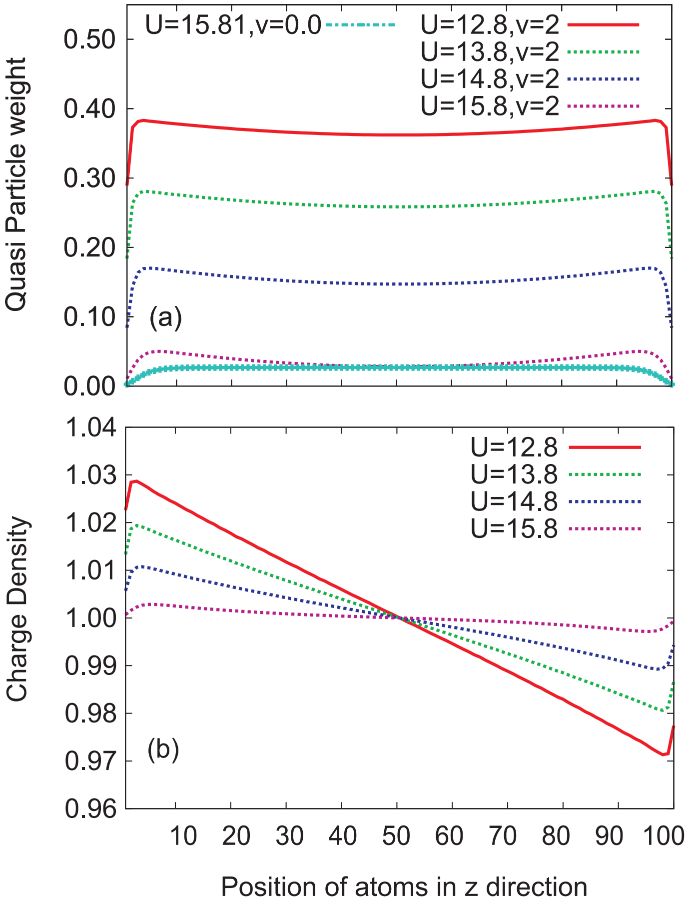

Figure 3.1: (a) QP weight distribution for $U < 16$, $N_z = 100$, and $v = 2$ and 0; (b) charge distribution for U < 16, $N_z = 100$, and $v = 2$. Note that for v = 0, the system is at local half-filling $n_i = 1$.

3.3.2 Numerical results

We solve the set of Eqs. (3.20)-(3.23) for a slab geometry and a linear distribution of the potential along the direction perpendicular to the slab in order to investigate its effect on the strong correlations. The spatial distribution of the QP weights and the charge densities are shown in Figs. 3.1(a) and 3.1(b) and Figs. 3.2(a) and 3.2(b) for different values of the Hubbard repulsion U for a slab of width $N_z = 100$ and $N_z = 90$ respectively. The presence of a potential profile causes charge distortion in the system, and because of the nature of the Gutzwiller renormalization factors that are minimum at half-filling ($n_i = 1.0$), it is predicted that any local deviation from half-filling may lead to larger QP weights when

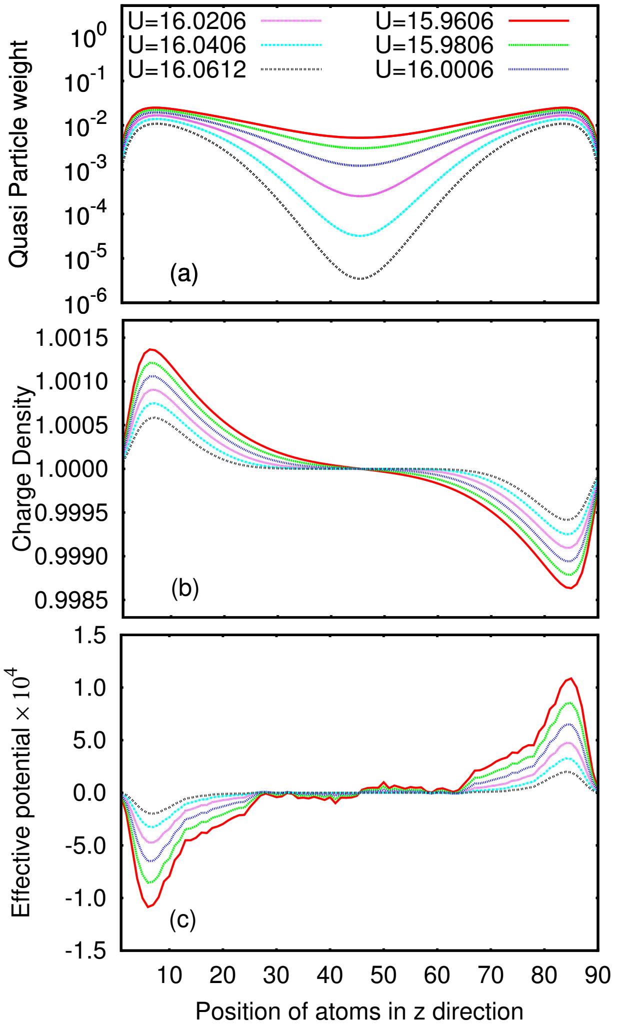

Figure 3.2: (a) QP weight distribution, (b) charge distribution, and (c) effective potential for $v = 2.0$ for $N_z = 90$. Notice the $U/2$ contribution is subtracted from the effective potential.

compared to the case without electric field.

In the presence of an electric field, for both $U < U_c$ and $U > U_c$ (where $U_c = 16$ for bulk), the maximum QP weight is achieved in few layers beneath the surface as is obvious from Figs.3.1(a) and 3.2(a). For $U < U_c$ akin to the zero electric-field case, the minimum QP weight is achieved at the surface sites. In contrast, for $U > U_c$, the QP weight of

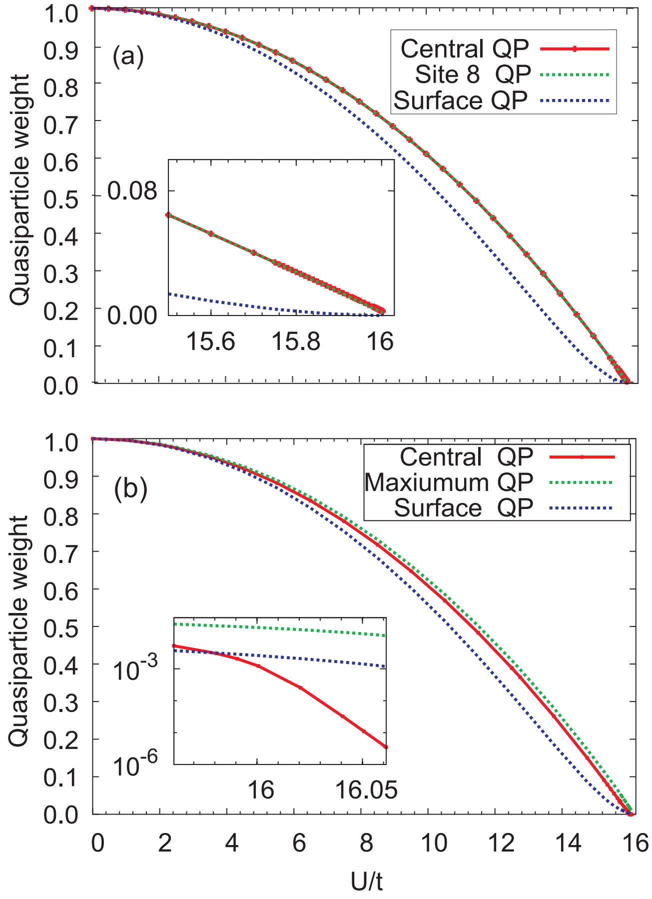

Figure 3.3: QP weight of various sites versus Hubbard repulsion for $N_z = 90$, (a) $\upsilon = 0$, and (b) $\upsilon = 2$.

the central atoms starts to dramatically drop to extremely low values and creates a dead region as is indicated in Fig. 3.2(a). This is presented more clearly in Figs. 3.3(a) and 3.3(b) where we show the QP weight versus the Hubbard repulsion for three significant locations (surface, near surface, and bulk) for both $\upsilon = 0.0$ and 2.0. The formation of the dead zone leads to charge being trapped near the surfaces of the slab because the tunneling through the bulk is suppressed. This charge trapping prevents the system to exhibit a metal-insulator transition even for values of the Hubbard repulsion larger than the bulk U_c. This result is contrary to the zero-field case where for U close to U_c , the surface region forms a dead zone instead of the central region. Therefore, in the absence of an electric field, the QP weight is maximal in the central parts as shown in Fig. 3.1(a). This is due to the fact that the surface sites have a lower kinetic energy (due to lower coordination

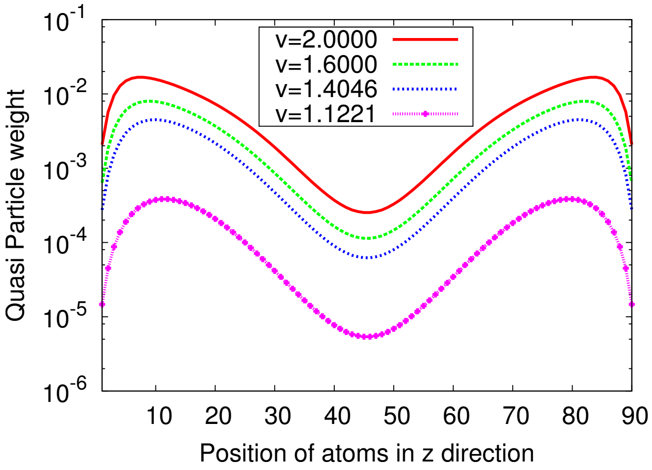

Figure 3.4: QP weight distribution for various potential difference for $U = 16.0602$ where $N_z = 90$.

number at the surface). Interestingly, surface sites will always have a finite (but low) QP weight, as long as the bulk QP weight is finite. The surface sites are always able to gain kinetic energy from the central sites that have the highest QP weight, which act as a source of kinetic energy [118, 119] .

In Figs. 3.2(b) and 3.2(c), the spatial distribution of the charge densities and the effective potential are shown for different values of $U > U_c$. Both of these two quantities behave similarly to the QP weight. The charge density is maximum in the same location in which we have the maximum QP weight, while for the sites with charge density near local half-filling ($n_i = 1.0$), we have the lowest QP weight and this is where the electric field has the weakest effect. The deviations of the carrier densities from half-filling correspond to larger electron density for sites with lower effective potential and hole density for sites with higher effective potential as shown in Fig. 3.2(c). The charge frustration is responsible for the nonzero QP weight for these sites near the surfaces of the system even for $U > U_c$.

Figure 3.4 shows the change of QP weight throughout the system as the potential (v) difference is increased for $U = 16.0602$. Notice that the location of the maximal QP weight slowly shifts toward the surface and at the same time its value increases with electric field. As a consequence, the size of the central dead zone reduces with increasing applied potential (v) difference. One should note that when measuring an I-V curve, only the in-plane conductivity will exhibit metallic behavior because the z-axis conductivity will be dominated by the bulk insulating layer.

In order to better understand the formation of the dead zone with suppressed QP

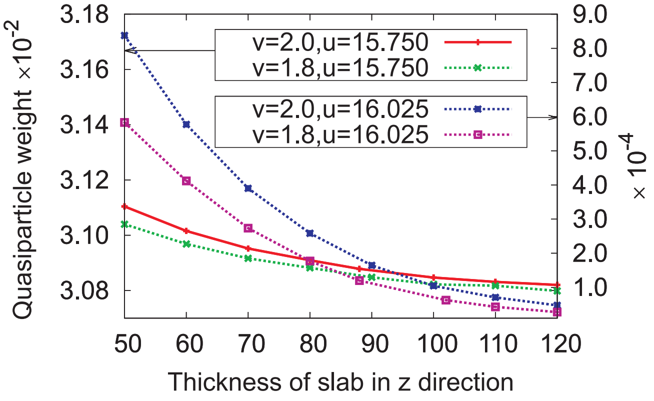

Figure 3.5: QP weight at the center of the slab versus width for $v = 1.8, 2$, and two values of the Hubbard repulsion $U = 15.75, 16.025$.

weight, we plot in Fig. 3.5 the dependence of the central QP weight on the thickness of the slab. This is shown for two values of the potential difference, $v = 1.8$ and 2, and for two values of the Hubbard repulsion, above and below the critical $U_c, U = 15.75$ and 16.025, respectively. As discussed previously, in the presence of an electric field, sites near the surface will always have larger QP weight due to the accumulation of surface charge. This will ensure that the central region will always have its QP weight enhanced due to its proximity to regions with increased kinetic energy. As shown in Fig. 3.5, we can distinguish two regimes, depending whether the Hubbard repulsion is above or below the critical value obtained in the absence of the electric field. When $U < U_c$, the QP weight of the central sites converges toward a finite value since even in the absence of the electric field, the system is still metallic, albeit with a small QP weight. When $U > U_c$, the homogeneous system should be insulating with vanishing QP weight. Instead, even if the electric field is screened in the central region, the QP weight will never exactly vanish because it is in contact with a doped region with finite QP weight. We can infer that for large enough electric fields and as long as the slab is finite, the QP weight will never vanish.

Next, we discuss the possible appearance of a critical field value above which the system is metallic. We plot in Fig. 3.6(a) the maximum and central QP weights for four values of $\delta U = U - U_c$ as a function of potential difference v. Note that for larger Hubbard repulsions, the minimization procedure is not stable if the maximum QP is strongly suppressed, and thus we have converged solutions only above certain field strengths. We observe that as the electric field increases, the difference between the maximal and central QP weights increases in all situations since the maximum will be near the surface.

This can be also seen in Fig. 3.6(b), where the location of the maximum QP weight is plotted as a function of electric field. For low-field values, the maximum is located at

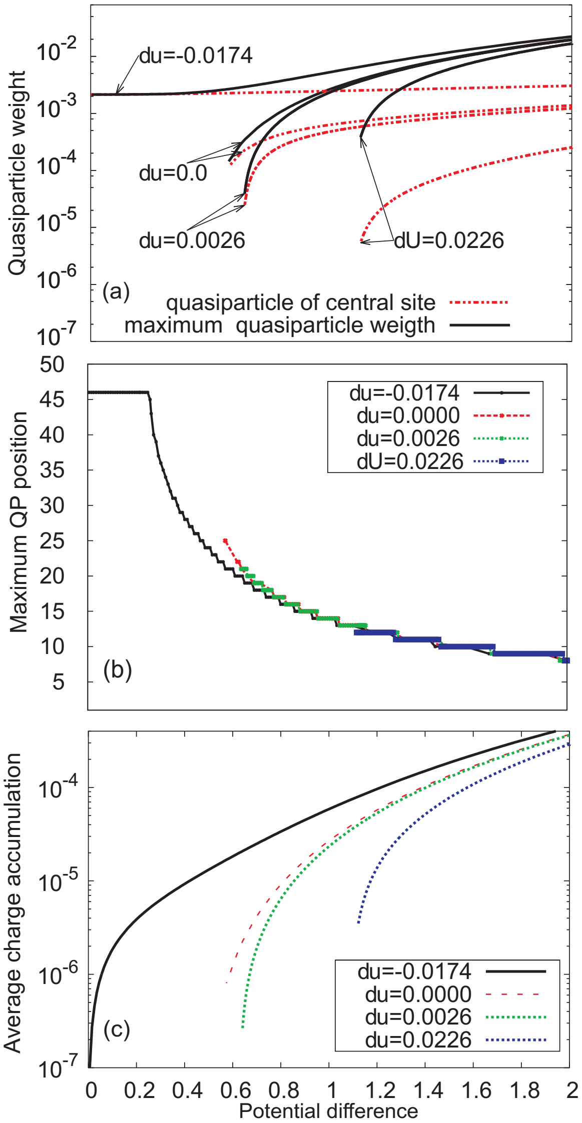

Figure 3.6: (a) Maximum and central QP weight, (b) position of maximum QP weight, (c) average charge accumulation versus v for $\delta U = U - U_c = 0.0226, 0.0026, 0.0,$ and -0.0174 with $N_z = 90$.

the center of the slab not only due to the vanishing charge accumulation near the surface ($n_{accumulated} = 1/N_z \sum_{\sigma} \sum_{i=1}^{N_z} |n_{i\sigma} - 0.5|$) [shown in Fig. 3.6(c)], but also due to the in-

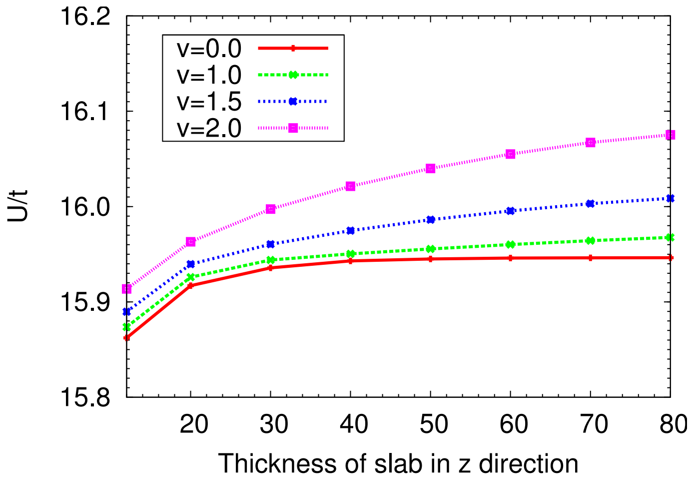

Figure 3.7: Critical Hubbard repulsion for which the maximal QP weight is $Z = 5.0\times10^{-3}$ versus slab thickness for different electric fields.

crease in the correlation length near vanishing charge distortion (charge accumulation). Although the electron density might have a local maximum/minimum near the surface due to the presence of the electric field, a long correlation length will ensure that the suppression due to the existence of the surface recovers only deep into the central regions.

It is important to note that for $\delta U = -0.0174$, the QP weight recovers its bulk value when the electric field goes to zero, while for $\delta U > 0.0$, it decreases rapidly at a finite critical v_c . Although our method breaks down when the QP weight is very small, the results hint toward a true metal-insulator phase transition when the Hubbard repulsion totally screens the electric field. Next, we discuss the effect of slab dimensions and in Fig. 3.7 we show as a function of thickness the value of the Hubbard repulsion for which the maximum QP weight is $Z = 5.0 \times 10^{-3}$. This will give a lower bound for the slab critical U_c in the presence of a perpendicular electric field. We observe that U_c is larger for larger thicknesses and stronger fields v. Again, this is related to the amount of charges localized near the surfaces. When U increases, the QP weight corresponding the probability of the electrons to tunnel through the central parts is being reduced, which makes charge relaxation more difficult. In other words, by increasing the Hubbard repulsion, the system tries to screen the charges in order to lower the energy, while on the other hand, the increase of U suppresses the metallic behavior of the central part and thus hinders the charge relaxation. This can be better understood by considering the average charge density in half of the slab ($n_{average} = 2/N_z \sum_{\sigma} \sum_{i=1}^{N_z/2} n_{i\sigma}$), which increases slowly with the slab's thickness

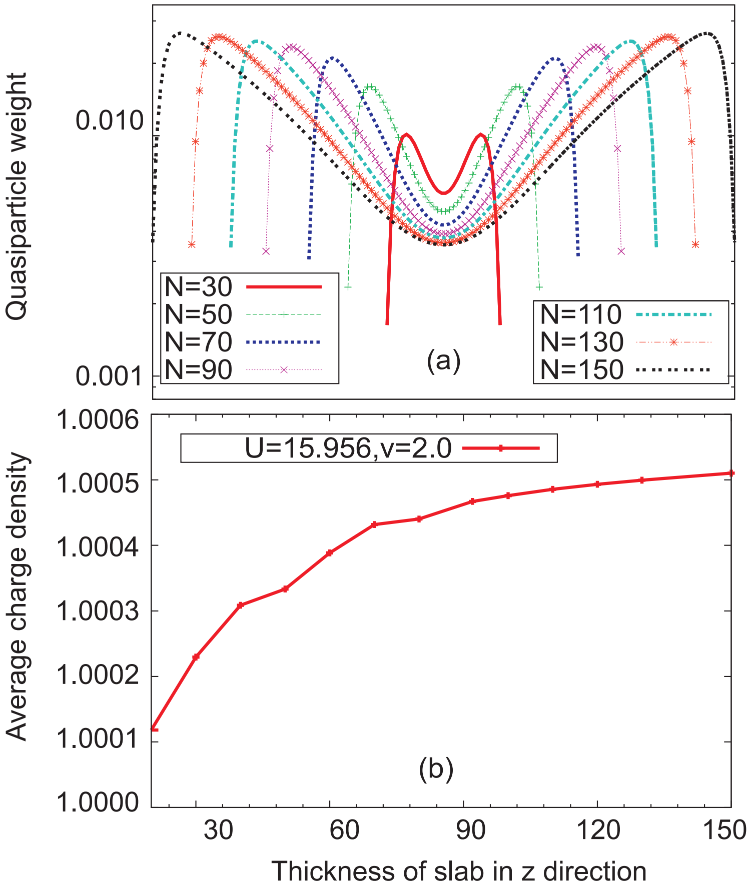

Figure 3.8: (a) QP weight distribution of different sites for various slab thicknesses. (b) The charge density averaged over half of the slab for different thicknesses. Here, $U = 15.956$ and $v = 2$.

as indicated in Fig. 3.8(b). The numerical calculations indicate that even for $U > U_c$, we did not obtain a clear asymptotic behavior for maximum QP weight by increasing the slab width. One may expect that an asymptotic solution is reachable for thicker slabs, but this turns out to be beyond our numerical resources.

3.4 Conclusions

In conclusion, we described the Mott metal insulator in a slab geometry in the presence of a perpendicular external electric field by calculating the site-dependent QP weight. This is done by using an inhomogeneous GA, which is exact in the limit of infinite dimensions.

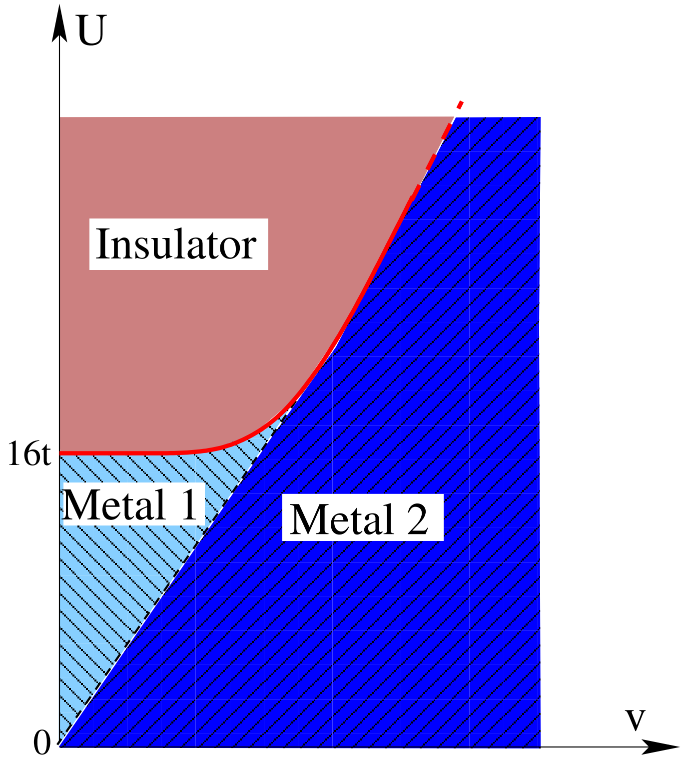

Figure 3.9: Sketch of the possible electric-field-induced changes on the phase diagram. The two metallic regions differ only in the location of the maximum QP weight: center of slab in region 1 and near surface in region 2.

Increasing the Hubbard repulsion in the presence of an external electric field leads to the formation of a dead insulating zone at the center of the thin film. The formation of the dead zone for $U > 16$ occurs before complete screening of the electric field and, therefore, charge trapping occurs at the surface. This causes the MIT to be shifted in the presence of the external field. We therefore show that even though the QP weight of the central region is (bulk) strongly suppressed for $U > U_c$, the surface layers remain metallic and with larger QP weight. Although our calculation can not give a definitive answer on whether a critical value v_c/N_z of the electric field exists, below which the slab becomes insulating, it shows that a rapid change in the maximum QP weight and charge accumulation will occur above v_c. The resulting phase diagram is sketched in Fig. 3.9 and shows the electric-field-induced shift of the metal-insulator transition. We uncover two metallic regions, depending whether the maximum QP weight is achieved in the center of the slab (region 1) or near the surface (region 2). Analytical or numerical methods, which can accurately probe the insulating region, will shine light on the exact nature of this transition. From an experimental point of view, our results are relevant for transport measurements in thin films. In the presence of an external electric field perpendicular to an insulating film, one could use the surface states for transport since the charge transfer at the surface creates two-dimensional underdoped and overdoped regions. In the same time, transport perpendicular to the thin film is suppressed due to the dead insulating zone, thus protecting the surface states from leakages. The electric field needed to create the surface states is also much lower than the breakdown field needed to pass current across the insulating zone.

Chapter 4

Field effect on surface states in a doped Mott-Insulator thin film

Surface effects of a doped thin film made of a strongly correlated material are investigated both in the absence and presence of a perpendicular electric field. We use an inhomogeneous GA for a single band Hubbard model in order to describe correlation effects. For low doping, the bulk value of the QP weight is recovered exponentially deep into the slab, but with increasing doping, additional Friedel oscillations appear near the surface. We show that the inverse correlation length has a power-law dependence on the doping level. In the presence of an electrical field, considerable changes in the QP weight can be realized throughout the system. We observe a large difference (as large as five orders of magnitude) in the QP weight near the opposite sides of the slab. This effect can be significant in switching devices that use the surface states for transport.

4.1 Introduction

The MIT based on carrier doping of a Mott insulator has been investigated experimentally and theoretically [14, 38]. Recently, the formation of a superconducting phase was observed at the interface of a Mott and band insulator and the possible tuning of these transitions by an external electric field was reported [7]. Moreover a three terminal setup was implemented by Son et al. who induced hole doping in a thin Mott insulator film from a doped band insulator through the application of a voltage difference between the drain and the gate terminals [120].

The results of this chapter were published as: Davoud Nasr Esfahani, L. Covaci and F. M. Peeters, Phys. Rev. B. **87**, 035131 (2013).

For the above class of phenomena inhomogeneities and proximity effects play an essential role. In order to deal with such systems one needs a theoretical model that is able to include correlation effects in heterostructures while not being too computationally expensive such that one has the possibility to consider large enough system sizes. This is crucial especially for the investigation of systems where surfaces and finite size effects are significant such as thin films made of strongly correlated materials. The interface between a band insulator and a strongly correlated system has been studied theoretically with a two site DMFT [121] and the SBMFT [116]. Such studies predict the formation of a two dimensional electron gas at the interface which arises due to charge reconstruction. Surface correlation effects were studied theoretically in half filled heterostructures modeled by a single band Hubbard model [122]. Also the penetration of metallic behavior into a Mott insulator was studied both within the GA and DMFT for the half filled case [29, 118]. Surface correlation effects of a doped semi-infinite Hubbard model were investigated within an embedded DMFT for both single band and multi-band systems [119, 123]. Within this method, due to numerical limitations, only few surface layers (up to 6) can be used in order to address site dependent correlation effects. When the correlation length is large, this method is not reliable any more.

In order to describe position dependent electronic correlation effects in a slab geometry we employ the GA. While GA works only for the metallic phase, it gives reliable information about the QP weight of particles at different spatial locations. For heterostructures, GA was found to be in good qualitative agreement with the more refined DMFT method for the half filled case [118]. While GA and SBMFT are equivalent for zero temperature [110], in two site DMFT, like GA, the bulk QP weight is governed by a simple power law and there is only a correction to U_c when compared with the linearized DMFT [89, 124]. Generally, GA over-estimates the QP weight at all dopings but it is considered to be accurate enough to describe low energy excitations and is routinely used for interpolations in combination with DMFT methods [14].

The aim of this chapter is to investigate the spatial dependence of the charge density and the QP weight of a doped correlated slab and to understand the correlation effects in the presence of an external electric field. We predict significant changes in the QP weight throughout the system. This study is motivated by potential applications in nanoscale switching devices with spatial controllable conductivity through the application of an external electric field.

The outline of the chapter is as follows: after a brief derivation of the saddle point equations for a slab geometry (section 4.2) the results for a doped correlated slab are presented in section 4.3.1. Next the effect of an electric field is discussed in section 4.3.2 and finally we present our conclusions in section 4.4.

4.2 Model and Method

The simplest Hamiltonian that is able to capture the essential physics of strongly correlated systems is the single band Hubbard model,

$$\hat{H}_U = -\sum_{\langle ij\rangle\sigma} t_{ij} c^{\dagger}_{i\sigma} c_{j\sigma} + \sum_i U \hat{n}_{i\sigma}\hat{n}_{i\bar{\sigma}}, \tag{4.1}$$

where t_{ij} are the hopping amplitudes, $\langle ij\rangle$ is summation over nearest neigthbour sites and U is the Hubbard energy describing the Coulomb interaction between two particles with opposite spin located on the same site ($\sigma =\uparrow,\downarrow$). In the presence of an external electric field the model becomes [78]:

$$\hat{H} = \hat{H}_U + \sum_{i\sigma} v_i \hat{n}_{i\sigma}, \tag{4.2}$$

where v_i is the position dependent potential. In spite of the simple form of the Hubbard model, exact solutions exist only for $d = 1$ and $d = \infty$ [38, 86, 108] and therefore we are forced to work with approximations. If one is only concerned about ground state properties or low energy excitations [125], one of the choices is the GA (GA) which is the infinite dimension limit of the Gutzwiller wave function (GWF) [85, 88]. GWF is a many body wave function with an additional degree of freedom used to reduce the weight of higher energy configurations. In the single band Hubbard model these configurations are on-site double occupancies obtained when two particles with opposite spin reside on the same site. The GWF is written as:

$$|\psi_G\rangle = \prod_i \hat{P}_i |\phi_0\rangle, \tag{4.3}$$

where i is the lattice site index and the projector operators are defined as $\hat{P}_i = g_{e,i}\hat{e}_i + g_{\sigma,i}\hat{s}_{\sigma,i} + g_{\bar{\sigma},i}\hat{s}_{\bar{\sigma},i} + g_{d,i}\hat{d}_i$. The operators $\hat{e} = (1-\hat{n}_{i\sigma})(1-\hat{n}_{i\bar{\sigma}})$, $\hat{s}_\sigma = \hat{n}_{i\sigma}(1-\hat{n}_{i\bar{\sigma}})$ and $\hat{d} = \hat{n}_{i\sigma}\hat{n}_{i\bar{\sigma}}$ are local projectors of zero, singly and doubly occupied states, $|\varphi_0\rangle$ is a noninteracting Fermi sea and consist of both spin up and spin down states and the g coefficients are variational parameters. The following local constraints have to be satisfied in order to remove the local contributions in the diagrammatic expansion of various expectation values [89],

$$\langle \hat{P}^{\dagger}_i \hat{P}_i\rangle_0 = 1, \tag{4.4}$$

$$\langle \hat{P}^{\dagger}_i \hat{P}_i c^{\dagger}_{i\sigma} c_{i\sigma}\rangle_0 = \langle c^{\dagger}_{i\sigma} c_{i\sigma}\rangle_0. \tag{4.5}$$

Where $\langle\ldots\rangle_0$ represents the expectation value with respect to $|\varphi_0\rangle$. The explicit form of the above constraints is the following:

$$g_{i\sigma}{}^2\langle\hat{e}_i\rangle_0+\sum_{\sigma}g_{i\sigma}{}^2\langle s_{i\sigma}\rangle_0+g_{d,i}{}^2\langle\hat{d}_i\rangle_0=1, \tag{4.6}$$

$$g_{i\sigma}{}^2\langle s_{i\sigma}\rangle_0+g_{d,i}{}^2\langle\hat{d}_i\rangle_0=\langle\hat{n}_{i\sigma}\rangle_0. \tag{4.7}$$

In the limit of infinite dimensions the effect of the projectors P_i requires the renormalization of the hopping amplitudes between different sites. These renormalization factors can be written as:

$$\sqrt{q_{i\sigma}}=\frac{g_{e,i}g_{\sigma,i}\sqrt{\langle\hat{e}_i\rangle_0\langle\hat{s}_{\sigma,i}\rangle_0}+g_{d,i}g_{\bar{\sigma},i}\sqrt{\langle\hat{d}_i\rangle_0\langle\hat{s}_{\bar{\sigma},i}\rangle_0}}{\sqrt{\langle n_{i\sigma}\rangle_0(1-\langle n_{i\sigma}\rangle_0)}}. \tag{4.8}$$

By substituting Eqs. (4.6) and (4.7) into Eq. (4.8) one arrives at an expression for $\sqrt{q}_{i\sigma}$ that is only a function of $g_{d,i}$, $\langle\hat{n}_{i\sigma}\rangle_0$ and $\langle\hat{n}_{i\bar{\sigma}}\rangle_0$ as:

$$\sqrt{q_{i\sigma}}=\frac{\sqrt{(1-\langle\hat{n}_i\rangle_0+d_i)(\langle\hat{n}_{i\sigma}\rangle_0-d_i)}+\sqrt{d_i(\langle\hat{n}_{i\bar{\sigma}}\rangle_0-d_i)}}{\sqrt{\langle n_{i\sigma}\rangle_0(1-\langle n_{i\sigma}\rangle_0)}},$$

where $d_i=g_{d,i}^2\langle\hat{n}_{i\sigma}\rangle_0\langle\hat{n}_{i\bar{\sigma}}\rangle_0$ is the probability of double occupancy that is calculated within $|\psi_G\rangle$ and $\langle\hat{n}_i\rangle_0=\langle\hat{n}_{i\sigma}\rangle_0+\langle\hat{n}_{i\bar{\sigma}}\rangle_0$. Moreover, in addition to Eq .(4.8) the relation $\langle\hat{n}_{i\sigma}\rangle_{gutzwiller}=\langle\hat{n}_{i\sigma}\rangle_0$ holds in the limit of infinite dimensions. By considering the above relations the total energy functional of an inhomogeneous system has the following form,

$$\begin{aligned}\langle\hat{H}\rangle_G &= \sum_{\langle ij\rangle,\sigma}-t_{ij}\sqrt{q_{i\sigma}}\sqrt{q_{j\sigma}}\langle\hat{c}_{i\sigma}^{\dagger}\hat{c}_{j\sigma}\rangle_0+\sum_{i,\sigma}v_i\langle\hat{n}_{i\sigma}\rangle_0,\\ &+ \sum_i Ug_{d,i}^2\langle\hat{n}_{i\sigma}\rangle_0\langle\hat{n}_{i\bar{\sigma}}\rangle_0,\end{aligned} \tag{4.9}$$

Where $\langle\rangle_G$ means expectation over Gutzwiller wave finction. The conditions $\langle\psi_G|\psi_G\rangle=\langle\varphi_0|\varphi_0\rangle$ and $\langle\varphi_0|\varphi_0\rangle=1$ are used in the above relation, the first relation itself is a consequence of the infinite dimensional limit and the second relation is just the normalization condition for $|\phi_0\rangle$. Away from half filling the problem of minimizing the energy functional is difficult because the renormalization factors, $q_{i\sigma}$, are functions of $\langle\hat{n}_{i\sigma}\rangle_0$. Therefore it is impossible to simply vary the above energy functional with respect to $\langle\phi_0|$. A possible approach, similar to DFT, is to start with an arbitrary value for $\langle\hat{n}_{i\sigma}\rangle_0$ and then to expand the energy functional as function of $\langle \hat{n}_{i\sigma} \rangle_0$ up to linear order around the starting $\langle \hat{n}_{i\sigma} \rangle_0$. This allows us to vary the energy functional with respect to $\langle \phi_0 |$, moreover this variation together with the normalization condition for $| \phi_0 \rangle$ leads one to solve an eigenvalue problem, and a new value of $\langle \hat{n}_{i\bar{\sigma}} \rangle_0$ can be calculated by using the resulted wave function. This should be done until the desired convergence of the wave-function or energy functional is achieved. However, to avelliate this complication, instead of calculating the expectation value $\langle \hat{n}_{i\sigma} \rangle_0$, we introduce a set of new variational parameters $n_{i\sigma}$s that will play the role of local noninteracting occupancies (local noninteracting density matrices) which appear in the renormalization factors and double occupancies. It is then possible to let $n_{i\sigma}$ vary independently from $| \phi_0 \rangle$. The energy functional that should be optimized has now the following form for a simple cubic slab geometry with periodic boundary conditions in the $x - y$ plane with free (001) surfaces:

$$\begin{aligned}
\langle \hat{H} \rangle_G \quad &= \frac{1}{N_{k_\parallel}} \sum_{i,k_\parallel,\sigma} (q_{i\sigma} \epsilon_{k_\parallel} + v_i) \langle \phi_0 | \hat{c}^\dagger_{ik_\parallel \sigma} \hat{c}_{ik_\parallel \sigma} | \phi_0 \rangle \\
&- \frac{1}{N_{k_\parallel}} \sum_{\langle ij \rangle k_\parallel \sigma} \sqrt{q_{i\sigma}} \sqrt{q_{j\sigma}} t \langle \phi_0 | \hat{c}^\dagger_{ik_\parallel \sigma} \hat{c}_{jk_\parallel \sigma} | \varphi_0 \rangle \\
&+ \sum_{i\sigma} \lambda_{i\sigma} (\frac{1}{N_{k_\parallel}} \sum_{k_\parallel} \langle \phi_0 | \hat{c}^\dagger_{ik_\parallel \sigma} \hat{c}_{ik_\parallel \sigma} | \phi_0 \rangle - n_{i\sigma}) \\
&+ \mathit{\Lambda} (\sum_{i\sigma} n_{i\sigma} - \frac{N_{total}}{N_{k_\parallel}}) + E_{NI} (1 - \langle \varphi_0 | \varphi_0 \rangle), \\
&+ \sum_i U g^2_{d,i} n_{i\sigma} n_{i\bar{\sigma}},
\end{aligned} \tag{4.10}$$

where $\epsilon_{k_\parallel} = -2t(\cos k_x + \cos k_y)$, the Lagrange multipliers $\lambda_{i\sigma}$ are introduced to fix $n_{i\sigma}$ to $\langle \hat{n}_{i\sigma} \rangle_0$. Λ is introduced to fix the total number of particles (N_{total} or equivalently total number of occupied states), E_{NI} is considered to make sure that $| \varphi_0 \rangle$ is normalized, i and j are index of layers in the z direction and $N_{k_\parallel} = N_{k_x} N_{k_y}$ is the total number of k-points. The optimization of the Lagrange function is performed through an iterative procedure, starting with a minimization with respect to $| \varphi_0 \rangle$, which leads to a Schrödinger-like eigenvalue problem that has to be solved for each k-point and spin component σ:

$$\begin{aligned}
&\sum_i (q_{i\sigma} \epsilon_{k_\parallel} + v_i + \lambda_{i\sigma}) \hat{c}^\dagger_{ik_\parallel \sigma} \hat{c}_{ik_\parallel \sigma} | \varphi_0 \rangle - \\
&\sum_{\langle ij \rangle} \sqrt{q_{i\sigma}} \sqrt{q_{j\sigma}} t \hat{c}^\dagger_{ik_\parallel \sigma} \hat{c}_{jk_\parallel \sigma} | \varphi_0 \rangle = E_{k_\parallel, \sigma} | \varphi_0 \rangle,
\end{aligned} \tag{4.11}$$

The resulting non-interacting many-body ground state energy and wave-function are computed in the following way: $E_{NI} = \frac{1}{N_{k_\parallel}} \sum_{k_\parallel, n\sigma}^{occupied} E_{k_\parallel, n\sigma}$ and $|\varphi_0\rangle = \prod_{k_\parallel, n\sigma}^{occupied} \hat{c}^\dagger_{k_\parallel, n\sigma}|0\rangle$, where n is the quantum number for the energy levels of each k point. The above non-interacting state $|\varphi_0\rangle$, which is now implicitly a function of all the variational parameters $\lambda_{i\sigma}$, $n_{i\sigma}$, g_i and Λ, should be inserted into Eq. (4.10) which becomes,

$$\langle\hat{H}\rangle_G = E_{NI}(n_{i\sigma}, \lambda_{i\sigma}, g_{d,i}, |\varphi_0\rangle) - \sum_{i,\sigma} \lambda_{i\sigma} n_{i\sigma} + \Lambda(\sum_{i,\sigma} n_{i\sigma} - \frac{N_{total}}{N_{k_\parallel}}) + \sum_i U g^2_{d,i} n_{i\sigma} n_{i\bar{\sigma}}.$$

In the next step we search for the stationary points of the above Lagrange function of a slab geometry for a paramagnetic system with $n_{i\sigma} = n_{i\bar{\sigma}} = n_i$ and $\langle\hat{n}_{i\sigma}\rangle_0 = \langle\hat{n}_{i\bar{\sigma}}\rangle_0$ as:

$$\frac{\partial\langle\hat{H}\rangle_G}{\partial g_{d,i}} = \frac{2}{N_{k_\parallel}} \frac{\partial q_{i\sigma}}{\partial g_{d,i}} (\tilde{t}_i + \sum_j \delta_{i,j\pm1} \sqrt{\frac{q_{j\sigma}}{q_{i\sigma}}} \tilde{t}_{ij}) + 2U{n_i}^2 g_{i,d} = 0, \tag{4.12}$$

$$\frac{\partial\langle\hat{H}\rangle_G}{\partial n_i} = \frac{2}{N_{k_\parallel}} \frac{\partial q_{i\sigma}}{\partial n_i} (\tilde{t}_i + \sum_j \delta_{i,j\pm1} \sqrt{\frac{q_{j\sigma}}{q_{i\sigma}}} \tilde{t}_{ij}) + 2(\Lambda - \lambda_i) + 2U{g_{i,d}}^2 n_i = 0, \tag{4.13}$$

$$\frac{\partial\langle\hat{H}\rangle_G}{\partial \lambda_i} = \frac{2}{N_{k_\parallel}} \langle\varphi_0| \sum_{k_\parallel} \hat{c}^\dagger_{ik_\parallel\sigma} \hat{c}_{ik_\parallel\sigma} |\varphi_0\rangle - 2n_i = 0, \tag{4.14}$$

$$\frac{\partial\langle\hat{H}\rangle_G}{\partial \Lambda} = (2\sum_i n_i - \frac{N_{total}}{N_{k\parallel}}) = 0, \tag{4.15}$$

where the spin index of renormalization factors and $\lambda_{i\sigma}$ is droped due to paramagnetic condition, $\tilde{t}_i = \sum_{k_\parallel} \epsilon_{k_\parallel} \langle\varphi_0|\hat{c}^\dagger_{ik_\parallel\sigma}\hat{c}_{ik_\parallel\sigma}|\varphi_0\rangle$, $\tilde{t}_{ij} = -t\sum_{k_\parallel} \langle\varphi_0|\hat{c}^\dagger_{ik_\parallel\sigma}\hat{c}_{jk_\parallel\sigma}|\varphi_0\rangle$ and N_{total} is the total number of particles. $\tilde{t}_{i,i+1}$ and $\tilde{t}_{0,1}$ are equal to zero at edge of the slab. This set of nonlinear equations can be solved by using a nonlinear solver based on Newton and/or Quasi-Newton methods. Notice that $|\phi_0\rangle$ is still implicitly a function of the variational parameters and has to be updated again through Eq.(4.11) during the evaluations of the saddle point equations throughout the optimization procedure. This means that we are all the time working with a $|\phi_0\rangle$ which satisfies the condition $\frac{\delta\langle\hat{H}\rangle_G}{\delta\langle\phi_0|} = 0$.

It should be noticed that together with the saddle point equations the electrostatic forces due to long-range electron-electron and electron-ion interactions should be in principle considered. However since the back ground permitivity of strongly correlated materials is usually very high [112], we tested the solutions with various high values of background permitivity and observed that long-range screening is negligible. We therefore set the value of the back ground permitivity to infinity in our calculations and ignore these effects. In order to numerically solve the set of saddle point equations, we use a 16×16 Monkhorst-Pack [115] k-grid for which the total energy is well converged. We report results for q_i as being the position dependent QP weight, which is a measure of the mobility of the particles within Fermi liquid theory. The inverse of the QP weight is proportional to the mass renormalization which becomes divergent for $q_i = 0$ corresponding to an insulating phase [117]. We further consider a potential difference v between two sides of the slab (in z direction), which results in a linear potential profile throught the slab between $-v/2$(for layer number 1) to $v/2$ (for layer number L_z). The parameters U and v are scaled by the tight binding parameter t, furthermore, we set $e = a = 1$ where e is charge of the particles and a is the lattice constant. The doping value δ is defined as $\delta = 1 - N_{total}/N_{halffilled}$, with $N_{halffilled} = N_{k\|} \times L_z$ which is half of the total number of states $2 \times N_{k\|} \times L_z$, where the factor 2 is related to the number of spin components. Moreover, in order to impose paramagnetic condition we consider $N_{occupied,\sigma} = N_{occupied,\bar{\sigma}} = N_{total}/2$, where $N_{occupied,\sigma}$ is the number of occupied states with spin σ in $|\phi_0\rangle$ (notice that there is not any hopping process in single particle part of the Hamiltonian which hop between states with different spin). Hereafter, the reported values for charge densities consist of summation of the charge density of both spin components. Throughout this work the thickness of the slab is taken $L_z = 90$ in units of the lattice constant.

4.3 Results

4.3.1 Hole doped correlated slab

In Fig. 4.1(a) we depict the charge distribution near the surface for different values of doping and $U = 16.2$, which is larger than the bulk critical U for the half-filled case, i.e. $U_C^{bulk,hf} = 16$. The surface region in which the charge density recovers its bulk value is doping dependent, resulting in the doping dependent correlation length. Higher doping corresponds to lower correlation length.

In the inset of Fig.4.1(a) we present the charge transfer from the bulk to the surface ($n_{surface} - n_{bulk}$). The doping dependence of this charge transfer is non-monotonic and is maximum around $\delta = 0.15$. While our results for the charge transfer are in agreement with recent DMFT calculations for a hole doped semi-infinite single band Hubbard model [119] in the limit of large enough doping, our scaling analysis shows that considering only few layers for the QP calculation may not be enough, specially for values of doping near half filling for which the correlation length is larger that 6 lattice constants. In Fig. 4.1(b) the spatial distribution QP weights $(q_i - q_{bulk})$ are plotted for different values of doping and

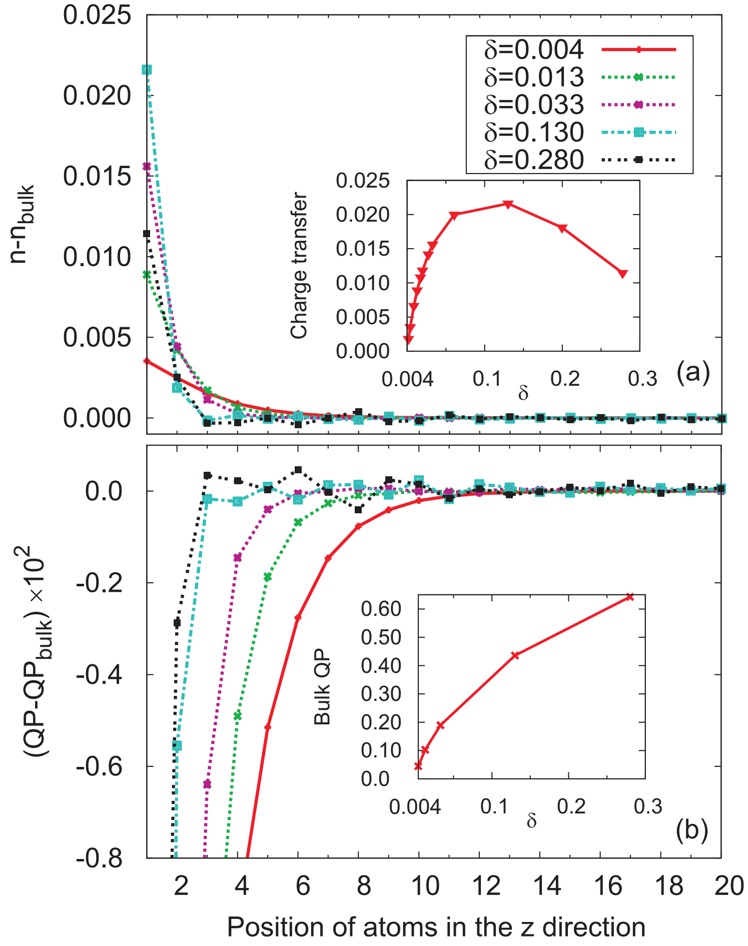

Figure 4.1: (a) Charge distribution for different dopings. Inset: charge transfer from bulk to surface as a function of doping; (b) QP weight relative to the bulk QP weight near the surface for different dopings. Inset shows the doping dependence of the bulk QP weight.

$U = 16.2$. Like in the half-filled case [118] the QP of particles near the surface sites is suppressed due to the reduced coordination number together with the charge transfer to the surface sites from the bulk, which in turn results in a lack of kinetic energy and an enhancement of correlation effects. One can also observe Friedel oscillations which are more pronounced for higher doping due to lower correlation lengths.

The inset of Fig. 4.1(b) shows the doping dependence of the bulk QP weight, q_{bulk}, which is in agreement with previous works and shows that by increasing the doping, correlation effects are weaker. The correlation length can also be extracted from the spatial distribution of the QP weight near the surface. Similar to the dependence of the charge den-

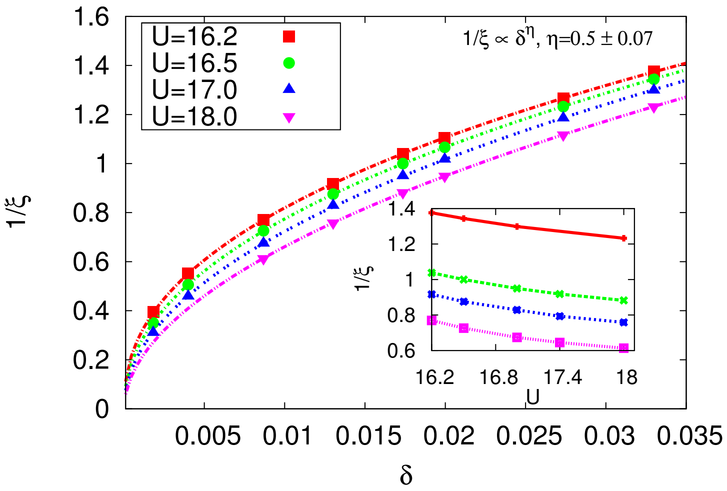

Figure 4.2: Inverse correlation length as function of doping for values of $U = 16.2, 16.5, 17.0, 18.0$. The inset shows the inverse of the correlation length as function of U for four values of δ=0.009, 0.013, 0.017, 0.032 from buttom to top curves.

sity, the QP weight recovers its bulk value within a characteristic length scale that depends on the correlation length. Friedel oscillations can also be observed but are suppressed for lower doping. Following [33] we observe that the spatial distribution of $\sqrt{q(x)} - \sqrt{q_{bulk}}$ is well fitted by an exponential decay for different values of the Hubbard repulsion and doping:

$$\sqrt{q(x)} = \sqrt{q_{bulk}} + (\sqrt{q_{surface}} - \sqrt{q_{bulk}})e^{-\frac{1}{\xi}(x-1)}, \tag{4.16}$$

where ξ is the correlation length and x the number of layer, starting from $x = 1$. Since the correlation length, ξ, depends on both U and δ, by fitting separately the spatial distribution of the QP weight we extract the corresponding correlation lengths. The results are summarized in Fig. 4.2, where $1/\xi$ is plotted as a function of doping for different values of the Hubbard repulsion. We can extract a simple power-law dependence for the inverse correlation length: $\dfrac{1}{\xi} = A\delta^{\eta}$, with a mean-field-like exponent [29, 118], $\eta = 0.5 \pm 0.07$, and a prefactor A that is only a function of U. The inset of Fig. 4.2 shows the inverse correlation length as a function of U for different dopings and, as expected, it is enhanced for higher Hubbard repulsions. The power law dependence of the correlation length versus doping shows that for half-filling the correlation length diverges which is a signature of the MIT that occurs for $U > U_c^{bulk,hf}$. A similar dependence of the correlation length versus Hubbard repulsion is observed for half-filling but when $U < U_c^{bulk,hf}$ [118]. In the latter case the criticality is governed by the Hubbard repulsion rather than the doping level.

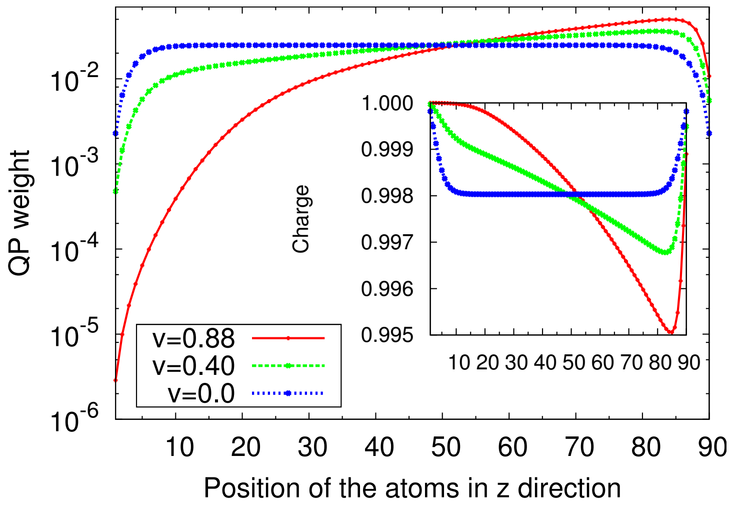

Figure 4.3: QP weight distribution and charge distribution (inset) for $U = 16.2$, $\delta = 0.002$ and three different values of the electric field.

4.3.2 The effect of electric field

The effect of an external electric field perpendicular to the slab on the spatial distribution of the QP weight is shown in Fig. 4.3 for $U = 16.2$, $\delta = 0.002$ and different values of the potential difference (v). The inset shows the charge distribution for the same parameters. The main effect of the electric field is to redistribute the charges within the slab, however in the strongly correlated regime when the Hubbard repulsion exceeds a certain crossover value, correlation effects enhance the charge transfer from less correlated sites to more correlated ones. This correlation enhanced charge redistribution results in the accumulation of charges near the surface layers, bringing one side of the slab very close to half-filling. This effect is largest for $U > U_c^{bulk,hf}$. To better clarify the correlation effects on the surface states of a correlated slab in the presence of an electric field we depict in Fig. 4.4 the charge and QP distribution of a slab consisting of 90 layers thick and a potential difference $v = 0.88$. The charge distribution for $U = 15.22$ shows peaks near the surfaces, as expected, however this behavior disappears for $U = 15.74$ and $U = 16.2$. This shows a clear crossover regime related to the enhancement of correlation effects. On the other hand the naive expectation that the effect of an increased Hubbard repulsion is only to screen out the electric field, fails to explain the behavior of the system in the presence of the electric field in the strong coupling regime. As shown in Fig. 4.4 by increasing the Hubbard repulsion, the charges do not go away from the surface but instead are accumulated at the surface. This mechanism of charge transfer from the places with enhanced delocalization to the places with enhanced correlations leads to a non-trivial enhancement

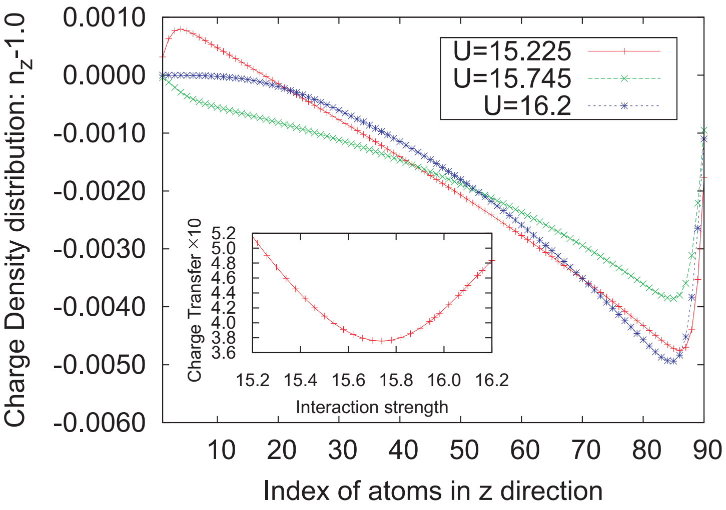

Figure 4.4: Charge distribution; the inset shows the charge transfer as function of U for fixed $v = 0.88$ and $\delta = 0.002$

of QP difference between the surfaces for large Hubbard repulsions.

To further understand the charge redistribution enhancement due to correlation effects, we present in the inset of Fig. 4.4 the charge difference between the layers with highest charge density and the layers with lowest charge density as function of U. This can be considered as a measure of the charge transfer throughout the system. As is clear from the inset of Fig. 4.4 there is a crossover value for U, given a fixed doping $\delta = 0.002$ and potential difference $v = 0.88$. Above this value the effect of the U plays a different role in the charge redistribution in the system. While below the crossover interaction the Hubbard repulsion competes with v to prevent charge redistribution due to potential difference, above the crossover it enhances the charge redistribution in favor of v. As is obvious from Fig. 4.3 the maximum QP weight is already achieved after a few layers from the surface on that side of the slab where the deviation of the charge density from half-filling is maximal. The reason that the QP weight is not maximal exactly at the surface is because of the suppression of the kinetic energy near the surface. On the other side of the slab, for larger electric fields the charge transfer assures that the charge density is near half-filling. Therefore, due to local correlation effects the QP weight is strongly suppressed. While the charge density near the surface is very close to half-filling (i. e. $n - 1 \simeq 10^{-7}$) one may infer that the residual QP indicated in Fig. 4.3 for $x = 1$ is mostly due to the proximity of the surface site to sites with higher QP weight rather than due to the local doping effect of these regions. In order to better understand the dependence of the QP weight on opposite sides of the slab, in Fig. 4.5 we show the QP weight for layers $x = 1$ and $x = 90$ as

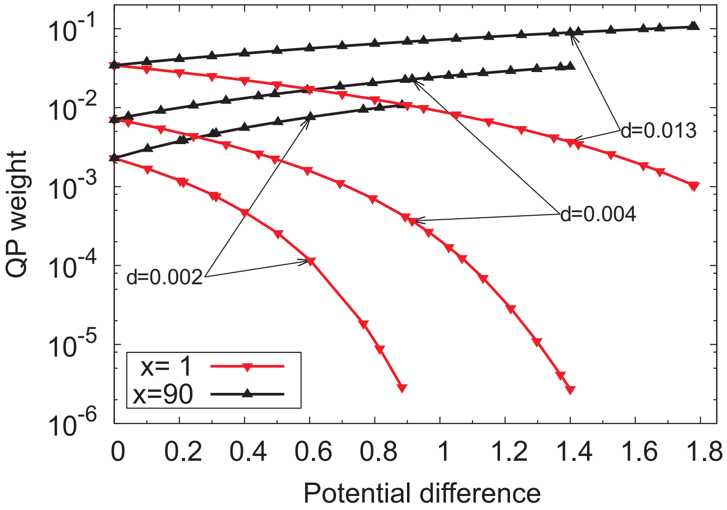

Figure 4.5: QP for x=1 and x=90 as function of potential difference for $U = 16.2$ and three values of δ.

function of potential difference for three different values of doping.

The QP weights on the two surfaces differ by *many orders of magnitude*. For larger doping, higher electric fields are needed in order to achieve the same QP weight difference. This is because of the competing influence of doping and Hubbard repulsion on the correlation effects. The huge difference in QP weight near the two surfaces could be used for creating a transistor-like device made of strongly correlated materials. By using the surface states to conduct current one can simply switch on/off the device by switching the polarity of the gate. Thus, turning on/off the electric conduction is now a consequence of the surface resistance ratio of the two sides.

4.4 Conclusions

By using an inhomogeneous Gutzwiller approach applied to the paramagnetic single band Hubbard model for a slab geometry we described a hole doped Mott thin-film. In the absence of applied electric field we calculated the position dependent charge density and QP weight and showed that the inverse correlation length has a power law dependence on doping.

When a perpendicular electric field is applied, charges will accumulate on one side of the slab. This correlation enhanced charge redistribution will in turn induce a large difference in the QP weight on the two sides of the slab, which was found to be as large as five orders of magnitude. We propose that a three terminal device with surface contacts can take advantage of this effect. For resistance switching purposes one would expect large on/off ratios of surface resistances when the electric field switches polarity.

Chapter 5

Surface correlation effects in two band strongly correlated slabs

Using an extension of the Gutzwiller approximation for an inhomogeneous system, we study the two band Hubbard model with unequal band widths for a slab geometry. The aim is to investigate the mutual effect of individual bands on the spatial distribution of QP weight and charge density, especially near the surface of the slab. The main effect of the difference in band width is the presence of two different length scales corresponding to the QP profile of each band. This is enhanced in the vicinity of the critical interaction of the narrow band where an orbitally selective Mott transition happens and a surface dead layer forms for the narrow band. For the doped case, two different regimes of charge transfer between the surface and the bulk of the slab are revealed. The charge transfer from surface/center to center/surface depends on both the doping level and the average relative charge accumulated in each band. Such effects could be of importance also when describing the accumulation of charges at the interface between structures made of multi-band strongly correlated materials.

5.1 Introduction

The surface depletion of the QP weight of strongly correlated materials has been studied both theoretically and experimentally [33,36,126,127]. The reduced QP weight at the surface of V_2O_3, a prototype material that exhibits a successive Mott transition at finite critical

---

The results of this chapter were published as: D Nasr Esfahani, L Covaci, F Peeters, J. Phys.: Condens. Matter **26**, 075601 (2014).

interaction, was also studied experimentally [36]. It was shown that the perturbation induced by the surface propagates exponentially deep inside the bulk material with a well defined length scale which is only a function of bulk properties and not the strength of the perturbation [33]. Moreover the effect of the charge transfer from less correlated to more correlated regions has been studied for both single and two band Hubbard models, and was shown to be more pronounced when an external electric field is applied [34, 119, 123].

On the other hand, for a multi-band system with different band widths, the existence of an orbital selective Mott transition emerges as a new promising degree of freedom in the system [128–132]. This in turn gives a hint on the influence of the inter-orbital charge transfer and crystal field effects on the charge transfer from the bulk to surface. From a theoretical point of view there has been a broad range of studies for inhomogeneous systems, based on single band [29, 32, 34, 118, 133] and multiband [123] Hubbard models, in order to investigate the effects of surfaces and interfaces. It was found that correlation effects that emerge as propagation of perturbation in the QP weights and the charge transfer play an important role for the understanding of the behavior of the system near the surfaces.

Since the strength of the interactions and charge doping lead to the enhancement of the correlation length near the Mott transition [33, 34], one needs a theoretical tool that is able to deal with large enough system sizes in order to properly consider the effect of surfaces/interfaces on the charge density and QP profile as function of the interaction strength and doping level of the system.

In order to describe the position dependent electronic correlation effects in a slab geometry we employ the Gutzwiller approximation (GA). While GA works only for the metallic phase, it gives reliable information about the QP weight of electrons at different spatial locations. For inhomogeneous systems, GA was found to be in good qualitative agreement with the more refined dynamical mean field theory (DMFT) in the half filled case [118]. GA and SBMFT are equivalent for zero temperature [110], moreover it was found that GA is qualitatively in agreement with linearized DMFT (it uses one bath site impurity solver) in which the inclusion of more bath sites does not change the overall behavior of the QP structure as function of interaction [134].

Throughout this chapter we only include density-density interactions in the Hamiltonian, in this case the QP weight structure of GA is in qualitative agreement with more accurate methods based on DMFT combined with a numerical renormalization group (NRG) as impurity solver [135]. The inclusion of full rotationally invariant terms not only changes the structure of QP profile quantitavely but it also induces qualitative differences, i.e. unlike density-density interaction the order of transition is not first order when full rotational terms are included. However, the inclusion of rotationally invariant terms within the Gutzwiller approximation does not capture the same behavior as NRG/DMFT calculations and it only slightly changes the critical interaction in comparison to the density-density case [136]. Generally, GA over-estimates the QP weight at all doping values but it was considered to be accurate enough to describe low energy excitations and is routinely used for interpolations in combination with DMFT methods [14].

In this chapter we systematically investigate the spatial dependence of the charge density and the QP weight of the different bands of a two band Hubbard model and further describe the correlation effects of individual bands as a function of doping. The outline of this chapter is as follows: a derivation of the saddle point equations for a doped correlated slab and the numerical scheme is briefly explained in section 5.2. The numerical results of a half filled correlated slab are presented in section 5.3.1 and the effect of doping is discussed in section 5.3.2. Finally we present our conclusions in section 5.4.

5.2 Model and Method

We consider a simple two band Hubbard model that is able to capture the essential physics of multi-band strongly correlated systems,

$$\begin{aligned} \hat{H}_U &= -\sum_{\langle ij\rangle mm'\sigma} t_{ij}^{mm'\sigma} c_{im\sigma}^{\dagger} c_{jm'\sigma} \\ &+ \sum_{im\sigma} v_{im\sigma} \hat{n}_i^{m\sigma} + \sum_i \hat{H}_i^{int}, \end{aligned} \tag{5.1}$$

where m and σ are the orbital and spin index ($\sigma = \uparrow, \downarrow$) respectively, $t_{ij}^{mm'\sigma}$ are the hopping amplitudes between site i and j, $\langle ij\rangle$ indicates summation over nearest neighbor sites, the local potentials $v_{im\sigma}$ are introduced to mimic the crystal field splitting or the effect of external electric field for a translationaly broken system [78] and $\hat{n}_i^{m\sigma} = c_{im\sigma}^{\dagger} c_{im\sigma}$. For a two band model, the interaction part of the Hamiltonian with only density-density interactions is defined as follows:

$$\begin{aligned} \hat{H}_i^{int} = &\sum_{m=1,2;\sigma} \frac{U}{2} \hat{n}_i^{m\sigma} \hat{n}_i^{m\bar{\sigma}} + \sum_{m\neq m';\sigma\sigma'} \frac{U'}{2} \hat{n}_i^{m\sigma} \hat{n}_i^{m'\sigma'} \\ - &\sum_{m\neq m';\sigma} \frac{J}{2} \hat{n}_i^{m\sigma} \hat{n}_i^{m'\sigma}, \end{aligned} \tag{5.2}$$

where U is the intra-orbital coulomb interaction between electrons in a single orbital, J is Hund coupling and $U' = U - 2J$ is inter-orbital Coulomb interaction. Notice, here we neglect the exchange and pair hopping terms. As is explained in the introduction we choose this choice for interacting part because in this case the results of GA are in qualitative agreement with NRG/DMFT [135]. Because we are only interested in ground state properties we employ the Gutzwiller approximation (GA) which is suitable for ground state properties and low energy excitations [125]. GA is the infinite dimension limit of the Gutzwiller wave function (GWF) [89], which is a many body wave function with an additional degree of freedom that is introduced in order to reduce the weight of higher energy configurations. The GWF is written as:

$$|\psi_G\rangle = \prod_i \hat{P}_i|\phi_0\rangle, \tag{5.3}$$

where i is the lattice site index and the projector operators are defined as,

$$\hat{P}_i = \sum_{\Gamma\Gamma'} \lambda_{i\Gamma\Gamma'}|\Gamma\rangle_{i\,i}\langle\Gamma'|, \tag{5.4}$$

$\{|\Gamma\rangle\}$ is a complete eigen basis for the local part of the Hamiltonian, and the operators $|\Gamma\rangle_{i\,i}\langle\Gamma'|$ act as local projectors at each site i. The way to choose these projectors and consequently the relative variational parameters depends on the problem at hand. For our case the number of variational parameters for a two band system with a diagonal non-interacting density matrix is equal to 16 (see section 5.2.1). $|\varphi_0\rangle$ is the non-interacting Fermi sea and consists of a Slater determinant of all flavors of the system. Local constraints have to be satisfied in order to remove local contributions in the diagrammatic expansion of various expectation values. These constraints have the following form when the density matrix of $|\phi_0\rangle$ is diagonal [88, 89, 137],

$$\begin{aligned} C_i^{(0)}(\{\hat{n}^{m\sigma}\},\{\lambda_\Gamma\}) &= \langle\hat{P}_i^\dagger\hat{P}_i\rangle_0 - 1 = 0, && (5.5)\\ C_i^{(m\sigma)}(\{\hat{n}^{m\sigma}\},\{\lambda_\Gamma\}) &= \langle\hat{P}_i^\dagger\hat{P}_i\hat{c}_{im\sigma}^\dagger\hat{c}_{im\sigma}\rangle_0 \\ &- \langle\hat{c}_{im\sigma}^\dagger\hat{c}_{im\sigma}\rangle_0 = 0. && (5.6)\end{aligned}$$

Where $\langle\ldots\rangle_0$ represents the expectation value with respect to $|\varphi_0\rangle$. In the limit of infinite dimensions the effect of the projectors P_i requires the renormalization of the hopping amplitudes between different sites. When the density matrix of the local non-interacting part of the Hamiltonian is diagonal one may write these renormalization factors as [89, 137]:

$$q_{m'\sigma'}^{m\sigma} = \delta_{mm'}\delta_{\sigma\sigma'}\frac{1}{n_i^{m'\sigma'}}\langle P\hat{c}_{im\sigma}^\dagger P^\dagger\hat{c}_{im'\sigma'}\rangle_0. \tag{5.7}$$

Moreover, the relation $\langle\hat{n}_i^{m\sigma}\rangle_G = \langle\hat{n}_i^{m\sigma}\rangle_0$ holds in the limit of infinite dimensions for our case, where $\langle\rangle_G$ means expectation over Gutzwiller wave function. By considering the above relations the total energy functional of an inhomogeneous system becomes of the following form,

$$\begin{aligned}\langle\hat{H}\rangle_G &= \sum_{\langle ij\rangle,mm'\sigma} -t_{ij}^{mm'\sigma} q_i^{m\sigma} q_j^{m'\sigma} \langle\hat{c}^\dagger_{im\sigma}\hat{c}_{jm'\sigma}\rangle_0 \\ &+ \sum_{im\sigma} v_{im\sigma}\langle\hat{n}_i^{m\sigma}\rangle_0 + \sum_i H_i^{int}(\{\lambda_\Gamma, \langle\hat{n}_i^{m\sigma}\rangle_0\}),\end{aligned} \tag{5.8}$$

The conditions $\langle\psi_G|\psi_G\rangle = \langle\varphi_0|\varphi_0\rangle$ and $\langle\varphi_0|\varphi_0\rangle = 1$ has to also be satisfied, the first relation itself is a consequence of the infinite dimensional limit and the second relation is just the normalization condition for $|\phi_0\rangle$. For the evaluation of the renormalization factors and other expectation values in the system we use the relations Eq. (5.5)-(5.7). The explicit form of the renormalizations, constraints and the local interaction part is presented in section 5.2.1. In addition one should notice that in the former energy functional relation we consider that the constraints $C_i^{(0)}(\{\hat{n}^{m\sigma}\},\{\lambda_\Gamma\})$ and $C_i^{(m\sigma)}(\{\hat{n}^{m\sigma}\},\{\lambda_\Gamma\})$, are satisfied by substituting the exact form of the constraints. This should be done by expressing some of the variational parameters as function of the others by solving explicitly the constraints. By doing so, the number of independent variational parameters is reduced by the number of constraints. This leaves us with an energy functional as a function of some independent variational parameters and local density matrices. As is obvious from the form of the energy functional Eq. (5.8) it has two different components, which have to be optimized, the Slater part $|\phi_0\rangle$ and the variational parameters $\{\lambda_\Gamma\}$. Moreover due to the presence of the local densities in the Hamiltonian we end up with a nonlinear eigenvalue problem. One straight way to optimize the energy functional is to use an explicit form of the constraints in the renormalization factors, then fix the variational parameters and perform an optimization with respect to the Slater part of the functional, $|\phi_0\rangle$. This part should be done similar to self-consistent DFT calculations (by choosing a trial wave function and solving the eigenvalue problem iteratively). After fixing $|\phi_0\rangle$, and therefore the local densities, an optimization with respect to the variational parameters should be performed. This two-step optimization has to be done iteratively until one reaches the convergence of $|\phi_0\rangle$ or of the variational parameters. However, we choose a different way to deal with the optimization problem. Instead of calculating the expectation value $\langle\hat{n}_i^{m\sigma}\rangle_0$, we introduce a set of new variational parameters $n_i^{m\sigma}$ that will play the role of local noninteracting occupancies $\langle\hat{n}_i^{m\sigma}\rangle_0$ (local noninteracting density matrices) which appear in the renormalization factors and the expectation value of the local interaction. It is then possible to let $n_i^{m\sigma}$ vary independently from $|\phi_0\rangle$. The Lagrange function that should be optimized has now the following form for a simple cubic slab with periodic boundary conditions in the $x-y$

plane and free (001) surfaces:

$$\begin{aligned}
\mathcal{L} &= \frac{1}{N_{k_\parallel}} \sum_{ik_\parallel, mm'\sigma} (q_i^{m\sigma} q_i^{m'\sigma} \epsilon_{ik_\parallel}^{mm'\sigma} + \delta_{m,m'} v_{im\sigma}) \langle \phi_0 | \hat{c}^\dagger_{imk_\parallel\sigma} \hat{c}_{im'k_\parallel\sigma} | \phi_0 \rangle \\
&- \frac{1}{N_{k_\parallel}} \sum_{\langle ij\rangle k_\parallel, mm'\sigma} q_i^{m\sigma} q_j^{m'\sigma} t_{\perp i}^{mm'\sigma} \langle \phi_0 | \hat{c}^\dagger_{imk_\parallel\sigma} \hat{c}_{jm'k_\parallel\sigma} | \varphi_0 \rangle + \Lambda(\frac{N_{total}}{N_{k_\parallel}} - \sum_{im\sigma} n_i^{m\sigma}) \\
&+ \sum_{im\sigma} \eta_{im\sigma}(\frac{1}{N_{k_\parallel}} \sum_{k_\parallel} \langle \phi_0 | \hat{c}^\dagger_{ik_\parallel m\sigma} \hat{c}_{ik_\parallel m\sigma} | \phi_0 \rangle - n_i^{m\sigma}) + E_{NI}(1 - \langle \varphi_0 | \varphi_0 \rangle) \\
&+ \sum_i H_i^{int}(\{\lambda_\Gamma, n^{m\sigma}\}) + \sum_{im\sigma} \gamma_i^{(m\sigma)} C_i^{(m\sigma)}(\{\lambda_\Gamma, n^{m\sigma}\}) \\
&+ \sum_i \gamma_i^{(0)} C_i^{(0)}(\{\lambda_\Gamma, n^{m\sigma}\}),
\end{aligned} \tag{5.9}$$

where $\epsilon_{ik_\parallel}^{mm'\sigma} = -2t_{\parallel i}^{mm'\sigma}(\cos k_x + \cos k_y)$, the Lagrange multipliers $\eta_{im\sigma}$ are introduced to fix $n_i^{m\sigma}$ to $\langle \hat{n}_i^{m\sigma} \rangle_0$, Λ is introduced to fix the total number of electrons (N_{total}, or equivalently total number of occupied states), E is considered to make sure that $|\varphi_0\rangle$ is normalized, i and j are layer indices in the z direction, $N_{k_\parallel} = N_{k_x} N_{k_y}$ is the total number of k-points, $\gamma^{(m\sigma)}$ and $\gamma^{(0)}$ are introduced in order to satisfy the local constraints. The optimization of the Lagrange function Eq. (5.9) is performed through an iterative procedure, starting with a minimization with respect to $|\varphi_0\rangle$, which leads to a Schrödinger-like eigenvalue problem that has to be solved for each k-point and spin component σ:

$$\begin{aligned}
&\sum_{imm'} (q_i^{m\sigma} q_i^{m'\sigma} \epsilon_{ik_\parallel}^{mm'\sigma} + \delta_{mm'}(v_{mi\sigma} + \eta_{im\sigma})) \hat{c}^\dagger_{ik_\parallel m\sigma} \hat{c}_{ik_\parallel m'\sigma} | \varphi_0 \rangle \\
&\quad - \sum_{\langle ij\rangle mm'} q_i^{m\sigma} q_j^{m'\sigma} t_{ij}^{mm'\sigma} \hat{c}^\dagger_{ik_\parallel m\sigma} \hat{c}_{jk_\parallel m'\sigma} | \varphi_0 \rangle = E_{k_\parallel,\sigma} | \varphi_0 \rangle .
\end{aligned} \tag{5.10}$$

The resulting non-interacting many-body ground state energy and wave-function are computed in the following way: $E_{NI} = \frac{1}{N_{k_\parallel}} \sum_{k_\parallel, n\sigma}^{occupied} E_{k_\parallel, n\sigma}$ and $|\varphi_0\rangle = \prod_{k_\parallel, n\sigma}^{occupied} \hat{c}^\dagger_{k_\parallel, n\sigma} |0\rangle$, n is the quantum number for the energy levels of each k-point. The above non-interacting state $|\varphi_0\rangle$, which now is an implicit function of all the variational parameters $\eta_{im\sigma}$, $n_i^{m\sigma}$, λ_{Γ_i} and Λ should be substitute back into the equation Eq. (5.9), by doing this the Lagrange

Table I.The configuration state and relative interaction energies.

No.	State	Energy	No.	State	Energy
1	$\|0\rangle$	0	9	$\|\downarrow,\downarrow\rangle$	$U-3J$
2	$\|\uparrow,0\rangle$	0	10	$\|0,\uparrow\downarrow\rangle$	U
3	$\|\downarrow,0\rangle$	0	11	$\|\uparrow\downarrow,0\rangle$	U
4	$\|0,\uparrow\rangle$	0	12	$\|\uparrow,\uparrow\downarrow\rangle$	$3U-5J$
5	$\|0,\downarrow\rangle$	0	13	$\|\downarrow,\uparrow\downarrow\rangle$	$3U-5J$
6	$\|\uparrow,\uparrow\rangle$	$U-3J$	14	$\|\uparrow,\uparrow\downarrow\rangle$	$3U-5J$
7	$\|\uparrow,\downarrow\rangle$	$U-2J$	15	$\|\downarrow,\uparrow\downarrow\rangle$	$3U-5J$
8	$\|\downarrow,\uparrow\rangle$	$U-2J$	16	$\|\uparrow\downarrow,\uparrow\downarrow\rangle$	$6U-10J$

function has the following form,

$$\begin{aligned}
\mathcal{L} &= E_{NI}(\{n_i^{m\sigma}\},\{\eta_{im\sigma}\},\{\lambda_{\Gamma_i}\},\{\gamma_i^{(0)}\},\{\gamma_i^{(m\sigma)}\},|\varphi_0\rangle) \\
&- \sum_{i,m\sigma}\eta_{im\sigma}n_i^{m\sigma} + \Lambda(\frac{N_{total}}{N_{k_{\|}}} - \sum_{i,m\sigma}n_i^{m\sigma}) \\
&+ \sum_i H_i^{int}(\{\lambda_\Gamma, n^{m\sigma}\}) + \sum_{im\sigma}\gamma_i^{(m\sigma)}C_i^{(m\sigma)}(\{\lambda_\Gamma, n^{m\sigma}\}) \\
&+ \sum_i \gamma_i^{(0)}C_i^{(0)}(\{\lambda_\Gamma, n^{m\sigma}\}).
\end{aligned} \tag{5.11}$$

In the next step we search for the stationary points of the above Lagrange function.

5.2.1 Renormalization factors and constraints

We present here detailed expressions for the normalization factors and local expectation values used in the functional Eq. (5.9). In our calculations we consider only density-density interactions. Moreover the local density matrix is diagonal as can be seen from Eqs. (5.2) and (5.1). By considering these assumptions it is apparent that the configuration states of the local Hamiltonian Eq. (5.2) are the eigenvectors of the local part of the Hamiltonian. These are summarized in the Table.I. Therefore, the Gutzwiller projector can be expressed as a function of the projectors onto the configuration states of the local Hamiltonian as follows,

$$\hat{P} = \sum_I \lambda_I|I\rangle\langle I|, \tag{5.12}$$

where I belongs to the configurations that are shown in Table I and the projectors $|I\rangle\langle I|$ are defined as follows [89],

$$\hat{m}_I = |I\rangle\langle I| = \prod_{m\sigma\in I} \hat{n}_{m\sigma} \prod_{m\sigma\notin I} (1 - \hat{n}_{m\sigma}). \tag{5.13}$$

Considering the above assumptions, a straightforward algebra leads to the following expression for the renormalization factors (by using Eqs.(5.7) or (2.82)).

$$q^{m\sigma}_{m'\sigma'} = \delta_{mm'}\delta_{\sigma\sigma'}\frac{1}{1-n^{m\sigma}}\sum_I \lambda_I \lambda_{I\cup m\sigma} m_{0I}, \tag{5.14}$$

Where $m_{0I} = \langle\phi_0|\hat{m}_I|\phi_0\rangle$ .The constraints and local interaction parts are given by the following expressions respectively,

$$\begin{aligned} C_i^{(0)}: \quad & \sum_I \lambda_I^2 m_{0I} - 1 = 0, \\ C_i^{(m\sigma)}: \quad & \sum_{I:m\sigma\in I} \lambda_I^2 m_{0I} - \langle n^{m\sigma}\rangle_0 = 0, \\ & \langle \hat{H}_{int}\rangle = \sum_I E_I \lambda_I^2 m_{0I}. \end{aligned} \tag{5.15}$$

5.2.2 Saddle point equations and numerical scheme

Here we present the explicit form of the saddle point equations. Starting from Eq. (5.11) the following equations are obtained by using the Hellman-Feynman relation:

$$\forall \quad \lambda_{\Gamma_i} : \partial_{\lambda_{\Gamma_i}}\mathcal{L} = \frac{1}{N_{k_\parallel}} K_{\lambda_{\Gamma_i}} + \partial_{\lambda_{\Gamma_i}} H_i^{int}(\{\lambda_\Gamma, n^{m\sigma}\}) + \partial_{\lambda_{\Gamma_i}} F_i(\{\lambda_\Gamma, n^{m\sigma}\}) = 0, \tag{5.16}$$

$$\forall \quad n_{ir\sigma} : \partial_{n_{ir\sigma}}\mathcal{L} = \frac{1}{N_{k_\parallel}} K_{n_{ir\sigma}} + \partial_{n_{ir\sigma}} H_i^{int}(\{\lambda_\Gamma, n^{m\sigma}\}) + \partial_{n_{ir\sigma}} F_i(\{\lambda_\Gamma, n^{m\sigma}\}) - \eta_{ir\sigma} = 0, \tag{5.17}$$

$$\forall \quad \eta_{ir\sigma} : \partial_{\eta_{ir\sigma}}\mathcal{L} = \frac{1}{N_{k_\parallel}} \langle\varphi_0| \sum_{k_\parallel} \hat{c}^\dagger_{im\sigma k_\parallel\sigma}\hat{c}_{im\sigma k_\parallel\sigma}|\varphi_0\rangle - n_i^{m\sigma} = 0, \tag{5.18}$$

$$\forall \quad \gamma_i^{(r\sigma)} : \partial_{\gamma_{ir\sigma}}\mathcal{L} = C_i^{(r\sigma)}(\{\lambda_\Gamma, n^{r\sigma}\}) = 0, \tag{5.19}$$

$$\forall \quad \gamma_i^{(0)} : \partial_{\gamma_{i0}}\mathcal{L} = C_i^{(0)}(\{\lambda_\Gamma, n^{m\sigma}\}) = 0, \tag{5.20}$$

$$\partial_\Lambda \mathcal{L} = (\frac{N_{total}}{N_{k_\parallel}} - \sum_{im\sigma} n_i^{m\sigma}) = 0, \tag{5.21}$$

where,

$$\begin{aligned}
K_{\lambda_{\Gamma_i}} &= \sum_{mm'\sigma} [\tilde{t}_i^{mm'\sigma}(q_i^{m\sigma}\partial_{\lambda_{\Gamma_i}} q_i^{m'\sigma} + q_i^{m'\sigma}\partial_{\lambda_{\Gamma_i}} q_i^{m\sigma}) \\
&+ \sum_j 2\delta_{i,j\pm1}\tilde{t}_{ij}^{mm'\sigma}\partial_{\lambda_{\Gamma_i}} q_i^{m\sigma} q_j^{m'\sigma}], \\
K_{n_{ir\sigma}} &= \sum_{mm'\sigma} [\tilde{t}_i^{mm'\sigma}(q_i^{m'\sigma}\partial_{n_{ir\sigma}} q_i^{m\sigma} + q_i^{m\sigma}\partial_{n_{ir\sigma}} q_i^{m'\sigma}) \\
&+ \sum_j 2\delta_{i,j\pm1}\tilde{t}_{ij}^{mm'\sigma} q^{jm'\sigma}\partial_{n_{ir\sigma}} q^{im\sigma}], \\
F_i(\{\lambda_\Gamma, n^{m\sigma}\}) &= \gamma_i^{(0)} C_i^{(0)}(\{n^{m\sigma}, \lambda_\Gamma\}) + \sum_{r\sigma} \gamma_i^{(r\sigma)} C_i^{(r\sigma)}(\{n^{m\sigma}, \lambda_\Gamma\})
\end{aligned}$$

with $\tilde{t}_{imm'\sigma} = \sum_{k_\parallel} \epsilon_{ik_\parallel}^{mm'\sigma} \langle\varphi_0|\hat{c}^\dagger_{ik_\parallel m\sigma}\hat{c}_{ik_\parallel m'\sigma}|\varphi_0\rangle$, $\tilde{t}_{ij}^{mm'\sigma} = -t_{ij}^{mm'\sigma} \sum_{k_\parallel} \langle\varphi_0|\hat{c}^\dagger_{ik_\parallel m\sigma}\hat{c}_{jk_\parallel m'\sigma}|\varphi_0\rangle$ and N_{total} is the total number of electrons. $\tilde{t}_{i,i+1}$ and $\tilde{t}_{0,1}$ are equal to zero at the edge of the slab. This set of nonlinear equations can be solved by using a nonlinear solver based on Newton and/or quasi-Newton methods. Notice that $|\phi_0\rangle$ is still implicitly a function of the variational parameters and has to be updated again through (5.10) during the evaluation of the saddle point equations throughout the optimization procedure. This means that we are at all times working with a $|\phi_0\rangle$ which satisfies the condition $\frac{\delta\mathcal{L}}{\delta\langle\phi_0|} = 0$. It should be noticed that together with the saddle point equations the electrostatic forces due to the long-range electron-electron and electron-ion interactions should be in principle considered. However since the back ground permittivity of strongly correlated materials is usually very high [112], we tested the solutions with various high values of background permittivity and observed that long-range screening is negligible [133]. We therefore set the value of the back ground permittivity to infinity in our calculations and ignore these effects. The above set of equations are useful as long as we are sure that there is charge transfer between different sites and orbitals. Otherwise if for some reason (for instance when the system is half filled) the density matrix is fixed, the optimization procedure will be much more simple than what was discussed here. If this is the case then it will be more efficient to minimize the energy functional as function of λ_Γ in one step, this should be done by using a constrained minimizer like sequential quadratic programming (SQP) [138] or doing minimization by moving along a constrained steepest descent direction [139], and calculate $|\phi_0\rangle$ through Eq. (5.10) in the next step. These two steps should be done iteratively until one reaches the convergence of variational parameters. At least for half filling the parameters $\eta_{im\sigma}$ are homogeneous for all sites and both bands and does not affect the

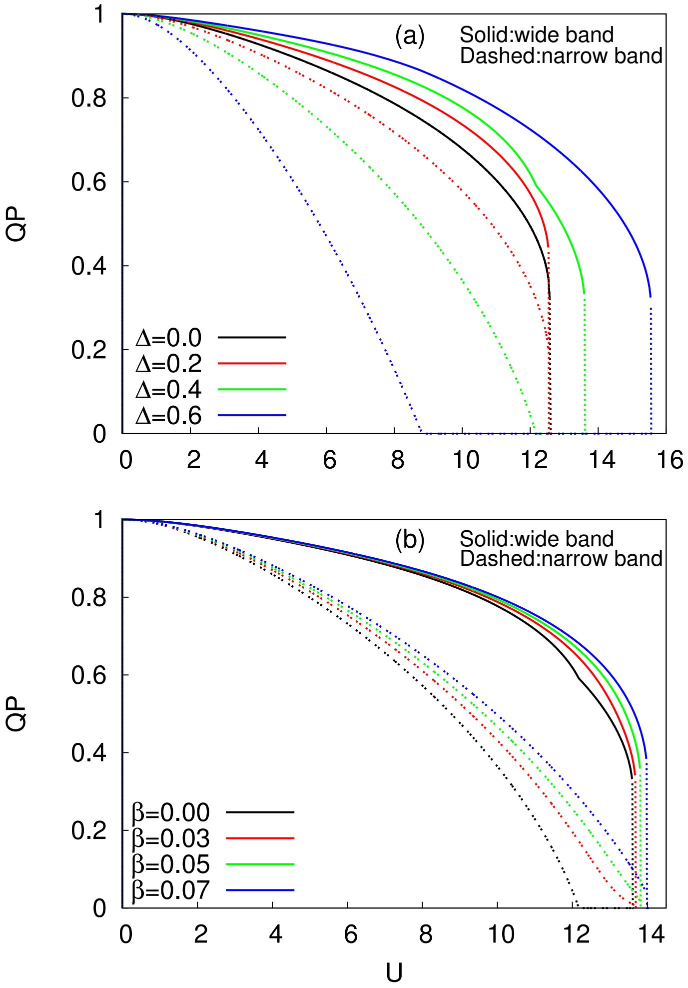

Figure 5.1: (a) QP weight of WB (solid) and NB (dashed) as function of interaction for $J = 0.1U$ and different band differences; (b) QP weight of QP weight of WB (solid) and narrow band (dashed) as function of interaction for $J = 0.1U$ $\Delta = 0.4$ and different in-plain mixing parameter β.

optimization. We compared the results of the later approach and those achieved from the direct solution of saddle point equations,they confirmed each other with great accuracy.

To solve the saddle point equations it is best to find a rough solution with a lower number of k-point mesh (for instance 8×8) and use this solutions as starting point to a denser k-points. In order to numerically solve the set of saddle point equations, we use a 32×32 Monkhorst-Pack [115] k-grid for which the total energy is well converged. We

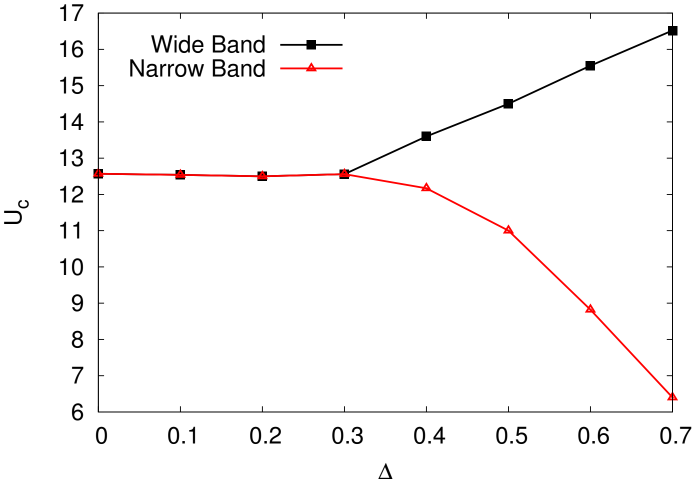

Figure 5.2: Critical interaction (U_c) as function of different band width differences.

finish this part with a hint that using a Monkhrost-Pack grid with a shift is very beneficial to ensure convergence to an accurate solution when it fails to find solutions for un-shifted k-grid.

5.3 Numerical results

In this section we report results for $Q_i^{m\sigma} = (q_i^{m\sigma})^2$ as being the position dependent QP weight of different bands, which is a measure of the mobility of the electrons within Fermi liquid theory. The inverse of the QP weight is proportional to the mass renormalization which becomes divergent for $Q_i^{m\sigma} = 0$ corresponding to an insulating phase [117]. Throughout this work the thickness of the slab is taken to be $L_z = 50$ in units of the lattice constant, furthermore we consider paramagnetic condition is imposed which means spin symmetry is considered in the rest i. e. $N_\sigma = N_{\bar{\sigma}} = N_{total}/2$, which N_σ is the number of occupied states for spin component σ in $|\phi_0\rangle$ (notice that there is not any hopping process in single particle part of the Hamiltonian which hop states with different spin). Moreover, total number of particles at half filling is $N_{total} = N_{Halffilled} = 2 \times N_{k_{\|}} \times L_z$, which is half of total number of states $4 \times N_{k_{\|}} \times L_z$ for a two band model with spin. The correlation length, ξ, is defined as the length scale over which the surface QP recovers its bulk value. This can be extracted by fitting the position dependent square root of the QP weight with the following formula [118],

$$q(x) = q_{bulk} + (q_{surface} - q_{bulk}) e^{-\frac{1}{\xi}(x-1)}, \tag{5.22}$$

where $q(x)$ is the square root of the position dependent QP weight in the perpendicular direction to the slab. Δ is defined as the bandwidth difference such that the hopping amplitude of wide band (WB) being $t_{\perp,WB} = t_{\parallel,WB} = t_0 + \Delta$ and the hopping amplitude of narrow band (NB) being $t_{\perp,NB} = t_{\parallel,NB} = t_0 - \Delta$. β is defined as the in-plane mixing such that $t_{\parallel WB,NB} = \beta, t_{\perp WB,NB} = 0$. The parameters U, J , β and Δ are scaled with $t_0 = 1$. Furthermore, in the following we consider $e = a = 1$ where e is charge of the particles and a is the lattice constant. Hearafter, the repoted values for the charge densities consist of summation over both spin components.

5.3.1 Correlated slab at half filling

We first present in Fig. 5.1, the bulk QP weight of different band width differences at half filling as a function of interaction strength. Notice here bulk means the center of a large slab or a translationaly invariant simple cubic system with nearest neighbor hopping elements, where the QP weight of both coincides when the slab thickness is large enough. For our case with a slab size with 50 layers the QP of the central layer is almost equal to that of the bulk. These results agree with those obtained in other works using different approaches [129,130]. As expected from previous works, a two band Hubbard model with density-density interactions shows a first order phase transition if J is finite.

In Fig. 5.1(a) the QP weight of both bands is plotted as function of interaction for different values of Δ. As is clear from the figure, for small values of Δ both the WB and NB exhibit a first order phase transition at a single critical interaction. On the other hand for sufficiently large band width differences a second order MIT occurs for the NB at values of the interaction significantly lower from those of the WB. The difference between the critical values of the interaction for the NB and WB is shown in Fig. 5.2 for different values of Δ. In Fig. 5.1(b) the influence of the off-site hybridization is considered. We observe that, due to a gain of kinetic energy from the WB, the MIT for the NB is suppressed. This effect is more pronounced for larger values of the hybridization mixing parameter, β. We can conclude here that any mixing between the bands will transfer energy from one band to the other and the band-selective Mott transition will be suppressed.

We next show in Fig. 5.3 the spatial dependence of the QP weight profile for a system with equal band width and for different values of the interaction U while we choose the values of J such that the system is in the vicinity of the Mott transition. As can be seen from the inset of Fig. 5.3, the diverging correlation length (that is a signature of MIT for systems with continuous phase transition) is not seen here and only for very small values of J one may see a large correlation length near the Mott transition point, although still finite at the transition point. As expected, the reason for this behavior is the existence of the first order phase transition, which occurs for the bulk and presents a finite QP weight

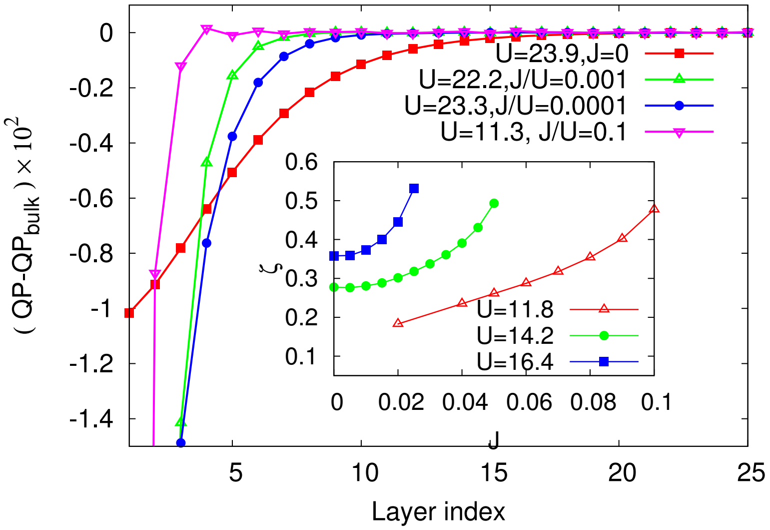

Figure 5.3: QP weight profile for different values of U and J, each case is very near the critical point. Inset: correlation length for different values of interaction (U) as function J.

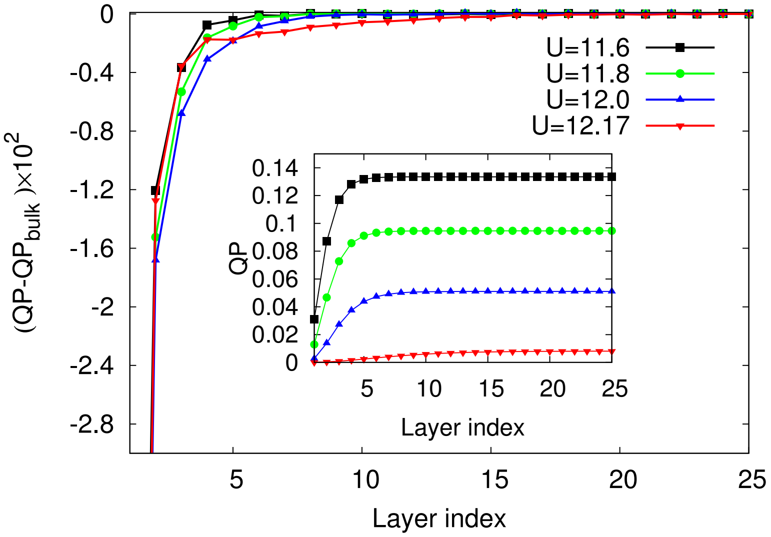

Figure 5.4: QP weight profile for WB for different values of interaction for $J = 0.1U$ and $\Delta = 0.4$. Inset: the same plot but for NB.

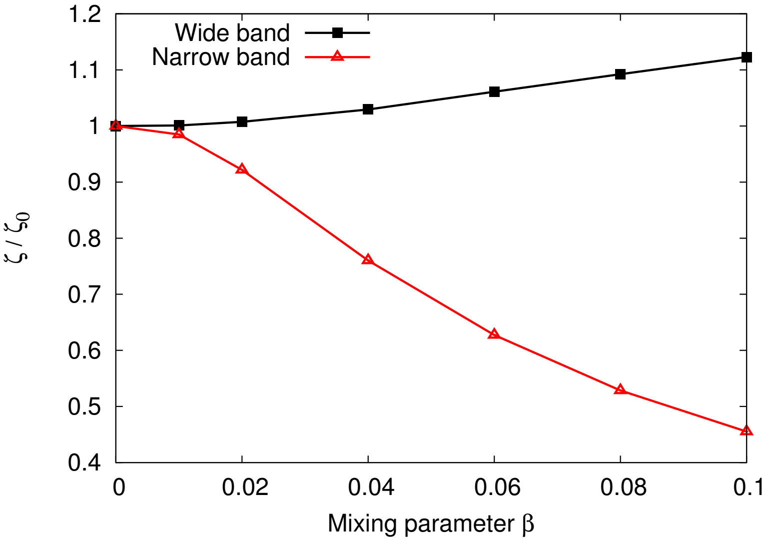

Figure 5.5: The ratio of the correlation length to the one obtained for $\beta = 0.0$ as function of mixing parameter β for $U = 12.0$,$J = 0.1U$ and $\Delta = 0.4$.

at the transition point. To better see the effect of finite J on the QP weight profile we plot in the inset of Fig. 5.3 the correlation length as function of J for different values of U. We find that the correlation length is enhanced by increasing the value of J. End points at the top of each line (related to individual U in the inset) are the places in which by even a tiny increase of J a MIT happens for the slab.

In Fig. 5.4 the QP weight profile of the WB is plotted for different values of U with $J = 0.1U, \Delta = 0.4$ and $\beta = 0$. By considering these parameters the NB suffers from a Mott MIT at $U \simeq 12.2$. When approaching U_c^{NB} one can observe, in the inset of Fig. 5.4, the depletion of the QP weight of the NB near the surface. The proximity to U_c^{NB} not only causes a QP weight reduction but also leads to an enhancement of the correlation length for NB. By approaching U_c^{NB} one may recognize that the correlation length of WB is also increased (QP of WB recovers its bulk value in larger distances from the surface) due to enhanced correlations induced from the NB. To quantify the correlation effects as usual we fit the resulting correlation lengths to a power law as $\xi_{NB} = A(U - U_c^{NB})^{-\nu}$, with the resulting value of the exponent being a mean-field-like $\nu \simeq 0.5$. The fittings were performed for different values of band differences Δ. We found that both the exponent and the pre-factor in the fitting are insensitive to the parameters of the system, within the accuracy of our numerical results. Similar mean field behavior was seen before for the single band Hubbard model [118], which also undergoes a continuous phase transition at the critical interaction strength.

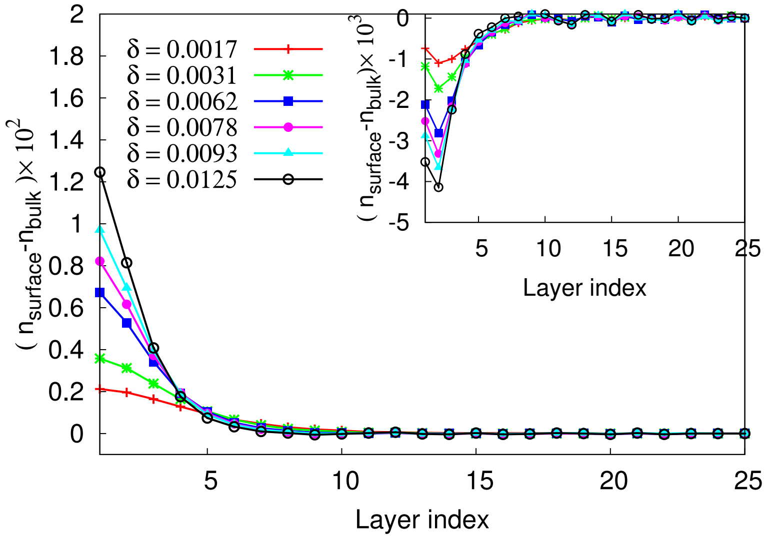

Figure 5.6: The charge distribution of NB as function of doping with $U = 12.3$, $J = 0.1U$, $\Delta = 0.4$ and $\beta = 0.0$. Inset: Charge distribution for WB with the same parameters of NB.

Next we study the effect of the hybridization on the QP profile. In Fig. 5.5 we depict the ratio of correlation length of both NB and WB with respect to the values obtained for zero hybridization. As discussed before, the effect of the hybridization is to remove the MIT for NB by transferring kinetic energy from the WB. This then leads to a reduction of the correlation length for NB in comparison with the zero hybridization case. On the other hand the WB shows only a small enhancement of the correlation length in comparison with the change of the NB correlation length, which is due to the loss of kinetic energy and therefore the small enhancement of correlation effects. The WB acts as an energy reservoir for the NB.

5.3.2 Doped correlated slab

Another interesting aspect is the effect of doping on the QP weight and the charge transfer between the bands and between surface and bulk. For the separated band case due to absence of hybridization, we find that it is more numerically efficient to fix the charge density for each band individually and to consider separate equations for satisfying the charge conservation for each band. In this case if we consider the Lagrange multipliers Λ_{WB} and Λ_{NB} for fixing the total densities $N_{NB,total}$ and $N_{WB,total}$ for each band, then the

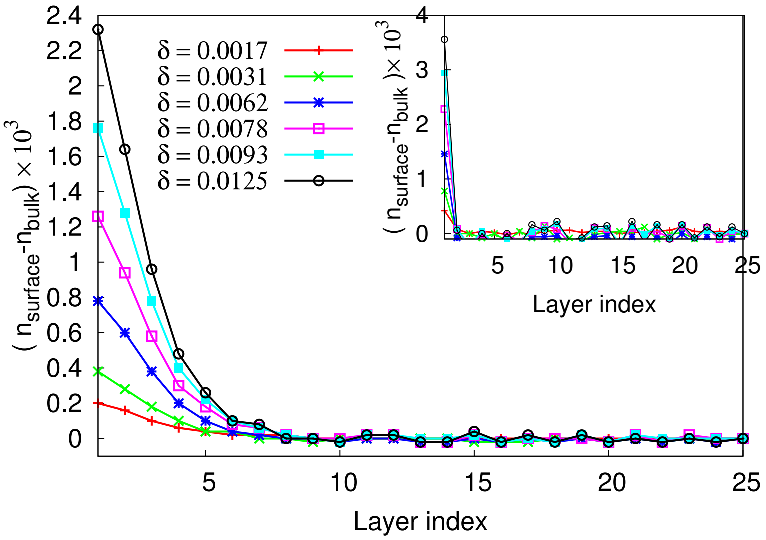

Figure 5.7: The charge distribution of NB as function of doping with $U = 12.0$, $J = 0.1U$, $\Delta = 0.4$ and $\beta = 0.001$. Inset: Charge distribution for WB with the same parameters of NB.

chemical potential can be calculated as

$$\Lambda = 1/(1+a)\Lambda_{NB} + a/(1+a)\Lambda_{WB}, \tag{5.23}$$

where $a = N_{NB,total}/N_{WB,total}$. For the separated bands N_{total} could be written as $N_{total} = N_{NB,total} + N_{WB,total}$ that $N_{NB,tot}$ and $N_{WB,tot}$ are known beforehand, in the rest of paper equally doped bands means $N_{NB,total} = N_{WB,total}$, where $N_{s,total} = N_{s,\sigma} + N_{s,\bar{\sigma}}$ with $s = WB, NB$.

Here we define $\delta = 1 - N_{total}/N_{Halffilled}$. For mixed bands the average occupation of each band is not known apriori and these can be calculated only after solving equations Eq. (5.16)-(5.21).

For equally doped bands, Fig. 5.6 shows that there is a charge transfer from the center of the slab to the surface for the NB, while for the WB the opposite happens. This implies that when the two bands are equally doped, for the NB both the reduced coordination number and charge transfer from the center to the surface lead to an enhancement of the correlation effects at the surface. For the WB correlation effects are only enhanced due to the reduced coordination number while the charge transfer from the surface to the center decreases the correlation effects at the surface. As usual, by measuring the correlation length of the NB one can find a power law relation for correlation length as function of NB doping as $\xi_{NB} = \delta_{NB}^{-\nu}$, which extrapolates to infinity in the vicinity of $\delta_{NB} = 0$ as long

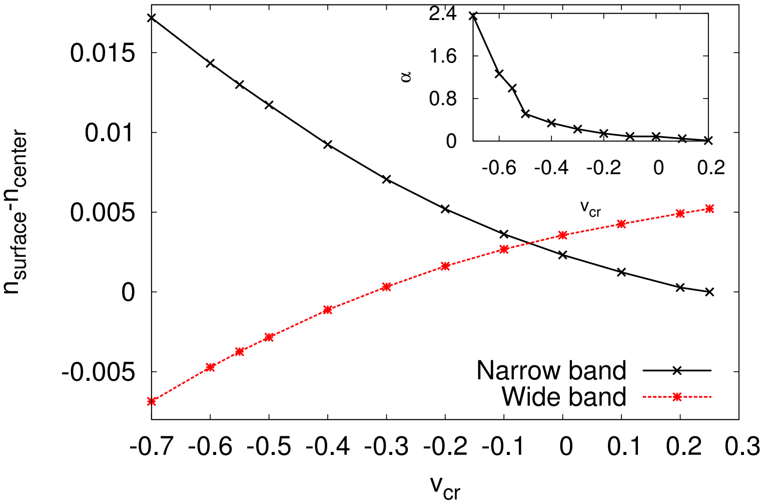

Figure 5.8: Charge transfer as function of crystal field splitting v_{cr} with $U = 12.0$, $J = 0.1U$, $\Delta = 0.4$,$\beta = 0.001$ and $\delta = 0.0078$. Inset: The evolution of $\alpha = \dfrac{1 - \langle n_{NB} \rangle}{1 - \langle n_{WB} \rangle}$ as function of v_{cr}.

as $U > U_c^{NB,Halffilled}$. By fixing the charge density of each band, a potential difference between two bands, $\Lambda_{WB} - \Lambda_{NB}$, is induced. This in turn shows the tendency of the system to have charge transfer from the WB (less correlated band) to the NB (more correlated band) in the absence of this potential difference (not shown here).

To better understand this, we consider a small value of off-site hybridization between the bands, $\beta = 0.001$. The resulting charge density profile is presented in Fig 5.7 where the NB is near half filling due to general charge transfer from the WB to the NB [128,131]. The spatial distribution of the charge density of the NB shows a similar behavior to the no-hybridization case, i.e. there is charge transfer from the center to the surface for NB. Contrary to equaly doped case, for the WB there is charge transfer from the center to the surface when $\beta = 0.001$.

In order to scan the evolution of the charge transfer between the bands and its influence on correlation effects we now impose a potential difference between the two bands in order to mimic possible crystal field splitting or local polarization effects of the bands. The evolution of the charge density distribution as function of crystal field potential, $v_{cr}^{\sigma} = v_{WB,i\sigma} - v_{NB,i\sigma}$, is depicted in Fig. 5.8 for both the WB and NB. It shows a clear dependence of the charge transfer between surface and bulk for both WB and NB on the relative average charge density accumulated in the different bands. This could be

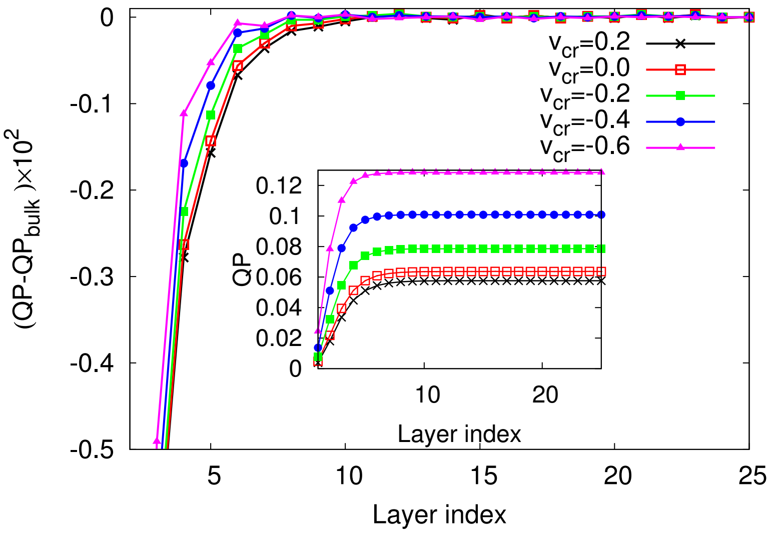

Figure 5.9: Evolution of quasi particle weight profile of WB as function of v_{cr} for $U = 12.0$, $J = 0.1U$, $\Delta = 0.4$, $\beta = 0.001$ and $\delta = 0.0078$. Inset: The same plot but for NB.

better understood from the inset of Fig. 5.8, where the relative doping of the two bands $\alpha = \dfrac{1-\langle n_{NB}\rangle}{1-\langle n_{WB}\rangle}$ is shown as function of v_{cr}. Here we define $\langle n_s\rangle = (1/N_{Layers})\sum_{i\sigma}\langle n_{is\sigma}\rangle$ for $s = NB, WB$. When $\alpha \to 1$ the system approaches to the equally doped bands case where the system is in a less correlated regime, alternatively when $\alpha \to 0$ the NB is near half filling and system is switches to a more correlated regime.

To see this, we finally depict in Fig. 5.9 the effect of v_{cr} on the QP profiles of the WB and NB near the surface. This also shows that when $\alpha \simeq 1$ ($v_{cr} \simeq -0.55$) the system is in a less correlated regime since the QP of NB is larger and the QP profile of the NB recovers its bulk value in a smaller distance from the surface, i.e. the correlation length is short. The QP of the WB shows clear Friedel-like oscillations. On the other hand, when $\alpha \simeq 0.0$ ($v_{cr} \simeq 0.2$), both the NB and WB have larger correlation length and the Friedel oscillations seen in the WB are more suppressed, therefore signaling the enhancement of correlation effects.

5.4 Conclusions

In conclusion we studied the influence of correlation effects on the charge and QP weight profile of a two band Hubbard model with density-density interactions. We found that as long as the values of the Hund's coupling J is finite, due to the existence of a first order MIT, no diverging correlation length, even very near the transition point is seen. As a consequence, due to the short correlation length, the surface QP weight recovers very fast its bulk value even very near transition point. Only when the value of J is very small, a long correlation length could be seen near the critical point while it is still finite. When the band widths are not equal, for sufficiently large band width difference, the NB suffers from a continuous MIT at a smaller critical interaction U_c^{NB}, well before the first order transition. Due to the continuous nature of this band selective transition, the NB shows a diverging correlation length at the transition point which follows an expected mean-field-like power law behavior as function of the interaction strength with an exponent insensitive to the band width difference. This in turn leads to the formation of an extended surface dead zone layer for the NB. For the doped system we reveal two different mechanisms of charge transfer to the surface for the WB. When $\alpha = \dfrac{1 - \langle n_{NB} \rangle}{1 - \langle n_{WB} \rangle} \ll 1$ interaction effects near the surface are enhanced due to reduced coordination number and charge transfer from the center to the surface for both bands. In this case the NB is near half-filling and the system is in a more correlated regime. However in the limit $\alpha \simeq 1$, there is charge transfer from the center to the surface for NB, while for the WB charges are repelled from the surface to the center of the slab. Such effects could be of importance not only near at surfaces but also at interfaces with other insulating materials.

Chapter 6

Non-linear response to electric field in extended Hubbard models

The electric-field response of a one-dimensional ring of interacting fermions, where the interactions are described by the extended Hubbard model, is investigated. By using an accurate real-time propagation scheme based on the Chebyshev expansion of the evolution operator, we uncover various non-linear regimes for a range of interaction parameters that allows modeling of metallic and insulating (either charge density wave or spin density wave insulators) rings. The metallic regime appears at the phase boundary between the two insulating phases and provides the opportunity to describe either weakly or strongly correlated metals. We find that the *fidelity susceptibility* of the ground state as a function of magnetic flux piercing the ring provides a very good measure of the short-time response. Even completely different interacting regimes behave in a similar manner at short time-scales as long as the fidelity susceptibility is the same. Depending on the strength of the electric field we find various types of responses: persistent currents in the insulating regime, dissipative regime or damped Bloch-like oscillations with varying frequencies or even irregular in nature. Furthermore, we also consider the dimerization of the ring and describe the response of a correlated band insulator. In this case the distribution of the energy levels is more clustered and the Bloch-like oscillations become even more irregular.

The results of this chapter submited to Phys. Rev. B.

6.1 Introduction

The investigation of real time dynamics of a closed system consisting of interacting particles is important not only for the evaluation of experimentally relevant quantities, but also supplies reliable information about the general properties of the Hamiltonian as long as one measures an appropriate set of observables throughout the propagation process [140]. This is of interest especially when the dimension of the Hilbert space is very large and accessing the whole energy spectrum is not possible. There exist several approaches to face the problem of real time propagation of closed interacting systems. Among them are the numerically exact polynomial expansions [141] or the approximate Lanczos propagation method [142], the state of art time dependent density matrix renormalization group (tDMRG) [143] and non-equilibrium dynamical mean field theory (nDMFT) [144, 145]. The common thread for all these methods is that it is not necessary to access the whole spectrum in order to evaluate time dependent expectation values, hence this makes it feasible to investigate a large class of interacting systems.

There exist several theoretical investigations on the real time dynamics of the Hubbard Hamiltonian as a standard model for interacting lattice fermions, part of which focused on real time quench dynamics [146–150], real time studies based on the relaxation dynamics of specifically prepared exited states [151] as well as the effect of an external electric field [144, 152–158]. The electric break down of a one-dimensional Mott insulator has been theoretically investigated [159, 160] and the analysis was based on a LZ [98, 99] mechanism, which showed an exponential decay of the probability of the initial ground-state as function of time in short time scales. The decay rate is a function of an exponential function with an exponent proportional to square of the charge gap of the system [160], however this is not universal and the dependence of the exponent on the charge gap could deviate from quadratic type for specific cases [161]. We found there are situations in which the breakdown is not simultaneous with the overlap of ground-state with only the first excited state but also with higher energy states (see Fig. 6.3)(b)). This happens especially for insulating systems with larger charge gaps. This therefore makes inappropriate the use of a simple two level approximation and the LZ parameter as a basis for comparing different insulating systems. In order to alleviate these discrepancies of the two level approximation we employ the recently proposed *fidelity susceptibility* [102] as a measure for the change of basis-set as function of external field. This quantity is unbiased and can be calculated numerically exact. Throughout this work we use it as a basis for comparing the response of different insulating systems to a constant electric field for short time scales.

Beyond the short time-scale ground-state decay, a question that grasped the attention is how much does the electric field response at longer time scales depends on ground-state properties and/or interaction parameters. A notable phenomenon that definitely depends on longer time scales and is beyond the ground state decay mechanism based on the LZ tunneling is the appearance of Bloch oscillations (BO). The existence of Bloch oscillations has already been proven experimentally in semiconductor super-lattices [162–165]. Furthermore, the damping of Bloch oscillations in a closed interacting system subjected to an uniform electric field has been described theoretically within the Falikov-Kimbal model [144], the one-dimensional Hubbard spin-less model [166], where it is shown an integrable system shows current oscillations with frequencies smaller than the normal BO when subjected to uniform weak field, and in the one dimensional Holstein model [167], where authors report the presence of an stationary state which carries a finite current. Furthermore BO in electric break down of a 3-dimensional Hubbard model [155] is investigated. By using an extended Hubbard model one has the opportunity to design the interaction parameters in order to have better understanding about the mechanism of the break down in short time scales and formations of BO in larger time scales. It is the aim of this chapter to investigate the differences between the non-linear response of different kinds of closed systems of interacting fermions both in the insulating and the metallic regimes. We achieve this by employing a real time propagation scheme together with the ground-state and spectral analysis. Based on our analysis it appear to be impossible for a closed system to have an stationary state which carries finite stationary current.

Notice here that from the experimental point of view, the special case of electric breakdown of 1D Mott insulators has been realized experimentally either with a strong electric field [168, 169] or through photo-induced metal insulator transitions in pump probe experiments [170, 171]. Further interest was recently triggered by the realization of fermionic optical lattice experiments, where the electric field effect on systems with designed interactions could be realized [55, 56, 172, 173].

This chapter is organized as follows: in sectrion 6.2 we present our model under study together with a brief description of the theoretical and numerical schemes. In section 6.3.1 we present our analysis of the response to constant electric field for a system of weakly interacting fermions, while in section 6.3.2 we perform the same study but for strongly interacting fermions. Finally, in section 6.4 we give our conclusions.

6.2 Model and Method

Our model under investigation is a one-dimensional closed system of interacting charged fermions with periodic boundary conditions. It can be described in the second-quantization formalism by an extended Hubbard model as follows:

$$\begin{aligned}\hat{H} &= -\sum_{\langle ij\rangle\sigma}[h_{ij}(t)\hat{c}^{\dagger}_{i\sigma}\hat{c}_{j\sigma}+h.c.]+\sum_{\langle ij\rangle}\frac{1}{2}V_{ij}\hat{n}_i\hat{n}_j \\ &+ \sum_i U\hat{n}_{i\sigma}\hat{n}_{i\bar{\sigma}}, \end{aligned} \tag{6.1}$$

where $\langle..\rangle$ represents the summation over the nearest neighbor sites. $\hat{c}^{\dagger}_{i\sigma}$ and $\hat{c}_{j\sigma}$ are the creation and annihilation fermion operators. The fermion density is defined as usual as $\hat{n}_i = \hat{n}_{i\uparrow}+\hat{n}_{i\downarrow}$ with $\hat{n}_{i\sigma} = \hat{c}^{\dagger}_{i\sigma}\hat{c}_{i\sigma}$. The first term in Eq. (6.1) represents the kinetic energy, where the hopping amplitude is taken to be time-dependent and by using the Peierls substitution becomes $h_{ij}(t) = h_{ij}(0)e^{\frac{ie}{\hbar}\phi(t)}$ with $h_{i,i+1}(0) = [h_0 + (-1)^i\eta]$. $\phi = \phi_{tot}/L$ is the total magnetic flux piercing the ring divided by the number of sites and η models a dimerization term. Hereafter we consider $\hbar = e = a = 1$, where a is lattice constant. Interactions are either local between fermions with opposite spins, described by U, or non-local between fermions sitting on neighboring sites, described by V_{ij}. All of the coupling constants which are reported in the following are scaled with $h_0 = 1$. Throughout this work we consider an electric field, which is given by the time derivative of the flux, $\tilde{F} = -\dot{\phi}(t)/a$, in units of $h_0/(ea)$. In the following the time values are presented in units of $\hbar/h_0$, and all of the cases we consider are at half filling with $N_\uparrow = N_\downarrow = L/2$.

Starting from parameters at $t = 0$ we find the ground state of the resulting Hamiltonian and propagate it while considering the change of the coupling parameters as function of time. To find the solution of the time-dependent Schrödinger equation,

$$H(\phi(t))|\psi(t)\rangle = i|\dot{\psi(t)}\rangle, \tag{6.2}$$

one may write it as a superposition of the instantaneous eigenstates of the time-dependent Hamiltonian as,

$$|\psi(t)\rangle = \sum_n c_n(t)|n_\phi(t)\rangle, \tag{6.3}$$

where $|n_\phi(t)\rangle$ are the instantaneous eigenstates of $H(\phi(t))$, with,

$$H(\phi(t))|n_\phi(t)\rangle = E_n(t)|n_\phi(t)\rangle. \tag{6.4}$$

By substituting $|\psi(t)\rangle$ as expressed by Eq. (6.3) into the Schrödinger equation and by using the change of variables as $\tilde{c}_n(t) = c_n(t)e^{i\theta_n(t)}$, with,

$$\theta_n(t) = \int_0^t E_n(\tau)d\tau - i\int_0^t \langle n_\phi(\tau)|\dot{n}_\phi(\tau)\rangle d\tau, \tag{6.5}$$

one obtains the following set of coupled differential equations for the coefficients $\tilde{c}_n(t)$,

$$\dot{\tilde{c}}_n(t) = -\sum_{m\neq n} e^{i\theta_{nm}(t)}\tilde{c}_m(t)\langle n_\phi(t)|\dot{m}_\phi(t)\rangle, \tag{6.6}$$

where $\theta_{nm}(t) = \theta_n(t) - \theta_m(t)$, this change of variables is in fact a gauge transformation because $\theta_{nm}(t)$ is purely real [100]. The change of basis set as function of time manifests itself in the $\langle n_\phi(t)|\dot{m}_\phi(t)\rangle$ term in the right-hand side of Eq. (6.6). By starting from an eigenstate of the Hamiltonian at $t = 0$ with $|c_n(0)| = 1$, as long as the terms $\langle n_\phi(t)|\dot{m}_\phi(t)\rangle \simeq 0$ during the evolution, then one arrives at the adiabatic regime where $|\psi(t)\rangle$ only follows the eigenstate of the instantaneous Hamiltonian and the coefficients $|c_n(t)| = 1$ only consist of a phase that is a combination of a geometrical Berry and a dynamical phase. For the non adiabatic regime, Eq. (6.6) not only ensures the change in the magnitude of $c_n(t)$ but each coefficient further accumulates a complicated phase consisting of dynamical and Berry phases produced by the other states. If we consider the ground-state as the starting state for the time evolution, the quantity that measures the change of basis set as function of the external parameter ϕ is the *ground-state fidelity* [101] which is defined as

$$\Xi(\phi) = |\langle\psi_0(\phi)|\psi_0(\phi + \delta\phi)\rangle|. \tag{6.7}$$

By using perturbative arguments it is possible to see that there is a close relationship between the ground-state fidelity and the coefficients that appear in Eq. (6.6),

$$\langle n_\phi(t)|\dot{m}_\phi(t)\rangle = \dot{\phi}\frac{\langle n_\phi(t)|\partial_\phi H(\phi(t))|m_\phi(t)\rangle}{(E_n - E_m)}. \tag{6.8}$$

Therefore the change in the ground-state wave-function under an infinitesimal change of flux can be written as:

$$|\psi_0(\phi + \delta\phi)\rangle = \Lambda\left[|\psi_0(\phi)\rangle + \delta\phi\sum_{n\neq 0}\frac{\langle n_\phi|\partial_\phi H(\phi)|\psi_0(\phi)\rangle}{E_0 - E_n}|n_\phi\rangle\right], \tag{6.9}$$

where Λ is a normalization factor. After normalization and considering $\delta\phi << 1$ one obtains that

$$|\langle\psi_0(\phi)|\psi_0(\phi + \delta\phi)\rangle|^2 = 1 - (\delta\phi)^2\chi_\Xi(\phi), \tag{6.10}$$

where $\chi_\Xi(\phi)$ is the *fidelity susceptibility* which is defined as [102, 103],

$$\chi_\Xi(\phi) = \frac{1 - \Xi^2(\phi)}{(\delta\phi)^2} = \sum_{n\neq 0}\frac{|\langle\psi_0(\phi)|\partial_\phi H(\phi)|n_\phi\rangle|^2}{(E_0 - E_n)^2}. \tag{6.11}$$

The leading term in the fidelity expansion is of the order of $\delta\phi^2$. When comparing the terms in the right-hand side of Eq. (6.11) with terms that appear in the right-hand side of Eq. (6.6) one may infer that a larger $\chi_{\Xi}(\phi)$ leads to a more non-adiabatic character of the transition due to the driving of the system by an external electric field. We will use the ground-state fidelity susceptibility in the following sections as a basis for the comparison of the short term response of different kinds of interacting fermions modeled by Eq. (6.1). We do this in particular when the system is subjected to a constant and uniform electric field. Although the instantaneous eigenstate representation of the time-dependent Schrödinger equation is very insightful, the solution of Eqs. (6.6) is either very difficult or outright impossible for systems where the Hilbert space is very large and having the eigenstates at each moment is very computationally expensive. For the case of interacting fermions with spin the dimension of the Hilbert space for a small system which consists only 10 sites at half filling is ~ 63000, which makes solving Eqs. (6.6) almost impossible. An alternate way to deal with the time-dependent Schrödinger equation is to exploit the form of the unitary time evolution operator:

$$\hat{U}(t) = \mathcal{T}e^{-i\int_0^{t_f}\hat{H}(\tau)d\tau} \simeq \prod_k^N e^{-i\hat{H}(t_k)\delta t}, \tag{6.12}$$

where $\delta t = t_f/N$. Therefore, the problem is reduced to a stepwise change of the Hamiltonian and relaxation of the system with a time step equal to δt. Over each time-step the Hamiltonian is considered to be time-independent and the relaxation of the wave function can be easily performed, by using the Chebyshev propagation method [174], which considers an expansion of the evolution operator. The wave-function at $t_i + \delta t$ can now be written as:

$$\begin{aligned} |\psi(t_k + \delta t)\rangle &= e^{-ib\delta t}[J_0(a\delta t)I \\ &+ \sum_{s=1}^{\infty} 2(-i)^s J_s(a\delta t)T_s(\tilde{H})]|\psi(t_k)\rangle, \end{aligned} \tag{6.13}$$

where $\tilde{H} = (\hat{H} - bI)/a$ with $b = (E_{max} + E_{min})/2$ and $a = (E_{max} - E_{min})/(2-\epsilon)$. J_s are s-th order Bessel functions of the first kind and $\mathrm{T}_s(x)$ are the Chebyshev polynomials which obey the recursion relation, $T_s(x) = 2xT_{s-1}(x) - T_{s-2}(x)$. ϵ is introduced in order to make sure that the absolute value of the extreme eigenvalues of $\tilde{H}$ is less than 1. This is crucial for the Chebyshev method because the arguments of Chebyshev polynomials accept only values in the interval $[-1, 1]$. We truncate the series in Eq. (6.13) such that the propagated wave function becomes normalized up to machine accuracy in order to reduce error accumulation during the stepwise propagations. Moreover this also ensures that the propagation operator is unitary up to machine accuracy. Having the wave function at each time-step, then the coefficients from Eq. (6.1), $c_n(t) = \langle n_\phi(t)|\psi(t)\rangle$, could be calculated for analysis purposes only whenever it is necessarily or possible to do so. In order to have some insight about the nature of the wave-function, $|\psi(t)\rangle$, we further calculate the structure factors that are defined as,

$$C_X(q) = \frac{2}{L^2}\sum_{i=1}^{L}\sum_{j=1}^{L/2} e^{iqr_{i,i+j}}\bar{X}_{i,i+j}, \tag{6.14}$$

where $\bar{X}_{s,k} = \langle \hat{X}_s\hat{X}_k\rangle - \langle \hat{X}_s\rangle\langle \hat{X}_k\rangle$, s and k are the site indices (summation over $L/2$ for j is introduce because $\bar{X}_{s,k}$ is symmetric around $\bar{X}_{s,s+L/2}$ due to the periodic boundary condition we considered)and $r_{s,k}$ is the distance between site s and site k. We report spin density wave (SDW) order parameter $O_{SDW} = C_{\hat{S}}(\pi)$ with $\hat{S}_s = 1/2(\hat{n}_{s\sigma} - \hat{n}_{s\bar{\sigma}})$ and charge density wave (CDW) as $O_{CDW} = C_{\hat{n}}(\pi)$, where $\hat{n}_s = \hat{n}_{s\sigma} + \hat{n}_{s\bar{\sigma}}$ is the local density operator. We also report the value of the current as function of time, which is defined as the expectation value of the current operator, $\hat{J} = \frac{i}{L}\sum_{\langle sk\rangle\sigma}[h_{sk}(t)\hat{c}^\dagger_{s\sigma}\hat{c}_{k\sigma} - h.c.]$.

6.3 Results

In the following we set $h(0) = h_0 = 1$ and all the coupling constants are scaled with h_0. Moreover we define the uniform electric field, $\tilde{F}$, as $\phi(t) = -\tilde{F}t$. For the sake of simplicity we define $F = \tilde{F}/2\pi$. We consider the time steps to be $\delta t = 0.005$. We have tested all the results against a finer time grid in order to ensure that there is no quantitative difference over the parameter range considered here.

We start by showing in Fig. 6.1 the fidelity susceptibility, $\chi_\Xi(\phi)$, at $\phi = 0.1\pi$ for a system consisting of 10 sites at half-filling for different values of U and as a function of V, we use $\delta\phi = 10^{-3}$ for the calculations presented in Fig. 6.1. As is clear from the inset of Fig. 6.1, $\chi_\Xi(\phi)$ acquires the largest value at $\phi_{anti} = 0.1\pi$, which is an anti-crossing point between the ground-state and an excited state. Notice that here we calculate $\chi_\Xi(\phi)$ numerically exact with the use of the Lanczos method and do not use the perturbative form introduced in Eq. (6.11).

Notice that the susceptibility is largest, almost diverging, at specific values of V for each U, whenever the relation $U \simeq 2V$ is satisfied. This relation represents the boundary which separates the SDW and CDW phases [175], and was obtained within the DMRG approach for 1D chains of larger dimensions. However, it is obvious that $\chi_\Xi(\phi_{anti})$ can provide a good estimate on the location of the SDW-CDW phase boundary, although it

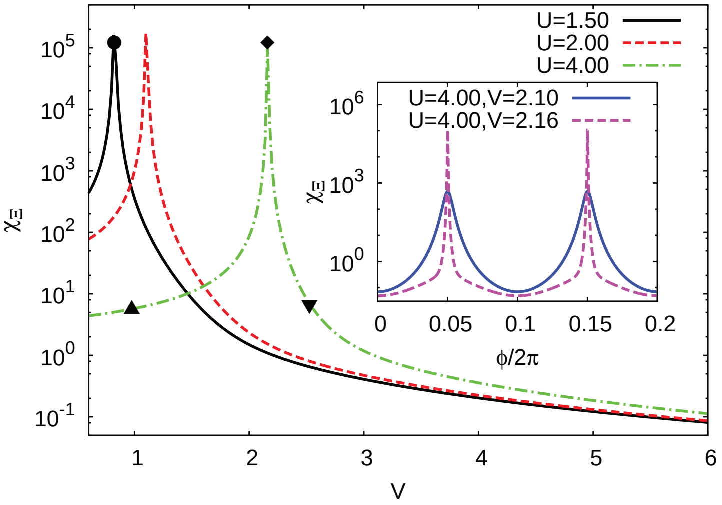

Figure 6.1: Fidelity susceptibility for a ring with $L_{sites} = 10$ and $N_\uparrow = N_\downarrow = 5$ at $\phi = 0.1\pi$ as function of interactions. The inset shows the fidelity susceptibility as function of $\phi/2\pi$ for different sets of parameters. The points represent specifically chosen pairs of parameters U, V in order to model a weakly interacting metal (circle), a SDW insulator (triangle), a CDW insulator (upside down triangle) and a strongly interacting metal (diamond).

does not provide any information about the details of the wave-function (whether it describes SDW or CDW).

In order to compare the non-linear response of different kinds of interacting systems we analyze different sets of interaction and hopping parameters. In particular we study three different cases: first we consider a system with $U = 1.5$ and $V = 0.82$, marked with a circle in Fig. 6.1, which shows an almost diverging $\chi_\Xi(\phi_{anti})$ and has a vanishingly small charge gap, $\Delta_{charge}(\phi_{anti}) \simeq 10^{-3}$, and therefore could be considered as a *weakly interacting metal*. Secondly, we use a dimerization parameter $\eta = 0.4$, which opens up a gap ($\Delta_{charge}(\phi_{anti}) = 1.74$) and the system behaves as a *correlated band insulator* (BI). Finally, we choose a stronger interacting system with $U = 4.0$ and three different values of V =0.94, 2.56 and 2.16. Two values, $V = 0.94$ (a *SDW insulator*, marked with a triangle in Fig. 6.1, $\Delta_{charge}(\phi_{anti}) = 1.44$) and $V = 2.56$ (a *CDW insulator*, marked with an upside down triangle in Fig. 6.1, $\Delta_{charge}(\phi_{anti}) = 1.36$) are chosen such that $\chi_\Xi(\phi_{anti})$ is the same. We also consider $V = 2.16$ on the phase boundary between SDW and CDW with an almost diverging $\chi_\Xi(\phi_{anti})$ (marked with a diamond in Fig. 6.1). The latter case also has a vanishingly small charge gap but it should be considered as a *strongly interacting metal*.

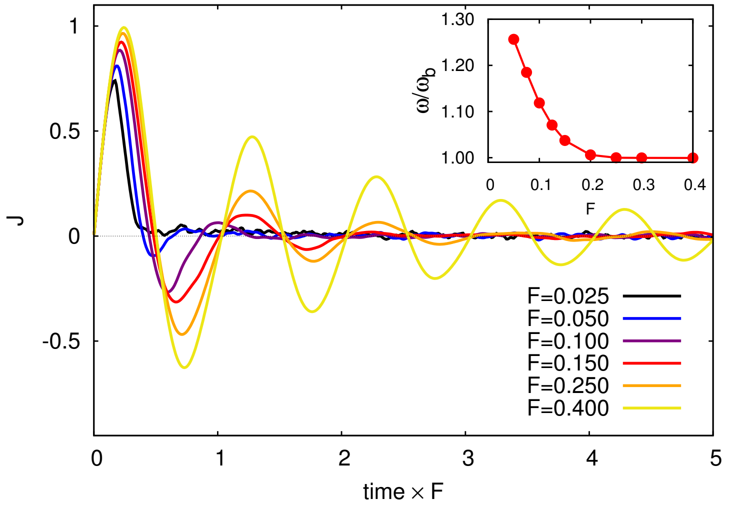

Figure 6.2: Current as function of time for a ring with $U = 1.5$, $V = 0.82$, $L_{sites} = 10$, $N_{\uparrow} = N_{\downarrow} = 5$ and for different electric field strengths. Inset: the frequency of the BO for different electric fields and the same parameters of the main graph with $\omega_b = F$.

6.3.1 Weakly interacting system

In Fig. 6.2 we show the current as function of time for a system with $U = 1.5$ and $V = 0.82$ for different electric field strengths. For illustrative purposes we start the analysis of the graph from the largest field, $F = 0.4$, where it shows a regular damped BO in the time domain of interest. As we stated previously, $\chi_{\Xi}(\phi_{anti})$ is largest at the anti-crossings, thus the probability transfer from the ground-state to excited states (also in analogy with LZ theory) is enhanced. Therefore at each anti-crossing there is a high probability of transfer from a right going wave ($-\partial E_n(\phi)/\partial\phi > 0$) to another right going wave. When the field is strong enough this transfer is very efficient such that the wave-function has a significant overlap with *only one* of the eigenstates of the instantaneous Hamiltonian. Finally when the maximum energy is reached, the wave-function will start having significant overlap with left-going states and the current will change sign. This reflection for the high field case happens exactly at $t = (2F)^{-1}$.

To better understand the above description of the large field response, we plot in Fig. 6.3(a) the eigenstates of the instantaneous Hamiltonian as a function of time for a smaller system, with $L = 6$ at half-filling, for $F = 0.4$ and the same interaction parameters. Both the size of the points and their color code represent the magnitude of the overlap of the time-dependent wave-function with the instantaneous eigenstates of $\hat{H}(t)$. Note that the spectrum is periodic with $2\pi/L$, thus the first anti-crossing happens at $tF = 0.5/L = 0.833$. This smaller ring shows very similar behavior to the one presented in Fig. 6.2 when subjected to a strong field, except that the magnitude of the current is smaller. The formation of a coherent path for the probability transfer throughout the spectrum and the reflection at the topmost state when $t = (2F)^{-1}$ can be clearly seen. However, a dissipative loss of the probability to both left-going and right-going waves is possible and the current becomes damped as function of time. For higher fields the probability transfer is more efficient, which means that the damping of BO is suppressed.

Weak fields. Looking back to Fig. 6.2, the weakest field response, for $F = 0.025$, is comprised of two non-linear effects. First, the state with high probability is reflected sooner, well before it arrives at the other edge of the spectrum. This could be inferred from the fact that the current changes sign sooner than in the high field case. Second, when the field is weak the probability transfer to excited states is smaller, which means that at each higher energy anti-crossing there is a finite probability of remaining in the state with lower energy, which will contribute with a negative sign to the total current. Therefore after an initial increase in current, the wave-function will overlap with equally right-going and left-going instantaneous states and one ends up with a quasi-stationary regime in which the current is very small and fluctuates around zero.

We further elucidate this behavior by expressing the current as function of instantaneous eigenstates of $\hat{H}(t)$,

$$\langle \hat{J} \rangle = \sum_{n} c_n(t)^2 \langle n|\hat{J}|n\rangle + \sum_{n\neq m} c_n(t) c_m(t) e^{i(\gamma_n - \gamma_m)} \langle m|\hat{J}|n\rangle \tag{6.15}$$

where $c_n(t) = |\langle n_\phi(t)|\psi(t)\rangle|$ describes the magnitude of the overlaps of the time-dependent wave-function with the instantaneous eigenstates and $\gamma_n = arg(\langle n_\phi(t)|\psi(t)\rangle)$ describe the phases acquired by the wave-function. We plot in Fig. 6.4(a), for $F = 0.025$ and $L = 8$, $c_n(t)$ as function of the current for each eigenstate at time $tF = 2.51$. Observe that the probability amplitudes as function of current are approximately symmetrically distributed between left-going and right-going states, this in turn implies that the first term of Eq. (6.15), i.e. the diagonal expectation value of the current, becomes approximately equal to 0. Moreover, the phases, γ_n, which are presented in Fig. 6.4(b) are distributed uniformly between 0 and 2π therefore leading to the dephasing of non-diagonal terms in Eq. (6.15), and finally the total current is approximately equal to zero.

One should notice that for the case with $L = 8$ the current is not completely equal to zero, but it acquires a small but finite value that fluctuates around zero, indicating the fact that the number of eigenstates that contribute is small due to finite size effects. These fluctuations are suppressed for larger systems as we show in the following sections.

Intermediate fields. We next analyze the response to intermediate fields between the full dissipative case for $F = 0.025$ and the full oscillating one for $F = 0.4$. When

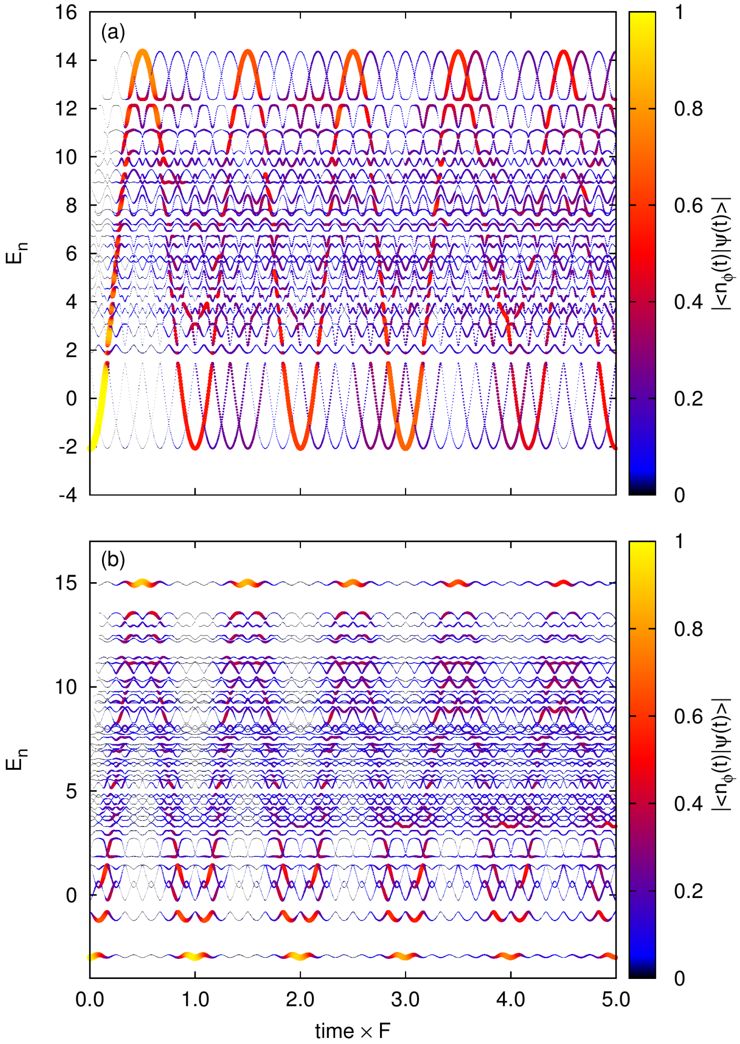

Figure 6.3: (a) Eigenvalues of the instantaneous Hamiltonian as function of time for a system with L=6 at half filling, U=1.5,V=0.82, F=0.4. The colors and the size of the points are given by the overlap of the time-dependent wave-function with the instantaneous eigenstates, $|\langle n_\phi(t)|\psi(t)\rangle|$; (b) The same as (a) but with a dimerization parameter $\eta = 0.4$ and F=4.0.

the electric field strength is increased the reflection of the high probability state gradually approaches the largest eigenstate of the spectrum. This could be clearly recognized in Fig. 6.2 where the time, tF, for which the current changes its sign approaches 0.5. At the same time the BO period, which is generally less than F^{-1}, gradually approaches F^{-1}.

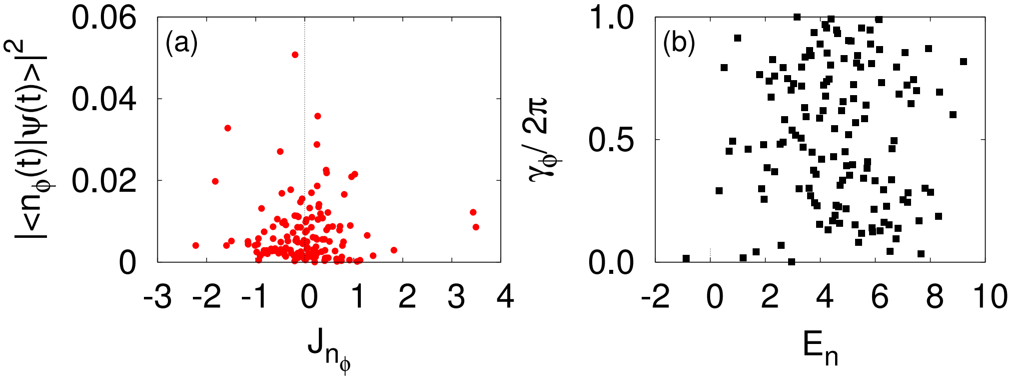

Figure 6.4: (a) $|\langle n_\phi(t)|\psi(t)\rangle|$ for $L_{sites} = 8$ and $N_\uparrow = N_\downarrow = 4, U = 1.5, V = 0.82$ and F=0.025 at $tF = 2.51$, $|n_\phi(t)\rangle$ are the eigenstates of instantaneous Hamiltonian; (b) $\gamma_n = arg(\langle n_\phi(t)|\psi(t)\rangle)$ for the same parameters.

This is shown in the inset of Fig. 6.2 where we plot the frequency of BO as function of field strength. A similar behavior was also reported in metallic spin-less systems subjected to an uniform electric field [166]. Our investigation should also be relevant to that case.

Here, we mention that similar to the electric breakdown case, where a mapping to a quantum random walk [176] on a semi-infinite chain was proposed, here the problem of BO damping also could be mapped to a quantum random walk but on a chain with two edge states. However, as we will present in the following, the actual long time response to an electric field depends strongly on the probability transfer between subsequent states throughout the whole spectrum. It is therefore necessary to design a random walk for which the probability transfer is also randomized but taken from specific distributions, which could be chosen based on the level statistics of the Hamiltonian [177].

Dimerization. In Fig. 6.5, we show the current as function of time for a system with the same interactions as in the metallic case but with a dimerization parameter $\eta = 0.4$. We call this state a correlated band insulator (BI). The general arguments presented for the metallic case hold here, however there are also differences, which we explain in the following. As expected, dimerization induces the opening of a charge gap ($\Delta_{charge}(\phi_{anti}) = 1.74$) and the electric field breakdown is postponed to larger fields. Additionally, a dissipative regime appears only at $F = 0.2$. At this field strength the breakdown has already happened and the instantaneous ground state has a very small contribution to $|\psi(t)\rangle$. For larger fields, i.e. $F = 0.4$, first the current starts to show irregular oscillations, then at $F = 0.6$ the current becomes oscillatory but with a frequency of the BO larger than F. Finally, at even larger fields, $F = 4.0$, the current is oscillatory with $\omega = F$. This is

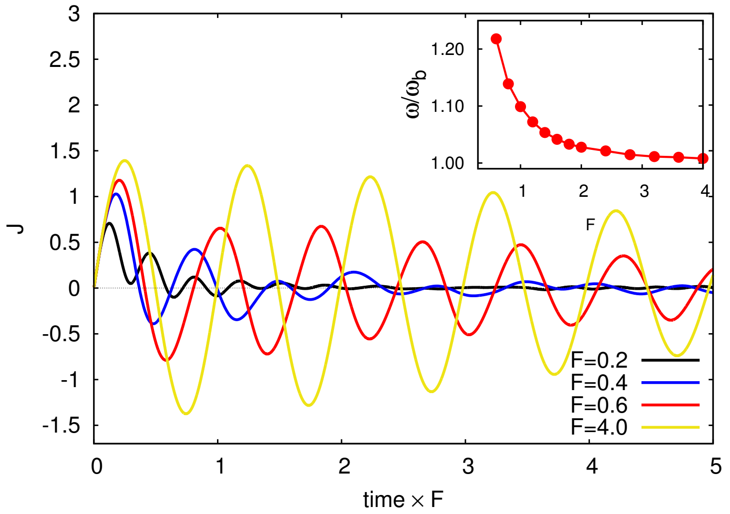

Figure 6.5: Current as function of time for a dimerized ring with $L_{sites} = 10$ and $N_\uparrow = N_\downarrow = 5, U = 1.5, V = 0.82, \eta = 0.4$ (see the definition of the hopping parameter following Eq. 6.1) and for different electric field strengths. The inset shows the frequency of the Bloch oscillations for different electric fields and the same parameters of the main graph with $\omega_b = F$.

achieved for much larger fields than the ones presented for the weakly interacting metal, as shown in the inset of Fig. 6.5. The first notable difference between the metal and the correlated BI is that here BOs with smaller frequencies survive for longer times. This is different from the metallic case where BOs with smaller frequencies are strongly damped. Furthermore, one may expect that the dimerization may only postpone the breakdown and the transition to the oscillatory behavior should not be affected as long as the dimerization only affects the low energy part of the spectrum by opening up a ground-state charge gap. However, the presence of long lasting BO with the period less than F^{-1} implies the presence of states with small χ_Ξ in the middle of the spectrum and which reflects a high probability state back.

Roughly speaking, these states could be at the edge of a cluster of eigenstates, and are separated by a large gap from the next subsequent state and therefore play the rule of an edge state. However, we emphasize that not only the gap but also the actual value of χ_Ξ of each eigenstate are important factor that affect the non-adiabatic behavior of the system. In order to visualize again the overlap of the time-dependent wave-function with the whole spectrum, we turn back to Fig. 6.3(b), where the overlap with the instantaneous eigenstates of $\hat{H}(t)$ is plotted as function of time for a smaller dimerized system with

$L = 6$, $\eta = 0.4$ and $F = 4.0$. Again the smaller ring behaves the same as a larger system with $L = 10$ when subjected to strong fields. As is clear from the plot the recurrences of the ground-state and the state with largest energy occur periodically at F^{-1}. A noticeable feature of the propagation in the dimerized systems is the fact that the overlap of $|\psi(t)\rangle$ with the instantaneous eigenstates is very nonlocal in the energy domain, meaning that the path of high probability transition is broadened in comparison to the metallic system. Noticeably, the wave-function starts to have finite overlap around the first anti-crossing not only to the first excited state but also with the second excited state. Therefore, a two level approximation (LZ-like) is not appropriate for the ground-state breakdown.

The dimerization leads to a stronger insulator not only in the sense that it postpones the electric field breakdown, but it also largely affects the overlap with states located in the middle of the spectrum. In short, while the breakdown and the appearance of the dissipative behavior mostly depends on the low energy part of the spectrum, the transition from the dissipative to the oscillatory behavior largely depends on the clustering of eigenstates in the middle of the spectrum.

6.3.2 Strongly interacting system

For the cases with strong interactions, as stated before, we choose $U = 4.0$ and three different nearest neighbor interactions, $V = 0.94$ (SDW insulator), $V = 2.56$ (CDW insulator) and $V = 2.16$ (metallic case). For the insulating cases we choose the interaction parameters such that both cases acquire the same ground state $\chi_{\Xi}(\phi_{anti})$ as seen in Fig. 6.2.

We plot, in Fig. 6.6(a), the current as function of time for a very small electric field, i.e. $F = 0.002$, for a ring of size $L = 10$. Both insulating systems appear to be in the adiabatic regime, where the current shows an oscillatory behavior with a period equal to F/L. However, the metallic case shows oscillations with a doubled period, $2F/L$. The main reason for this comes from the fact that for the metallic case the probability is transfered completely to the first excited state due to very large $\chi_{\Xi}(\phi_{anti})$, i.e. it cannot be considered in the adiabatic regime even at these small fields. This is illustrated in Fig. 6.6(b), where the energies of the first three states of the $\hat{H}(t)$ are shown as function of time (and implicitly as a function of flux), together with the overlap of $|\psi(t)\rangle$ to these three states. As is obvious, because of the very large χ_{Ξ}, there is a very large overlap to the first excited state after the first anti-crossing, however the field is very small such that it cannot overcome the gap between the first excited and second excited state. $|\psi(t)\rangle$ only has an extremely small overlap with second excited state, which leads to the fact that the probability is reflected back to the ground state and one ends up with current oscillations with a period twice of the adiabatic expectation. The breakdown field is now achieved when the gap between the first and second excited states is overcome.

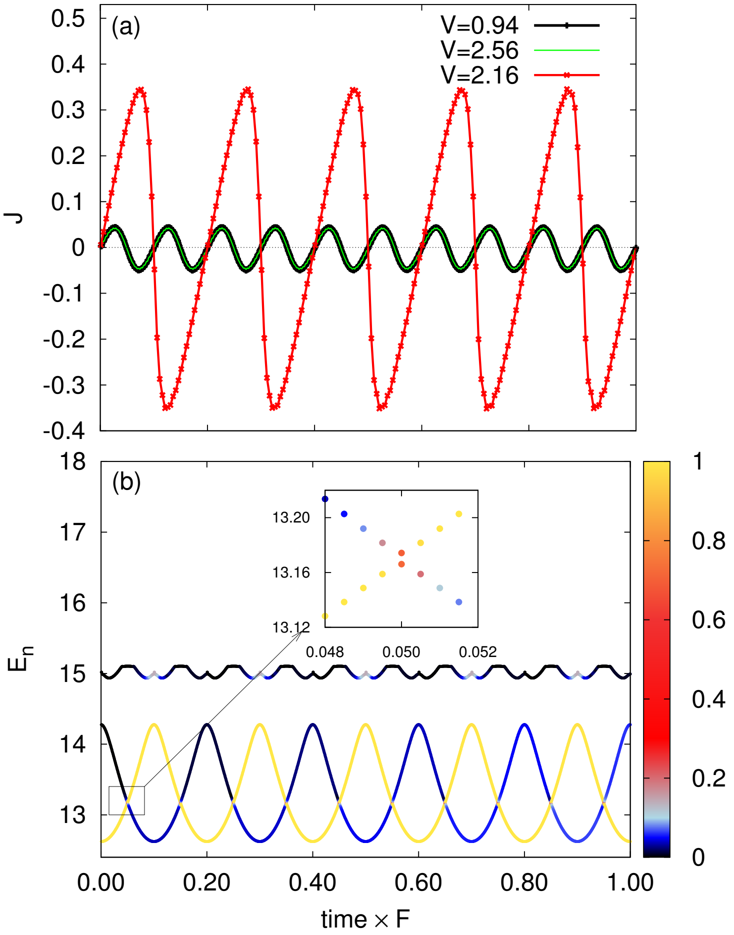

Figure 6.6: (a) Current as function of time for very small field $F = 0.002$ for different interactions; (b) The energy dispersion of the first three exited states of instantaneous Hamiltonian together with the overlap of these states with $|\psi(t)\rangle$ the as function of time for U=4.0,V=2.16. The inset of panel (b) shows a zoom-in into the into anti-crossing region. Colors represent the overlap of the time-dependent wave-function with the instantaneous eigenstates.

We next describe the response of strongly interacting systems to larger fields. In Fig. 6.7 we present the current as function of time for different field strengths and for the three interaction choices introduced previously. For $F = 0.1$ all the cases shows a dissipative behavior, however the insulating ones show small peaks in the current before it arrives at the quasi-stationary zero-current state. The period of these peaks is approximately equal

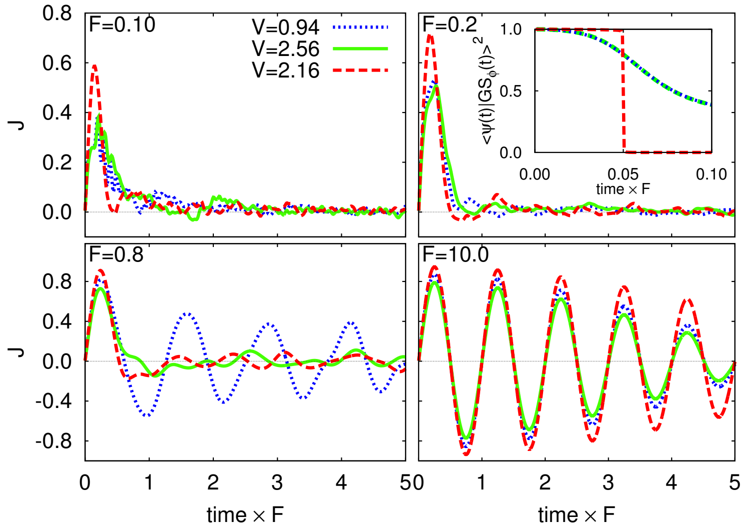

Figure 6.7: Current as function of time for different interactions and different field strength. The inset shows the square of the overlap of $|\psi(t)\rangle$ with the instantaneous ground state of $H(t)$ for different interactions and $F = 2.0$.

to F/L, which therefore implies that the overlap of $|\psi(t)\rangle$ with the instantaneous ground state does not vanish quickly and manifest itself as small peaks in the current. This is not the case for $V = 2.16$ where the overlap with the ground state is lost immediately at the anti-crossing (see the inset of Fig. 6.7 for $F = 0.2$) and the current behaves smoothly from the beginning of the evolution. For stronger fields, $F = 0.2$, the change of the current is large, such that the current fluctuations due to the finite overlap with the ground-state disappear.

In the inset of Fig. 6.7 we show the square of the overlap of $|\psi(t)\rangle$ with the ground-state of the instantaneous Hamiltonian. It is clear that for the two insulating cases for which we set $\chi_{\Xi}(\phi_{anti})$ to be equal, the decay of the ground-state is identical. Furthermore, in the dissipative cases for $F = 0.1$ and $F = 0.2$ both insulating cases behave almost in the same way even for larger times even though the interaction strengths are very different and one describes an SDW insulator while the other one an CDW insulator with different excitation. This means that by setting $\chi_{\Xi}(\phi_{anti})$ the same, not only the ground-state decay is identical but also the tunneling to the lower part of the spectrum behaves very similarly. When the field is increased to $F = 0.8$, the SDW insulator with $V = 0.94$ starts to show Bloch-like oscillations with large amplitude. On the other hand the metallic and CDW cases are still in the dissipative regime with a vanishingly small long-time current. For even larger fields, $F \simeq 1.6$ (not shown here), all three cases show oscillations with large

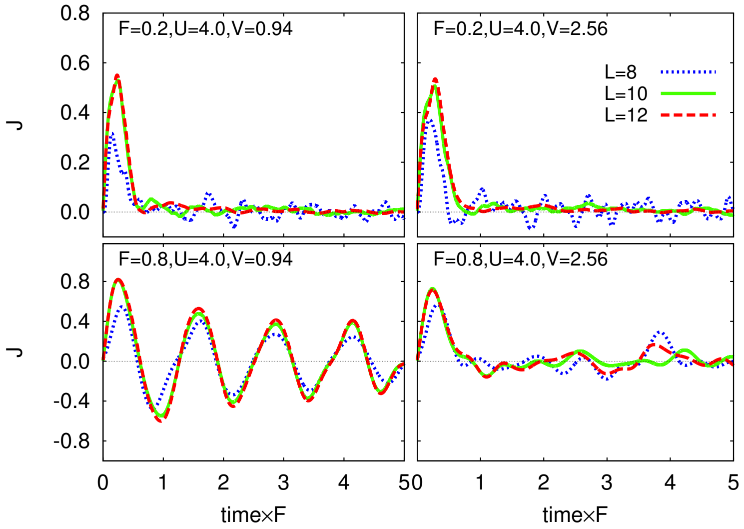

Figure 6.8: Current as function of time for different interactions and different field strengths and different sizes.

amplitude but which are irregular. It is only when the strength of the electric field is very large, $F = 10.0$, that all the cases show regular BO as shown in Fig. 6.7.

Finite size effect. To see the effect of the size of the system on the transition from a dissipative to an oscillatory pattern, we plot in Fig. 6.8 the current as function of time for different sizes for $V = 0.94$ (SDW insulator) and $V = 2.56$ (CDW insulator). We observe that for all cases the fluctuations of the current in the dissipative regime ($F = 0.2$) are suppressed for larger sizes. This is due to the fact that $|\psi(t)\rangle$ acquires overlap with a much larger number of states when the size is increased. This implies that a more efficient dephasing of the current is achieved (see the discussion following Eq. 6.15). However, in the strong-field regime, once the transition to oscillatory behavior occurs, the size effect is negligible, showing that the sizes of the gaps in the middle of the spectrum do not depend strongly on the size, at least not for the strong interactions considered here.

Order parameters. In Fig. 6.9, we show the SDW and CDW order parameters as function of time for the two insulating cases. As is clear from Fig. 6.9(b) for the SDW ordered system, O$_{SDW}$ only drops gradually as function of time, however at the same time O$_{CDW}$ is enhanced at the beginning of the evolution (see Fig. 6.9(a)). This further implies the presence of a CDW state near the bottom of the spectrum [178]. Finally at longer times both order parameters dissipates during the evolution arriving at a quasi-stationary state with almost vanishing value for larger times. The CDW ordered system shows a similar behavior but with reversed O_{CDW} and O_{SDW} contributions (see Fig. 6.9(a) and (b)).

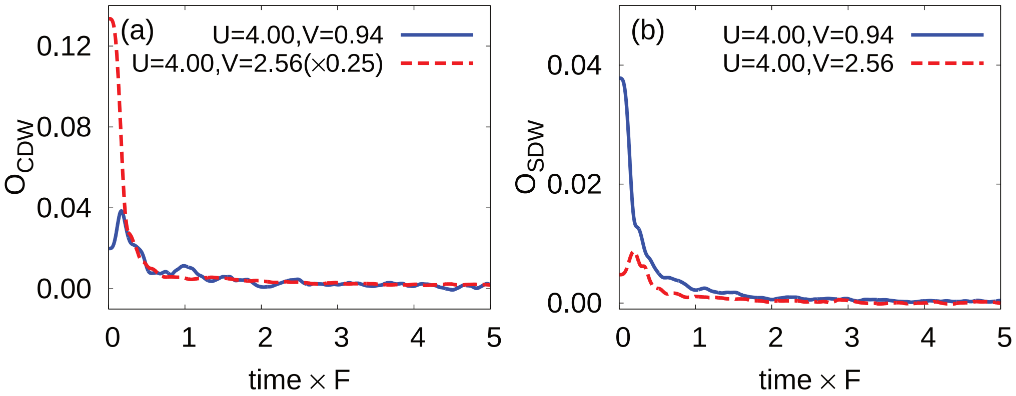

Figure 6.9: (a) CDW order parameter as function of time for a system with L=12 at half filling derived with $F = 0.2$; (b) SDW order parameter as function of time and the same parameters as in plot(a).

Therefore , the transient regime shows that since the two order parameters are in competition, the mechanism of destroying the dominant order is the proliferation of the competing one.

6.4 Conclusions

In conclusion we investigated the nonlinear response of a closed interacting fermionic system as modeled by an extended Hubbard model. Weakly interacting metallic system at the boundary of SDW-CDW, shows a dissipative behavior for low fields. The main reason for this is the fact that $|\psi(t)\rangle$ acquires overlap with large number of left going and right going states. This in turn implies that the quasi-stationary state acquires zero current. Bloch oscillations start smoothly with a frequency larger than F. The main reason for this is the fact that the reflection happens at the lower part of the spectrum, thus effectively decreasing the bandwidth. Upon increasing the field strength the probability transfer at each anti-crossing is more efficient. This leads to a more regular recurrences of the ground state and the topmost excited state with period of F^{-1}, which can be seen from the oscillations in the current.

Upon dimerization of the metallic system, the formation of the dissipative regime is postponed to larger fields due to the formation of a charge gap. However, the main difference between the dimer case and the metallic system resides in the fact that, first, it shows irregular current oscillations before they turn into regular BO and second, the BO with larger frequencies survive for large times, in analogy with the metallic case subjected to strong field. This implies the existence of states at the middle of the spectrum with low $\chi_{\Xi}(\phi)$ (or roughly speaking the formation of large mid gaps in the relevant excitations) that play the role of a band-edge state and reflect back the overlap probability at the middle part of the spectrum even for large electric fields. Finally, the dimerized system also shows regular BO with period equal to F^{-1} for large enough electric fields. The value for which the dimerized system shows regular BO are much larger than those found for the metallic system even though the interactions are identical.

For stronger interacting systems when the interactions are chosen such that the ground-state $\chi_{\Xi}(\phi_{anti})$ is the same for both cases, then the ground state decay for both CDW insulator and SDW insulator behaves exactly the same. This similarity of the ground-state decay manifests itself even for larger times and for both low and high field dissipative regimes. However significant differences arise between the two cases for large electric fields. While SDW shows oscillatory behavior with large magnitude the CDW insulator and strong interacting metallic system only shows irregularities with small oscillations. Different from the weakly interacting metallic system and the dimer case, in the strongly interacting regime these irregularities are extended to intermediate fields and only for very large fields, $F = 10.0$, regular BO with a period of F^{-1} are observed. This effect appears to be little affected by size, since the SDW and CDW insulators, for L=10 and L=12, show the same qualitatively and even quantitatively behavior. This implies that the reorganization of the spectrum is affected much more by the interaction than by the finite size induced discreteness.

Chapter 7

Structural transitions in monolayer MoS_2 by lithium adsorption

Based on first-principles calculations, we study the relative structural stability of the T and H phase of monolayer MoS_2 upon Li doping. Our calculations show that the H structure of MoS_2 is stable for single-side adsorption for arbitrary concentrations of lithium atoms. However, it is possible to energetically stabilize the T phase of MoS_2 against H if Li atoms are adsorbed on both sides of the MoS_2 layer. However, the resulting T structure is dynamically unstable against distortions towards in-plane clustering of the molybdenum atoms. Two processes are examined that allow for two-sided adsorption of Li atoms on MoS_2 supported by a substrate. First, the penetration of Li atoms through the MoS_2 layer is investigated. Our calculations show that the amount of energy needed to pass through a pure MoS_2 layer is of the order of $\sim$ 2 eV, which is too large to make penetration possible. However, when the MoS_2 layer is covered with Li atoms the amount of energy that Li atoms should gain to pass the layer is drastically reduced by at least two order of magnitude and penetration becomes feasible. Another way to achieve two-side adsorption which we investigate is the migration of Li atoms from the edge of the sample.

7.1 Introduction

In recent years transition metal dichalcogenides (TMDs), such as MoS_2, have gained renewed interest due to their layered structures. The weak van der Waals interaction between these layers make it possible to exfoliate monolayers [179] from the bulk. These

---

The results of this chapter submited to Journal of Physical Chemistry.

monolayers consist of an hexagonally-packed sheet of metal ions sandwiched between two hexagonal layers of chalcogen atoms. Consequently, the monolayers come in two varieties, called T and H, in which the metals have octahedral or trigonal prismatic coordination, respectively (see Fig. 7.1). Due to their two-dimensional (2D) nature, TMDs exhibit a broad range of properties which make them attractive for potential applications in nanoelectronics. A notable example is the potential use of MoS_2 monolayers to overcome the scaling problem of the current semiconductor electronic FET which is attracting an increasing amount of interest from the scientific community [40, 180–183]. Other applications for MoS_2 are in lithium-ion batteries, since it was recently shown that MoS_2 mono- and multilayers exhibit a large lithium storage capacity [184–187], or as ultrasensitive photodetectors [188].

A large amount of theoretical work on MoS_2 has arisen in the last couple of years. A tight-binding model has been developed for monolayer and multilayered structures [189], and numerous $ab\ initio$ calculations have appeared. These studies mainly correspond to properties of semiconducting H (see Fig. 7.1) phase of MoS_2 and metallic T structure has been less noticed. An example of the former is the theoretical investigation of the magnetic properties of H-MoS_2 in the presence of non-metallic adatoms [190], where authors studied the geometric and magnetic properties of only H phase of MoS_2, when non-metallic adatoms H, B, C, N, O, and F are adsorbed on monolayers H-MoS_2, spatially extended magnetic ordering was reported, in comparison to their work we consider geometrical aspects of both T and H phase under influence of metallic Li adatoms. Another example is the incorporation of Li atoms at MoS_2/graphene interfaces [191], where authors studied adsorption properties of Li-adatoms at the interface of MoS_2/graphene for H phase. They further studied the penetration of Li adatoms from Mo site to V site (see Fig. 7.6) for H phase at the interface, in contrast, here we consider the diffusion of Li atoms through the monolayer MoS_2 in different conditions.

For pure MoS_2 the semiconducting H structure was found to be more stable than the metallic T structure, both in bulk and monolayer form [192]. However, experimental and theoretical research on the structural stability of different MoS_2 bulk allotropes shows that the intercalation of Li atoms can stabilize the metallic 1T structure [193–195], in contrast, here we study possible stabilization of 1T for monolayers. Stable 1T structures can also be realized by substitutional doping of MoS_2 with Re atoms [196]. The main reason for this appears to be the charge doping caused by the Re donor atoms, differ from this work we consider stabilization of 1T MoS_2 monolayer by including Li adatoms.

In this chapter, we investigate the possibility of obtaining a H→T transition in monolayer MoS_2 through Li adsorption using *ab initio* calculations. We systematically investigate the effect of the concentration of Li atoms on the structural properties of monolayer MoS_2. We also examine the possibility of a two-sided adsorption process in which Li

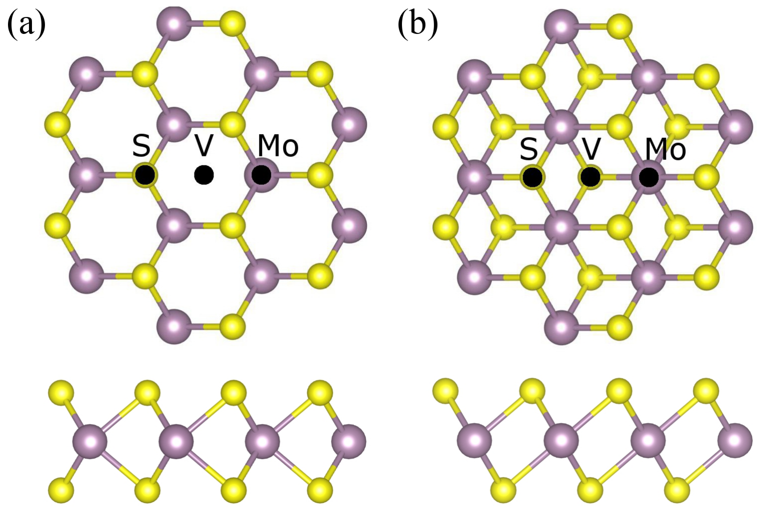

Figure 7.1: Top and side views of the H (a) and T (b) structures of MoS_2. The Li adsorption sites are marked with black dots.

atoms penetrate through the MoS_2 layer or diffuse from the edge of the sample to arrive at the adsorption sites of the other side. Our work is organized as follows. First we give the computational details of our first-principles calculations. Then we examine the most stable configurations of isolated Li atoms on MoS_2 for the two different phases, H and T. Next we investigate how the concentration of Li atoms on one side of the MoS_2 layer changes the relative stability of the H and T crystal structure. We also perform *ab initio* molecular dynamics calculations to support our findings. These calculations are followed by an examination of two-sided adsorption. Two ways to achieve this two-sided adsorption are investigated: (i) by the diffusion of Li atoms through the MoS_2 layer and (ii) by diffusion along the other side of the sample. Finally we examine the actual transition from the H structure to the T structure and calculate the energy barrier for this process.

7.2 Computational details

Our first-principles calculations are based on DFT as implemented in the Vienna *ab initio* simulation program (VASP) [197]. The exchange-correlation energy is described by the Perdew-Burke-Ernzerhof (PBE) [72] functional and the single-particle Kohn-Sham equations are solved by using the projector-augmented wave (PAW) method [198, 199]. An energy cutoff of 400 eV is used for the plane-wave basis and a 12×12 Monkhorst-Pack

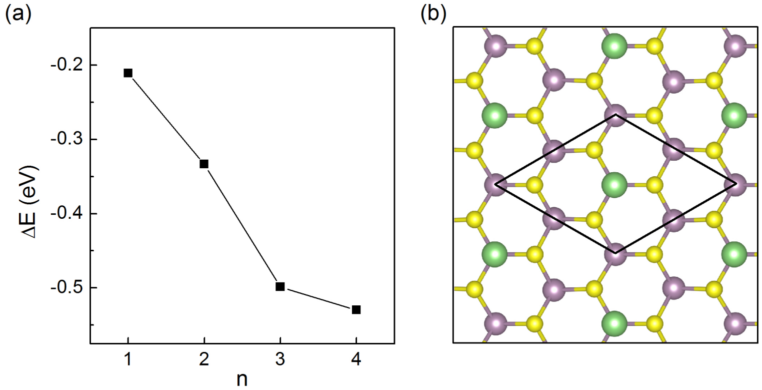

Figure 7.2: Li adsorption for different concentrations. (a) The energy difference between the H and T structure for one Li atoms per $n \times n$ MoS_2 supercell. (b) A 2×2 MoS_2 supercell with one Li atom adsorbed at the Mo site.

k-point grid is used for Brillouin zone integrations. All the structures are relaxed with residue forces of less than 0.01 eV/Å. Due to periodic boundary conditions, artificial interactions between neighboring layers are present in the calculations. These are reduced by a vacuum layer of 30 Å and dipole corrections. We also perform *ab initio* molecular-dynamics simulations. The basis cutoff energy is lowered to 300 eV in that case to increase the speed of the simulations and the supercell size is taken constant. The Verlet algorithm is used to integrate Newton's equations of motion and we make use of a microcanonical (NVE) ensemble with velocities assigned according to the Maxwell-Boltzmann distribution at a temperature of 300 K.

7.3 Results

First we look for the most stable position of an isolated Li atom on top of a MoS_2 monolayer for the two phases, H and T. For this we investigated 3 different adsorption sites (see Fig. 7.1), namely on top of a S atom (*S*), on top of the Mo atom (*Mo*), and above the vacancy in the H phase or the S atom at the other side of the T structure (*V*). Li atoms adsorbed at other positions were found to relax into one of the 3 previous adsorption sites. The binding energies were calculated in a 3×3 supercell and are given in Table 7.1. In this table, we also provide the distance from the Li atom to the Mo layer, d_{Mo}, and the shortest Li-S bond lengths, d_{S}. The most stable adsorption site for the H phase is found to be above the Mo atom, while for the T structure the vacancy site, *V*, is preferred. Additional calculations showed that at higher concentrations (one Li atom per 2×2 supercell), the *Mo* adsorption site is more favorable for both the H and T structures.

Table 7.1: The adsorption energy E_a (in eV), the adsorption distance from the Mo layer, d_{Mo}, and the Li-S bond lengths, d_{S}, for Li adsorption in a 3×3 MoS_2 supercell.

		S	*Mo*	*V*
H	E_a	-1.162	-1.917	-1.755
	d_{Mo}	3.800	3.000	3.065
	d_{S}	2.268	2.361	2.384
T	E_a	-4.801	-4.350	-5.410
	d_{Mo}	3.374	3.051	3.092
	d_{S}	2.376	2.213	2.367

We can now use these most stable configurations to investigate the relative stability of the H and T phase as a function of Li concentration. In order to model different concentrations, we place single Li atoms into various MoS_2 supercells, namely a 4×4, 3×3, 2×2, and 1×1 supercell. In this way, the Li atoms form a triangular monolayer on the MoS_2 with decreasing lattice parameters (see Fig. 7.2(b)). The variation of the energy difference between the H and T structure as a function of the supercell size is shown in Fig. 7.2(a). It is clear that the energy difference between the two structures (divided by the number of unit cells in each supercell) decreases with increasing concentrations. However, we do not observe any H to T transition for adsorbed Li atoms at any concentration. To be sure that our triangular model of Li adatoms is not too restrictive, we also performed unrestricted molecular dynamics simulations in a large rectangular supercell (16×16.5 $\mathring{A}^2$) with initial randomly placed Li atoms (see Fig. 7.3(a)). After a while, the Li atoms relax into a triangular lattice, corresponding to 1 Li atom per Mo atom (see Fig. 7.3(b)). This indicates that adsorbed Li atoms will tend to cluster into triangular monolayers of the same size as the underlying MoS_2 substrate. This structure corresponds to the highest concentration of Li atoms that we investigated before(see Fig.7.2(a)) and was shown to be insufficient to cause a H→T transition. Therefore, more Li atoms are needed to induce this transition. Starting from the highest concentration of a single layer of Li atoms on MoS_2 (i.e. 1 Li atom per MoS_2 unit cell), we can add more Li atoms to the system in order to enhance the stability of the T structure. In Table 7.2, we show the formation energies of different configurations for both phases of the MoS_2 crystal with two adsorbed Li atoms per unit cell. We find that by increasing the concentration of Li atoms at one side of the MoS_2 layer, the H→T transition does not occur. However, our calculations show also that the most stable configuration for both H and T structures are those with one Li atom at each

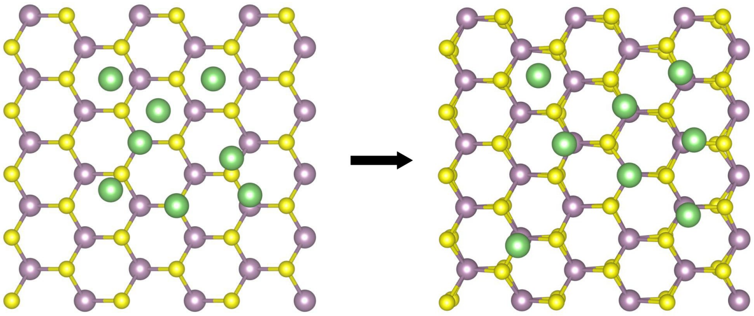

Figure 7.3: Molecular dynamics simulation of Li atoms on MoS_2: the initial (left) and final (right) structure. Note that one Li atoms appears to be caught at a *V* adsorption site.

side of the layer. Moreover, the T structure becomes energetically more stable than the H structure in that case. The difference in energy between the two most stable H and T Li_2MoS_2 structures (No. 5 and 11 in Table 7.2) becomes $E_H - E_T = 437$ meV upon two-sided Li adsorption. The adsorption energy and the Bader [200, 201] charges of the Li atoms for the different configurations are presented in Table 7.2. The adsorption energy is defined as E_a=$E_{\text{tot}} - (E_{\text{MoS}_2} + n.E_{\text{Li}})$, where n is the number of adsorbed Li atoms. For one-sided (OS) adsorption, the Bader charges show that the Li atoms that are closest to the MoS_2 layer are strong electron donors ($\approx$ 0.8e/Li atom) while the other ones are less important (except for configurations 2 and 3 which do not follow this general trend). For two-sided (TS) adsorption, both Li atoms can donate electrons equally so that the total charge transfer to the MoS_2 layer is much larger in that case (about twice as large).

Although two-sided Li adsorption is possible for a free-standing MoS_2 monolayer, it might be difficult to achieve if the MoS_2 is placed on a substrate, as is usually the case in an experimental setup. In the latter case, the Li atoms should be able to penetrate the MoS_2 layer or migrate from the edges of the sample between the substrate and the MoS_2 monolayer. In the present analysis we limit ourselves to perfect MoS_2 layers without defects. We first look at the possibility for Li atoms to pass through the MoS_2 layer. To do this we examine whether the Li atoms can penetrate through the H structure by passing through the center of a Mo-S hexagon (position *V* in Fig. 7.1). In practice, we calculate the binding energy of a single Li atom at a fixed distance from the MoS_2 layer in a 3×3 supercell (the distance is kept constant during relaxation by taking the out-of-plane coordinates of the Li and the 3 closest Mo atoms fixed, while the other coordinates and the supercell size are relaxed). This binding energy is defined in a similar way as the adsorptions energy (see above) and vanishes for infinite separation. The binding energy of the Li atom at various distances from H-MoS_2 are presented in Fig. 7.4 (squares). As can be seen from the the figure, the energy is reduced when the Li atom moves from infinity towards the surface

Table 7.2: The adsorption energy E_a and the Bader charges of Li atoms for different configurations of Li_2MoS_2. Results for both one-sided (OS) and two-sided (TS) adsorption are shown.

No.	struct.	Li pos.	OS/TS	E_a(eV)	charge (|e|)
1	H	(Mo, Mo)	OS	-3.599	(+0.7,-0.1)
2	H	(Mo, S)	OS	-3.701	(-0.1,+0.6)
3	H	(Mo, V)	OS	-3.691	(+0.0,+0.5)
4	H	(Mo, V)	TS	-3.606	(+0.8,+0.8)
5	H	(Mo, Mo)	TS	-3.727	(+0.8,+0.8)
6	T	(Mo, Mo)	OS	-3.409	(+0.7,-0.1)
7	T	(Mo, V)	OS	-3.401	(+0.8,-0.2)
8	T	(Mo, S)	OS	-3.322	(+0.8,-0.1)
9	T	(V, V)	OS	-3.301	(+0.8,-0.2)
10	T	(V, S)	OS	-3.244	(+0.8,-0.2)
11	T	(Mo, Mo)	TS	-4.164	(+0.8,+0.8)
12	T	(Mo, V)	TS	-4.000	(+0.8,+0.8)
13	T	(V, V)	TS	-3.906	(+0.8,+0.8)

of the the MoS_2 layer. A bound state is found at approximately 3 Å from the (middle of the) MoS_2 layer with an energy of 1.735 eV. Further approaching the surface and passing through the layer is difficult due to an energy barrier of 2.509 eV. This barrier is too large to make penetration of Li atoms possible at room temperature or even at larger accessible temperatures. One can imagine that Li atoms that arrive at the MoS_2 surface will first adsorb at a single side with the formation of triangular clusters as describedabove. The presence of this adsorbed layer can have a significant impact on the penetration barrier of other Li atoms. This can be anticipated from the observed charge transfer which causes a lateral expansion of the MoS_2 crystal. Consequently, the holes (the empty space around V positions, see Fig. 7.1(a)) in the crystal become wider and a decrease in the penetration barrier can be expected. To examine this process, we apply the same procedure as described above to calculate the binding energy of a Li atom at fixed distances from a H-MoS_2 monolayer with Li atoms located on top of all Mo atoms. The results are also presented in Fig. 7.4 (circles) and it can be seen that the situation has drastically changed with respect to the pure MoS_2 case. Multiple bound states are found to exist when the Li atom approaches the system and eventually passes through. A first bound state is observed when the approaching Li atom adsorbs on the Li layer. A second one, when the Li atom passes through the Li layer and stabilizes between this Li layer and the upper S atoms of

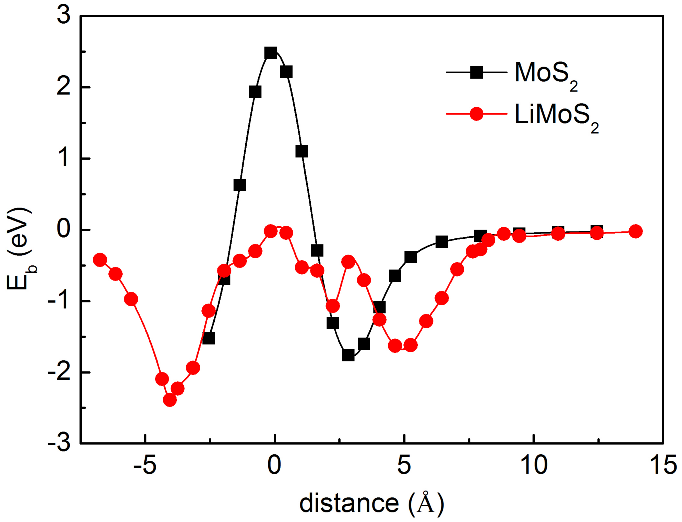

Figure 7.4: The binding energy of a Li atom when it approaches and penetrates a pure and Li-covered MoS_2 layer from infinity (right).

the MoS_2 crystal.

A final stable state is reached when the Li atom passes through the MoS_2 layer and adsorbs at the other side of the crystal. The difference between this case and the pure case is that a much smaller energy gain is needed to pass through the MoS_2 layer. The energy barrier is only $\sim$ 2 meV and allows the Li atoms to penetrate the slab. As stated before, one of the reasons for this is that when the Li atoms are deposited on top of the MoS_2, an increase of the lattice constant of about $\sim$ 1 % is observed. This increase in the lattice constant makes it easier for the Li atoms to pass through the MoS_2 layer. An additional cause for the decrease in barrier size is found in the flexibility of the material after Li adsorption. In Fig. 7.5, we show the energy as a function of strain for pure MoS_2 and MoS_2 with Li atoms adsorbed on one side. The last system appears to be substantially more easy to stretch, especially for the large distortions that are required to get the Li through the layer. Besides diffusion through the MoS_2 layer, Li atoms might also be able to migrate from the edges of the sample and adsorb at the other side of the MoS_2 monolayer. For this to happen, the in-plane migration barriers should be small enough to allow the Li atoms to jump from one unit cell to the other. In Fig. 7.6 the migration barrier is shown along the line from *Mo* to *V*. The height of the barrier is 0.24 eV which is small enough for migration to occur and it is in agreement with previous calculations [202]. Note, however, that this calculation does not take into account the influence of the underlying substrate. This effect is difficult to include because it depends on the actual composition and roughness of the

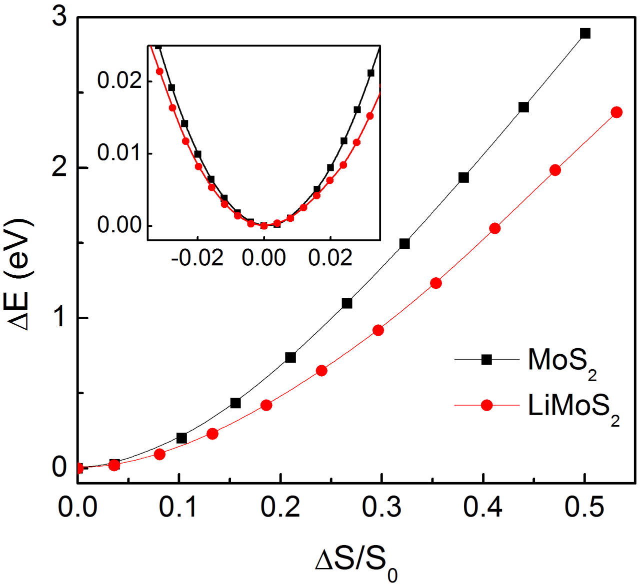

Figure 7.5: Variation of the energy as a function of surface expansion with the equilibrium unit cell surface area and ΔS is the difference of unit cell surface area from S_0. Inset: the same graph but zoomed close to zero strain.

surface of the substrate.

Now that we showed how two-sided adsorption might occur and how this stabilizes the T structure over the H structure, we will investigate the actual structural transition for a Li covered MoS_2 layer in the following. The barrier for the transition is calculated for both pure MoS_2 and Li_2MoS_2 (i.e. MoS_2 with 2 Li atoms per unit cell). The transition can be regarded as a shift of one S layer in the H structure to the position V (see Fig. 7.1(a)). Therefore, we calculate the barrier energy of the $H \rightarrow T$ by fixing the Mo atoms and shearing one S layer from the H structure towards the T structure, while the other atoms and the cell parameters are allowed to relax.

The results of these calculations are shown in Fig. 7.7. The transition barrier is significantly reduced from 1.55 eV for the pure MoS_2 layer to 130 meV for the Li-covered MoS_2 layer. Also note that the T structure becomes significantly more stable after Li adsorption. An interesting process is observed during the transition from the H to T structure Li_2MoS_2. When the S layer of one side is shifted to the V position, the Li atoms at that side tend to follow the S layer for some time and then gradually go back to their initial position. This observation suggests that the Li atoms mediate the transition and reduce the barrier considerably.

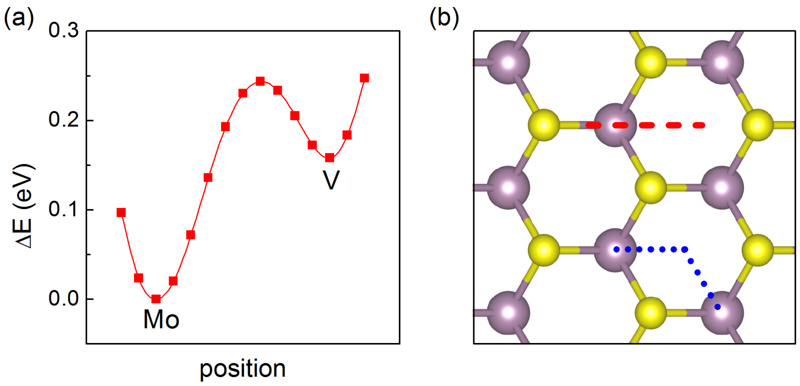

Figure 7.6: Diffusion of Li atom along the MoS$_2$ surface. (a) The diffusion barrier to go from adsorption site *Mo* to *V*. (b) The dashed line shows the line along which the barrier in (a) was calculated while the dotted line shows the preferred diffusion path to go from one unit cell to another.

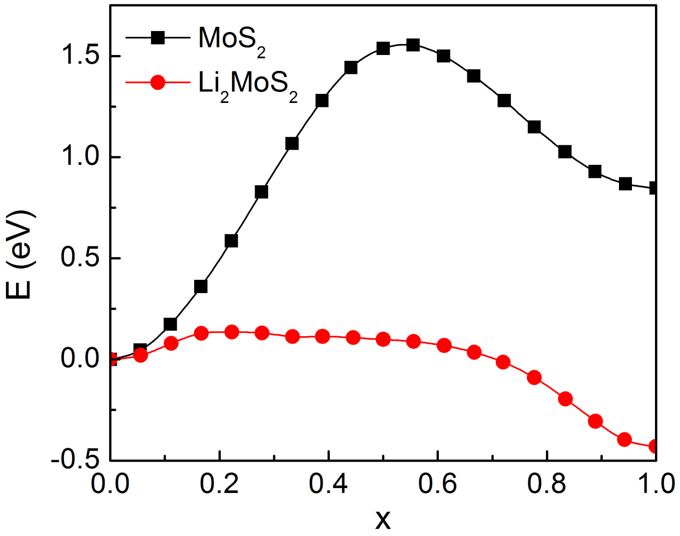

Figure 7.7: Energy of intermediate configurations of the H→T structure as a function of the reaction coordinate for pure and Li-covered MoS$_2$.

Finally, we examine whether the resulting two sided Li adsorbed T structure is dynamically stable. To do this we calculate phonon dispersions based on small displacement method as is implemented in "phon" code [203]. This analysis relies on properties of phonon dispersions which is calculated based on force constant matrix. This force con-

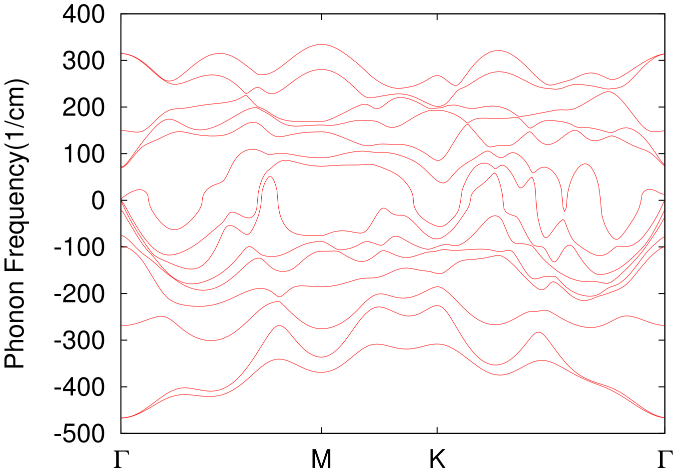

Figure 7.8: Phonon dispersion for the T Li_2MoS_2 along selected directions, configuration number 11 in 7.2.

stant matrix has to be calculated for a larger super-cell than the primitive unit cell. The size of the super-cell should be large enough such that the elements if force constant matrix has fallen off at the boundary of the super-cell. For the stability analysis of the T Li_2MoS_2, we therefore choose a 4×4 super-cell and we calculate the phonon dispersions. The resulting dispersion is presented in Fig .7.8. Clearly the presence of large imaginary eigenfrequency in phonon spectrum in Fig. 7.8 is the signature of dynamical instability of perfect T Li_2MoS_2, even thought it is energetically more favorable against two side adsorbed H structure. By considering this fact, we therefore performed an unrestricted lattice optimization for a 2×2 super lattice of T Li_2MoS_2 (configuration number 11 in 7.2). The resulting optimized structure is presented in Fig. 7.9 with lattice constants $a = 6.830\mathring{A}, b = 6.716\mathring{A}$ with the angle between them $\gamma = 60$.

As is clear from the Fig. 7.9(a) the Mo atoms form diamond like clusters which are marked with A, B, C and D, with the bond lengths $d_{Mo(AB)} = d_{Mo(DC)} = 2.958\mathring{A}$, $d_{Mo(AD)} = d_{Mo(BC)} = 2.993\mathring{A}$, $d_{Mo(BE)} = 3.892\mathring{A}$ and $d_{Mo(BF)} = 3.725\mathring{A}$. Another feature of the distorted T structure is the fact that the Li atoms slightly deviate from their high symmetry positions on the top of Mo atoms as clearly could be seen in Figs. 7.9 (a) and (b). This deformations further leads to reduction of total energy 285 meV/Mo in comparison with perfect T Li_2MoS_2 (configuration number 11 in 7.2). In short based on our analysis, the perfect T structure could not be stabilized at least by Li adsorptions although it is energetically more favorable than Li adsorbed H structure.

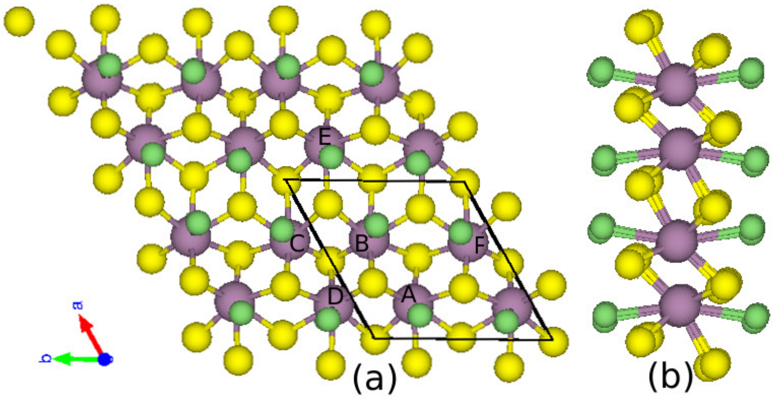

Figure 7.9: Top view (a) and side view (b) of the two sided Li adsorbed distorted T structure (distorted version of configuration number 11 in 7.2).

7.4 Conclusions

In conclusion, we studied the possibility of stabilizing the naturally unstable T structure of MoS_2 monolayers by adsorption of Li adatoms. We found that adsorption of Li atoms on one side of the layer could not lead to a H $\rightarrow$ T transition. However, it does lead to a general trend of stabilizing the T structure when including more Li adatoms. We found that the T structure could be stabilized against the H structure energetically as long as two adatoms are included on both sides of the layer. However, phonon calculations shows that this structure is unstable against distortions towards clustering of the molybdenum atoms. To examine a realization of this structure we studied whether it is possible for the Li atoms to pass through the MoS_2 layer and arrive at the other side. By choosing the V site (see Fig. 7.1(a)) as the penetration path of Li atoms, we found the penetration barrier for pure MoS_2 to be 2 eV. The penetration barrier for a system that is covered with one layer of Li atoms on one side drastically reduces the barrier to almost 0 eV. The main reason for this observation appears to be the reduction in stiffness of MoS_2 in the presence of Li adsorbates. This reduction in stiffness is most clear at the larger distortions which are required for the penetration of Li atoms. For very small distortions the stiffness does not show much difference between pure and Li-covered MoS_2. Finally we calculate the energy barrier of H$\rightarrow$T for a pure and completely covered MoS_2 structure. The transition barrier of 1.5 eV for the pure case is reduced to 130 meV for Li_2MoS_2, which is low enough for the transition to occur. The Li atoms were shown to play a crucial role in the reduction of the barrier size by mediating the transition.

Chapter 8

Summary and future prospects

8.1 Concluding remarks of the thesis

Recent limitations on the application of silicon devices force the community to replace silicon based devices by new materials. One of the attractive class of materials are compounds that they consist transition metal elements in their chemical composition, thanks to recent fabrication advancements new mono-layer or multilayer artificial materials could be designed for specific purposes. In my thesis I used different many-body techniques in order to understand the general behavior of thin-films made of strongly correlated materials as well as the effect of external electric field in adiabatic and non-adiabatic regimes.

In chapter 3, we extend the inhomogeneous Gutzwiller approximation (GA) [33, 118] to a more generic case, which gives the opportunity to include local potentials for large translationaly broken systems. This in turn allows us to exploit this feature to mimic the effect of external electric field in slab geometries. By using our extension of GA we described the Mott metal insulator transition in a slab geometry in the presence of a perpendicular external electric field by calculating the site-dependent quasi-particle (QP) weight. Increasing the Hubbard repulsion in the presence of an external electric field leads to the formation of a dead insulating zone at the center of the thin film. The formation of the dead zone for interactions larger that critical interaction (U_c) , where U_c is the critical bulk metal to insulator transition interaction without electric field, occurs before complete screening of the electric field and, therefore, charge trapping occurs at the surface. This causes the metal insulator transition (MIT) to be shifted in the presence of the external field. We therefore show that even though the QP weight of the central region is (the bulk) strongly suppressed for $U > U_c$, the surface layers remain metallic and with larger QP weight. Although our calculation can not give a definitive answer on whether a critical value for the electric field exists, below which the slab becomes insulating, it shows that a rapid change in the maximum QP weight and charge accumulation will occur above a finite electric field. Analytical or numerical methods, which can accurately probe the insulating region, will shine light on the exact nature of this transition. From an experimental point of view, our results are relevant for transport measurements in thin films. In the presence of an external electric field perpendicular to an insulating film, one could use the surface states for transport since the charge transfer at the surface creates two-dimensional underdoped and overdoped regions. In the same time, transport perpendicular to the thin film is suppressed due to the dead insulating zone, thus protecting the surface states from leakages. The electric field needed to create the surface states is also much lower than the breakdown field needed to pass current across the insulating zone.

In chapter 4, by using an inhomogeneous GA applied to the paramagnetic single band Hubbard model for a slab geometry we described a hole doped Mott thin-film. By considering a large system with number of layers equal to 90, we therefore performed a scaling analysis for QP weight profile and correlation length as function of doping. In the absence of applied electric field we calculated the position dependent charge density and QP weight and showed that the inverse correlation length has a power law dependence on doping as long as $U > U_c$. This differs from the results in [118] and [33] where authors found a power low scaling as function of interaction. In terms of experimental realization our doping dependent correlation length is easier to observe [36].

When a perpendicular electric field is applied, charges will accumulate on one side of the slab, which differ from a naive expectation that charges should be repelled from the places with larger interaction, the charge redistribution is enhanced after increasing the interaction. This correlation enhanced charge redistribution will in turn induce a large difference in the QP weight on the two sides of the slab, which was found to be as large as five orders of magnitude. We propose that a three terminal device with surface contacts can take advantage of this effect. For resistance switching purposes one would expect large on/off ratios of surface resistances when the electric field switches polarity.

In chapter 5, we studied the influence of correlation effects on the charge and QP weight profile of a translationaly broken system (slab geometry) which is modeled by a two band Hubbard model with density-density interactions. To do this, we extend for the first time the problem of inhomogeneous GA to multiband systems. This extension therefore allow us to study large systems while the computational effort is much less than dynamical mean field theory (DMFT) for multi band inhomogeneous systems [119] where authors considered only 6 layers in their study. By using this extension further we studied cases where there are two bands with different band widths. We did this calculations both at half filling and away from half filling. By using our inhomogeneous GA for multi band systems, we therefore consider the proximity to orbital selective Mott transition [129–131] point for slab geometries, where there are two different length scales for correlation length corresponding to NB (narrower band) and WB (wider band). We found that as long as the values of the Hund's coupling J is finite, due to the existence of a first order MIT, no diverging correlation length, even very near the transition point is seen. As a consequence, due to the short correlation length, the surface QP weight recovers very fast its bulk value even very near transition point. Only when the value of J is very small, a long correlation length could be seen near the critical point while it is still finite. When the band widths are not equal, for sufficiently large band width difference, the NB suffers from a continuous MIT at a smaller critical interaction (U_c^{NB}), well before the first order transition. Due to the continuous nature of this band selective transition, the NB shows a diverging correlation length at the transition point which follows an expected mean-field-like power law behavior as function of the interaction strength with an exponent insensitive to the band width difference. This in turn leads to the formation of an extended surface dead zone layer for the NB. For the doped system we reveal two different mechanisms of charge transfer to the surface for the WB. When $\alpha = \dfrac{1-\langle n_{NB}\rangle}{1-\langle n_{WB}\rangle} \ll 1$, the $\langle\rangle$ means average charge density accumulated at each band, interaction effects near the surface are enhanced due to reduced coordination number and charge transfer from the center to the surface for both bands. In this case the NB is near half-filling and the system is in a more correlated regime. However in the limit $\alpha \simeq 1$, there is charge transfer from the center to the surface for NB, while for the WB charges are repelled from the surface to the center of the slab. Such effects could be of importance not only near at surfaces but also at interfaces with other insulating materials.

In chapter 6, we investigated the nonlinear response of a closed interacting fermionic system as modeled by a 1D extended Hubbard model with periodic boundary conditions. In this study, we investigated the nonlinear response of the system for both short time and large time scales by using Chebishev propagation method [174]. In contrast to previous studies [159, 160, 176], where they used Landau-Zener [98, 99] Hamiltonian in order to study the breakdown criteria, for gapped systems we used fidelity susceptibility [102] as a measure for comparison of short time response between different systems with different interaction strengths. For many body systems such as Hubbard models which there are large number of states in their spectrum, this quantity (the fidelity susceptibility), is unbiased against two level approximation which often has been used in previous works [159, 160, 176]. For larger time scales we analyze the problem of Bloch oscillations (BO). In our analysis we linked the variation of BO frequencies as function of field strength in a convincing way to particular properties of the spectrum.

We therefore, proceeded our study first by looking at weakly interacting metallic system at the boundary of spin density wave (SDW) and charge density wave (CDW). This system shows a dissipative behavior for low fields, when the wavefunction acquires overlap with large number of left going and right going states. This in turn implies that the quasi-stationary state acquires zero current. BO start smoothly with a frequency larger than F, where F is equal to the electric field used in Peierls substitution divided by 2π. The main reason for this is the fact that the reflection happens at the lower part of the spectrum, thus effectively decreasing the bandwidth. Upon increasing the field strength the probability transfer at each anti-crossing is more efficient. This leads to a more regular recurrences of the ground state and the topmost excited state with period equal to $1/F$, which can be seen from the oscillations in the current. Upon dimerization of the metallic system, the formation of the dissipative regime is postponed to larger fields due to the formation of a charge gap. However, the main difference between the dimer case and the metallic system resides in the fact that, first, it shows irregular current oscillations before they turn into regular BO and second, the BO with larger frequencies survive for large times, in analogy with the metallic case subjected to strong field. This implies the existence of states at the middle of the spectrum with low fidelity susceptibility (or roughly speaking the formation of large mid gaps in the relevant excitations, that play the role of a band-edge state and reflect back the overlap probability at the middle part of the spectrum even for large electric fields. Finally, the dimerized system also shows regular BO with period equal to $1/F$ for large enough electric fields. The value for which the dimerized system shows regular BO are much larger than those found for the metallic system even though the interactions are identical. For stronger interacting systems when the interactions are chosen such that the ground-state fidelity susceptibility is the same for both cases, then the ground state decay for both CDW insulator and SDW insulator behaves exactly the same. This similarity of the ground-state decay manifests itself even for larger times and for both low and high field dissipative regimes. However significant differences arise between the two cases for large electric fields. While SDW shows oscillatory behavior with large magnitude the CDW insulator and strong interacting metallic system only shows irregularities with small oscillations. Different from the weakly interacting metallic system and the dimer case, in the strongly interacting regime these irregularities are extended to intermediate fields and only for very large fields, regular BO with a period of $1/F$ are observed. This effect appears to be little affected by size, since the SDW and CDW insulators, for $L = 10$ and $L = 12$, show the same qualitatively and even quantitatively behavior. This implies that the reorganization of the spectrum is affected much more by the interaction than by the finite size induced discreteness.

In chapter 7, by using first principle calculations based on density functional theory (DFT) we studied the possibility of stabilizing the naturally unstable metallic T structure of MoS_2 monolayers against insulating H structure by adsorption of Li adatoms. For pure MoS_2 the semiconducting H structure was found to be more stable than the metallic T structure, both in bulk and monolayer form [192]. However, experimental and theoretical research on the structural stability of different MoS_2 bulk allotropes shows that the intercalation of Li atoms can stabilize the metallic 1T structure [193–195]. Stable 1T monolayer structures can also be realized by substitutional doping of MoS_2 with Re atoms [196]. We found that adsorption of Li atoms on one side of the monolayer MoS_2 could not lead to a H → T transition. However, it does lead to a general trend of stabilizing the T structure when including more Li ad-atoms. In contrast we found that the T structure could be energetically stabilized against the H structure as long as two adatoms are included on both sided of the layer. However, we found that two sided Lithium absorbed T structure is still dynamically unstable and it was distorted toward a distorted T structure which contains in-plane clustering of Molybdenum atoms (see Fig. 7.9). To examine the possibility to this new structure we studied whether it is possible for the Li atoms to pass through the MoS_2 layer and arrive at the other side. By choosing the V site (see Fig. 7.1(a)) as the penetration path of Li atoms, we found the penetration barrier for pure MoS_2 to be 2 eV. The penetration barrier for a system that is covered with one layer of Li atoms on one side drastically reduces the barrier to almost 0 eV. The main reason for this observation appears to be the reduction in stiffness of MoS_2 in the presence of Li adsorbates. This reduction in stiffness is most clear at the larger distortions which are required for the penetration of Li atoms. For very small distortions the stiffness does not show much difference between pure and Li-covered MoS_2. Finally we, calculated the energy barrier of H→T for a pure and completely covered MoS_2 structure. The transition barrier of 1.5 eV for the pure case is reduced to 130 meV for Li_2MoS_2, which is low enough for the transition to occur. The Li atoms were shown to play a crucial role in the reduction of the barrier size by mediating the transition. The main mechanism for this stabilization appear to be the charge transfer from the Li atoms to the MoS_2 layers, therefore this study hints toward a tunable stabilization of metallic T structure by using electric field for insulating H structure which partially is modified with ad-atoms.

8.2 Future prospects

In chapters 3, 4 and 5, I studied proximity effects in the paramagnetic phase of the different translationaly symmetry broken systems, furthermore we considered the effect of an external electric field. One interesting ongoing problem is to study magnetism in strongly correlated thin film systems, in particular the proximity effect in systems with magnetic ordered phases. As an example one may consider the interface between a magnetic ordered phase and a non-ordered phases, in order to see how magnetism could penetrate in the non-ordered phase. The effect of external fields, either magnetic or electric fields, is very important, and may further lead to new ways of tuning magnetic phases with external electric field and vice versa. Again the GA is one of the ways one may use to perform these investigations. While it is much less expensive computationally in comparison to other methods, it could capture the essence of correlation effects, which makes it a good candidate for these kind of studies, which throughout this thesis I gained experience on the formulation and implementation of the GA and I implemented a code that could perform the Gutzwiller projections for generic local interactions.

Another interesting problem is the effect of non-local correlations beyond the infinite dimension approximation. This also could be performed based on a real space version of the diagrammatic expansion of Gutzwiller wave function by following the guidelines in reference [204].

In chapter 6, I used the fidelity susceptibility for the short time comparison of real time dynamics of a closed interacting system. Although the fidelity susceptibility does not provide any information about the nature of the phases, it could be used as a generic order parameter in order to uncover the transition points when an external parameter is changed. While this concept is mostly used for 1D systems, it is an interesting problem to extend it for strongly correlated systems in two or three dimensions. In particular, the implementation of the fidelity calculation in the dynamical mean field (DMFT) frame work is an interesting problem. For zero temperature this is straightforward by using the exact diagonalization (ED) combined with DMFT approach, that I already implemented. However, for finite temperature a new definition of the fidelity should be realized based on the guidelines from reference [102]. Another important aspect is the real time dynamics of inhomogeneous systems subjected to time dependent external electric or magnetic fields. These investigations also could be performed by using a real space version of time dependent GA [205].

In chapter 7, I studied the possible stabilization of the T structure of the MoS_2 against the H structure. I performed this by inclusion of Lithium ad-atoms. However the problem was designed to find out the effect of electrostatic doping of MoS_2, but in the plane wave implementation of DFT calculations inducing charge into the monolayers is technically impossible. The reason for this is the fact that the energy is proportional to the distance of the two charged layers and therefore total energy calculations for the charged slabs depends on the amount of the vacuum and therefore is not unique. This is only an artifact of repeating layers in the direction perpendicular to the layer, and is specific to the plane wave implementation. Therefore, it is interesting to resolve this technical problem of plain wave implementations by using the ideas of reference [206]. Furthermore, specific to the MoS_2 problem, it is also interesting to perform a stability analysis based on non-repeating cell DFT implementations. Another interesting problem for the MoS_2 is mobility engineering of carriers by using different substrates and/or adatoms combined with an external electric field. These combinations further may lead to tunable stabilization of the T structure and therefore improving the mobility of the carriers.

Chapter 9

Samenvatting en toekomstperspectieven

9.1 Afsluitende bemerkingen

Recente tekort komingen in micro-elektronia apparaten gelaseert om silicium dwingen de gemeenschap om silicium te vervangen door andere materialen. Een van de meest aantrekkelijke zijn samengestelde materialen die transitiemetalen bevatten in hun chemische samenstelling. Dankzij recente fabricatieverbeteringen kunnen nieuwe éénlagige en meerlagige artificiële materialen ontworpen worden voor specifieke doelen. In mijn thesis gebruik ik verschillende veel-deeltjes-technieken om zowel het algemene gedrag te begrijpen van dunne films van sterk gecorreleerde materialen als het effect van elektrische velden in adiabatische en niet-adiabatische regimes.

In hoofdstuk 3, breiden we voor de eerste keer de Gutzwiller-benadering (GA) [33, 118] uit naar algemenere gevallen wat de mogelijkheid geeft om lokale potentialen mee te nemen voor systemen met gebroken translatiesymmetrie. Dit laat op zijn beurt toe om deze eigenschap te gebruiken om het effect van uitwendige elektrische velden na te bootsen in een 'slab'-geometrie. Met onze uitbreiding van GA hebben we de Mott-metaal-isolatorovergang beschreven in een slab-geometrie in de aanwezigheid van een loodrect elektrisch veld door het berekenen van het plaatsafhankelijke quasideeltjes (QP) gewicht. Het verhogen van de Hubbard-afstoting in de aanwezigheid van een uitwendig elektrisch veld leidt tot de vorming van een dese isolerende zone in het centrum van de dunne film. De vorming van dese zone voor interacties groter dan de kritische interactie (U_c), waar U_c de kritische bulk metaal-isolator transitie interactie voorstelt, gebeurt voor de volledige afscherming van het elektrisch veld waardoor er lading kan opgesloten geraken aan het oppervlak. Daarom tonen we dat hoewel het QP-gewicht van het centrale deel sterk onderdrukt is voor U>U$_c$ de opervlaktelagen metallisch blijven met hoger QP-gewicht. Hoewel onze berekeningen niet eenduidig aantonen dat er een kritische waarde voor het elektrisch veld bestaat, waaronder de slab isolerend wordt, laten ze wel zien dat er een snelle verandering optreedt in de maximale QP- waarde en dat er ladingsophoping zal optreden boven een eindig elektrisch veld. Analytische en numerieke methoden waarmee de isolerende delen goed onderzocht kunnen worden kunnen verduidelijking brengen over de juiste aard van deze overgang. Vanuit experimenteel standpunt zijn onze resultaten van belang voor transportmetingen in dunne filmen. In de aanwezigheid van een uitwendig elektrisch veld loodrecht op de isolerende film, kan men gebruik maken van oppervlaktetoestanden voor transport omdat de ladingsoverdracht aan het oppervlak tweedimensionale onder- en overgedopeerde gebieden creëert. Tezelfdertijd wordt transport loodrecht op de dunne film onderdrukt door de geïsoleerde zone zodat de oppervlaktetoestanden beschermd zijn tegen lekkage. Het elektrisch veld dat nodig is om de oppervlaktetoestanden voort te brengen is ook veel kleiner dan het veld dat nodig is om stroom door het isolerende gebied te sturen.

In hoofdstuk 4, beschreven we een gatengedopeerde dunne Mott-film met behulp van een inhomogene GA toegepast op het paramagnetische enkelbands Hubbard-model voor een slab-geometrie. Om grote systemen te bekijken met 90 lagen hebben we daarom een schalingsanalyse uitgevoerd voor het QP-gewichtsprofiel en de correlatielengte als functie van de dopering. We berekenden de posistie-afhankelijke ladingsdichtheid en QP-gewicht in de afwezigheid van een elektrisch veld en toonden aan dat de inverse correlatielengte een machtswet volgt als funcite van de dopering zolang dat $U > U_c$. Dit resultaat is verschillend van de resultaten in [118] en [33] waar de auteurs een machtswet-schaling vonden als funcite van de interactie. Experimenteel gezien is onze doperingsafhankelijke correlatielengte gemakkelijker te observeren.

Wanneer een loodrecht elektrisch veld wordt aangebracht zullen de ladingen opgehoopt worden aan een kant van de slab. Deze door correlatie versterkte ladingsherverdeling zal op haar beurt een groot verschil in QP-gewicht teweeg brengen tussen de twee kanten van de slab. Dit verschil kan wel vijf grootteordes bedragen. We suggereerden dat een toestel met drie uitgangen en oppervlaktecontacten gebruik kan maken van dit effect. Voor toepassingen met grote weerstandswisselingen kan men grote aan/uit-ratios verwachten van de oppervlakteweerstand als de polariteit van het elektrisch veld omgedraaid wordt.

In hoofdstuk 5, bestudeerden we de invloed van correlatie-effectenop het ladings- en QP-gewichtsprofiel van systemen met gebroken translatiesymmetrie (slab-geometrie) welke gemodelleerd worden met een tweebands Hubbard-model met dichtheid-dichtheid -sinteracties. Om dit te verwezenlijken hebben we voor de eerste keer het probleem van inhomogene GA uitgebreid naar veelbandensystemen. Deze uitbreiding laat ons daardoor toe om grote systemen te bestuderen terwijl de computationele kosten veel kleiner blijven dan de dynamische gemiddelde-veldentheorie (DMFT) voor mutibandsystemen [119] waar de auteurs slechts 6 lagen konden bekijken in hun studie. Door deze uitbreiding verder te gebruiken, hebben we gevallen bestudeerd waar er twee banden zijn met verschillende bandbreedtes. We deden deze berekeningen zowel voor halfgevulde banden en bandvullingen weg van half gevulde banden. Met behulp van onze inhomogene GA voor multibandsystemen beschouwen we the nabijheid tot het orbitaalselectieve Mott-transitiepunt [129–131] voor slabgeometrieën, waar er twee verschillende lengteschalen zijn voor de correlatielengte corresponderend met de NB (smallere band) en WB (wijde band).

We vonden dat de waarde van de Hund-koppeling J eindig is door een eersteorde MIT, zolang er geen divergerende correlatielengte waargenomen werd en dit, zelfs dichtbij het overgangspunt. Als gevolg van de korte correlatielengte wordt de waarde van de oppervlakte QP zeer snel hersteld tot de bulkwaarde, zelfs in de buurt van het overgangspunt. Enkel als de waarde van J zeer klein is wordt er een lange correlatielengte waargenomen nabij het kritische punt waar het nog steeds eindig is. Als de bandbreedtes niet gelijk zijn zal, wanneer het verschil groot genoeg is, de NB (nauwe band) lijden onder de continue MIT bij een kleinere waarde voor de kritische interactie U_c^{NB}, ruim voor de eersteorde overgang. Door de continue aard van deze bandselectieve overgang, toont de NB een divergerende correlatielengte nabij het transitiepunt welke een verwachte gemiddelde veld-achtige machtswet volgt als functie van de interactiesterkte met een exponent die ongevoelig is voor de bandbreedte. Dit leidt op zijn beurt tot de vorming van een uitgebreid doods gebied voor de NB. Voor het gedopeerde gebied ontvouwen we twee verschillende mechanismen voor de ladingsoverdracht naar het oppervlak van de WB (wijdere band). Wanneer $\alpha = \dfrac{1 - \langle n_{NB} \rangle}{1 - \langle n_{WB} \rangle} \ll 1$, $\langle \rangle$ betehent de gemiddelde ladingsdichtheid is in elke band, dan worden interactie-effecten in de buurt van het oppervlak versterkt door het gereduceerde coördinatiegetal en de ladingsoverdracht van het centrum naar het oppervlak voor beide banden. In dat geval is de NB bijna half bezet en bevindt het systeem zich in een meer gecorreleerd regime. Maar in de limiet $\alpha \simeq 1$ is er een ladingsoverdracht van het centrum naar het oppervlak voor NB terwijl voor de WB de ladingen afgestoten worden van het oppervlak naar het centrum van de slab. Zulke effecten kunnen niet enkel van belang zijn aan oppervlakken maar ook aan tussenvlakken met andere isolerende materialen.

In hoofdstuk 6, hebben we de niet-lineaire respons onderzocht van een gesloten interagerend fermionsysteem met een eendimensionaal uitgebreid Hubbard model met periodische randvoorwaarden. In de studie onderzochten we de niet-lineaire repons van het systeem voor zowel korte als lange tijsschalen met de Chebishev-popagatiemethode [174]. In tegenstelling tot vorige studies [159, 160, 176], waar men gebruik maakte van de Landau-Zener [98,99] hamiltoniaan on de afbraakcriteria te bestuderen voor systemen met een bandkloof, gebruikten wij de betrouwbaarheidssusceptibiliteit [102] als een maat voor de vergelijking van de korte-tijdsrepons tussen verschillende systemen met verschillende interacties. voor veeldeeltjessystemen zoals Hubbard-modellen waarbij er veel toestanden zijn is deze grootheid niet beïnvloed door de twee-niveaubenadering die vaak in vroegere studies gebruikt werd [159, 160, 176]. Voor grotere tijdschalen analyseren we het probleem van Bloch-oscillaties (BO). In onze analyse maakten we een link tussen de variatie van de BO-frequenties als een functie van de veldsterkte op een overtuigende manier en de specifieke eigenschappen van het spectrum.

We zetten onze studie daarom eerst voort door te kijken naar een zwak interagerend metallisch systeem aan de grens van ladingsdichtheidsgolf (CDW) en spindichteheidsgolf (SDW). Dit systeem, vertoont dissipatief gedrag voor kleine velden als de golffuncties overlappen met grote hoeveelheden links- en rechtsgaande toestanden. Dit impliceert op zijn beurt dat de quasistationaire toestand overeenkomt met een verdwijnende stroom. Bloch-oscillaties (BO) beginnen glad met een frequentie groter dan F, waar F gelijk is aan het elektrisch veld gebruikt in de Peierls substitutie gedeeld door 2π. De hoofdreden hiervoor is het feit dat de reflectie gebeurt aan het lagere deel van het spectrum, zodat de bandbreedte effectief verkleind wordt. Door de veldsterkte te vergroten wordt de waarschijnlijkheidsoverdracht aan elke anti-kruising effciënter. Dit leidt tot een meer regelmatig voorkomen van de grondtoestand en de bovenste geëxciteerde toestand met periode F^{-1}, wat kan worden waargenomen in de stroomschommelingen. Dimerizatie van het metallisch systeem zorgt ervoor dat de vorming van het dissipatieve regime verschoven wordt naar sterkere velden door de vorming van een ladingskloof. Maar het grootste verschil tussen het dimeer- en het metallisch geval ligt in het feit dat het, ten eerste, onregelmatige stroomschommelingen toont voordat het verandert in een regelmatig BO en dat, ten tweede, de BO met grotere frequenties voor langere tijden overleeft, analoog aan het metallisch geval onderworpen aan sterke velden. Dit impliceert dat het bestaan van toestanden in het midden van het spectrum met lage betrouwbaarheids susceptibiliteit (of, ruwweg gezegd, de vorming van grote mid-gaptoestanden in de relevante excitaties) een rol spelen de in randtoestanden van de band en die de overlapwaarschijnlijkheid terug reflecteren in het middelste deel van het spectrum, zelfs voor grote elektrische velden. Ten slotte toont het gedimerizeerde systeem ook regelmatige BO met een periode gelijk aan F^{-1} voor elektrische velden die sterk genoeg zijn. De waarde waarvoor dit gebeurt zijn veel groter dan die voor het metallisch systeem hoewel de interacties identiek zijn. Wanneer voor sterker interagerende systemen de interacties zo gekozen worden dat de susceptibiliteit van de grondtoestand hetzelfde is voor beide gevallen, dan gedraagt het verval van de grondtoestand voor zowel de CDW (ladingsdichtheidsgolf) isolator als de SDW (spindichtheidsgolf) zich op dezelfde manier. Deze gelijkenis van het grondtoestandverval manifesteert zich zelfs voor langere tijden en voor zowel zwakke als sterke veld dissipatieve regimes. Er duiken echter belangrijke verschillen op tussen de twee gevallen voor sterke elektrische velden. Terwijl SDW een schommelend gedrag met grote amplitude vertoont, tonen de CDW-isolator en het sterk interagerende metallische systeem enkel onregelmatigheden met kleine schommelingen. In tigenstelling met het zwak interagerende metallisch systeem en het dimeer geval, zijn deze onregelmatigheden in het sterk interagerende regime uitgebreid naar intermediaire velden en enkel voor zeer sterke velden, $F = 10.0$, wordt een regelmatig BO met een periode F^{-1} waargenomen. Dit effect blijkt nauwelijks te worden beïnvloed door de grootte, want de SDW- en CDW-isolatoren, voor $L = 10$ en $L = 12$, tonen hetzelfde kwalitatief en zelfs kwantitatief gedrag. Dit impliceert dat de reorganisatie van het spectrum meer beïnvloed wordt door de interactie dan door de discreetheid die veroorzaakt wordt door de eindige afmeting.

In hoofdstuk 7, onderzochten we met behulp van ab initio-berekeningen gebaseerd op dichtheidsfunctionaaltheorie (DFT) de mogelijkheid om de onstabiele T-structuur van enkellaags MoS_2 te stabiliseren door adsorptie van Li atomen. Voor pure MoS_2, werd gevonden dat de halfgeleidende H-structuur stabieler was dan de metallische T-structuur, zowel in enkellaags als bulk toestand [192]. Maar experimenteel en theoretisch onderzoek naar de stabiliteit van verschillende MoS_2 bulkallotropen toont aan dat de intercalatie van Li atomen de metallische T-structuur kan stabiliseren [193–195]. Stabiele 1T enkellagige structuren kunnen ook gerealiseerd worden substitutionele dopering van MoS_2 met Re atomen.

We vonden dat adsorptie van Li atomen aan één zijde van de laag niet kon leiden tot een H→T overgang. Er was echter wel een algemene trend naar stabiele T-structuren wanneer er meer Li atomen aanwezig waren. In tegenstelling hiermee, vonden we dat de T-structuur wel gestabiliseerd kon worden indien er twee adatomen aan beide kanten aanwezig waren. Maar we vonden wel dat de T-structuur met Li geadsorbeerd aan 2 kanten nog altijd dynamisch onstabiele is en dat het vervormt tot een gestoorde T-structuur waarbij Mo atomen clusteren. Om de realisatie van deze structuur te onderzoeken, bestudeerden we de mogelijkheid dat de Li atomen door de laag heen geraakten om de andere zijde te bereiken. Door de V-plaats (zie Fig. 7.1(a)) als doorgangspad te kiezen voor de Li atomen vonden we een barrière van 2 eV voor puur MoS_2. De barrière voor een systeem dat reeds bedekt is met Li atomen verdween vrijwel helemaal. De hoofdreden voor deze observatie bleek de vermindering in stijfheid van de MoS_2 in de buurt van Li atomen. Deze reductie in stijfheid is het meest zichtbaar voor de grote vervormingen die nodig zijn om de Li atomen door te laten. Voor zeer kleine vervormingen is er weinig verschil in stijfheid tussen puur en met Li bedekte MoS_2. The transitiebarrière van 1.5 eV voor het onbedekte geval wordt gereduceerd tot 130 meV voor Li_2MoS_2, wat laag genoeg is om de transitie te laten gebeuren. We toonden aan dat de Li atomen een regulerende rol spelen in het verminderen van de hoogte van de barrière.

9.2 Toekomstperspectieven

In hoofdstukken 3, 4 en 5 heb ik de nabijheidseffecten in de paramagnetische fase van verschillende systemen met gebroken translatiesymmetrie besproken alsook het effect van een uitwendig elektrisch veld. Een interessant onopgelost probleem is magnetisme in systemen van sterk gecorreleerde dunne filmen en in het bijzonder de nabijheidseffecten in systemen met magnetisch geordende fasen. Als voorbeeld kan men de scheiding tussen een magnetisch geordende en ongeordende fase beschouwen, om te zien hoe het magnetisme in de ongeordende fase doordringt. Het effect van externe velden, zowel elektrische als magnetische, is heel belangrijk en kan leiden naar nieuwe manieren om magnetische fases te manipuleren met een elektrisch veld en omgekeerd. Men kan opnieuw de Gutzwiller-benadering gebruiken om dit onderzoek uit te voeren. Terwijl het computationeel veel voordeliger is dan andere methodes, kan het toch de essentie van correlatie-effecten beschrijven wat het tot een goede methode maakt voor dit soort studies. Doorheen deze thesis heb ik ervaring opgeilaan met het formuleren en implementeren van de Gutzwiller-benadering en heb ik een code gemaakt die Gutzwiller-projecties kan maken voor algemene lokale interacties. Een ander interessant probleem is het effect van niet-lokale correlaties voorbij de oneindige-dimensies-benadering. Dit kan ook gedaan worden met een reële ruimte versie van de diagrammatische expansie van de Gutzwiller-golffunctie door de richtlijnen in ref. [204] te volgen.

In hoofdstuk 6 heb ik de fideliteitssusceptibiliteit gebruikt voor een vergelijking op korte tijd van de reële tijds dynamica van gesloten interagerende systemen. Hoewel de fideliteitssusceptibiliteit geen informatie levert over de aard van de fases kan het gebruikt worden als een algemene ordeparameter om overgangspunten te ontdekken als de externe parameter veranderd wordt. Hoewel dit concept meestal gebruikt wordt voor 1D systemen is het een interessant probleem om dit uit te breiden naar twee of drie dimensies. In het bijzonder vormt de implementatie van de betrouwbaarheidsberekening in het dynamische gemiddelde velden theorie (DMFT)-kader een interessant probleem. Voor de nulpuntstemperatuur is het vanzelfsprekend om de exacte diagonalisatie (ED) te gebruiken in combinatie met de DMFT-benadering die ik reeds geïmplementeerd heb. Maar voor eindige temperaturen moet een aangepaste definitie voor de betrouwbaarheid ontwikkeld worden op basis van de richtlijnen die gegeven werken in Ref. [102]. Een ander belangrijk aspect is de dynamica van inhomogene systemen die onderworpen worden aan tijdsafhankelijke elektrische of magnetische velden. Deze studie kan ook gedaan worden door gebruik te maken van ruimteversies van de tijdsafhankelijke Gutzwiller-benadering [205].

In hoofdstuk 7 heb ik de mogelijkheid onderzocht om de T-structuur van MoS_2 t.o.v. de H-structuur te stabiliseren. Deze studie werd gedaan met het toevoegen van Li atomen, maar het probleem had oorspronkelijk te maken met het elektrolytisch doperen van MoS_2. Maar in de vlakke-golven-implementatie van de DFT-berekeningen is het technisch onmogelijk om ladingen in de lagen te introduceren. De reden hiervoor is het feit dat de energie tussen twee geladen lagen recht evenredig is met de afstand tussen de lagen waardoor de energieberekeningen van de geladen lagen afhankelijk zijn van de hoeveelheid vacuum er tussen en dus niet uniek zijn. Dit is enkel een artefact van de periodische lagen in de richting loodrecht op de laag en is specifiek voor vlakke-golven-implementaties. Daarom is het interessant om deze technische moeilijkheden op te lossen met behulp van de ideeën van Ref. [206]. Bovendien kan het ook interessant zijn om niet-periodische DFT-implementaties te gebruiken. Een ander interessant probleem voor MoS_2 het is veranderen van de mobiliteit van de ladingsdragers door gebruik te maken van verschillende substraten en/of adatomen gecombineerd met een elektrisch veld. Deze combinaties kunnen verder leiden tot een aanpasbare stabilisatie van de T-structuur en daardoor het verhogen van de mobiliteit.

Bibliography

[1] K.F. Wang, J.-M. Liu, and Z.F. Ren. *Advances in Physics*, 58(4):321–448, 2009.

[2] G. E. Moore. *Electronics*, 38.

[3] David K. Ferry. *Science*, 319(5863):579–580, February 2008. PMID: 18239115.

[4] You Zhou and Shriram Ramanathan. Correlated electron materials and field effect transistors for logic: A review. *Critical Reviews in Solid State and Materials Sciences*, 38(4):286–317, January 2013.

[5] R. Myslewski. *PCs and Chips*, ch. Intel's TriGate gamble: It's now or never, July 2011.

[6] M. Copel, M. A. Kuroda, M. S. Gordon, X.-H. Liu, S. S. Mahajan, G. J. Martyna, N. Moumen, C. Armstrong, S. M. Rossnagel, T. M. Shaw, P. M. Solomon, T. N. Theis, J. J. Yurkas, Y. Zhu, and D. M. Newns. *Nano Lett.*, 13(10):4650–4653, October 2013.

[7] A. D. Caviglia, S. Gariglio, N. Reyren, D. Jaccard, T. Schneider, M. Gabay, S. Thiel, G. Hammerl, J. Mannhart, and J.-M. Triscone. *Nature*, 456(7222):624–627, December 2008.

[8] D. B. McWhan and J. P. Remeika. *Phys. Rev. B*, 2:3734–3750, Nov 1970.

[9] Jan M. Tomczak, Ferdi Aryasetiawan, and Silke Biermann. *Phys. Rev. B*, 78:115103, Sep 2008.

[10] F. J. Morin. *Physical Review Letters*, 3(1):34–36, July 1959.

---

[11] Dieter Vollhardt. In *AIP Conference Proceedings*, volume 1297, pages 339–403. AIP Publishing, November 2010.

[12] Elbio Dagotto. *Rev. Mod. Phys.*, 66:763–840, Jul 1994.

[13] K. Andres, J. E. Graebner, and H. R. Ott. *Phys. Rev. Lett.*, 35:1779–1782, Dec 1975.

[14] G. Kotliar, S. Y. Savrasov, K. Haule, V. S. Oudovenko, O. Parcollet, and C. A. Marianetti. *Reviews of Modern Physics*, 78(3):865–951, August 2006.

[15] Masatoshi Imada, Atsushi Fujimori, and Yoshinori Tokura. *Rev. Mod. Phys.*, 70:1039–1263, Oct 1998.

[16] Henrik Kajueter and Gabriel Kotliar. *Phys. Rev. Lett.*, 77:131–134, Jul 1996.

[17] G. A. Sawatzky and D. Post. *Phys. Rev. B*, 20:1546–1555, Aug 1979.

[18] Kevin E. Smith and Victor E. Henrich. *Phys. Rev. B*, 50:1382–1390, Jul 1994.

[19] Shik Shin, Yasuhisa Tezuka, Toyohiko Kinoshita, Takehiko Ishii, Takayuki Kashiwakura, Masanori Takahashi, and Yoshiyuki Suda. *Journal of the Physical Society of Japan*, 64(4):1230–1235, April 1995.

[20] R Zimmermann, R Claessen, F Reinert, P Steiner, and S Hšekufner. *Journal of Physics: Condensed Matter*, 10(25):5697–5716, June 1998.

[21] Börje Johansson. *Phys. Rev. B*, 19:6615–6619, Jun 1979.

[22] L. Z. Liu, J. W. Allen, O. Gunnarsson, N. E. Christensen, and O. K. Andersen. *Phys. Rev. B*, 45:8934–8941, Apr 1992.

[23] A. Sekiyama, T. Iwasaki, K. Matsuda, Y. Saitoh, Y. Ǒnuki, and S. Suga. *Nature*, 403(6768):396–398, January 2000.

[24] K. Maiti, D. D. Sarma, M. J. Rozenberg, I. H. Inoue, H. Makino, O. Goto, M. Pedio, and R. Cimino. *EPL*, 55(2):246, July 2001.

[25] A. Sekiyama, H. Fujiwara, S. Imada, S. Suga, H. Eisaki, S. I. Uchida, K. Takegahara, H. Harima, Y. Saitoh, I. A. Nekrasov, G. Keller, D. E. Kondakov, A. V. Kozhevnikov, Th. Pruschke, K. Held, D. Vollhardt, and V. I. Anisimov. *Phys. Rev. Lett.*, 93:156402, Oct 2004.

[26] R. Eguchi, T. Kiss, S. Tsuda, T. Shimojima, T. Mizokami, T. Yokoya, A. Chainani, S. Shin, I. H. Inoue, T. Togashi, S. Watanabe, C. Q. Zhang, C. T. Chen, M. Arita, K. Shimada, H. Namatame, and M. Taniguchi. *Phys. Rev. Lett.*, 96:076402, Feb 2006.

[27] M. Yano, A. Sekiyama, H. Fujiwara, Y. Amano, S. Imada, T. Muro, M. Yabashi, K. Tamasaku, A. Higashiya, T. Ishikawa, Y. Ōnuki, and S. Suga. *Phys. Rev. B*, 77:035118, Jan 2008.

[28] G. Panaccione, M. Altarelli, A. Fondacaro, A. Georges, S. Huotari, P. Lacovig, A. Lichtenstein, P. Metcalf, G. Monaco, F. Offi, L. Paolasini, A. Poteryaev, O. Tjernberg, and M. Sacchi. *Phys. Rev. Lett.*, 97:116401, Sep 2006.

[29] R. W. Helmes, T. A. Costi, and A. Rosch. *Physical Review Letters*, 101(6):066802, August 2008.

[30] R. Bulla and M. Potthoff. *Eur. Phys. J. B*, 13(2):257–264, January 2000.

[31] H. Zenia, J. K. Freericks, H. R. Krishnamurthy, and Th. Pruschke. *Phys. Rev. Lett.*, 103:116402, Sep 2009.

[32] M. Potthoff and W. Nolting. *Phys. Rev. B*, 60(11):7834–7849, September 1999.

[33] Giovanni Borghi, Michele Fabrizio, and Erio Tosatti. *Physical Review Letters*, 102(6):066806, February 2009.

[34] D. Nasr Esfahani, L. Covaci, and F. M. Peeters. *Phys. Rev. B*, 87(3):035131, January 2013.

[35] D Nasr Esfahani, L Covaci, and F M Peeters. *Journal of Physics: Condensed Matter*, 26(7):075601, 2014.

[36] F. Rodolakis, B. Mansart, E. Papalazarou, S. Gorovikov, P. Vilmercati, L. Petaccia, A. Goldoni, J. P. Rueff, S. Lupi, P. Metcalf, and M. Marsi. *Phys. Rev. Lett.*, 102(6):066805, February 2009.

[37] N. Aetukuri C. Rettner D.N. Esfahani F.M. Peeters et. al. K. Martens, J.W. Jeong. *unpublished*.

[38] Antoine Georges, Gabriel Kotliar, Werner Krauth, and Marcelo J. Rozenberg. *Reviews of Modern Physics*, 68(1):13–125, January 1996.

[39] A. K. Geim and I. V. Grigorieva. *Nature*, 499(7459):419–425, July 2013.

[40] Branimir Radisavljevic and Andras Kis. *Nat Mater*, 12(9):815–820, September 2013.

[41] Gabriel Kotliar and Dieter Vollhardt. *Physics Today*, 57(3):53–59, March 2004.

[42] M. Nakano, K. Shibuya, D. Okuyama, T. Hatano, S. Ono, M. Kawasaki, Y. Iwasa, and Y. Tokura. *Nature*, 487(7408):459–462, July 2012.

[43] Jaewoo Jeong, Nagaphani Aetukuri, Tanja Graf, Thomas D. Schladt, Mahesh G. Samant, and Stuart S. P. Parkin. *Science*, 339(6126):1402–1405, March 2013. PMID: 23520104.

[44] Fumihiko Nakamura, Mariko Sakaki, Yuya Yamanaka, Sho Tamaru, Takashi Suzuki, and Yoshiteru Maeno. *Sci. Rep.*, 3, August 2013.

[45] A. Beaumont, J. Leroy, J.-C. Orlianges, and A. Crunteanu. *Journal of Applied Physics*, 115(15):154502, April 2014.

[46] J. Lappalainen, S. Heinilehto, H. Jantunen, and V. Lantto. *J Electroceram*, 22(1-3):73–77, February 2009.

[47] G. Stefanovich, A. Pergament, and D. Stefanovich. *J. Phys.: Condens. Matter*, 12(41):8837, October 2000.

[48] S. Guenon, S. Scharinger, Siming Wang, J. G. Ramirez, D. Koelle, R. Kleiner, and Ivan K. Schuller. *EPL*, 101(5):57003, March 2013.

[49] B. Corraze, E. Janod, L. Cario, P. Moreau, L. Lajaunie, P. Stoliar, V. Guiot, V. Dubost, J. Tranchant, S. Salmon, M.-P. Besland, V. Ta Phuoc, T. Cren, D. Roditchev, N. Stephant, D. Troadec, and M. Rozenberg. *Eur. Phys. J. Spec. Top.*, 222(5):1046–1056, July 2013.

[50] A. Zimmers, L. Aigouy, M. Mortier, A. Sharoni, Siming Wang, K. G. West, J. G. Ramirez, and Ivan K. Schuller. *Phys. Rev. Lett.*, 110:056601, Jan 2013.

[51] V. Guiot, L. Cario, E. Janod, B. Corraze, V. Ta Phuoc, M. Rozenberg, P. Stoliar, T. Cren, and D. Roditchev. *Nat Commun*, 4:1722, April 2013.

[52] N. F. Quackenbush, J. W. Tashman, J. A. Mundy, S. Sallis, H. Paik, R. Misra, J. A. Moyer, J.-H. Guo, D. A. Fischer, J. C. Woicik, D. A. Muller, D. G. Schlom, and L. F. J. Piper. *Nano Lett.*, 13(10):4857–4861, October 2013.

[53] Mengkun Liu, Harold Y. Hwang, Hu Tao, Andrew C. Strikwerda, Kebin Fan, George R. Keiser, Aaron J. Sternbach, Kevin G. West, Salinporn Kittiwatanakul, Jiwei Lu, Stuart A. Wolf, Fiorenzo G. Omenetto, Xin Zhang, Keith A. Nelson, and Richard D. Averitt. *Nature*, advance online publication, July 2012.

[54] Immanuel Bloch, Jean Dalibard, and Wilhelm Zwerger. *Rev. Mod. Phys.*, 80(3):885–964, July 2008.

[55] Tilman Esslinger. *Annual Review of Condensed Matter Physics*, 1(1):129–152, August 2010.

[56] Michael Köhl, Henning Moritz, Thilo Stöferle, Kenneth Günter, and Tilman Esslinger. *Phys. Rev. Lett.*, 94:080403, Mar 2005.

[57] Schawlow AL. Hansch TW. *Opt. Commun.*, 13.

[58] Cohen-Tannoudji C. Dalibard J. *J. Opt. Soc Am. B.*, 6.

[59] Letokhov VS. *JETP Lett.*, 7.

[60] Minogin VG. Letokhov VS. *Phys.Lett. A.*, 61.

[61] Ovchinnikov YB Grimm R, Weidemuller M. *Advances in atomic molecular, and optical physics.*, 42.

[62] E. Tiesinga, B. J. Verhaar, and H. T. C. Stoof. *Phys. Rev. A*, 47:4114–4122, May 1993.

[63] Cheng Chin, Rudolf Grimm, Paul Julienne, and Eite Tiesinga. *Rev. Mod. Phys.*, 82:1225–1286, Apr 2010.

[64] P. Dirac. *Proceeding of the Royal Society(London)*, A 123:714, 1929.

[65] M. Levy. *Proc. Nat' Acad. Sci. USA*, 76:6062, 1979.

[66] E. Lieb. *Int. J. Quant. Chem.*, 24:243, 1983.

[67] J. C. Slater. *Physical Review*, 81(3):385–390, February 1951.

[68] D. M. Ceperley and B. J. Alder. *Physical Review Letters*, 45(7):566–569, August 1980.

[69] John P. Perdew and Yue Wang. *Physical Review B*, 45(23):13244–13249, June 1992.

[70] W. Kohn and L. J. Sham. *Physical Review*, 140(4A):A1133–A1138, November 1965.

[71] J. P. Perdew. *International Journal of Quantum Chmistry*, 30(3):451–451, 1986.

[72] John P. Perdew, Kieron Burke, and Matthias Ernzerhof. *Phys. Rev. Lett.*, 77(18):3865–3868, October 1996.

[73] C. S. Wang, B. M. Klein, and H. Krakauer. *Physical Review Letters*, 54(16):1852–1855, April 1985.

[74] T. C. Leung, C. T. Chan, and B. N. Harmon. Ground-state properties of fe, co, ni, and their monoxides: Results of the generalized gradient approximation. *Physical Review B*, 44(7):2923–2927, August 1991.

[75] A. D. Becke. *Physical Review A*, 38(6):3098–3100, September 1988.

[76] Chengteh Lee, Weitao Yang, and Robert G. Parr. *Physical Review B*, 37(2):785–789, January 1988.

[77] J. Hubbard. *Proceedings of the Royal Society of London. Series A. Mathematical and Physical Sciences*, 276(1365):238–257, November 1963.

[78] M. Graf and P. Vogl. *Physical Review B*, 51(8):4940–4949, February 1995.

[79] Philipp Werner, Armin Comanac, Luca de' Medici, Matthias Troyer, and Andrew J. Millis. *Physical Review Letters*, 97(7):076405, August 2006.

[80] Andreas M. Läuchli and Philipp Werner. *Physical Review B*, 80(23):235117, December 2009.

[81] G. Alvarez. *Computer Physics Communications*, 180(9):1572–1578, September 2009.

[82] C. Lanczos. *J. Res. Nat. Bur. Stand.*, 49.

[83] A.N. Krylov. *Izv. Akad. Nauk SSSR, Otd. Mat. Estest.*, 7.

[84] B. E. Clements, E. Krotscheck, J. A. Smith, and C. E. Campbell. *Physical Review B*, 47(9):5239–5252, March 1993.

[85] Martin C. Gutzwiller. *Physical Review Letters*, 10(5):159–162, March 1963.

[86] Walter Metzner and Dieter Vollhardt. *Physical Review B*, 37(13):7382–7399, May 1988.

[87] Walter Metzner and Dieter Vollhardt. *Physical Review Letters*, 62(3):324–327, January 1989.

[88] Florian Gebhard. *Physical Review B*, 41(13):9452–9473, May 1990.

[89] J. Bünemann, W. Weber, and F. Gebhard. *Phys. Rev. B*, 57(12):6896–6916, March 1998.

[90] Jörg Bünemann, Florian Gebhard, Torsten Ohm, Stefan Weiser, and Werner Weber. In Prof Dr Anant V. Narlikar, editor, *Frontiers in Magnetic Materials*, pages 117–151. Springer Berlin Heidelberg, January 2005.

[91] J. W. Negele and H Orland. *Quantum Many-Particle Systems*. Persus Books Publishing, 1998.

[92] A. N. Rubtsov, V. V. Savkin, and A. I. Lichtenstein. *Phys. Rev. B*, 72:035122, Jul 2005.

[93] J. E. Hirsch and R. M. Fye. *Phys. Rev. Lett.*, 56:2521–2524, Jun 1986.

[94] Michel Caffarel and Werner Krauth. *Phys. Rev. Lett.*, 72:1545–1548, Mar 1994.

[95] M. Potthoff and W. Nolting. *Phys. Rev. B*, 59:2549–2555, Jan 1999.

[96] Lewin Boehnke, Hartmut Hafermann, Michel Ferrero, Frank Lechermann, and Olivier Parcollet. Orthogonal polynomial representation of imaginary-time green's functions. *Phys. Rev. B*, 84:075145, Aug 2011.

[97] Anders W. Sandvik. *Phys. Rev. B*, 57:10287–10290, May 1998.

[98] C. Zener. *Proc R. Soc. A*, 137:696, 1932.

[99] L. D. Landau. *Phys. Z. Owjetunion*, 2:46, 1932.

[100] Michael Tomka, Anatoli Polkovnikov, and Vladimir Gritsev. *Phys. Rev. Lett.*, 108:080404, Feb 2012.

[101] Paolo Zanardi and Nikola Paunković. *Phys. Rev. E*, 74:031123, Sep 2006.

[102] Wen-Long You, Ying-Wai Li, and Shi-Jian Gu. *Phys. Rev. E*, 76(2):022101, August 2007.

[103] S. Greschner, A. K. Kolezhuk, and T. Vekua. *Phys. Rev. B*, 88:195101, Nov 2013.

[104] A. Cavalleri, Th. Dekorsy, H. H. W. Chong, J. C. Kieffer, and R. W. Schoenlein. *Physical Review B*, 70(16):161102, October 2004.

[105] Hyun-Tak Kim, Byung-Gyu Chae, Doo-Hyeb Youn, Sung-Lyul Maeng, Gyungock Kim, Kwang-Yong Kang, and Yong-Sik Lim. *New Journal of Physics*, 6(1):52, May 2004.

[106] Dmitry Ruzmetov, Gokul Gopalakrishnan, Jiangdong Deng, Venkatesh Narayanamurti, and Shriram Ramanathan. *Journal of Applied Physics*, 106(8):083702, October 2009.

[107] A. Husmann, J. Brooke, T. F. Rosenbaum, X. Yao, and J. M. Honig. *Physical Review Letters*, 84(11):2465–2468, March 2000.

[108] Elliott H. Lieb and F. Y. Wu. *Physical Review Letters*, 20(25):1445–1448, June 1968.

[109] Gabriel Kotliar and Andrei E. Ruckenstein. *Physical Review Letters*, 57(11):1362–1365, September 1986.

[110] J. Bünemann and F. Gebhard. *Physical Review B*, 76(19):193104, November 2007.

[111] W. F. Brinkman and T. M. Rice. *Physical Review B*, 2(10):4302–4304, November 1970.

[112] P. Lunkenheimer, S. Krohns, S. Riegg, S. G. Ebbinghaus, A. Reller, and A. Loidl. *The European Physical Journal Special Topics*, 180(1):61–89, December 2009.

[113] B. S. Garbow J. J. More and K. E. Hillstrom. User guide for minpack-1, argonne national laboratory report anl-80-74, argonne, ill., 1980. 47.

[114] K. E. Hillstrom J. J. More, D. C. Sorensen and B. S. Garbow. The minpack project, in sources and development of mathematical software, w. j. cowell, ed., prentice-hall, pages 88-111 (1984).. 47.

[115] Hendrik J. Monkhorst and James D. Pack. *Phys. Rev. B*, 13(12):5188–5192, June 1976.

[116] Andreas Rüegg, Sebastian Pilgram, and Manfred Sigrist. *Physical Review B*, 75(19):195117, May 2007.

[117] P. Fazekas. World Scientific Publishing Company, Incorporated, 1999.

[118] Giovanni Borghi, Michele Fabrizio, and Erio Tosatti. *Physical Review B*, 81(11):115134, March 2010.

[119] Reza Nourafkan and Frank Marsiglio. *Physical Review B*, 83(15):155116, April 2011.

[120] Junwoo Son, Siddharth Rajan, Susanne Stemmer, and S. James Allen. *Journal of Applied Physics*, 110(8):084503, October 2011.

[121] Satoshi Okamoto and Andrew J. Millis. *Physical Review B*, 70(24):241104, December 2004.

[122] M. Potthoff and W. Nolting. *Physical Review B*, 59(4):2549–2555, January 1999.

[123] Reza Nourafkan and Frank Marsiglio. *Physical Review B*, 84(7):075133, August 2011.

[124] Michael Potthoff. *Physical Review B*, 64(16):165114, October 2001.

[125] Jörg Bünemann, Florian Gebhard, and Rüdiger Thul. *Physical Review B*, 67(7):075103, February 2003.

[126] K. Maiti, Priya Mahadevan, and D. D. Sarma. *Phys. Rev. Lett.*, 80(13):2885–2888, March 1998.

[127] K. Maiti, Ashwani Kumar, D. D. Sarma, E. Weschke, and G. Kaindl. *Phys. Rev. B*, 70(19):195112, November 2004.

[128] Akihisa Koga, Norio Kawakami, T. M. Rice, and Manfred Sigrist. *Physical Review Letters*, 92(21):216402, May 2004.

[129] L. de Medici, A. Georges, and S. Biermann. *Phys. Rev. B*, 72(20):205124, November 2005.

[130] Michel Ferrero, Federico Becca, Michele Fabrizio, and Massimo Capone. *Phys. Rev. B*, 72(20):205126, November 2005.

[131] Luca de Medici, S. R. Hassan, Massimo Capone, and Xi Dai. *Physical Review Letters*, 102(12):126401, March 2009.

[132] Xin Wang, M. J. Han, Luca de' Medici, Hyowon Park, C. A. Marianetti, and Andrew J. Millis. *Physical Review B*, 86(19):195136, November 2012.

[133] D. Nasr Esfahani, L. Covaci, and F. M. Peeters. *Physical Review B*, 85(8):085110, February 2012.

[134] Y. Ono, M. Potthoff, and R. Bulla. *Phys. Rev. B*, 67(3):035119, January 2003.

[135] Th Pruschke and R. Bulla. *The European Physical Journal B - Condensed Matter and Complex Systems*, 44(2):217–224, March 2005.

[136] Frank Lechermann, Antoine Georges, Gabriel Kotliar, and Olivier Parcollet. *Phys. Rev. B*, 76(15):155102, October 2007.

[137] Michele Fabrizio. *Phys. Rev. B*, 76(16):165110, October 2007.

[138] J. Nocedal and S. Wright. Springer New York, 2006.

[139] Jörg Bünemann, Florian Gebhard, Tobias Schickling, and Werner Weber. *physica status solidi (b)*, 249(6):1282–1291, 2012.

[140] Anatoli Polkovnikov, Krishnendu Sengupta, Alessandro Silva, and Mukund Vengalattore. *Rev. Mod. Phys.*, 83:863–883, Aug 2011.

[141] Alexander Weiße, Gerhard Wellein, Andreas Alvermann, and Holger Fehske. *Rev. Mod. Phys.*, 78:275–306, Mar 2006.

[142] Marlis Hochbruck and Christian Lubich. *SIAM Journal on Numerical Analysis*, 34(5):1911–1925, October 1997.

[143] F. Verstraete, J. J. Garc-Ripoll, and J. I. Cirac. *Phys. Rev. Lett.*, 93:207204, Nov 2004.

[144] J. K. Freericks. *Phys. Rev. B*, 77:075109, Feb 2008.

[145] Martin Eckstein and Philipp Werner. *Phys. Rev. B*, 88:075135, Aug 2013.

[146] Martin Eckstein, Marcus Kollar, and Philipp Werner. *Phys. Rev. B*, 81(11):115131, March 2010.

[147] M. Eckstein, A. Hackl, S. Kehrein, M. Kollar, M. Moeckel, P. Werner, and F. A. Wolf. *Eur. Phys. J. Spec. Top.*, 180(1):217–235, December 2009.

[148] Corinna Kollath, Andreas M. Lauchli, and Ehud Altman. *Phys. Rev. Lett.*, 98:180601, Apr 2007.

[149] S. Genway, A. F. Ho, and D. K. K. Lee. *Phys. Rev. A*, 86(2):023609, August 2012.

[150] Marcos Rigol and Lea F. Santos. *Phys. Rev. A*, 82:011604, Jul 2010.

[151] K. A. Al-Hassanieh, F. A. Reboredo, A. E. Feiguin, I. Gonzalez, and E. Dagotto. *Phys. Rev. Lett.*, 100:166403, Apr 2008.

[152] Marcin Mierzejewski, Janez Bonča, and Peter Prelovšek. *Phys. Rev. Lett.*, 107:126601, Sep 2011.

[153] M. Mierzejewski, L. Vidmar, J. Bonča, and P. Prelovšek. *Phys. Rev. Lett.*, 106:196401, May 2011.

[154] Martin Eckstein and Philipp Werner. *Phys. Rev. Lett.*, 107(18):186406, October 2011.

[155] Martin Eckstein, Takashi Oka, and Philipp Werner. *Phys. Rev. Lett.*, 105:146404, Sep 2010.

[156] Hantao Lu, Shigetoshi Sota, Hiroaki Matsueda, Janez Bonča, and Takami Tohyama. *Phys. Rev. Lett.*, 109:197401, Nov 2012.

[157] Akira Takahashi, Hisashi Itoh, and Masaki Aihara. *Phys. Rev. B*, 77(20):205105, May 2008.

[158] M. Mierzejewski, J. Luczka, and J. Dajka. *J. Phys.: Condens. Matter*, 22(24):245301, June 2010.

[159] Takashi Oka, Ryotaro Arita, and Hideo Aoki. *Phys. Rev. Lett.*, 91(6):066406, August 2003.

[160] Takashi Oka and Hideo Aoki. *Phys. Rev. Lett.*, 95:137601, Sep 2005.

[161] Zala Lenarčič and Peter Prelovšek. *Phys. Rev. Lett.*, 108:196401, May 2012.

[162] J. Feldmann, K. Leo, J. Shah, D. A. B. Miller, J. E. Cunningham, T. Meier, G. von Plessen, A. Schulze, P. Thomas, and S. Schmitt-Rink. *Phys. Rev. B*, 46:7252–7255, Sep 1992.

[163] Karl Leo, Peter Haring Bolivar, Frank Bruggemann, Ralf Schwedler, and Klaus Kohler. *Solid State Communications*, 84(10):943 – 946, 1992.

[164] Christian Waschke, Hartmut G. Roskos, Ralf Schwedler, Karl Leo, Heinrich Kurz, and Klaus Kohler. *Phys. Rev. Lett.*, 70:3319–3322, May 1993.

[165] P. Voisin, J. Bleuse, C. Bouche, S. Gaillard, C. Alibert, and A. Regreny. *Phys. Rev. Lett.*, 61:1639–1642, Oct 1988.

[166] Marcin Mierzejewski and Peter Prelovšek. *Phys. Rev. Lett.*, 105:186405, Oct 2010.

[167] Lev Vidmar, Janez Bonča, Marcin Mierzejewski, Peter Prelovšek, and Stuart A. Trugman. *Phys. Rev. B*, 83(13):134301, April 2011.

[168] F. Sawano, I. Terasaki, H. Mori, T. Mori, M. Watanabe, N. Ikeda, Y. Nogami, and Y. Noda. *Nature*, 437(7058):522–524, September 2005.

[169] Y. Taguchi, T. Matsumoto, and Y. Tokura. *Phys. Rev. B*, 62(11):7015–7018, September 2000.

[170] S. Iwai, M. Ono, A. Maeda, H. Matsuzaki, H. Kishida, H. Okamoto, and Y. Tokura. *Phys. Rev. Lett.*, 91(5):057401, July 2003.

[171] H. Okamoto, H. Matsuzaki, T. Wakabayashi, Y. Takahashi, and T. Hasegawa. *Phys. Rev. Lett.*, 98(3):037401, January 2007.

[172] M. Greiner, O. Mandel, T. W. Hansch, and I. Bloch. *Nature*, 419:51–54, Sep 2002.

[173] Immanuel Bloch. *Nat Phys*, 1(1):23–30, October 2005.

[174] Rongqing Chen and Hua Guo. *Computer Physics Communications*, 119(1):19–31, June 1999.

[175] Satoshi Ejima and Satoshi Nishimoto. *Phys. Rev. Lett.*, 99:216403, Nov 2007.

[176] Takashi Oka, Norio Konno, Ryotaro Arita, and Hideo Aoki. *Phys. Rev. Lett.*, 94:100602, Mar 2005.

[177] D. Poilblanc, T. Ziman, J. Bellissard, F. Mila, and G. Montambaux. *Euro. Phys. Lett.*, 22(7):537, June 1993.

[178] Hantao Lu, Shigetoshi Sota, Hiroaki Matsueda, Janez Bonča, and Takami Tohyama. *Phys. Rev. Lett.*, 109(19):197401, November 2012.

[179] R. A. Gordon, D. Yang, E. D. Crozier, D. T. Jiang, and R. F. Frindt. *Phys. Rev. B*, 65(12):125407, March 2002.

[180] Ming-Wei Lin, Lezhang Liu, Qing Lan, Xuebin Tan, Kulwinder Dhindsa, Peng Zeng, Vaman M. Naik, Mark Ming-Cheng Cheng, and Zhixian Zhou. arXiv e-print 1207.4824, July 2012.

[181] K. Alam and R.K. Lake. 59(12):3250–3254, 2012.

[182] Youngki Yoon, Kartik Ganapathi, and Sayeef Salahuddin. *Nano Lett.*, 11(9):3768–3773, September 2011.

[183] Yifei Yu, Chun Li, Yi Liu, Liqin Su, Yong Zhang, and Linyou Cao. *Sci. Rep.*, 3, May 2013.

[184] Jie Xiao, Daiwon Choi, Lelia Cosimbescu, Phillip Koech, Jun Liu, and John P. Lemmon. *Chem. Mater.*, 22(16):4522–4524, August 2010.

[185] Kartick Bindumadhavan, Suneel Kumar Srivastava, and Sourindra Mahanty. *Chem. Commun.*, 49(18):1823–1825, February 2013.

[186] Haesuk Hwang, Hyejung Kim, and Jaephil Cho. *Nano Lett.*, 11(11):4826–4830, November 2011.

[187] Kun Chang and Weixiang Chen. *ACS Nano*, 5(6):4720–4728, June 2011.

[188] Oriol Lopez-Sanchez, Dominik Lembke, Metin Kayci, Aleksandra Radenovic, and Andras Kis. *Nat Nano*, 8(7):497–501, July 2013.

[189] E. Cappelluti, R. Roldan, J. A. Silva-Guillen, P. Ordejon, and F. Guinea. *Phys. Rev. B*, 88(7):075409, August 2013.

[190] Jiangang He, Kechen Wu, Rongjian Sa, Qiaohong Li, and Yongqin Wei. *Applied Physics Letters*, 96(8):082504, February 2010.

[191] R. H. Miwa and W. L. Scopel. *J. Phys.: Condens. Matter*, 25(44):445301, November 2013.

[192] C. Ataca, H. Sahin, and S. Ciraci. *J. Phys. Chem. C*, 116(16):8983–8999, April 2012.

[193] M. A. Py and R. R. Haering. *Can. J. Phys.*, 61(1):76–84, January 1983.

[194] Andrey N. Enyashin and Gotthard Seifert. *Computational and Theoretical Chemistry*, 999:13–20, November 2012.

[195] V. Petkov, S. J. L. Billinge, P. Larson, S. D. Mahanti, T. Vogt, K. K. Rangan, and M. G. Kanatzidis. *Phys. Rev. B*, 65(9):092105, February 2002.

[196] Andrey N. Enyashin, Lena Yadgarov, Lothar Houben, Igor Popov, Marc Weidenbach, Reshef Tenne, Maya Bar-Sadan, and Gotthard Seifert. *J. Phys. Chem. C*, 115(50):24586–24591, December 2011.

[197] G. Kresse and J. Furthmuller. *Phys. Rev. B*, 54(16):11169–11186, October 1996.

[198] P. E. Blochl. *Phys. Rev. B*, 50(24):17953–17979, December 1994.

[199] G. Kresse and D. Joubert. *Phys. Rev. B*, 59(3):1758–1775, January 1999.

[200] W. Tang, E. Sanville, and G. Henkelman. *J. Phys.: Condens. Matter*, 21(8):084204, February 2009.

[201] Edward Sanville, Steven D. Kenny, Roger Smith, and Graeme Henkelman. *Journal of Computational Chemistry*, 28(5):899–908, 2007.

[202] H. J. Chen, J. Huang, X. L. Lei, M. S. Wu, G. Liu, C. Y. Ouyang, and Xu B. *Int. J. Electrochem. Sci.*, 8(9):2196–2203, 2013.

[203] Dario Alfé. *Computer Physics Communications*, 180(12):2622–2633, December 2009.

[204] Jörg Bünemann, Tobias Schickling, and Florian Gebhard. *EPL (Europhysics Letters)*, 98(2):27006, 2012.

[205] E von Oelsen, G Seibold, and J Bünemann. *New Journal of Physics*, 13(11):113031, 2011.

[206] M. Otani and O. Sugino. *Phys. Rev. B*, 73:115407, Mar 2006.

Curriculum Vitae

Name:	**Davoud Nasr Esfahani**
Born:	21/03/1977, Esfahan, Iran
Contact:	U 206, Groenenborgerlaan 171 2020, Antwerp, Belgium
Email:	dd.nasr@gmail.com
Phone:	+32-484-308438

Education:

2010-2014(expected):	**PhD** Department of physics, University of Antwerp, Belgium.
2005-2008:	**MSC** Department of Physics, Isfahan University, Esfahan, Iran.
1995-2000:	**BCS** Department of Material Engineering, Isfahan University of Technology, Esfahan, Iran.

List of Publications:

- **Davoud Nasr Esfahani**, L. Covaci and F. M. Peeters, *Electric-field-induced shift of the Mott metal-insulator transition in thin films*, Phys. Rev. B. **85**, 085110 (2012).
- **Davoud Nasr Esfahani**, L. Covaci and F. M. Peeters, *Field effect on surface states in a doped Mott-insulator thin film*, Phys. Rev. B. **87**, 035131 (2013).
- **Davoud Nasr Esfahani**, L. Covaci and F. M. Peeters, *Surface correlation effects in two-band strongly correlated slabs*, D Nasr Esfahani, L Covaci, F Peeters, J. Phys.: Condens. Matter **26**, 075601 (2014).
- **Davoud Nasr Esfahani**, L. Covaci and F. M. Peeters, *Non-linear response to electric field in extended Hubbard models*, arXiv:1404.3529v1.
- **Davoud Nasr Esfahani**, O. Leenarts, B. Paroens and F. M. Peeters, *Structural transitions in monolayer* MoS_2 *by lithium adsorption*, submmited.
- K. Martens, J.W. Jeong, N. Aetukuri, C. Rettner, **D.N. Esfahani**, F.M. Peeters, L. Gao, B. Hughes, K. Roche, T. Topuria, P.M. Rice, A. Volodin, J. Van de Vondel5, V.V. Moshchalkov5, S. Van Beek, E. Simoen, B. Douhard, W. Vandervorst, G. Groeseneken, M.G. Samant, S.S.P. Parkin, *Localized Low Dimensional Charge State and Inhibited Field-Effect at the Strongly Correlated Semiconducting VO2 -Dielectric Interface*, preprint.

Conferences and Workshops

- School on Computational Modeling of Materials, 2^{nd}-3^{rd} Dec. 2010, University of Antwerp, Belgium.
- Hands on LDA+DMFT: The LDA+DMFT approach to strongly correlated materials, 5^{th}-11^{th} Oct. 2011, Julich, Germany.
- Correlated Electrons: From models tp Materials, Sep. 2012, Julich, Germany.
- Electronic Correlations and Disorder in Quantum Matter, Apr. 2012, Karlsruhe Institute of Technology.
- Innovations in Strongly Correlated Electronic Systems: Sachool and Workshop, Aug. 2012, ICTP, Italy.
- Frontier in Electronic Materials: Correlation Effects and Memristive Phenomenta, Jun. 2012, Aachen, Germany.

- Green's function methods: the next generation, Jun. 4 2013, University Paul Sabatier, Toulouse, France.

Research Interests

- Proximity effects in strongly correlated heterostructures.
- Generic quantum phase transitions, specially non-equilibrium quantum phase transitions.
- Structural phase transitions in two-dimensional materials.

Computer Skills

Operating systems:	Linux, Windows.
Packages:	Word, Excel, PowerPoint, Latex.
Scripts:	Python, Bash, Gnuplot.
Programming languages:	C/C++(Good), Fortran(moderate).
Libraries:	STL, MPI, Boost/Boost.MPI, CUSP(CUDA).
Scientific Libraries:	Lapack, Arpack++, SPECTS, MKL/Feast, MinPack.
Physics Libraries :	ALPS(DMFT part), TRIQS.
Mathematical software:	MATLAB.
DFT Package:	VASP.

Language Proficiency

- Persian (Native), English (Fluent).